Effect of Molecular Structure on the Optoelectronic Properties of Isoindigo-based Semiconductors

A Thesis Submitted to the College of Graduate and Postdoctoral Studies and Research

In Partial Fulfillment of the Requirements for the Degree of

Doctor of Philosophy

In the Department of Chemistry

University of Saskatchewan

Saskatoon

By

Anindya Ganguly

Supervisor: Dr. Timothy L. Kelly

Permission to Use

Head of the Department of Chemistry
University of Saskatchewan
110 Science Place
Saskatoon, Saskatchewan S7N 5C9
Canada

or

Dean
College of Graduate and Postdoctoral Studies
University of Saskatchewan
110 Science Place
Saskatoon, Saskatchewan S7N 5C9
Canada

Abstract

Organic electronics have developed rapidly over the past few decades. Despite this progress, device performance must be further improved before organic photovoltaic devices and organic field effect transistors can be widely commercialized. Therefore, both the design of new organic semiconductors and understanding how molecular structure affects the optoelectronic properties of these semiconductors are critically important. In this context, this thesis discusses the effect of molecular structure on the optoelectronic properties (e.g., oscillator strength, frontier orbital energies, optical band gap, and charge carrier mobilities) of organic semiconductors.

The thesis deals with two different types of structural modifications to isoindigo-based semiconductors. The first section focuses on the effect of linear-conjugation and cross-conjugation on the oscillator strength of molecular organic semiconductors based on a ring-expanded isoindigo derivative. Compared to isoindigo analogues, extending the conjugation of the π-system through ring fusion substantially red-shifted the absorption maximum of the HOMO to LUMO transition; however, the cross-conjugation significantly reduced the oscillator strength. As a result, the photocurrent was significantly lower for organic photovoltaic devices made with cross-conjugated materials compared to linearly conjugated materials.

The second section discusses the effect of torsional strain in two new polymeric semiconductors, namely poly(ethynyl-*alt*-isoindigo) and polybisisoindigo, on their electron mobilities. The electron mobilities are compared to the control polymer polyisoindigo, which exhibited a relatively poor electron mobility because of a large torsion angle. In the ethynyl-*alt*-isoindigo copolymer, the sterically unencumbered ethynyl spacer helps reduce the torsion angle between adjacent isoindigo units and conserve planarity in the polymer backbone. In polybisisoindigo, every second isoindigo unit was fused together, replacing a single bond between repeating units. This lowers the overall degree of torsional strain in the polymer chain. The increased planarity improved the electron mobility of these new polymers relative to polyisoindigo. Out of the two new polymers, thin-film transistors fabricated using polybisisoindigo displayed the highest electron mobility of 1.26×10^{-3} $cm^2/V\cdot s$. This was attributed to the extended conjugation of the ring-fused bisisoindigo-based system which increased

intra-chain electron transport along the polymer backbone. In addition, the larger size of this ring-fused π-system might have made polybisisoindigo less sensitive towards positional disorder.

In conclusion, a substitution pattern leading to linear conjugation is essential for high oscillator strengths. This increases the absorption coefficient of the material, resulting in a higher photocurrent when incorporated in photovoltaic devices. A minimized torsional strain in the semiconductor backbone is also crucial to improve the charge carrier mobilities.

Acknowledgements

Before anyone else, I want to thank my supervisor Prof. Timothy L. Kelly for his continuous support over the course of my PhD. Not only he supervised me to become a confident researcher, he also guided me to achieve a better writing and presentation skills. Moreover, I have gone through several health issues and I could never forget Tim's unconditional mental support to stay focused.

Many thanks to my advisory committee members- Prof. Jens Mueller, Prof. Michel Gravel, and Prof. Jeremy Lee for their valuable suggestions during our meetings. I am grateful to Prof. Matthew Paige and Prof. Ian Burgess for letting me use their instrument facilities. I am also thankful to Prof. Ron Steer for his valuable lessons and discussions.

I have been serving as a teaching assistant with different lab-managers over the past years. I greatly appreciate the support and suggestions I received from Dr. Pia Wennek, Dr. Alexandra Bartole-Scott, and Dr. Adrian Clark.

I want to thank all of the staffs of Department of Chemistry and Saskatchewan Structural Sciences Centre for their relentless effort to keep all the research facilities and instruments up and running.

All of my colleagues, especially the past and present Kelly group members were extremely cooperative and always ready to help. In particular, I want to thank Dr. Nicholas Randell, Philip Boutin, Soumya Kundu, Kyle Fransishyn and Chase Radford for the insightful discussions we had to develop a better understanding on several scientific topics.

I would not be able to reach this far in my academic life without the endless support of my parents and their faith in me. I must acknowledge my sisters for taking care of my old father and other family matters so I could stay focused on my research. Many thanks to my brother Arpan Gargari for teaching me Photoshop and Illustrator; I would not be able to produce the artwork I placed in this thesis without his lessons.

Finally, I want to thank my wife Arpita for her never ending support and joining me here in Saskatoon leaving her family back in India.

Dedications

I would like to dedicate this thesis to my mother, Late Indira Ganguly.

Table of Contents

List of Figures

List of Charts

List of Schemes

List of Equations

List of Tables

List of Abbreviations and Symbols

AFM	Atomic force microscopy
BBL	Poly(benzobisimidazobenzophenanthroline)
BGBC	Bottom-gate, bottom-contact
BGTC	Bottom-gate, top-contact
BHJ	Bulk heterojunctions
BTPD	5,5′-Dioctyl-1,1′-4H-bithieno[3,4-c]pyrrole-4,4′,6,6′ (5H,5′H)-tetrone
CB	Chlorobenzene
CCL	Crystalline correlation length
CF	Chloroform
D-A	Donor-acceptor
DFT	Density functional theory
DIO	1,8-Diiodooctane
DMF	*N*,*N*′-Dimethylformamide
DPV	Differential pulse voltammetry
DTS(PTTh2)2	5,5′-Bis{(4-(7-hexylthiophen-2-yl)thiophen-2-yl)-[1,2,5]thiadiazolo[3,4-c]pyridine}-3,3′-di-2 ethylhexylsilylene-2,2′-bithiophene
e	Elementary charge
EA	Electron affinity
$E_{F(m)}$	Fermi level of the gate electrode
E_g	Energy band gap
$E_{g,opt}$	Optical band gap

ETL	Electron transport layer
FET	Field effect transistor
FF	Fill factor
FMOs	Frontier molecular orbitals
$f_{\mathrm{osc(exp)}}$	Experimentally-determined oscillator strength
FWHM	Full-width at half-maximum
$g_{\mathrm{(m,sat)}}$	Transconductance in saturation regime
GIWAXS	Grazing-incidence wide angle x-ray scattering
$g_{\mathrm{(m,lin)}}$	Transconductance in linear regime
HOMO	Highest occupied molecular orbital
HTL	Hole transport layer
ICT	Intramolecular charge transfer
I_{DS}	Drain Current
I_{GS}	Gate current
$I_{\mathrm{ON}}/I_{\mathrm{OFF}}$	Current modulation ratio
IP	Ionization potential
IPCE	Incident photon-to-current efficiency
ITO	Indium doped tin oxide
J	Current density
J_0	Reverse saturation current density
J_{max}	Current density at maximum power point
J_{ph}	Photocurrent density
J_{SC}	Short-circuit current density

J-V	Current-Voltage
k_{b}	Boltzmann’s constant
L	Length of conduction channel
LUMO	Lowest unoccupied molecular orbital
MDMO-PPV	Poly[2-methoxy-5-(3′,7′-dimethyloctyloxy)-1,4-phenylenevinylene]
MEH-PPV	Poly[2-methoxy-5-(2-ethylhexyloxy)-1,4-phenylenevinylene]
MIS-FET	Metal-insulator-semiconductor
n	Empirical ideality factor
NIR	Near-Infrared
ODCB	*o*-dichlorobenzene
OFETs	Organic field-effect transistors
OPVs	Organic photovoltaics devices
PCM	Polarizable continuum model
P(NDI2OD-T2)	Poly{[N,N9-bis(2-octyldodecyl)-naphthalene-1,4,5,8-bis(dicarboximide)- 2,6- diyl]-alt-5,59-(2,29-bithiophene)}
P3HT	Poly(3-hexylthiophene)
pBTTT	Poly(2,5-bis(3-alkylthiophen-2-yl)thieno-[3,2-b]thiophene
PC$_{61}$BM	[6,6]-Phenyl C$_{61}$ butyric acid methyl ester
PC$_{71}$BM	[6,6]-Phenyl C$_{71}$ butyric acid methyl ester
PCDTBT	Poly[N-9′-heptadecanyl-2,7-carbazole-alt-5,5-(4′,7′-di-2-thienyl-2′,1′,3′ benzothiadiazole)]
PCE	Power conversion efficiency

PCPDTBT	Poly[2,6-(4,4-bis-(2-ethylhexyl)-4H-cyclopenta[2,1-b;3,4-b′]-dithiophene)-alt-4,7-(2,1,3-benzothiadiazole)]
PDI-FCN2	Bis(2,2,3,3,4,4,4-heptafluorobutyl)-dicyano-perylene tetracarboxylic diimide
PDMS	Polydimethylsiloxane
PEDOT/PSS	Poly(3,4-ethylenedioxythiophene)/polystyrene sulfonate
P_{max}	Maximum power density
PPVs	Poly(p-phenylenevinylene) derivatives
RDC	Relative degree of crystallinity
R_s	Series resistance
R_{sh}	Shunt resistance
SCLC	Space charge limited current
TDDFT	Time-dependent density functional theory
TGBC	Top-gate, bottom-contact
TGTC	Top-gate, top-contact
UV-vis	Ultra violet and visible light
V	Applied voltage
V_{DS}	Voltage applied between the source and drain electrodes
V_{GS}	Voltage applied to the gate electrode
V_{max}	Voltage at maximum power point
V_{OC}	Open circuit voltage
V_T	Thresold voltage
W	Width of conduction channel

μ	Charge carrier mobility
μ_e	Electron mobility
μ_h	Hole mobility
μ_{lin}	μ in linear regime
μ_{sat}	μ in saturation regime
Φ_m	Metal workfunction

Chapter 1 - Introduction

The year 1977 was the beginning of organic electronics. In this year, it was reported that polyacetylene could be doped to substantially improve its conductivity, paving the way toward the field of organic electronics.[1-2] Later in 2000, Alan Heeger, Alan MacDiarmid, and Hideki Shirakawa won the Nobel Prize in Chemistry for the discovery and development of conductive π-conjugated polymers. Their discovery opened up a new possibility of producing functional electronic devices with mechanical flexibility, impact resistance and optical transparency, which are challenging features to achieve with conventional silicon-based devices.

1.1 Organic Semiconductors

Most organic molecules are insulators because of the localized nature of their bonding, with large energy gaps between σ-σ^* and π-π^* orbitals. However, some conjugated organic polymers and conjugated molecules in the solid state can behave as semiconductors. Organic materials become semiconducting in nature because of delocalization of the π-electrons in a system with extended conjugation. To understand the semiconducting behavior of poly(acetylene), we can start from ethylene and gradually extend the π-conjugation length. In ethylene, π bonding and π^* antibonding orbitals represent the highest occupied molecular orbital (HOMO) and lowest unoccupied molecular orbital (LUMO), respectively (Figure 1.1). With an additional π-bond in 1,3-butadiene, there are two bonding and two antibonding orbitals. Noticeably, the energy gap between bonding and antibonding orbitals is smaller each time a π-bond is added. In the case of poly(acetylene), the conjugation is extended up to ‘n’ ethylene units, where the large number of π-orbitals are so closely spaced on the energy scale that it leads to a continuum of energy levels, considered as bands. For a poly(acetylene) chain with a semi-infinite length, the polymer is expected to be metallic; π-electrons should be fully delocalized over the entire chain, leading to equal bond lengths. However, in practice, poly(acetylene) has an alternating structure of single and double bonds generating two degenerate states. This is termed a Peierls distortion and generates a discrete band gap between the valence band (π-bonding orbitals) and the conduction band (π-antibonding orbitals). Hence, poly(acetylene) behaves as an organic semiconductor.

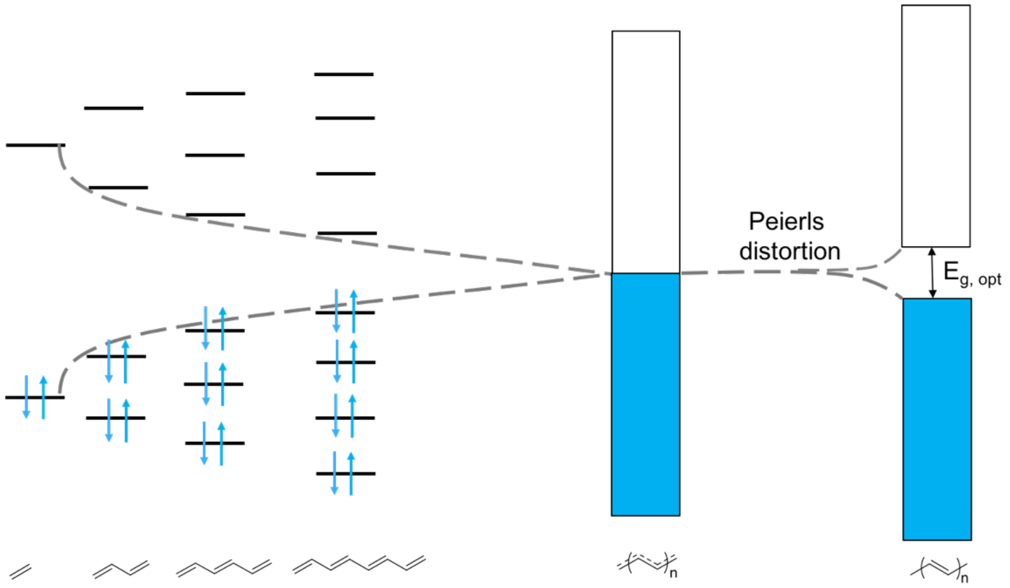

Figure 1.1 Depiction of band formation in polyacetylene starting from molecular orbital diagram of alkenes.

Unlike polymeric materials, extended conjugation is not enough to make an organic molecule a semiconductor. For example, in spite of five fused benzene rings in pentacene, the electronic structure does not lead to any energy continuum and only affords discrete energy levels. The interaction between organic molecules in the solid state is essential for imparting semiconductivity. The electronic coupling because of intermolecular π-π stacking further splits the energy levels of two stacked pentacene molecules. When the number of orbitals is large as in a macroscopic solid, it leads to the formation of narrow bands with a discrete band gap and semiconducting behavior (Figure 1.2).

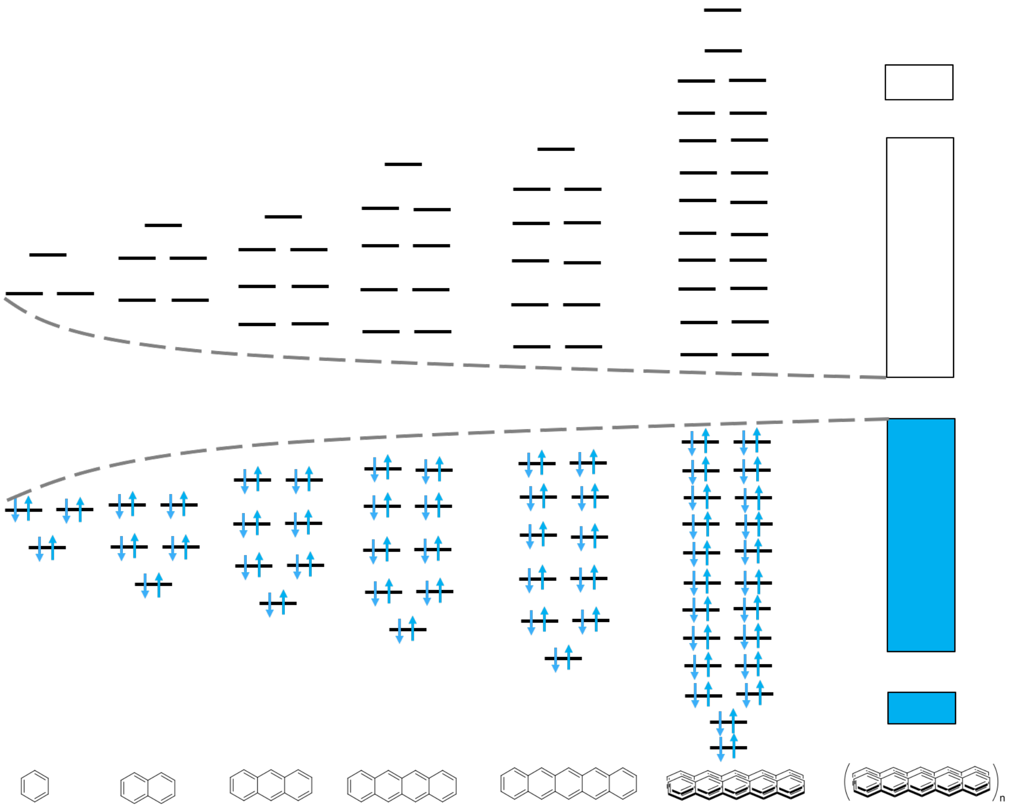

Figure 1.2 Depiction of band formation of pentacene in solid state.

The basic structure of organic semiconductors, therefore, is defined as π-conjugated networks stacked by weak van der Waals forces. However, the kinks and twists in the polymer chains or defects in the molecules limit the accessible conjugation length in the semiconductor, resulting in different conjugated segments. Because of this variation in conjugation length in polymers and poor overlap in molecular semiconductors, organic semiconductors do not form well-defined and highly-delocalized energy bands, as do inorganic semiconductors. Given the presence of energetic and positional disorder alongside the strong electron-phonon coupling, electrons in organic semiconductors are predominantly confined to individual molecules.[3-4] As a result, charge transport in organic semiconductors takes place through thermally-assisted hopping or tunneling of carriers between contiguous localized states.[5] Figure 1.3 illustrates the density of states plot of an organic semiconductor, centered around the HOMO and LUMO energies. As the degree of macroscopic delocalization is low compared to inorganic semiconductors, the full width at half maximum of these bands is significantly smaller; therefore, the terminology of molecular orbital theory (HOMO and LUMO) is often used instead of valence band and conduction band to describe these organic materials. The energy difference between the HOMO and LUMO can be measured by the onset of absorption in the solid-state UV-vis spectrum of the material and is termed the optical band gap ($E_{g,opt}$).

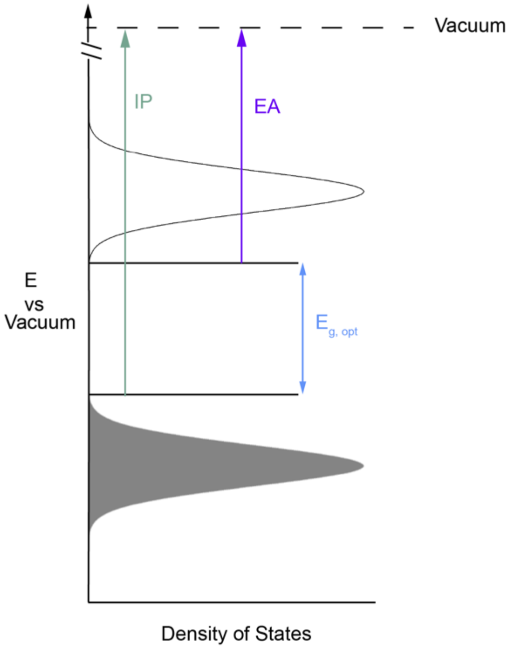

Figure 1.3 Density of states approximation of an organic semiconductor. It depicts the electron affinity (EA), ionization potential (IP), and optical band gap ($E_{g,opt}$).[6]

1.2 Organic Photovoltaics

Rapid population growth has led to a sharp increase in energy consumption across the globe. This global requirement is expected to rise by 28% between 2015 and 2040, as predicted by the US Energy Information Administration.[7] Fossil fuels have been the primary way of meeting this ever increasing demand over the last century. Greenhouse gases, released from burning of these fossil fuels, have increased the global temperature by 1.0 °C over the last 115 years (1901-2016).[8-9] Further use of fossil fuels will likely increase the global temperature by another 4.0 °C by the end of this century. Renewable energy is the safest alternative for meeting energy demands without affecting the climate.

In 1954, Chapin, Fuller, and Pearson invented the first solar cell incorporating a silicon p-n junction with a power conversion efficiency (PCE) of 6%.[10] However, photovoltaic technology remained a cost intensive way to produce power for a number of decades, primarily because of the energy intensive purification of silicon. Nevertheless, demand for sustainable energy resources has expedited the development of silicon technology. The average module price dropped to US\$0.40 W^{-1} in 2016 from US\$4 W^{-1} in 2006.[11] This cost reduction massively accelerated the commercial use of solar power. As a result, global photovoltaic capacity increased from 7 GW in 2006 to 300 GW in 2016.

This exponential growth of Si-based photovoltaics has encouraged researchers to explore other photovoltaic technologies, including organic photovoltaic devices (OPVs).[12] Organic semiconductors have certain advantages which can never be achieved with traditional inorganic semiconductors like silicon. In the case of inorganic semiconductors, atoms are held together by strong covalent or ionic bonds, leading to crystalline three-dimensional structures. These crystalline structures involve substantial orbital overlap, resulting in efficient charge transport via highly delocalized bands. However, these robust structural motifs do not allow processability from solutions at room temperature; rather, they are commonly deposited or patterned via energy intensive and expensive methods involving high temperature and vacuum. In contrast, organic semiconductors are discrete molecules or macromolecules held together by weak van der Waals forces. As a result, organic semiconductors are soluble in common organic solvents and can be processed from solution using low-cost deposition methods such as roll-to-roll printing. Given the weakly bound structure of organic materials, they can be mechanically flexible, which enables device fabrication on flexible substrates such as plastic, paper or even fabrics. Moreover, the frontier molecular orbitals (FMOs) of organic semiconductors can be tuned by modifying the molecular structures; therefore, the optoelectronic properties of these organic materials can be tailored as required. For example, organic materials can be synthesized with aesthetically pleasing colors when a solar panel needs to be installed on a backpack or fabric. The frontier molecular orbitals can also be tailored to absorb in the near-infrared (NIR) region so a cell can be transparent and installed on window glass.

1.2.1 Device Physics

To realize the potential of OPVs, understanding the fundamental device physics is important.[13-14] In a circuit, OPVs can be compared to batteries. In a battery, chemical energy is used to generate a cell potential between two terminals and power is extracted when a load is connected. As shown in Figure 1.4, solar energy is used in a solar cell compared to chemical energy in a battery. When a solar cell is illuminated, positive (hole) and negative (electron) charge carriers are generated and a voltage develops between the two terminals, analogous to the cell potential of a battery. This voltage between the isolated terminals (infinite resistance) is called the open-circuit voltage (V_{OC}). When both terminals are connected to a load (R2) this generates a voltage between 0 and V_{OC} and draws a current as per Ohm's law.

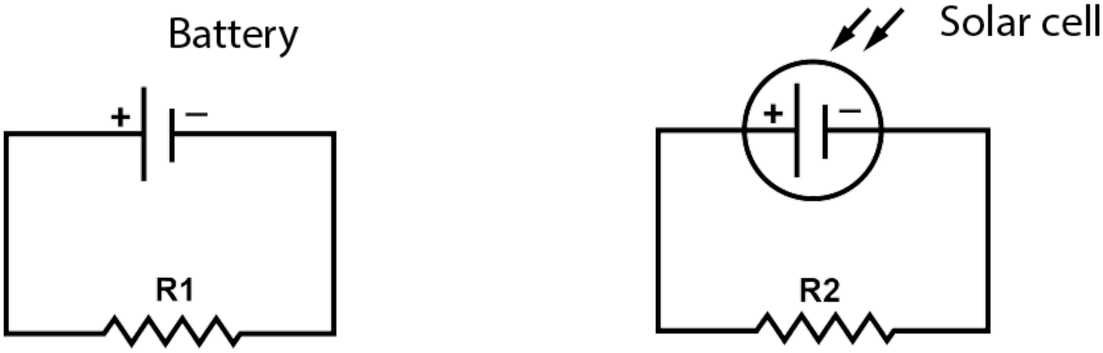

Figure 1.4 A solar cell is equivalent to a battery in a simple circuit.

Like other photovoltaic devices, OPVs are photodiodes and the basic device physics is similar to a silicon solar cell. In the absence of any light, a solar cell acts as a diode. An ideal diode is a device which allows current to flow in one direction between its terminals, but resists current flow in the opposite direction. When an external voltage is applied in the dark, a diode produces a current called the dark current. This dark current can be expressed by the Shockley diode equation (Equation 1.1).

$$J\,(V) = J_0[exp\left(\frac{eV}{k_b T}\right) - 1] \qquad \text{Equation 1.1}$$

J is the current density as a function of applied voltage V. J_0 is the reverse saturation current density. It is a measure of the leakage current through the diode and is usually very small. J_0 is independent of applied voltage but depends on temperature. The remaining terms include the elementary charge (e), Boltzmann's constant (k_b), and the temperature (T). When the cell is illuminated, another current is generated which is called the photocurrent (J_{ph}). The photocurrent always works against the dark current. Therefore, the Shockley diode equation can be modified as shown in Equation 1.2. Conventionally, in the field of photovoltaics, the direction of the photocurrent is considered positive, and the dark current is negative.

$$J\,(V) = J_{ph} - J_0[exp\left(\frac{eV}{k_bT}\right) - 1] \qquad \text{Equation 1.2}$$

In reality, no solar cell works according to the ideal circuit model in Figure 1.5; therefore, a modified circuit model is needed to represent the non-ideal behavior. As shown in Figure 1.5, two parasitic resistances are added to the equivalent circuit model. The resistance added in series is called the series resistance (R_s) and the resistance in parallel is called the shunt resistance (R_{sh}). The R_s impedes the photocurrent flow, and therefore it should be zero for an ideal cell. Specifically, the series resistance can build up because of a number of factors, such as interfacial Ohmic resistance and poor charge carrier mobility of the organic semiconductor. The shunt resistance functions to resist the current flow in alternative pathways. Therefore, unlike the series resistance, R_{sh} should be infinitely large for an ideal cell. A high shunt resistance reduces counterproductive pathways such as leakage current and geminate recombination, forcing the photocurrent to flow in the desired direction. The modified Shockley diode equation for a solar cell behaving non-ideally is presented in Equation 1.3. The term n in this equation represents the empirical ideality factor of a diode which is a measure of how closely the diode follows the ideal diode equation. Therefore, the term n measures the junction quality and indicates the type of recombination mechanisms that force a diode to deviate from ideality.

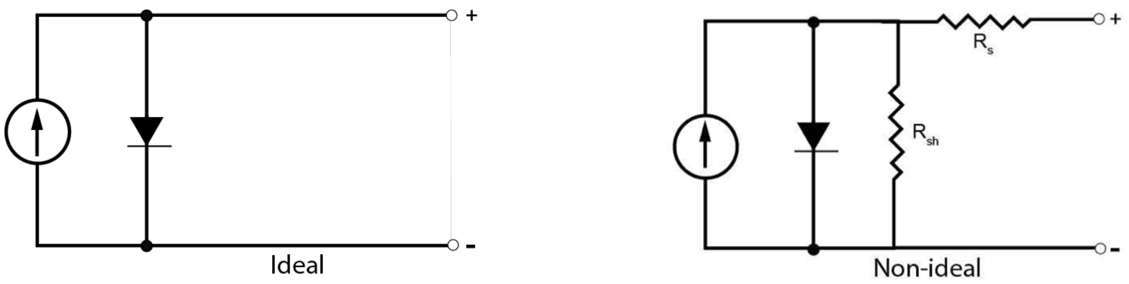

Figure 1.5 Equivalent circuit models for ideal and non-ideal solar cells.

$$J\,(V) = J_{ph} - J_0[exp\left(\frac{e(V + JR_s)}{nk_bT}\right) - 1] - \frac{(V + JR_s)}{R_{sh}} \qquad \text{Equation 1.3}$$

A solar cell would need to be tested against a series of loads to record its full *J-V* curve; however, a source measure unit is used to make the measurement easier where the diode potential is swept linearly and the output current is recorded. Figure 1.6 depicts the *J-V* characteristics of a solar cell which provides all the parameters needed to calculate its PCE. The maximum power density is denoted by P_{max} and represents the point where the product of current density and voltage has the highest value on the *J-V* curve. The *J* and *V* value at the maximum power density point are referred to as J_{max} and V_{max}, respectively. The short-circuit current density (J_{SC}) is the current density of a device when the voltage across the cell is zero. As mentioned earlier, the V_{OC} is the voltage when the terminals are not connected ($J = 0$). However, no power can be extracted at either of these two points. The product of J_{SC} and V_{OC} is an important parameter to define the fill factor (*FF*) of a device. The *FF* is defined as the ratio of P_{max} and the product of J_{SC} and V_{OC}. Graphically, the ratio of the area of the red rectangle to the area of the blue one in Figure 1.6 is the fill factor. Therefore, it is a measure of the 'squareness' of the *J-V* curve. In other words, the squarer the *J-V* curve, the higher the PCE of a cell. The PCE is the standard parameter used to compare the performance of a solar cell. It is defined as the ratio of power output from a solar cell to power input (P_{in}) from the illumination source. The shunt resistance (R_{sh}) and the series resistance (R_s) can roughly be calculated from a *J-V* curve assuming that any device behaves as a linear Ohmic resistor near V_{OC} and J_{SC}. The series resistance is equal to the inverse of the slope of the line as it passes through V_{OC} and the shunt resistance can be estimated by the inverse of the slope of the line passing through J_{SC}.

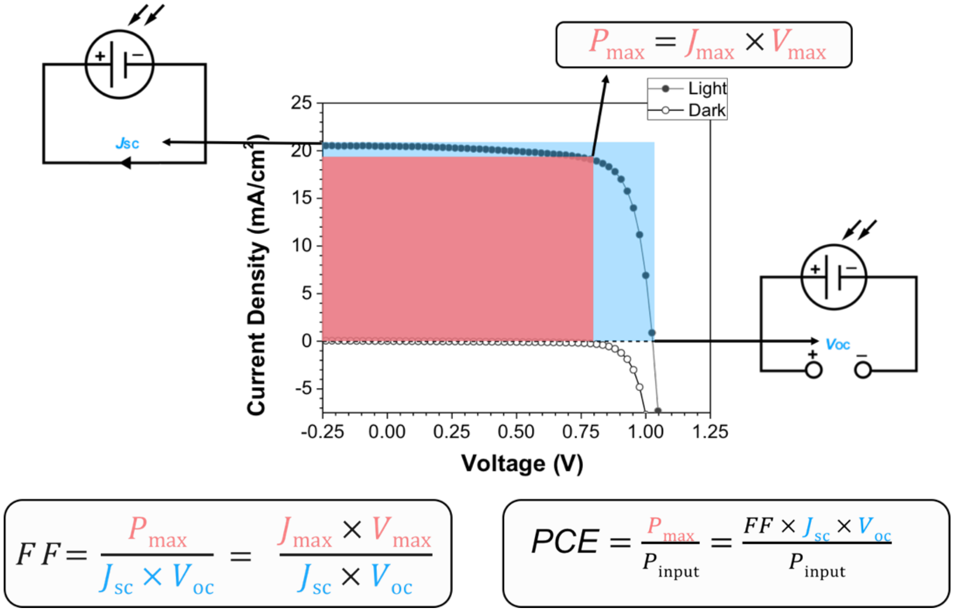

Figure 1.6 Sample *J-V* curves under light and dark, denoting the *J-V* parameters: V_{OC}, short circuit current density (J_{SC}), maximum power density (P_{max}), fill factor (*FF*), and PCE.

1.2.2 Working Principle

OPVs consist of a multilayered structure. The layer responsible for absorbing sunlight is called the active layer of a device. This active layer is sandwiched between electrodes and made of two semiconductors: a p-type semiconductor and an n-type semiconductor. The process of charge transfer at the interface of these two semiconductors is presented in Figure 1.7 a.[12-13, 15] Once the active layer of a cell is illuminated by sunlight, an exciton is generated because of the photo-excitation of one of the semiconductors. The excitons are predominantly generated in the p-type semiconductor when fullerene derivatives (Figure 1.7 b) are used as the n-type material because of their weak absorption in the visible region. An exciton is a bound electron-hole pair, which are attracted because of the electrostatic coulomb interaction. Because of the low dielectric permittivity of organic materials, the generated exciton cannot be dissociated into free charge carriers by ambient thermal energy. In order to dissociate into free charges, the exciton randomly diffuses towards the interface of the p-type and n-type semiconductors. After reaching the interface, the electron transfers to the LUMO level of the n-type material and the exciton dissociates. An energy offset greater than 0.3 eV between the LUMO level of the two semiconductors is usually required for an exciton to dissociate.[16-17] After the exciton dissociates, free electrons and holes diffuse to their respective electrodes and power can be extracted when the external circuit is completed. To achieve a commercially competitive PCE, all of the interfacial procedures described above need to be optimized. Hence, the following section will focus on each different layer separately.

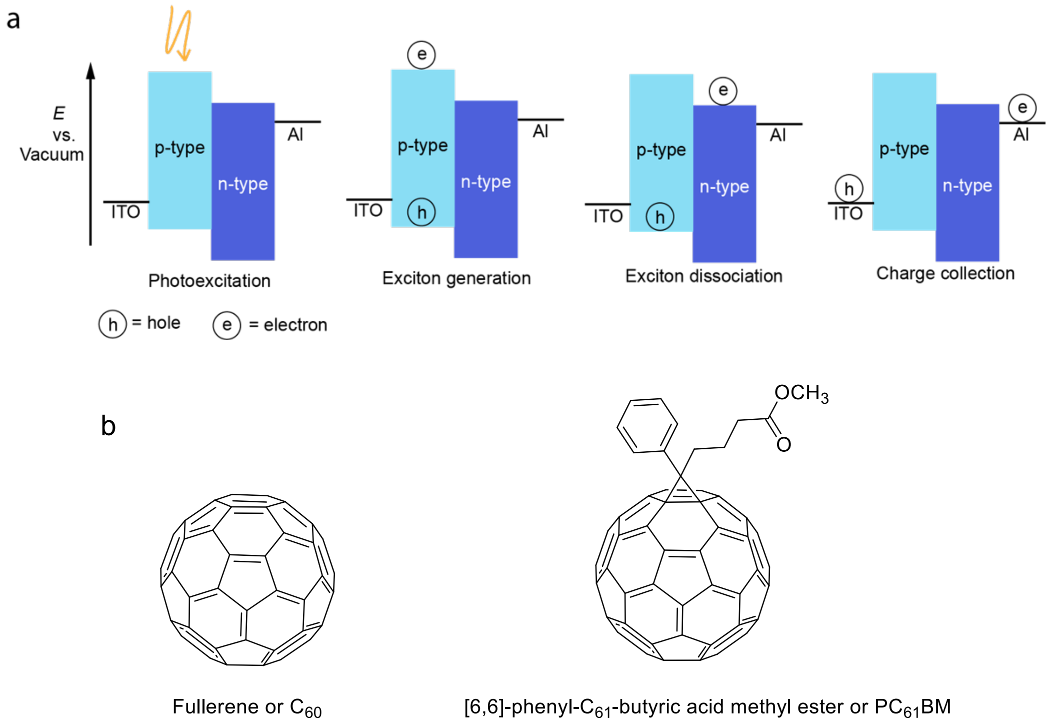

Figure 1.7 (a) Energy band diagram to depict the functioning of a simple organic photovoltaic device, (b) structure of C_{60} and phenyl-C_{61}-butyric acid methyl ester **(**$PC_{61}BM$).

1.2.3 Architecture

1.2.3.1 Active Layer

There are two different types of active layers commonly used for OPVs: planar heterojunctions and bulk heterojunctions (BHJ). A planar heterojunction is a bilayer structure where a layer of p-type material is in contact with another n-type material at a single junction (Figure 1.8). Tang et al. in 1986 were the first to report the planar heterojunction architecture; their device was composed of p-type copper phthalocyanine and n-type perylene diimide.[18] It showed a maximum PCE of 0.95%. These devices suffered from a poor J_{SC} (2 mA·cm^{-2}) because of a low driving force for charge separation and poorly absorbing active layers. The emergence of the carbon allotrope fullerene (C_{60}) as an n-type material took OPV research to the next level. After demonstrating photoinduced electron transfer from the p-type semiconductor poly[2-methoxy-5-(2-ethylhexyloxy)-1,4-phenylenevinylene] (MEH-PPV) to fullerene in 1992[19], Saricifitci et al. subsequently used a planar heterojunction of MEH-PPV:C_{60} as a photodiode sandwiched between indium tin oxide (ITO) and gold electrodes. Owing to the poor photocurrent density ($J_{SC} = 2.08 \times 10^{-3}$ mA·cm^{-2}), these devices exhibited a maximum PCE of only 0.04%.[20]

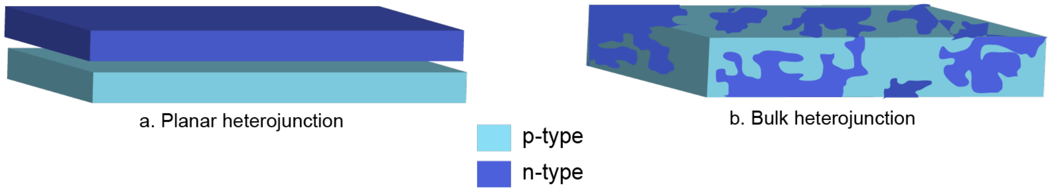
a. Planar heterojunction

b. Bulk heterojunction

Figure 1.8 Different type of active layers in OPVs – (a) planar heterojunction, and (b) bulk heterojunction.

Excitons in organic semiconductors have a limited diffusion length of 10-20 nm; therefore, only 20-40 nm of a 100 nm thick active layer effectively produces photocurrent. Excitons generated within 20 nm of the heterojunction between the p-type and n-type semiconductors can reach the interface to split into free charge carriers. This suggests that the ideal thickness of a polymer film should be no more than 40 nm, which is too thin to absorb all of the incident sunlight and generate a reasonable photocurrent. This fundamental problem of balancing the film thickness with efficient exciton dissociation was solved by Yu et al. in 1995 by introducing the BHJ layer.[21]

In a BHJ layer, a thin film is deposited from a single solution containing both p-type and n-type semiconductors which yields a phase separated blend of the two materials. The characteristic interpenetrated domain size is on the nanoscale, because of the mixing of the two components; therefore, excitons can reach the interfacial boundary before geminate recombination occurs (Figure 1.9). This solves the problem of inefficient charge extraction while having a 100 nm thick film for sufficient light absorption. In the report by Yu et al., a thin film was cast from a solution containing MEH-PPV and phenyl-C_{61}-butyric acid methyl ester. The maximum PCE achieved by these BHJ devices was 2.9% which was higher by two orders of magnitude compared to their planar heterojunction counterparts. Phase separation on the nanoscale was one of the critical factors allowing BHJs to achieve high photocurrent density. Further optimization of the film morphology is currently the focus of many researchers. One popular strategy is to use solvent additives while casting the film.[17, 22] 1,8-Diiodooctane (DIO), 1,8-octanedithiol, and chloronapthalene have all been successfully used to improve the PCE of devices. These are liquids with high boiling points, which helps slow down the crystallization of active layer components, relative to films cast without additives. Efforts to further optimize the blend morphology of BHJ layers are ongoing. The vacuum deposited planar heterojunction is also still a popular area of research; however, the work presented in this thesis uses exclusively the bulk heterojunction architecture.

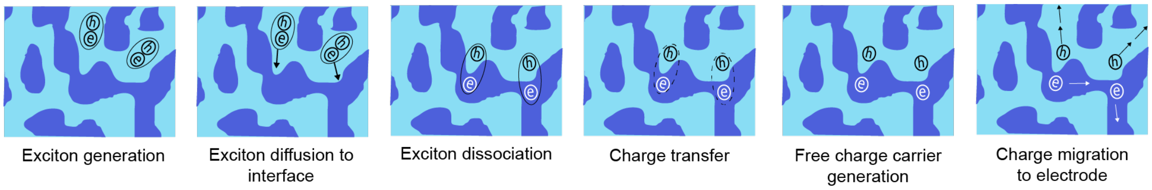

Figure 1.9 Charge separation and transfer in an active layer blend of a BHJ.

1.2.3.2 Interlayers and Electrodes

Even though the active layer is entirely responsible for harvesting solar energy, the other layers and electrodes of a BHJ architecture are also important as they play a major role in transporting and collecting charges. The architecture of OPVs was simple in its early period of development and consisted of three layers. An active layer was sandwiched between an ITO electrode and a thermally evaporated metal electrode. This basic structure was associated with two main disadvantages.[22] First, the mismatch between the workfunction of the electrodes and the frontier orbital energies of the active layer components often led to large energy barriers to charge extraction. This diminished both V_{OC} and the FF because of charge accumulation at the electrode-active layer interfaces. Second, ITO and metal electrodes have poor selectivity towards any specific charge carrier, making recombination at the electrode interfaces unavoidable. This lowers the shunt resistance and results in lower photocurrent density. Since both hole-conducting and electron-conducting domains are in contact with both electrodes because of the uniform generation of excitons throughout the active layer, this recombination loss is more evident for the BHJ architecture. To fix these two issues, ‘interlayers’ or ‘buffer layers’ are inserted between the active layer and the electrodes.[23-25] These materials are semiconductors with frontier orbitals tuned to selectively transport only a specific charge carrier. For instance, the HOMO of a hole transport layer (HTL) must be aligned with the HOMO of the p-type semiconductor of the active layer so it can transport the hole. In contrast, the LUMO of the HTL must be higher in energy than the LUMO of the n-type material to block electron transport. In a similar way, an electron transport layer (ETL) has the LUMO level aligned with the LUMO of the n-type material to allow the passage of an electron; however, it has a poorly aligned HOMO level compared to the p-type semiconductor to block holes. In addition to properly aligned HOMO or LUMO levels, these materials should meet other criteria: (i) providing Ohmic contacts between the electrodes and the active layer, (ii) have a sufficient charge carrier mobility to lessen resistive losses, (iii) must be optically transparent in the UV-Vis-NIR region to minimize optical losses, (iv) must be chemically inert and stable to prevent any unwanted reactions with the active layer and electrodes, and (v) should be able to produce mechanically robust films at low cost. Several classes of materials have been reported to be used as interlayers, such as conducting polymers, metal oxides, cross linkable materials, conjugated polymer electrolytes, self-assembled functional molecules and graphene-based materials.[26-27] By selecting the right interlayer material, a single electrode material can be used for transporting either holes or electrons. For example, ITO can be used both as a hole or electron collecting electrode. Based on this adaptability towards charge carrier selection, bulk heterojunction architectures can be of two different types: regular and inverted.

Figure 1.10 depicts the regular architecture of a BHJ. Here ITO acts as the anode to collect holes while Al serves as the cathode to collect electrons. To use ITO as the anode, a layer of poly(3,4-ethylenedioxythiophene):polystyrene sulfonate (PEDOT:PSS) is used as the HTL.[28] PEDOT is a polythiophene derivative with a high conductivity of 0.2-2 mS/cm used in conjunction with the polyelectrolyte PSS to increase its solubility in water. The LiF serves as the ETL and blocks the passage of holes by creating dipole across the active layer/LiF/Al interface which helps electrons to reach the electrode effectively, thereby avoiding recombination at the electrode surface. LiF also serves as a barrier to stop the degradation caused by the interaction between PCBM and the Al-electrode.[29] Since LiF is an electrical insulator with a band gap of 12 eV,[30] the LiF layer must be thin enough (< 1 nm) to minimize any additional series resistance.[29]

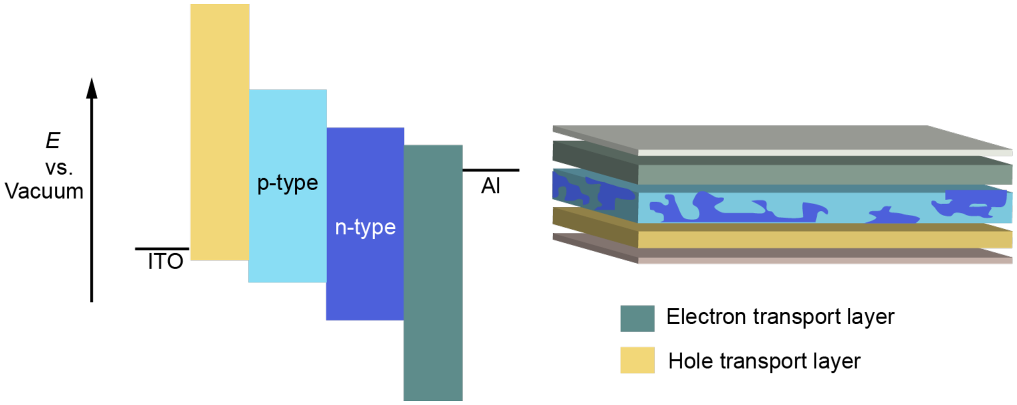

Figure 1.10 Energy level diagram of an OPV with regular architecture.

In the inverted architecture, the electrodes are reversed; ITO is used as the cathode, along with a high workfunction metal (e.g., Ag) as anode (Figure 1.11). In order to use ITO to collect electrons in this architecture, a layer of ZnO serves the role of the ETL. A hole transport layer such as MoO_3 is commonly deposited on top of the active layer.

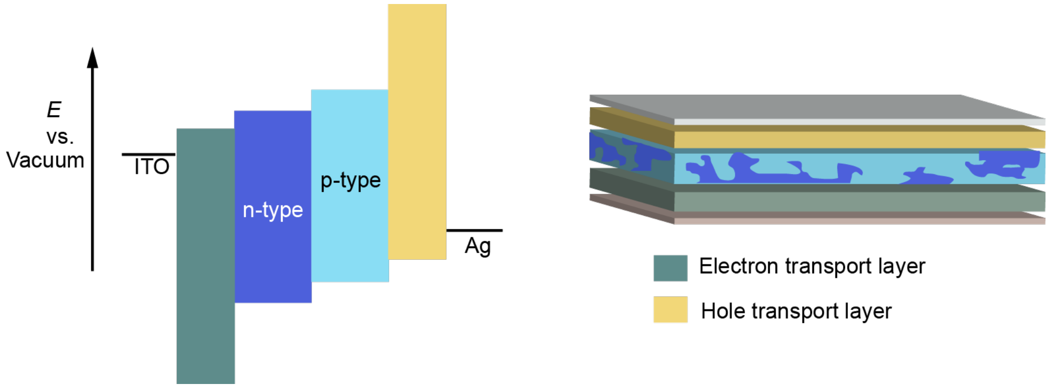

Figure 1.11 Energy level diagram of an OPV with inverted architecture.

The work presented in this thesis exclusively uses the regular architecture for OPV fabrication. However, it is worth mentioning that the inverted architecture is typically more stable than the regular one. The regular architecture suffers from degradation of the ITO anode because of etching by the acidic and hygroscopic PEDOT:PSS. Because of the hygroscopic nature of PEDOT:PSS, water molecules can also easily infiltrate into the active layer, leading to overall device degradation.[31] Furthermore, the regular architecture uses low work function metals such as Al or Ca as the cathode, which are prone to oxidation in ambient atmosphere. The inverted architecture eliminates the use of PEDOT:PSS and uses high work function metals, which makes it more stable.

1.3 Organic Thin-film Transistors

Soon after their invention by John Bardeen and Walter Brattain at Bell Laboratories in 1947,[32] transistors became a fundamental building block of modern electronic devices. Transistors are used to either amplify signals or as on-off switches. The field effect transistor (FET) is one of the various types of transistors. In the mainstream semiconductor industry, FETs are essential devices for constructing microprocessors, solid-state memories (e.g., DRAM, Flash), graphics adapters, mobile communication chips, and active-matrix displays.[33] Organic field-effect transistors (OFETs) are FETs fabricated with an organic semiconductor. Similar to OPVs, OFETs can be fabricated on mechanically flexible surfaces. The following example elaborates the possible applications of OFETs in electronics. Zschieschang et al. showed that OFETs can be incorporated on banknotes as an anti-counterfeiting feature.[34] OFETs are thinner (< 250 nm) than the thinnest silicon-based FETs (~ 20 μm), and work at low voltages (~ 3 V), making it easy to incorporate them in banknotes without damaging the paper. In addition, owing to the flexibility of organic semiconductors, OFETs can endure repeated crumpling, creasing and sharp folding. OFETs can also serve in medical applications. These flexible carbon-based electronic devices can be mechanically compliant with biological systems. Hence, this technology is potential to build artificial skin for burn victims and develop other prosthetics with tactile sensitivity, which can revolutionize cosmetic surgery.[35]

1.3.1 Device Physics

A field effect transistor is a three-terminal device which modulates the current flow between two electrodes, namely the source and drain electrodes, with the help of a bias applied to a third electrode called the gate electrode. The concept of the FET was first reported in 1930,[36] although the first successful devices were made later in 1960.[37] In this patented architecture, the gate electrode was electrically insulated from the conducting channel by a dielectric layer of SiO_2. This metal-insulator-semiconductor (MIS-FET) is the basic framework of OFETs (Figure 1.12). In this framework, the organic semiconductor and the gate electrode are capacitively coupled so that a voltage applied on the gate electrode can induce charges at the semiconductor-dielectric interface. These charge carriers can easily be drained through the drain electrode by applying another voltage between the source and drain electrodes.

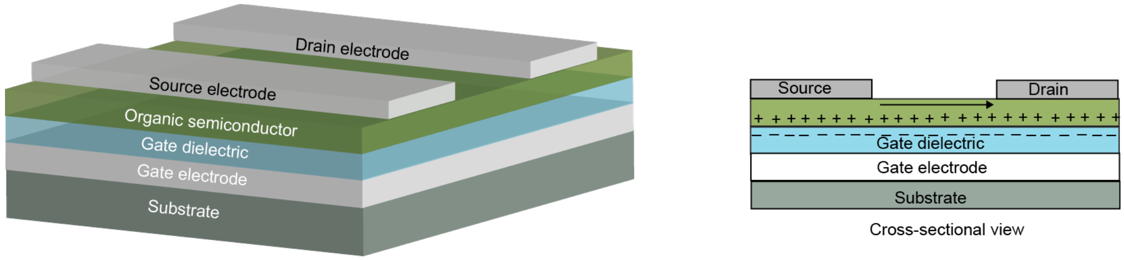

Metal-insulator-semiconductor (MIS) stucture for OFETs

Cross-sectional view

Figure 1.12 Metal-insulator-semiconductor structure of an OFET with a cross-sectional view.

The working principle of an OFET can be better explained by an energy-level diagram across an ideal semiconductor/insulator interface, presented in Figure 1.13.[38] The term ‘ideal’ here means that the bands are considered flat with zero applied voltage. The flat band condition at zero applied voltage is applicable only when $\Phi_m = IP - \frac{E_g}{2}$ (Figure 1.13a), where Φ_m is the metal workfunction (i.e. the amount of energy needed to remove one electron from the metal to a point in the vacuum). E_g is the energy band gap of the organic semiconductor. Under these conditions, the system is at thermal equilibrium and the Fermi levels are aligned. When a negative voltage ($V_{GS} < 0$, where V_{GS} denotes the voltage applied to the gate electrode with respect to the source electrode) is applied to the gate, the Fermi level of the gate electrode ($E_{F(m)}$) is raised, causing the HOMO and LUMO levels of the semiconductor to bend upward near the interface. This results in the accumulation of positive charges at the semiconductor-dielectric interface (p-channel transistor) and eventually forms a conduction channel between the source and drain electrodes (Figure 1.13b). When a negative voltage is applied between the source and drain electrodes ($V_{DS} < 0$), the accumulated charge is collected by the drain electrode resulting in an electric current (I_{DS}) (Figure 1.13c). The transport of negative carriers in this conduction channel is blocked because of mismatch of the LUMO of the organic semiconductor and the Fermi level of the metal contact. The transport physics in a n-channel transistor can be explained by the same reasoning. With a positive gate voltage with respect to the source ($V_{GS} > 0$), the frontier energy levels bend downward, which results in an accumulation of negative charge (n-channel transistor). This can be drained by applying a positive bias ($V_{DS} > 0$) on the source with respect to the drain electrode, generating a current I_{DS}(Figure 1.13d,e). The transport of positive carriers in n-channel transistors is blocked because of mismatch of the HOMO of the organic semiconductor and the Fermi level of the metal contact. As shown in Figure 1.13, it may seem that any organic semiconductor can be used to make both n-channel or p-channel transistors by changing the polarity of the applied gate voltage, although this is not true in most cases. In OFETs, the source and drain electrodes are in direct contact with an intrinsic semiconductor. The conduction of one carrier type is more efficient in most cases, depending on the difference in internal reorganization energies of the semiconductor and the workfunction of the electrodes relative to the HOMO and LUMO of the semiconductor. However, if a single semiconductor has a relatively small bandgap (i.e., on the order of a few hundred meV), then that material can be used as either a p-channel or n-channel transistor only by varying the polarity of the gate voltage; this is known as an ambipolar transistor. In this case, the barrier heights between the HOMO/LUMO of the semiconductor and the Fermi level of the source/drain contacts are quite low, allowing balanced and efficient charge transport of both holes and electrons. Most organic semiconductors possess a band gap larger than 1.5 eV; therefore injection of one type of charge carrier is usually preferred and they are not ambipolar.

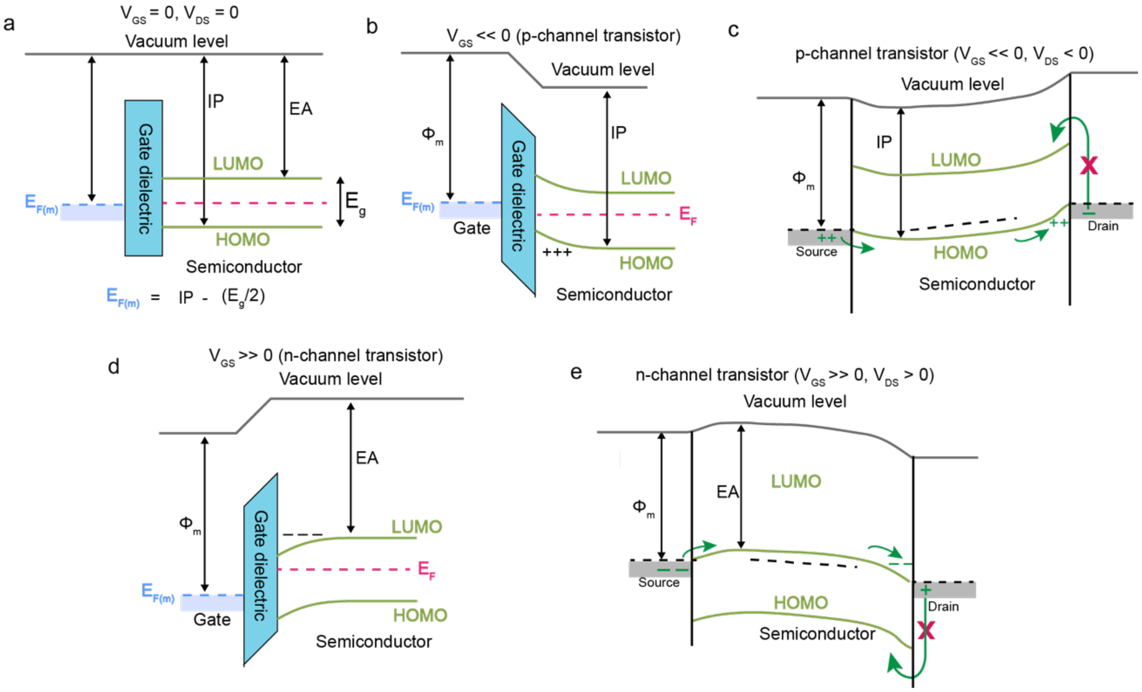

Figure 1.13 Energy level diagrams across the semiconductor-dielectric interfaces and along the conduction channel of the organic semiconductor - (a) flat band condition ($V_{GS} = 0$), (b) accumulation of positive charge carriers ($V_{GS} < 0$), and (c) transport of positive carriers from the source to drain through organic semiconductor for p-channel transistor, (d) accumulation of negative charge carriers ($V_{GS} > 0$); (e) transport of negative carriers from the source to drain through organic semiconductor for n-channel transistor. Here $\boldsymbol{\Phi_m}$ is the metal work-function. The *IP* and *EA* represent the ionization potential and electron affinity of the semiconductor, respectively. $E_{F(m)}$ and E_F are the Fermi energy level of the gate electrode and the organic semiconductor, respectively. E_g represents the energy band gap of the semiconductor.

1.3.2 Device Parameters

The performance of any OFET is commonly summarized by the following three critical parameters:[39-40]

Charge carrier mobility ($\boldsymbol{\mu}$): The charge carrier mobility is the average charge carrier drift velocity per unit applied electric field and describes how fast a charge carrier hops through the semiconducting layer. μ is usually calculated from either of these following two equations (Equation 1.4, and Equation 1.5). These standard equations are as follows:

$$\mu_{lin} = \frac{L}{WC_{ox}V_{DS}}\left(\frac{\partial I_{DS,lin}}{\partial V_{GS}}\right) \qquad \text{Equation 1.4}$$

$$\mu_{sat} = \frac{2L}{WC_{ox}}\left(\frac{\partial \sqrt{I_{DS,sat}}}{\partial V_{GS}}\right)^2 \qquad \text{Equation 1.5}$$

μ_{lin} is calculated from the linear regime of the plot I_{DS} *vs* V_{GS} where $\left(\frac{\partial I_{DS,lin}}{\partial V_{GS}}\right)$ is the slope of the plot. L and W are the length and width of the channel, respectively; C_{ox} is the capacitance of the insulator per unit area.

μ_{sat} is calculated from the saturated regime of the plot $\sqrt{I_{DS}}$ *vs* V_{GS} where $\left(\frac{\partial \sqrt{I_{DS,sat}}}{\partial V_{GS}}\right)$ is the slope of the plot in the saturation regime. Both of these above equations will be derived and explained in the following section.

Current modulation ratio (I_{ON}/I_{OFF}): The current produced between the source and drain (I_{DS}) must be extremely low and close to zero when no gate bias is applied, as there should be no available mobile charge carriers. This state of the device is known as the 'off' state. Similarly, the device is 'on' when the gate bias is used to induce charges. I_{ON} is the I_{DS} at maximal gate bias. Ideally, the I_{OFF} should be zero, which renders an infinite current modulation ratio. However, if there are a significant number of trap states in the film, these will have to be filled before the channel can conduct. Similarly, if the film is doped with unwanted impurities, it can have a non-zero I_{DS} at $V_{GS} = 0$. Therefore, the I_{ON}/I_{OFF} ratio is a measure of purity of the semiconductor and its susceptibility towards doping by its surroundings.

Threshold voltage (V_T): V_T defines the critical voltage at which the field effect becomes operable. Because of a mismatch between the Fermi level of the gate electrode and the HOMO/LUMO of the organic semiconductor, the flat band condition is not maintained in reality. This generates a potential and leads to band bending to achieve equilibrium. This requires a non-zero gate voltage to be applied to attain the flat band condition before any charge can be induced. This is typically known as the threshold voltage, V_T.

OFETs are typically characterized by two different types of current-voltage (*I*-*V*) characteristics, commonly known as the output and transfer characteristics (**Error! Reference source not found.**).[41] The current response (I_{DS}) as a function of source drain voltage (V_{DS}) swept at fixed gate voltages (V_{GS}) is known as the output characteristics (I_{DS}-V_{DS}) of a transistor (**Error! Reference source not found.**a). The current response (I_{GS}) as a function of V_{GS} swept at a fixed drain bias (V_{DS}) is called the transfer characteristics (I_{GS}-V_{GS}) of a transistor (**Error! Reference source not found.**b).

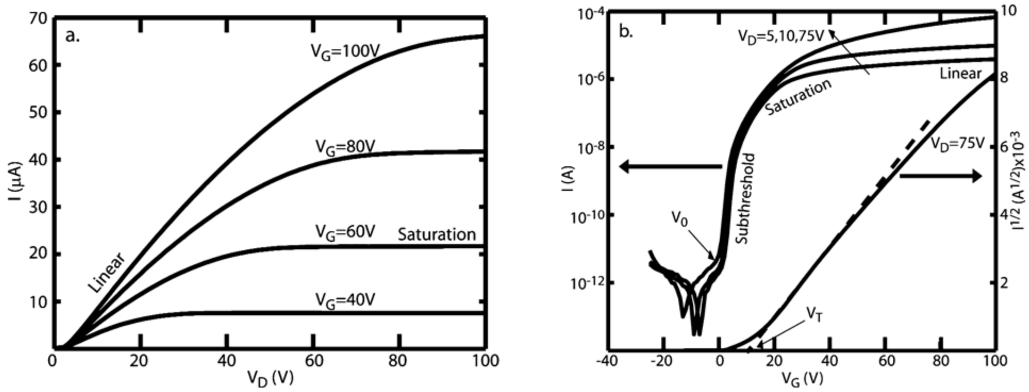

Figure 1.14 (a) Example of output characteristics (*I* vs. V_D at a fixed V_G); *I*, V_D and V_G are represented as I_{DS}, V_{DS} and V_{GS} in text, (b) Example of transfer characteristics (*I* vs. V_G). Reprinted with permission from *Chem. Mater.* 2004, *16*, 4436-4451.[41] Copyright © 2004, American Chemical Society.

These characteristics can be compared quantitatively using modeled *I-V* relationships derived from Ohm's law. As per Figure 1.15a, the application of a negative gate voltage accumulates an equal number of positive charges at the semiconductor-dielectric interface, assuming Ohmic contacts and zero-threshold ($V_T = 0$) operation. The charge density is uniform across the channel when there is no drain voltage applied ($V_{DS} = 0$). When a non-zero V_{DS} is applied, the accumulated charge density $q(x)$ at a given position x along the channel is proportional to the voltage difference [V_{GS} – $V(x)$] (Equation 1.6):

$$q(x) = n(x)et = C_{ox}[V_{GS} - V(x)] \qquad \text{Equation 1.6}$$

Here C_{ox} presents the capacitance of the insulator per unit area, $n(x)$ is the number density of charges in the channel, e is the fundamental unit of charge, t is the thickness of the charged layer in the channel. As mentioned before, a threshold gate voltage (V_T) is needed to turn on the field effect because of misalignment in the Fermi levels. This modifies Equation 1.6 to Equation 1.7:

$$q(x) = n(x)et = C_{ox}[V_{GS} - V_T - V(x)] \qquad \text{Equation 1.7}$$

At no applied drain-source voltage, the charge density should be uniform. Therefore, $V(x) = 0$ when $V_{DS} = 0$. However, there is a linear gradient in the charge distribution when V_{DS} is non-zero but less than V_{GS}. Given that the gradient is linear, the charge density (q_x) gradually decreases on going from the left hand side to the right hand side of the conduction channel (Figure 1.15b). Hence, the average value of q_x for a small value of V_{DS} is $C_{ox}[V_{GS} - V_T - V(x)]$, (i.e., the charge density (q_{avg}) at the center of the conduction channel). It changes Equation 1.7 to Equation 1.8.

$$q_{avg} = n_{avg}et = C_{ox}\left[V_{GS} - V_T - \frac{V_{DS}}{2}\right] \qquad \text{Equation 1.8}$$

where n_{avg} is the average carrier number density in the channel. To arrive at the *I-V* relationship of a OFET, we can start with Ohm's law. Ohm's law states that the current between two points in the conduction channel is directly proportional to the voltage across those two points. The constant of proportionality is resistance. Therefore, we can write

$$I_{DS} = \frac{V_{DS}}{R} \qquad \text{Equation 1.9}$$

Now, if we consider the definition of conductivity, the Equation 1.9 changes to

$$J_{DS} = \sigma E_{DS} \qquad \text{Equation 1.10}$$

Where J_{DS} is the current density and E_{DS} is the electric field between source and drain. σ is the conductivity of the channel. Substituting the value of J_{DS} and E_{DS} in Equation 1.10 we get Equation 1.11. Here L, W, t are the length, width and thickness of the channel, respectively.

$$\frac{I_{DS}}{tW} = \frac{\sigma V_{DS}}{L} \qquad \text{Equation 1.11}$$

Rearranging Equation 1.11 and replacing the value of σ by $n_{avg}e\mu$, we reach Equation 1.12. μ is the charge carrier mobility.

$$I_{DS} = \left(\frac{W}{L}\right)\left(n_{avg}et\right)\mu V_{DS} \qquad \text{Equation 1.12}$$

Now, substituting Equation 1.8 into Equation 1.12, we get the following relation (Equation 1.13):

$$I_{DS} = \left(\frac{W}{L}\right)\mu C_{ox}\left[V_{GS} - V_T - \frac{V_{DS}}{2}\right]V_{DS} \qquad \text{Equation 1.13}$$

This is usually written as Equation 1.14:

$$I_{DS} = \left(\frac{W}{L}\right)\mu C_{ox}\left[(V_{GS} - V_T)V_{DS} - \frac{V_{DS}^2}{2}\right] \qquad \text{Equation 1.14}$$

Equation 1.14 shows that the current rises linearly with the gate voltage and quadratically with the drain voltage. The linear dependency of I_{DS} on V_{GS} is satisfied when $V_{DS} < (V_{GS} - V_T)$; therefore, the term $\frac{V_{DS}^2}{2}$ can be neglected. Hence, the equation turns into the following (Equation 1.15):

$$I_{DS,lin} = \left(\frac{W}{L}\right)\mu_{lin}C_{ox}(V_{GS} - V_T)V_{DS} \qquad \text{Equation 1.15}$$

Equation 1.15 is the standard equation for the 'linear regime' and is pictorially depicted in Figure 1.15b.

The charge carrier mobilities (μ) in the linear region can be extracted from the fundamental parameter transconductance ($g_{m,lin}$). $g_{m,lin}$ is the ratio of I_{DS} over V_{GS}, which provides information on how gate voltage (V_{GS}) controls the drain current. Therefore, $g_{m,lin}$ is a measure of the sensitivity of an OFET. $g_{m,lin}$ is defined as follows (Equation 1.16):

$$g_{m,lin} = \frac{\partial I_{DS}}{\partial V_{GS}}|_{V_{DS}} = \left(\frac{W}{L}\right) C_{ox}\mu_{lin}V_{DS} \qquad \text{Equation 1.16}$$

This derivative can be used to calculate mobilities at a given V_{DS}. Moreover, the composite linear region mobility can be determined from the variation of $g_{m,lin}$ with V_{DS} (Equation 1.17).

$$\frac{\partial g_{m,lin}}{\partial V_{DS}} = \left(\frac{W}{L}\right) C_{ox}\mu_{lin} \qquad \text{Equation 1.17}$$

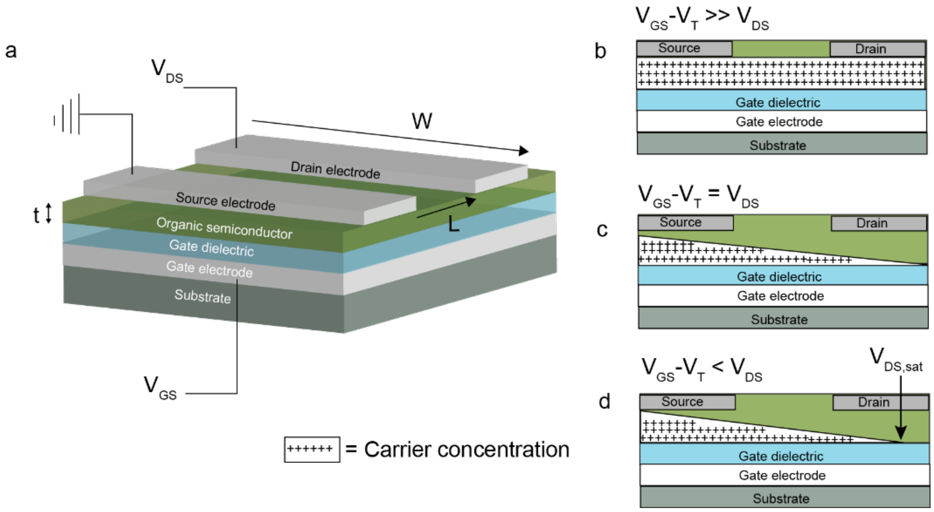

Figure 1.15 (a) Architecture of an OFET with relevant voltages, (b) Carrier concentration profile along the conduction channel ($V_{GS} - V_T >> V_{DS}$), (c) Pinch-off voltages when ($V_{GS} - V_T = V_{DS}$), (d) Carrier concentration profile in saturation region ($V_{GS} - V_T < V_{DS}$).

Referring back to Figure 1.15b, the channel has a nearly uniform carrier concentration when $V_{DS} << (V_{GS} - V_T)$. When V_{DS} is gradually increased, the charge carrier concentration is no longer uniform and gradually decreases from the source to the drain. As V_{DS} is increased, it eventually reaches the value $(V_{GS} - V_T)$ which pinches the channel. This is pictorially shown in Figure 1.15c and the corresponding voltage is called the 'pinch-off' voltage. It means there is no potential difference available between the drain electrode and the pinched off area of the channel, thus this region close to the surface of the drain electrode is depleted of any free carriers. If V_{DS} is further increased, this pinch-off point will only be pushed backward towards the source electrode. Given that the length of the device L is much longer than the width of this depletion region, further increase in V_{DS} does not afford any additional current as the integrated resistance between the pinch-off point and the drain electrode remains unaltered. However, the charge carriers are swept across the depletion region to the drain electrode because of high electric field. As the current reaches saturation, this regime is called the saturation region (Figure 1.15d). To derive the I-V relation of a OFET in this saturation region, $V_{DS} = (V_{GS} - V_T)$ can be substituted in Equation 1.14, which yields the following equations (Equation 1.18 and Equation 1.19):

$$I_{DS,sat} = \left(\frac{W}{2L}\right)\mu_{sat}C_{ox}(V_{GS} - V_T)^2 \qquad \text{Equation 1.18}$$

$$g_{m,sat} = \frac{\partial I_{DS}}{\partial V_{GS}}|_{V_{DS}} = \left(\frac{W}{L}\right)\mu_{sat}C_{ox}(V_{GS} - V_T) \qquad \text{Equation 1.19}$$

Hence, the slope of a line drawn through the linear part of $\sqrt{I_{DS}}$ vs V_{GS} is used to calculate μ_{sat} in the saturation regime (shown in **Error! Reference source not found.**b). The equation to calculate μ_{sat} is given in Equation 1.6. Equation 1.19 presents the expression of transconductance ($g_{m,sat}$) in the saturation regime. Despite the fact that the charge carrier mobility (μ) should be constant; μ_{lin} and μ_{sat} do not always agree. μ_{sat} is always higher than μ_{lin} as the contact resistance is less pronounced in the saturation regime. The threshold voltage (V_T) can be determined from the intercept of a tangent on the linear part of the plot $\sqrt{I_{DS}}$ vs V_{GS} (shown in **Error! Reference source not found.**b).

1.3.3 Device Architecture

A typical OFET, as previously mentioned, is built using three main components: (a) electrodes (gate, source, and drain), (b) a semiconductor layer which serves as a conduction channel between the source and drain electrodes, and (c) a dielectric layer that insulates the gate electrode from the semiconductor. OFETs can be fabricated with four different architectures based on the position of the electrodes. Based on the position of the gate electrode, OFETs can be constructed with either a top-gate or bottom-gate architecture. Each of these can be further categorized into two more architectures depending on the position of the source and drain electrodes, namely top-contact and bottom-contact. The ‘top-gate, top-contact (TGTC)’ architecture has organic semiconductor deposited on the substrate first, then source and drain electrodes are patterned onto the semiconductor layer (Figure 1.16a). It is followed by the deposition of the dielectric and the gate electrode. In the top-gate architecture, when the source and drain electrodes are deposited directly on the substrate, followed by the deposition of semiconductor layer, it is known as the ‘top-gate, bottom-contact (TGBC)’ design (Figure 1.16b). In this structure, the semiconductor layer is sandwiched between the dielectric layer and the substrate. As the nomenclature says, in the bottom-gate architecture, the gate electrode is directly deposited on the substrate, followed by the dielectric layer. If the semiconductor layer is then deposited on the top of the dielectric followed by source and drain electrodes on top, this is called a ‘bottom-gate, top-contact (BGTC)’ device (Figure 1.16c). When the source and drain electrodes are patterned directly on the dielectric layer, followed by the semiconductor layer on top, the ‘bottom-gate, bottom-contact (BGBC)’ architecture is formed (Figure 1.16d).

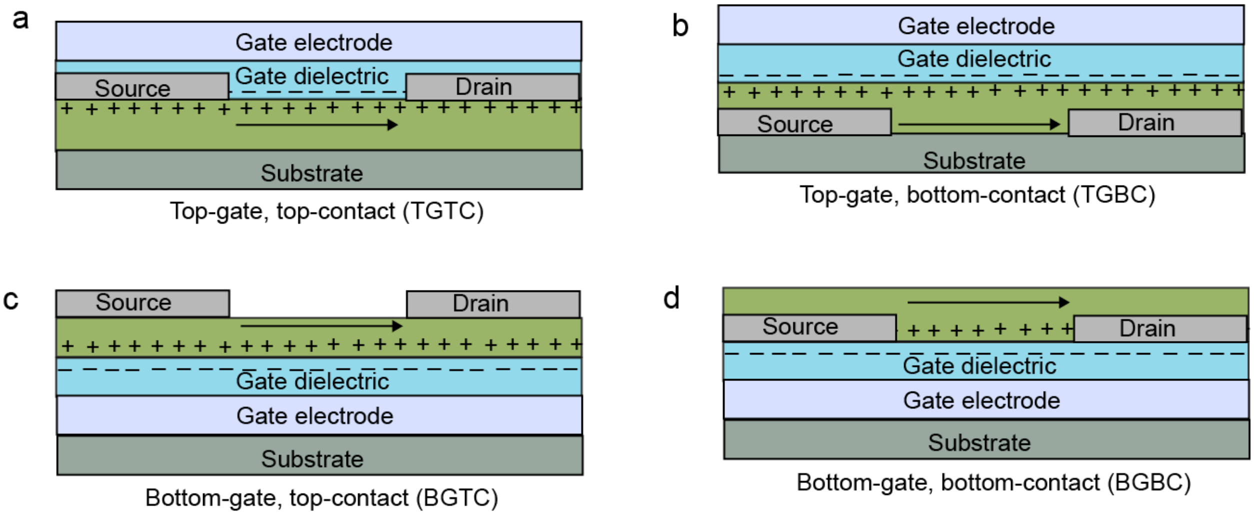

Top-gate, top-contact (TGTC)

Top-gate, bottom-contact (TGBC)

Bottom-gate, top-contact (BGTC)

Bottom-gate, bottom-contact (BGBC)

Figure 1.16 Different architectures of OFETs.

Each of these four architectures has their own benefits and limitations regarding device fabrication and performance. In the top gate structures (TGTC, TGBC), the semiconducting channel is encased within the other layers which increases device stability. In the top-contact structures (TGTC, BGTC), the semiconductor is deposited first, followed by deposition of the source and drain electrodes using a shadow mask. The contact resistance is minimized and charge carrier mobilities are higher because of intimate contact between the channel and the metal electrodes. In contrast, this architecture needs thermal evaporation of the metal electrodes which can sometimes damage the organic film. In addition, the vapor phase deposition method presets a barrier towards scalability, as the process is energy intensive. In order to construct the bottom-contact architectures (TGBC, BGBC), the source and drain electrodes are patterned on top of the dielectric before the organic layer is printed, which makes the dielectric surface non-uniform. Therefore, bottom-contact structures suffer from higher contact resistance and tend to exhibit a lower charge carrier mobility. However, the bottom-gate structures, especially the BGBC structure, can be readily integrated into low-cost, high throughput manufacturing processes.

1.4 Early Generations of Organic Semiconductors for OPVs and OFETs

Despite paving the way for organic electronics, poly(acetylene)[1-2] did not have much utility in commercial applications. Poly(p-phenylenevinylene) derivatives (PPV)[12] were the first generation of organic semiconductors to be used in OPVs. In PPV derivatives, phenyl rings are connected via vinylene units. The vinylene spacers help to maintain planarity in the polymer backbone by reducing the torsional strain between the hydrogen atoms at the *ortho* positions of neighboring phenyl units. MEH-PPV and poly[2-methoxy-5-(3′,7′-dimethyloctyloxy)-1,4-phenylenevinylene] (MDMO-PPV) are two of the most common PPVs, where the long alkoxy chains increase the solubility of these derivatives (Chart 1.1). PPVs were used for several crucial discoveries in organic electronics. MEH-PPV was used to demonstrate ultrafast photoinduced charge transfer from conjugated polymers to fullerene. In that account, Sariciftci et al. found that electron transfer from MEH-PPV to fullerene occurs on a picosecond time scale, which is two orders of magnitude faster than competing radiative and non-radiative recombination processes.[19] Based on this observation, Sariciftci et al. used MEH-PPV to fabricate the first polymer-fullerene solar cells.[20] However, the ultimate success of these materials was limited because of their low hole mobilities and large bandgaps. Next, poly(thiophene)-based polymers were introduced.[42] Poly(thiophene) derivatives were first synthesized in the 1980s; however McCullogh et al. first reported the synthesis of regioregular poly(3-hexylthiophene) (P3HT) in 1993, which became a benchmark p-type material for OPVs (Chart 1.1).[43] In addition to a lower band gap, the regioregularity of P3HT enhanced the crystallinity of the polymer in the solid-state, which increased its hole mobility (μ_h). However, early OPV devices using P3HT as the p-type material did not perform well until it was found that thermal annealing could improve the film morphology and polymer crystallinity.[44] P3HT remained at the forefront of mainstream OPV research for nearly a decade and contributed to much of the early success in this field. The optimization of P3HT based devices boosted the device efficiency to over 5%; however, this was not enough to be commercially relevant.[45-47] Relative to PPVs, P3HT had a narrower band gap; however, it was still too large to harvest red and near infrared photons. Moreover, P3HT-based photovoltaic cells also suffered from low V_{OC}. The difference between the LUMO of the n-type semiconductor and the HOMO of the p-type semiconductor is proportional to the open circuit voltage of the device, and a new generation of semiconductors was required with a lower HOMO level than P3HT. This led to a search for new materials and an advanced design strategy, namely the donor-acceptor structure. Using the donor-acceptor strategy, the frontier molecular orbitals of a semiconductor can be easily tuned, bringing more control over the optoelectronic properties of the semiconductor.

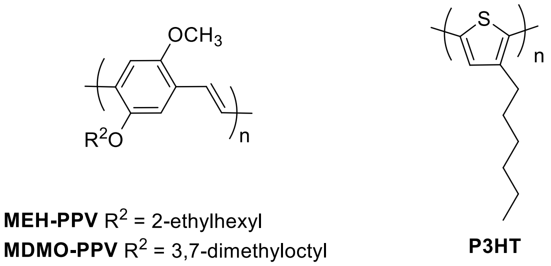

Chart 1.1 Structures of common PPV and thiophene-based polymers.

Unlike in OPVs, early success in the field of OFETs was achieved with molecular semiconductors rather than with polymers. Pentacene was used to develop p-channel transistors which exhibited a record hole mobility of 0.7 $cm^2/V{\cdot}s$, as reported by Gundlach and co-workers (Chart 1.2).[48] This was competitive with the hole mobility of hydrogenated amorphous silicon (0.5 $cm^2/V{\cdot}s$), which was the commercially used material to fabricate liquid crystal displays.[48] This success with pentacene inspired researchers to incorporate other acenes and their derivatives in

OFETs; however, these materials were always associated with the issues of insolubility and air-stability.[49] Several other families of oligomers such as oligothiophenes and oligoselenophenes have been employed in OFETs and have been useful as p-channel transistors.[50-51] Macromolecules have also been used to fabricate OFETs and have produced appreciable hole mobilities. Polythiophenes were one of the first families of polymers incorporated in OFETs. As seen in OPVs, regioregular P3HT exhibited a significantly higher hole mobility (0.05-0.1 $cm^2/V\cdot s$) than regiorandom P3HT.[52] The enhanced coplanarity because of the regioregularity of the P3HT increased the extent of π-conjugation along the polymer backbone and formed well-ordered domains beneficial for charge transport. To further improve the charge carrier mobility, McCulloch and coworkers synthesized poly(2,5-bis(3-alkylthiophen-2-yl)thieno-[3,2-b]thiophene (pBTTT) (Chart 1.2). The incorporation of the fused thieno-[3,2-b]thiophene unit introduced rotational invariance in the polymer backbone, which further helped in forming highly ordered crystalline domains. pBTTT exhibited an excellent hole mobility of 1.1 $cm^2/V\cdot s$.[53-54]

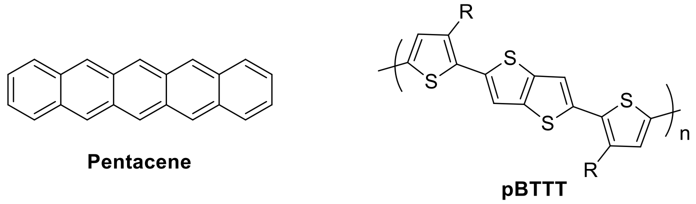
Pentacene

pBTTT

Chart 1.2 Structures of pentacene and pBTT.

In contrast to p-type semiconductors, the number of n-type semiconductors with a high electron mobility (μ_e) is relatively limited. Fullerenes were the first organic materials to exhibit appreciable electron mobility when employed in OFETs, but were not air-stable.[38] The first air stable n-channel OFET was developed by Bao and co-workers using hexadecafluorocopperphthalocyanine.[55] The next major advancement towards air-stable n-channel OFETs with appreciable electron mobility was reported by Jones and co-workers when they synthesized bis(2,2,3,3,4,4,4-heptafluorobutyl)-dicyano-perylene tetracarboxylic diimide (PDI-FCN_2) (Chart 1.3).[56] This perylene diimide derivative had a record electron mobility of 0.64 $cm^2/V\cdot s$ in air. Progress towards polymers with high electron mobilities has been relatively slow compared to the success of p-type polymers. In 2003, Babel and co-workers were able to synthesize poly(benzobisimidazobenzophenanthroline) (BBL) which demonstrated a field-effect electron mobility as high as 0.1 cm^2/V·s (Chart 1.3).[57-58] Within five years of this report, another major breakthrough was reported by Chen et al. when they synthesized the polymer poly{[N,N9-bis(2-octyldodecyl)-naphthalene-1,4,5,8-bis(dicarboximide)-2,6-diyl]-alt-5,59-(2,29-bithiophene)},(P(NDI2OD-T2) (Chart 1.3), and achieved a record mobility of 0.85 cm^2/V·s.[59] Numerous efforts have been made to develop different classes of small molecules and polymers for both p-channel and n-channel transistors, and this work has been reviewed in multiple accounts.[38, 60-62] More recently donor-acceptor semiconductors[63], have been employed in OFETs. The donor-acceptor design strategy was expected to lower the bandgap and lead to ambipolar OFETs.

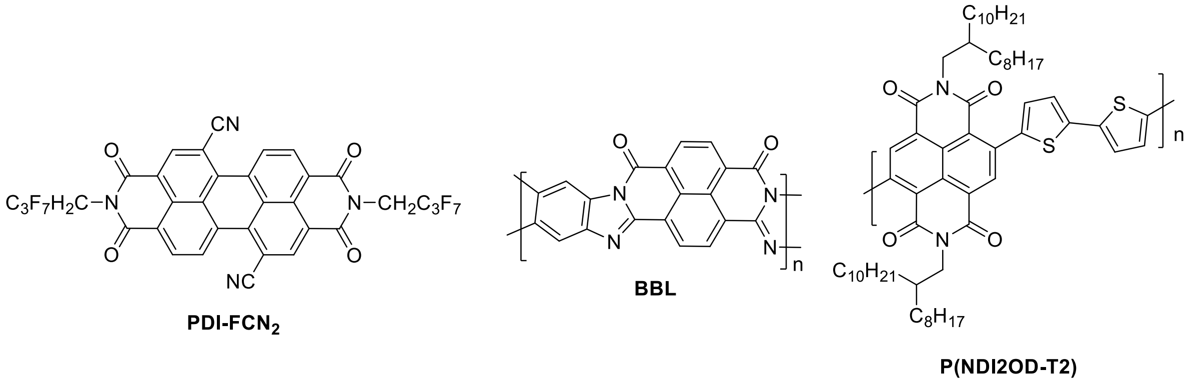

Chart 1.3 Structures of molecular and polymer semiconductors exhibited outstanding charge carrier mobility when incorporated in OFETs.

1.4.1 Donor-Acceptor Structures

Donor-acceptor (D-A) semiconductors are comprised of alternating electron-rich (donor) subunits and electron-deficient subunits (acceptor) (Chart 1.4). Since the frontier molecular orbitals of a donor are higher in energy compared to an acceptor, the orbital mixing between donor and acceptor is limited. Owing to this partial isolation of the frontier orbitals, the HOMO of the organic semiconductor is primarily localized on the donor unit, while the LUMO resides on the acceptor unit. This means that the HOMO and LUMO can be tuned separately. Given the fact that the HOMO of the donor is higher in energy than that of the acceptor and the LUMO of the acceptor is lower in energy than the LUMO of the donor unit, donor-acceptor materials typically produce a lower HOMO-LUMO gap than the parent donor and acceptor units. The energy gap is usually low enough in most donor-acceptor semiconductors to harvest near-infrared photons (Figure 1.17). In addition, when the HOMO-LUMO gap is small, the semiconductor can potentially conduct both holes and electrons when used in a OFET. Therefore, the donor-acceptor structure is an ideal design for producing ambipolar transistors. Given the partial localization of the frontier molecular orbitals, an electronic transition from HOMO to LUMO is usually associated with a degree of charge transfer character (i.e., a large transition dipole moment). This greatly enhances the optical extinction coefficient of the semiconductor, which in turn results in higher photocurrents when incorporated in photovoltaic devices. Although this partial isolation of the frontier orbitals positively impacts many semiconductor properties, complete isolation of the orbitals would greatly diminish the orbital overlap integral because of poor overlap between the HOMO and LUMO.

Donor-Acceptor Molecular Semiconductor

Donor-Acceptor Polymer Semiconductor

Chart 1.4 Donor-Acceptor molecular (HB194, based on merocyanine dye)[64] and polymer (a copolymer of diaminothiophene and dinitrothiophene)[65] semiconductors.

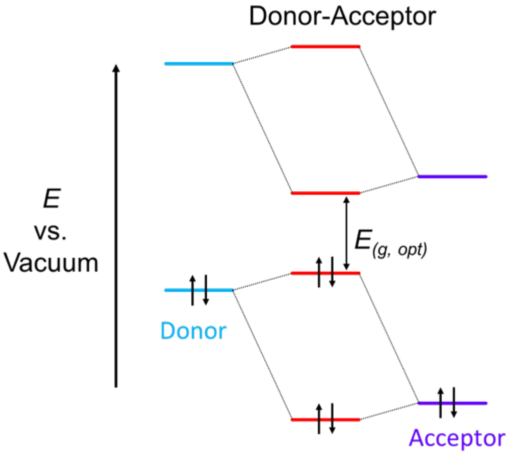

Figure 1.17 Formation of frontier molecular orbitals in a donor-acceptor semiconductor.

1.4.2 Benchmark Examples of the D-A Structure

The donor-acceptor strategy was first elucidated by Tour et al. in 1997 when they developed a copolymer of 3,4-diaminothiophene and 3,4-dinitrothiophene which had an optical band gap of 1.3 eV.[65] However, D-A structures were not popularized until 2006.[66] Leclerc and co-workers synthesized poly[*N*-9′-heptadecanyl-2,7-carbazole-alt-5,5-(4′,7′-di-2-thienyl-2′,1′,3′-benzothiadiazole)] (PCDTBT) utilizing *N*-alkyl-2,7-carbazole as donor units and benzothiadiazole as the acceptor unit (Chart 1.5).[67] PCDTBT has an electrochemical bandgap of 1.87 eV, and the deeper HOMO level centered on the carbazole unit led to a high V_{OC} of 0.9 V. It exhibited a power conversion efficiency of 3.6% with $\mathrm{PC_{61}BM}$ in photovoltaic devices. Although it did not outperform P3HT:PCBM devices initially, Park et al. incorporated PCDTBT in OPVs with [6,6]-phenyl $\mathrm{C_{71}}$ butyric acid methyl ester ($\mathrm{PC_{71}BM}$) as the n-type material and achieved an efficiency of 6.1%.[68] The phase separated blend of PCDTBT and $\mathrm{PC_{71}BM}$ produced a longer and better connected polymer network which improved the charge carrier mobility. The optimized morphology of the active layer and the higher absorption of $\mathrm{PC_{71}BM}$ compared to $\mathrm{PC_{61}BM}$ enhanced the $J_{\mathrm{SC,}}$ resulting in a higher PCE.

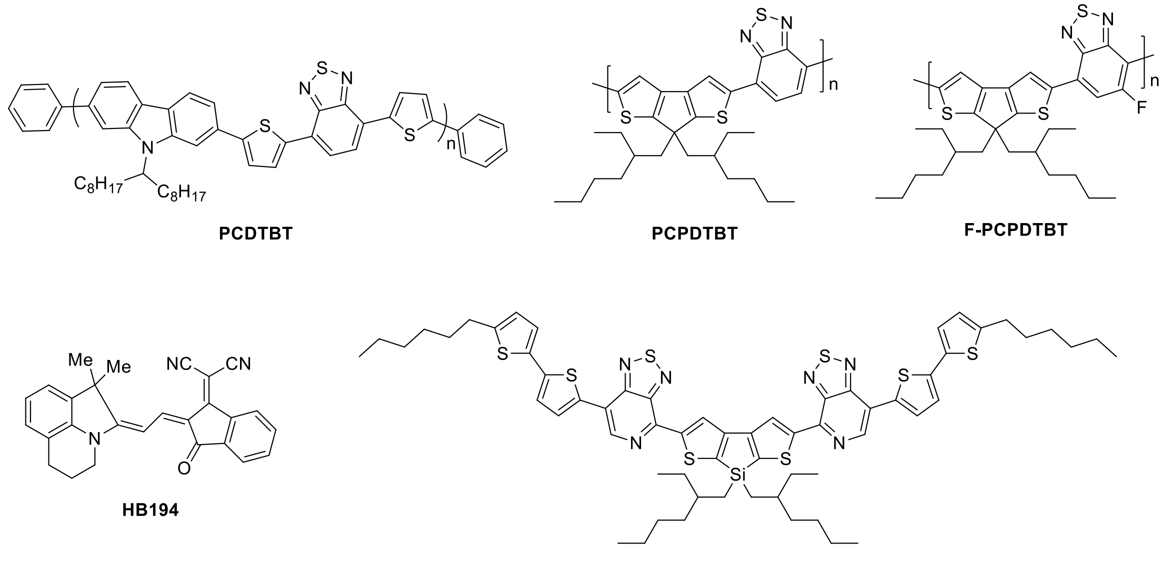

Chart 1.5 A few examples of benchmark donor-acceptor polymer and molecular semiconductors.

As another example, Muhlbacher et al. developed the p-type copolymer poly[2,6-(4,4-bis-(2-ethylhexyl)-4H-cyclopenta[2,1-b;3,4-b′]-dithiophene)-alt-4,7-(2,1,3-benzothiadiazole)] (PCPDTBT) utilizing cyclopentadithiophene as the donor unit and benzothiadiazole as the acceptor unit (Chart 1.5).[66] The estimated electrochemical bandgap was 1.73 eV and the solid state absorption strongly tailed up to 900 nm. PCPDTBT exhibited a PCE of 3.2% in photovoltaic devices when blended with $PC_{61}BM$. Hou et al. subsequently reported its hole mobility as 0.17 $cm^2/V \cdot s$ and speculated the lower reorganization energy of the fused ring thiophene derivatives led to better morphology, facilitating charge hopping.[69] The photovoltaic performance was further optimized by Schulz et al. using a PCPDTBT derivative where one of the hydrogen atoms of the benzothiadiazole was replaced by a fluorine atom (F-PCPDTBT) (Chart 1.5). The electronegative F-atom lowered the LUMO level of the polymer. This increased the open circuit voltage when incorporated in OPVs. Reduced geminate recombination also increased the FF and J_{SC}, leading to a PCE of 6.6%.[70]

Because of their unique advantages, donor-acceptor molecular semiconductors emerged in parallel with their polymer counterparts. These semiconductors have a well-defined molecular structure, definite molecular weight and high purity without batch to batch variations. The merocyanine dye HB194 was among the first molecular semiconductors exhibiting a PCE over 6%, as reported by Steinmann and co-workers (Chart 1.5).[64] The strong dipolar character and high polarizability of the merocyanine dye produced a high absorption coefficient, which is reflected in the remarkably high J_{SC} of the photovoltaic devices. Another classic p-type molecular semiconductor is 5,5′-bis{(4-(7-hexylthiophen-2-yl)thiophen-2-yl)-[1,2,5]thiadiazolo[3,4-c]pyridine}-3,3′-di-2 ethylhexylsilylene-2,2′-bithiophene, ($DTS(PTTh_2)_2$), where the [1,2,5]thiadiazolo[3,4-c]pyridine unit was incorporated as the acceptor building block in conjunction with a dithienosilole donor unit (Chart 1.5). The estimated bandgap was 1.5 eV. Two acceptor units were strategically added to both sides to deepen the HOMO of the molecule, resulting in a high V_{OC} when used in OPV devices. In a blend with $PC_{71}BM$, $DTS(PTTh_2)_2$ showed a PCE of 6.70%.

Since this strategy was proven successful, the synthesis of new donor and acceptor building blocks has become an intense area of research. In addition to examples just discussed, there are numerous other examples of DA semiconductors and a comprehensive review is beyond the scope of this thesis. Chart 1.6 presents some examples of commonly used donor and acceptor units. As discussed previously, dithienosilole and carbazole units have frequently been used and have resulted in remarkably high device performance, but the majority of donor units are structurally based on the thiophene skeleton and include oligothiophenes, thienothiophenes, benzodithiophenes, and dithienocylopentadiene.

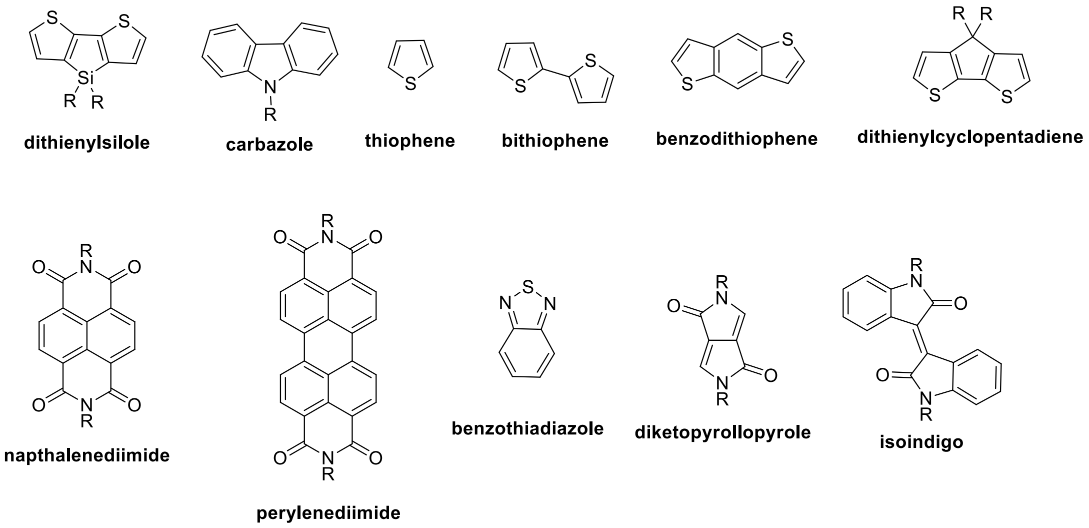

Chart 1.6 Common donor (top row) and acceptor (bottom row) units used as building blocks to develop organic semiconductors.

In contrast to donors, acceptor building blocks are based on functional groups such as amides and imides or electronegative heteroatoms like nitrogen and fluorine. Widely used examples include naphthalene diimide, perylene diimide, benzothiadiazole, diketopyrrolopyrrole, and isoindigo. The strongly electron deficient napthalene and perylene dimide materials are typically n-type semiconductors, while benzothiadiazole, diketopyrrolopyrrole, and isoindigo have been used to develop both p-type and n-type materials. This thesis is particularly focused on semiconductors based on the isoindigo acceptor unit and materials based on other acceptor units have been reviewed elsewhere.[22-23, 71-80]

All of these donor and acceptor units have been used to develop new organic semiconductors; a large number of these new materials behave as p-type semiconductors.

Therefore, fullerene derivatives predominantly served as the n-type component of OPV active layers for a long time. The highest PCE based on fullerene derivatives is 11.5% as certified by Newport Corporation.[81] The primary challenges of fullerene-based solar cells are the following. First, owing to the high symmetry of fullerenes, they exhibit exceptionally weak absorption in the visible and NIR regions.[82] Because of the weak complementary absorption of fullerenes, charge carriers are generated only from the p-type semiconductor, limiting the J_{SC}.[83] Second, the HOMO-LUMO gap of these materials cannot be easily tuned without changing the core structure of C_{60} or C_{70}. Third, the fullerenes easily crystallize to form nano-sized domains which tend to grow larger with time. This diminishes the long-term stability of OPVs.[84-85] As a result of these limitations, intensive research efforts have been dedicated to develop non-fullerene n-type materials to replace fullerene acceptors and push the PCE limit over 12%. The recent discovery of non-fullerene systems over the last few years has revolutionized the field of organic electronics, especially organic photovoltaics.[86-88] Owing to the broad absorption spectrum, high absorption coefficient, and high charge-carrier mobility of a new non-fullerene n-type material, a record PCE of 15.7% has been reported.[89] This is the highest efficiency of a single-junction OPV device. The work described in this thesis was started in late 2013, focusing on the development of novel donor-acceptor semiconductors based on modified isoindigo structures. Hence, a thorough review of these non-fullerene n-type semiconductors, which are revolutionizing organic photovoltaics, is again beyond the scope of this thesis and has been accomplished elsewhere.[90-92]

1.5 Isoindigo-based D-A Organic Semiconductors

Indigo is one of the oldest natural dyes used in the textile industry. The structure of isoindigo was first established by Von Bayer at the end of the 19th century. Isoindigo is a structural isomer of indigo, found in the leaves of Isatis tinctoria as a minor byproduct alongside other indigoid dyes. It is a dimer of oxidized indole derivatives where the two units are connected via an exocyclic double bond (Chart 1.7). Electron deficient lactam units of isoindigo made it a potential acceptor unit for organic semiconductor. Isoindigo can be synthesized in near quantitative yield from 6-bromoisatin and 6-bromooxindole. This yields 6,6′-dibromoisoindigo, where the bromine substituents are used as a synthetic handle to covalently connect additional units using Pd-catalyzed cross-couplings. Although isoindigo is fairly insoluble, the N-atoms of the lactam rings can be readily alkylated using alkyl halides and K_2CO_3 in *N,N′*-dimethylformamide (DMF), greatly improving its solubility. In addition to these synthetic advantages, isoindigo based semiconductors exhibits a broad absorption spectrum ranging over UV-Vis-NIR region. Since 2010, isoindigo has become a popular acceptor unit for both donor-acceptor molecular and polymeric semiconductors.

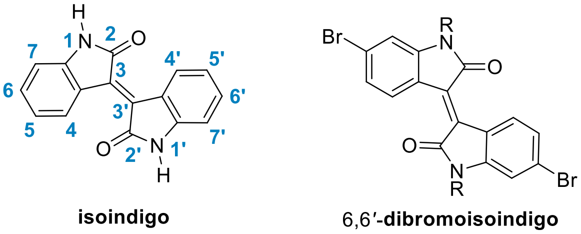

isoindigo

6,6′-dibromoisoindigo

Chart 1.7 Structure of isoindigo and 6,6′-dibromoisoindigo.

1.5.1 Isoindigo-based Molecular Organic Semiconductors

Molecular semiconductors have several potential advantages over their polymer counterparts, such as more reproducible syntheses and compatibility with column chromatography and recrystallization techniques for purification (compared to the time intensive Soxhlet purification of polymers). Given the synthetic reproducibility of molecular semiconductors, their device performance is much more consistent when compared to polymers, which suffer from large batch to batch variations. Several isoindigo-based molecular semiconductors have been synthesized and studied. The optoelectronic properties and device performances of the semiconductors reviewed in this section are tabulated in Table 1.1. Reynolds et al. were the first to incorporate isoindigo in donor-acceptor molecular semiconductors; they synthesized two molecules, one with a donor-acceptor-donor (**1**) and one with an acceptor-donor-acceptor structure (**2**) (Chart 1.8).[93] Both molecules possess a low HOMO level, which was essential to achieving a high V_{OC} in OPVs. Compounds **1** and **2** were used as the p-type semiconductor in OPVs, alongside $PC_{61}BM$ as the n-type material. They exhibited PCEs of 1.76%, and 0.55%, respectively. Poor *FF* and relatively low J_{SC} were responsible for the poor photovoltaic performance. Following this initial report, Reynolds and co-workers found that polydimethylsiloxane (PDMS), when used as a macromolecular additive, can boost the PCE of OPVs with the **2**:$PC_{61}BM$ system.[94] The additive turned out to reduce the domain sizes of **2** and $PC_{61}BM$; this enhances the probability of an exciton reaching a donor:acceptor interface and dissociating, thus increasing the J_{SC}. The PCE increased to 2.15% upon addition of 0.1 mg/mL PDMS as an additive. Reynolds et al. further developed two tailor-made additives (**3** and **4**), which are molecules sharing the same molecular structure as the donor, but with a slight variation in the structure.[95] The two additives had the hexyl group on the bithiophenes replaced with a bulky triisobutylsilyl group. The bulky end group of the additive molecule limited crystal growth, resulting in a morphology with smaller domains. The OPVs with a singly-substituted additive (**3**) exhibited a PCE of 2.24% compared to 1.30% without any additives.

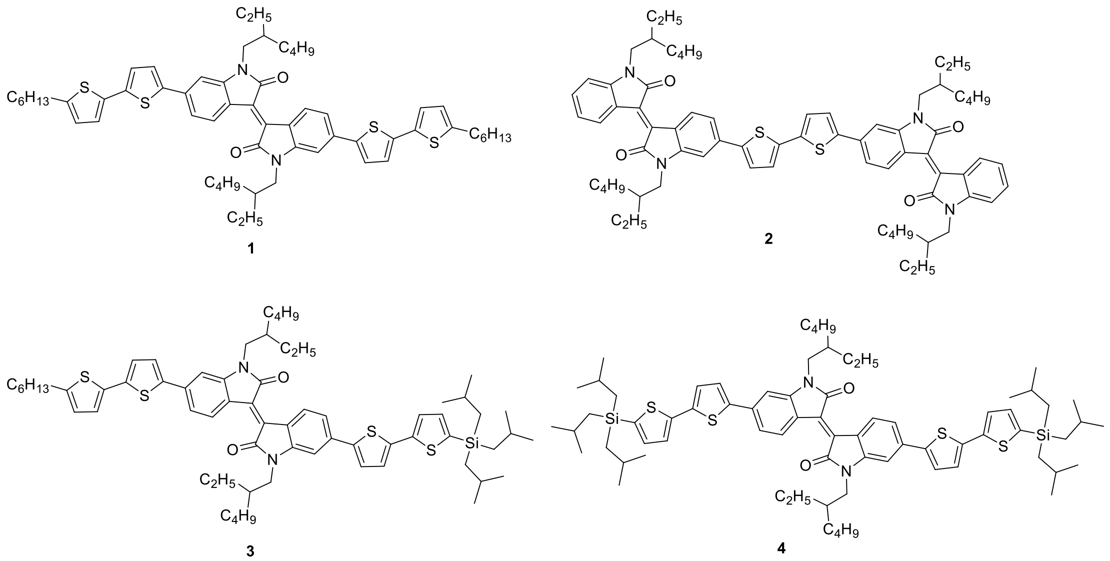

Chart 1.8 Isoindigo-based molecular semiconductors, **1**-**4**.

Table 1.1 Optoelectronic properties, hole mobility, and OPV performance of isoindigo-based molecular semiconductors **1-18**.

Compound	HOMO^{a} (eV)	LUMO^{a} (eV)	$E_{g,elec}$ (eV)	$E_{g,opt}$ (eV)	$\mu_h{}^{b}$ cm^2/V·s	$V_{OC}{}^{b}$ (V)	$J_{SC}{}^{b}$ mA·cm^{-2}	FF^{b} (%)	PCE^{b} (%)	Ref.
1	-5.60	-3.90	1.80	1.67	-	0.74	6.3	38	1.76	[93]
2	-5.60	-3.80	1.89	1.76	-	0.66	2.4	36	0.55	[93]
1	-	-	-	-	-	0.77	6.82	41	2.16	[94]
1	-	-	-	-	$1.7^{d} \times 10^{-5}$	0.82^{c}	6.14^{c}	45^{c}	2.24^{c}	[95]
5	-5.47	-3.60	1.87	1.81	1.4×10^{-2}	0.35	0.003	25.8	0.003	[96]
6	-5.11	-3.57	1.54	1.70	3.6×10^{-2}	0.93	6.58	42.8	2.60	[96]
7	-5.10	-3.63	1.47	1.60	9.7×10^{-4}	0.87	8.21	43.3	3.20	[96]
8	-5.47	-3.61	1.86	1.80	1.4×10^{-3}	0.55	0.21	20.4	0.04	[96]
9	-5.26	-3.62	1.64	1.77	3.2×10^{-5}	0.12	0.002	28.0	0.002	[96]
10	-5.39	-3.92	1.47	1.54	-	0.72	6.03	32.5	1.41	[97]
11	-5.33	-3.62	1.71	1.58	$3.44^{c} \times 10^{-5}$	0.83	3.29	51	1.39	[98]
12	-5.52	-3.61	1.91	1.62	$1.86^{c} \times 10^{-5}$	0.98	1.60	50	0.78	[98]
13	-5.56	-3.59	1.97	800	$3.66^{c} \times 10^{-3}$	0.95	4.46	45	1.92	[98]
14	-5.56	-3.82	1.55	850	-	0.86	11.75	58	5.62^{c}	[99]
15	-5.56	-4.07^{e}	-	1.59	-	1.05	2.36	56.1	1.39	[100]
16	-5.79	-4.21^{e}	-	1.58	-	0.74	0.85	37.3	0.23	[100]
17	-5.60	-3.69^{e}	-	1.91	-	1.06	0.68	38.4	0.28	[100]
18	-5.82	-3.91^{e}	-	1.91	-	0.92	1.49	39.8	0.54	[100]

^{a}HOMO/LUMO energies estimated from the onset of oxidation/reduction in voltammetry experiments, calibrated against Fc^{+}/Fc. ^{b}Device parameters of best performing devices. ^{c}Average device performance, ^{d}Hole mobilities measured using the single carrier devices based on space charge limited current (SCLC) method, all others are measured by incorporating the semiconductor in OFETs. ^{e}LUMO energy estimated from $E_{\text{LUMO}} = E_{\text{HOMO}} + E_{\text{g,opt}}$.

Lee et al. have also reported donor-acceptor-donor small molecules (**5**-**9**) using thiophene-based donors and isoindigo as the acceptor (Chart 1.9).[96] The absorption band corresponding to the lowest energy transition gradually red-shifts and the optical band gap decreases as the number of thiophene rings increases. This was attributed to the extended π-conjugation, which also caused strong π-π stacking of the conjugated backbone. Among these five materials (**5**-**9**), compound **7** with $PC_{71}BM$ exhibited the highest PCE of 3.2% when the active layer was cast with 0.1% DIO. OFETs were also fabricated to measure the charge carrier mobilities of these five semiconductors. All of them showed p-type behavior and **6** showed the highest hole mobility of 3.6×10^{-2} $cm^2/V \cdot s$, which resulted from the efficient π-π stacking of the conjugated backbone. With increasing conjugation, compound **7** was expected to show the highest hole mobility; however, its poor solubility in organic solvents led to an unfavourable morphology and reduced performance. Yang and coworkers also synthesized a molecule (**10**) similar to **7**, where thienothiophene was used as a part of the donor unit. The incorporation of a fused thiophene system increased the planarity and rigidity of the backbone to better extend the conjugation. **10** was the first isoindigo-based semiconductor used to fabricate solar cells with an inverted architecture. The devices made using **10**:$PC_{61}BM$ exhibited a poor PCE (1.41%) because of a poor morphology; however, the band gap (1.5 eV) and low lying HOMO (-5.39 eV) of **10** are beneficial properties for photovoltaic applications.[97]

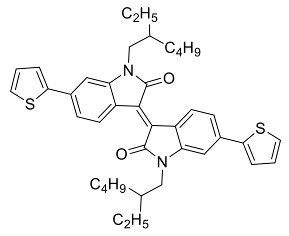

5

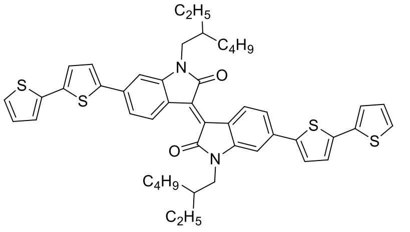

6

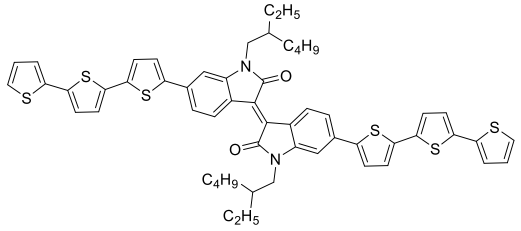

7

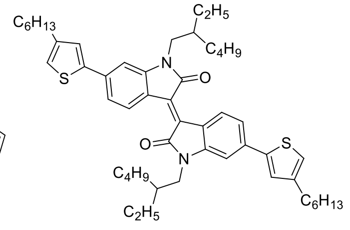

8

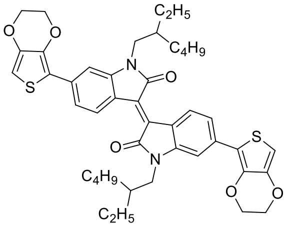

9

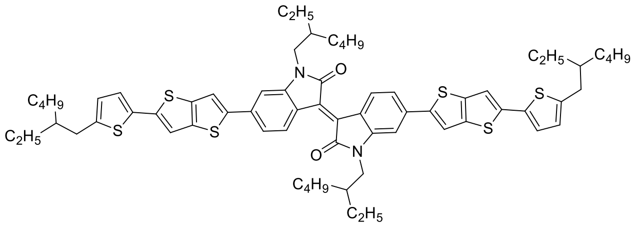

10

Chart 1.9 Isoindigo-based molecular semiconductors, **5**-**10**.

Tomassetti et al. also used a similar π-extended structure in their comparison of linear (**11**) and branched semiconductors (**12** and **13**) (Chart 1.10).[98] These three new molecules had isoindigo as the central unit, which was connected to either a linear or branched thiophene oligomer chain. The terminal thiophene units of the oligomer chain were connected to cyanoacrylate esters to develop an acceptor-donor-acceptor motif. The optical band gaps of all semiconductors were quite low, in the range of 1.55-1.62 eV. The photovoltaic performance of these molecules in blends with $PC_{61}BM$ was studied. The highest PCE was shown by the linear molecule **11** when the active layer was solvent annealed with dichloromethane to optimize the morphology. The solvent annealing led to smaller domain sizes, which produced a higher photocurrent when compared to the branched counterparts. The field effect mobility was also measured and **11** again exhibited the highest hole mobility. The linear structure of **11** afforded optimal crystallinity that produced the highest hole mobility. Recently, Jung et al. synthesized **14**, where the central isoindigo unit was connected to two diketopyrrolopyrrole moieties to achieve an acceptor-acceptor-acceptor motif. Owing to the electron deficient character of both isoindigo and diketopyrrolopyrrole, **14** had a deep HOMO (-5.52 eV) with an optical band gap of 1.46 eV.[99] The HOMO primarily resided on the isoindigo unit, while the LUMO was centered on the diketopyrrolopyrrole, as it is more electron deficient than isoindigo. Despite having an acceptor-acceptor-acceptor structure, **14** served as a p-type semiconductor when incorporated in photovoltaic devices in a blend with $PC_{71}BM$. These devices showed a PCE of 5.86%, which was attributed to the high V_{OC} of 0.86 V and J_{SC} of 11.75 $mA \cdot cm^{-2}$.

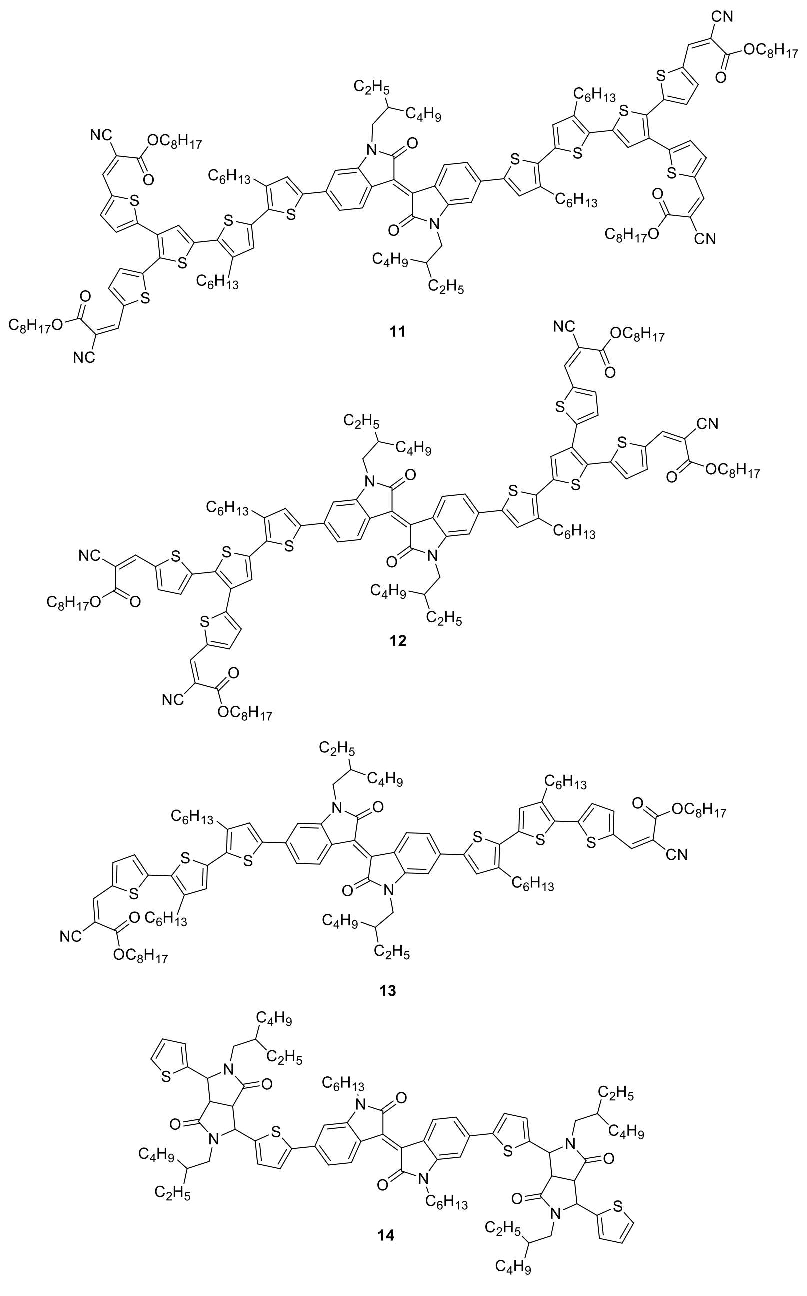
11

12

13

14

Chart 1.10 Isoindigo-based molecular semiconductors, **11-14**.

In order to replace fullerene derivatives in OPVs, Cao and co-workers synthesized four new n-type molecular semiconductors (**15 - 18**) with an acceptor-donor-acceptor structure (Chart 1.11).[100] All four molecules had the isoindigo unit as the acceptor with four different donor units: indacenodithiophene, dithienosilole, anthracene and pyrene (**15-18**). The LUMO levels of these materials were between 3.69 - 4.21 eV, making them comparable to fullerene derivatives. Solar cells were made with these semiconductors using P3HT as the typical donor material. Owing to a combination of high V_{OC} (1.05 V) and a higher J_{SC} (2.36 mA·cm^{-2}), the P3HT:**15** blend exhibited the highest PCE of 1.39%. The high-lying LUMO of **15** resulted in a high V_{OC}; the broad absorption, excellent planarity, and rigid core of **15** contributed to its higher photocurrents in OPVs compared to other three materials.

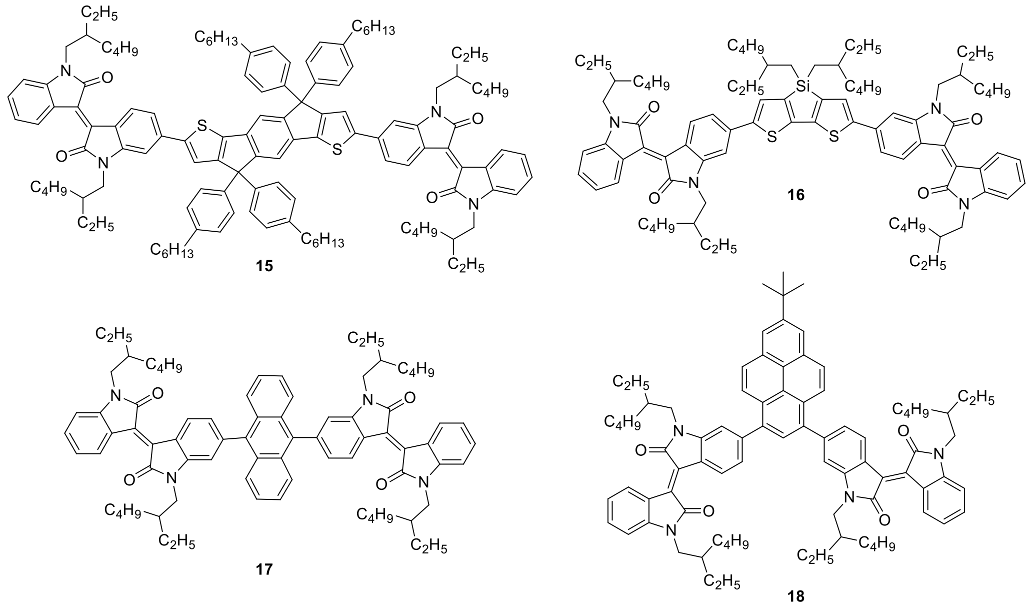

Chart 1.11 Isoindigo-based molecular semiconductors, **15-18**.

1.5.2 Isoindigo-based p-type Polymers

Polymer semiconductors also have several unique advantages over their molecular counterparts. π-Conjugated molecules tend to self-aggregate, which results in over-crystallization. This often produces larger domains in the active layer, which in turn causes inefficient exciton dissociation, leading to a poor J_{SC} in OPVs. In contrast, polymer films typically exhibit a mix of ordered and amorphous regions, preventing over-crystallization. In addition, thin films of conjugated molecules often have pin-holes and cracks, which hinder charge transport, whereas the quality of polymer films tends to be much higher. The carrier mobility is also often higher in polymer semiconductors as charges can easily transport via polymer chains rather than hopping from molecule to molecule.[101] The application of isoindigo in organic electronics started with molecular semiconductors; however, isoindigo-based polymers have developed in parallel with molecular materials. An extremely large number of different donor-acceptor polymers have been reported to serve as p-type semiconductors. These polymers have been comprehensively reviewed elsewhere, [102-105] hence, this section focuses on only a selected number of polymers which have performed well in devices. Thiophene and oligothiophenes were the simplest donor units with which to start exploring isoindigo-based (D-A) polymers. In 2011, Wang et al. synthesized a low band gap (E_g = 1.6 eV) copolymer (**19**) using isoindigo as the acceptor and thiophene as the donor unit (Chart 1.12).[106] The device fabricated with **19**/$PC_{71}BM$ blend and 2.5% (wt.) DIO exhibited a PCE of 3.0%, with a high open-circuit voltage of 0.89 V. The devices were further optimized by Ma et al. where they replaced $PC_{71}BM$ with $PC_{61}BM$, and achieved a PCE of 4.5%.[107] The 50% increase in the PCE was because of the enhanced photocurrent resulting from a more favorable morphology as $PC_{61}BM$ had a better miscibility with **19**. To further improve the J_{SC} exhibited by **19**, Wang et al. extended the conjugation length of the donor unit by replacing the thiophene unit with alkylated terthiophene (**20**).[108] The extended conjugation in **20** was expected to enhance the weak intensity of the high energy absorption bands in **19**, which would result in a higher J_{SC} in OPVs. Given the enhanced π-π stacking of polymer backbone arising from the increased planarity of the terthiophene unit, the optical band gap of the polymer was further lowered to 1.5 eV. This increased the J_{SC}, which led to an increased PCE of 6.3% when blended with $PC_{71}BM$. Inspired by this work, Ho et al. synthesized a series of polymers (**21-23**) using longer oligothiophenes along with **20** as a reference.[109] The intensity of the high energy absorption bands increased gradually with an increasing number of thiophene rings, and the HOMO levels were also raised because of the extended conjugation. The photovoltaic performance of these polymers when blended with $PC_{71}BM$ was interesting. The average PCE (6.52%) of **20** was on par with the previous report. Although the extended conjugation length and enhanced planarity of **21** increased the J_{SC}, the overall PCE was only 5.83%. The lower efficiency was attributed to an unfavourable morphology caused by the poor solubility of **21**. In contrast, **22** produced a lower photocurrent, which resulted in a lower PCE of 3.85%. The morphology of **22** in the active layer was predominantly amorphous, which imparted a poor hole mobility, lowering the PCE. The highest PCE (7.06%) among these four polymers was shown by **23**. The broad optical absorption and optimal crystallinity of the

23:$PC_{71}BM$ active layer resulted in a higher J_{SC} and *FF*, which in turn produced a higher PCE. Hu et al. synthesized isoindigo-quaterthiophene polymers (**24-26**) and studied the effect of fluorine atoms when substituted on either the donor unit (quaterthiophene) or acceptor unit (isoindigo).[110] Polymers **25** and **26** had a lower HOMO level compared to **24** because of the electron withdrawing F-atom on the polymer backbone. The polymer:$PC_{71}BM$ blend was used to fabricate photovoltaic devices using an inverted architecture. Both **25** and **26** showed a higher J_{SC} and *FF* in comparison with the non-fluorinated parent polymer **24**. Moreover, the fluorination on the donor unit appeared to be more effective; **25** showed temperature dependent aggregation which helped to achieve optimal crystallinity and increase the hole mobility. A PCE of 6.7% was achieved with the **25**:$PC_{71}BM$ system.

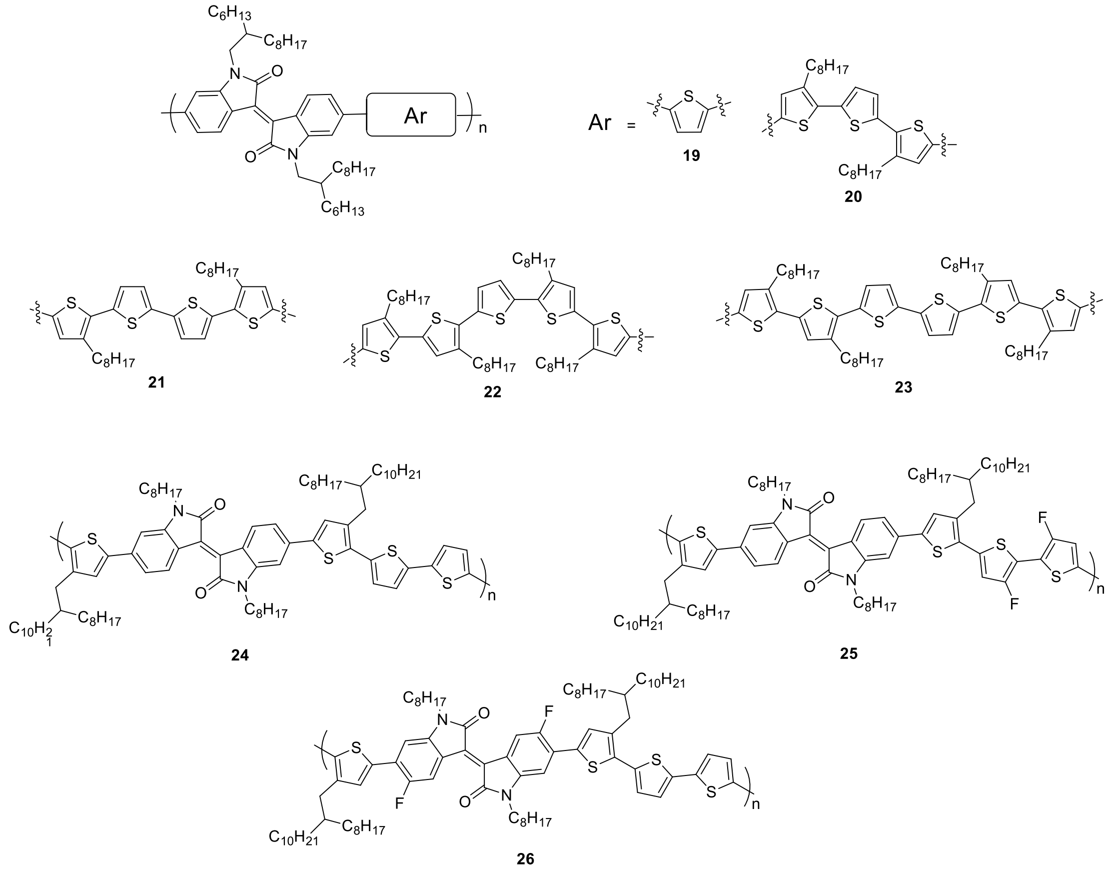

Chart 1.12 Isoindigo and oligothiophene-based copolymers, **19-26**.

Table 1.2 Optoelectronic properties, hole mobility, and OPV performance of isoindigo-based p-type polymer semiconductors **19-45**

Polymer	**HOMO[a] (eV)**	**LUMO[a] (eV)**	**$E_{g,elec}$ (eV)**	**$E_{g,opt}$ (nm)**	**μ_h[b] cm^2/V·s**	**V_{OC}[b] (V)**	**J_{SC}[b] mA·cm^{-2}**	**FF[b] (%)**	**PCE[b] (%)**	**Ref.**
19	-5.85	-3.88	1.97	1.59	-	0.89[c]	5.4[c]	63[c]	3.0[c]	106
19	-	-	-	-	-	0.91[c]	9.1[c]	0.54[c]	4.5[c]	107
20	-5.82	-3.83	1.99	1.50	-	0.70[c]	13.1[c]	69[c]	6.3[c]	108
20	-5.49	-3.90[e]	-	1.59	3.68[d] × 10^{-5}	0.73	13.8	63.61	6.39[c]	109
21	-5.48	-3.90[e]	-	1.58	3.17[d] × 10^{-4}	0.76	13.5	57.9	5.96[c]	109
22	-5.44	-3.86[e]	-	1.58	2.80[d] × 10^{-5}	0.72	8.3	61.8	3.65[c]	109
23	-5.37	-3.80[e]	-	1.57	8.93[d] × 10^{-5}	0.71	15.7	63.9	7.10[c]	109
24	-5.18	-3.67[e]	-	1.50	6.4[d] × 10^{-4}	0.73	10.3	47.1	3.5[c]	110
25	-5.30	-3.78[e]	-	1.52	3.4[d] × 10^{-3}	0.83	13.3	60.9	6.7[c]	110
26	-5.28	-3.77[e]	-	1.50	2.0[d] × 10^{-3}	0.73	11.4	54.8	4.6[c]	110
27	-5.65	-3.78	1.87	1.59	1.06	-	-	-	-	111
28	-5.56	-3.79	1.77	1.56	0.66	-	-	-	-	111
29	-5.84	-3.77	2.07	1.66	0.48	-	-	-	-	111
30	-5.90	-3.75	2.15	1.69	0.32	-	-	-	-	111
31	-5.70	-3.73	1.97	1.55	0.34	-	-	-	-	111
32	-5.54	-3.78	1.76	1.54	0.11	-	-	-	-	111
33	-5.80	-3.81	1.99	1.58	0.019	-	-	-	-	111
34	-5.48	-3.70	1.78	1.58	0.061	-	-	-	-	111
35	-5.44	-3.72	1.73	1.55	1.03 × 10^{-3}	-	-	-	-	111
36	-5.55	-3.70	1.85	1.65	1.35 × 10^{-4}	-	-	-	-	111
37	-5.38[f]	-3.76[e]	-	1.62	0.79	-	-	-	-	112
38	-5.20[f]	-3.59[e]	-	1.61	2.48	-	-	-	-	112
39	-5.45	-3.96	1.49	1.48	-	0.80	11.6	43.0	3.5	113
40	-5.33	-3.85	1.48	1.47	-	0.79	9.7	46.9	3.0	113
41	-5.31	-3.88	1.43	1.42	-	0.73	8.2	44.5	2.2	113
42	-5.24	-3.89	1.35	1.37	-	0.66	10.1	50.2	2.6	113
43	-5.55	-3.95	1.60	1.54	-	0.77	10.5	50	4.01	114
44	-5.70	-3.61	2.09	1.80	0.004	0.63	1.02	45	0.29	115
45	-5.62	-3.70	1.92	1.75	0.013	0.69	4.5	36	1.13	115

[a] HOMO/LUMO energies estimated from the onset of oxidation/reduction in voltammetry experiments, calibrated against Fc$^+$/Fc. [b] Average device performance. [c] Device parameters of best performing devices. [d] Hole mobilities measured using the single carrier devices based on SCLC method, all others are measured by incorporating the semiconductor in OFETs. [e] LUMO energy estimated from $E_{LUMO} = E_{HOMO} + E_{g,opt}$. [f] HOMO energy determined by photoelectron spectroscopy.

The planarity and strongly electron deficient nature of isoindigo encouraged Pei and coworkers to design and synthesize ten isoindigo-based polymers containing thiophene and selenophene donor units for OFET applications.[111] The idea of molecular docking was used to design and study the structure-property relationship of the polymers. As per the proposed model, when the donor unit was sterically unencumbered it could easily dock into the cavity created by the large isoindigo core. Two types of donor units were used: polymers **27-32** had centrosymmetric donor units, while the donor units in polymers **33**-**36** were axisymmetric (Chart 1.13). The centrosymmetric donor units were shown to promote π-π stacking because of their linear structure; therefore, the sterically free donor units docked into the isoindigo cavity fairly well, resulting in a higher hole mobility. In contrast, the axisymmetric donor units created a zigzag backbone which inhibited molecular docking and lowered the hole mobility. The polymers with centrosymmetric donor units showed hole mobilities over 0.1 $cm^2/V{\cdot}s$, while those with axisymmetric donor units had hole mobilities between 10^{-2} and 10^{-3} $cm^2/V{\cdot}s$. Instead of varying the donor unit, Bao et al. synthesized isoindigo-bithiophene copolymers (**38**) with different alkyl chains substituted on the lactam nitrogens of isoindigo. The n-hexyl chain had siloxane terminating groups.[112] This polymer was shown to have a significantly higher hole mobility (2.48 $cm^2/V{\cdot}s$) than the reference polymer (**37**). The increase in the hole mobility was attributed to a shorter π-π stacking distance in **38** (3.58 Å) as compared to **37** (3.75 Å).

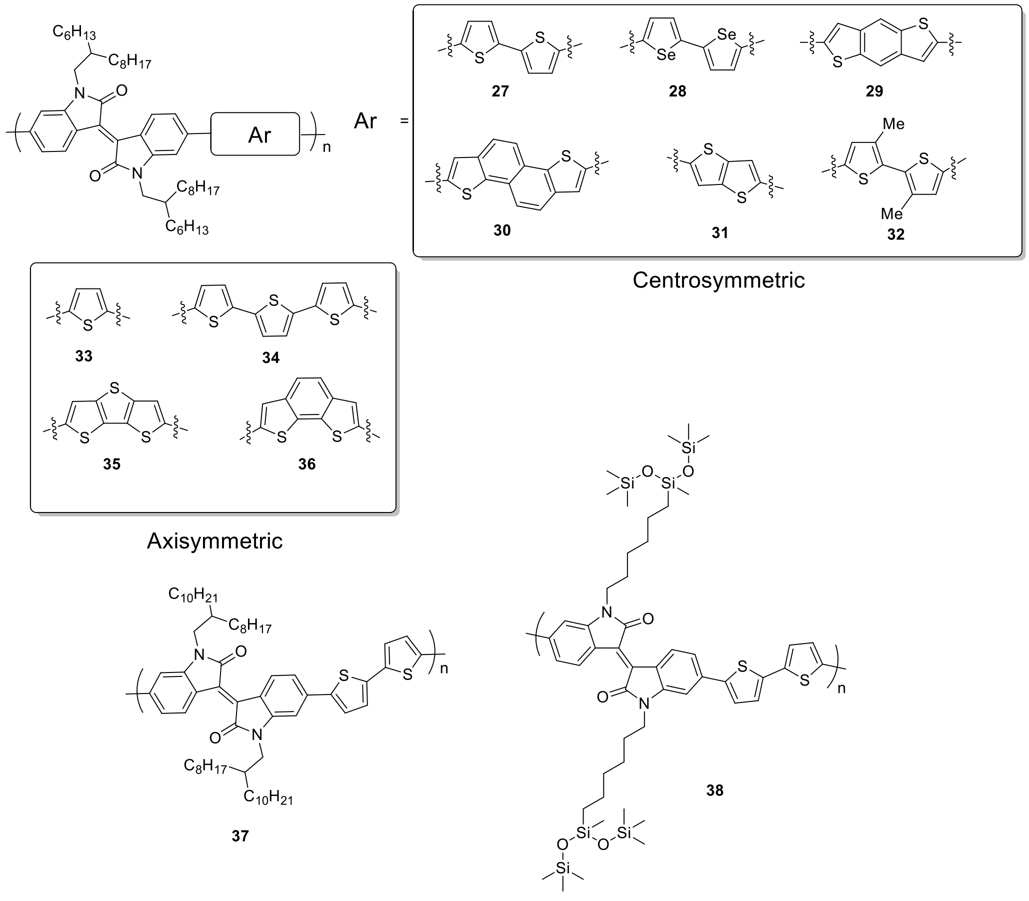

Chart 1.13 Isoindigo based polymer semiconductors, **27**-**38**.

Isoindigo was also paired with thiophene derivatives such as cyclopentadithiophene, and dithienosilole. In these two donor units, π-conjugation is extended over two thiophene rings while the presence of a bridging atom (such as carbon in cyclopentadithiophenes or silicon in dithienosilole) helps to planarize the polymer backbone. Ho et al. copolymerized isoindigo with cyclopentadithiophene, producing a series of four low band gap polymers (**39-42**) (Chart 1.14).[113] Combinations of n-octyl and branched 2-ethylhexyl chains were used on the acceptor and donor units, for a total of four possible combinations. The linear n-octyl chain was shown to promote intermolecular π-π interactions, as compared to the branched 2-ethylhexyl chain. This enhanced intermolecular interaction gradually raised the HOMO level as the number of n-octyl chains was increased from **39** to **42**. All polymers were incorporated in photovoltaic devices with $PC_{61}BM$. The reduced planarity because of branched side chains in **39** increased its miscibility with $PC_{61}BM$, which resulted in an optimal phase separation. This resulted in a higher J_{SC}. In addition, the deep HOMO of **39** (resulting from its branched side chains) led to a higher V_{OC} compared to the other three polymers, therefore, **39**:$PC_{61}BM$ exhibited the highest PCE of 4.0%. Isoindigo was copolymerized with dithienosilole by Stalder et al., and the resulting polymer (**43**) absorbed strongly in the visible and NIR region with an optical band gap of 1.54 eV, as calculated from the onset of absorption (805 nm).[114] Dithienosilole is a weak donor resulting in a deep HOMO (-5.55 eV). The copolymer was blended with $PC_{71}BM$ to serve as the active layer in solar cells with a regular architecture. Consistent with the deep HOMO, a high V_{OC} of 0.86 V was achieved. This report was again a good example where the role of a processing additive was critical. Without any additives, **43**:$PC_{71}BM$ only exhibited a PCE of 1.45% because of a low J_{SC}. The large domain sizes limited the donor-acceptor interfacial area, and exciton dissociation was not efficient enough to produce a large photocurrent. After processing the active layer with 4% DIO, the domain size was much smaller, which enhanced the J_{SC} from 2.82 mA/cm^2 to 10.49 mA/cm^2 and resulted in a PCE of 4.01%.

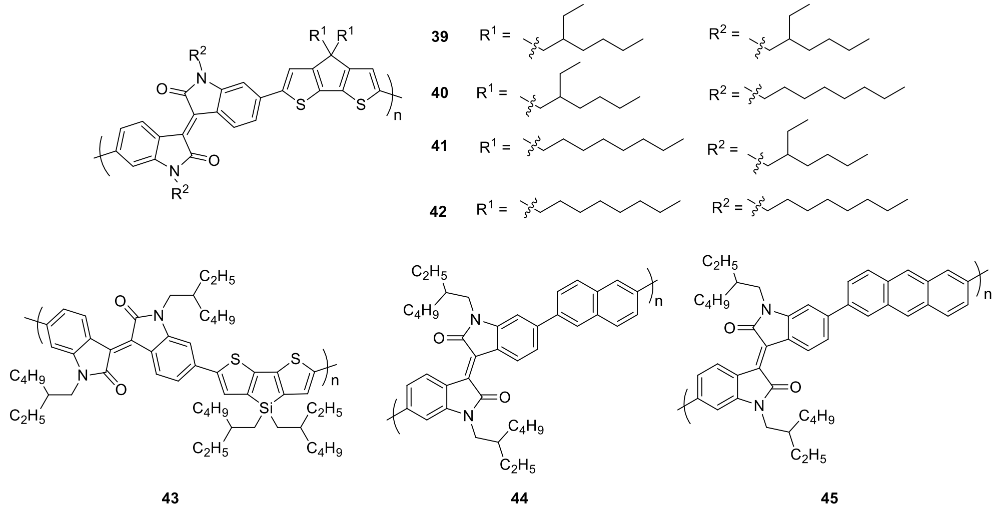

Chart 1.14 Copolymers of isoindigo with cyclopentadithiophene (**39-42**), dithienosilole **(43)**, napthalene **(44),** and anthracene **(45)**.

As mentioned in section **1.4**, early success in the field of OFETs was achieved using acenes, as the planar structure of fused acenes is ideal for charge transport. Owing to their rigid and planar backbone, napthalene and anthracene were copolymerized with isoindigo to produce **44**, and **45**.[115]

Both polymers had a wide absorption ranging from 300 - 700 nm with optical band gaps of 1.80 and 1.75 eV, respectively. Given the extended conjugation in anthracene as compared to napthalene, **45** appeared to aggregate more in the solid state, with a shorter π-π stacking distance. These two polymers were used to fabricate OFETs using a bottom gate, top contact architecture. The measured hole mobilities were 0.003 and 0.013 $cm^2/V{\cdot}s$ for **44** and **45**, respectively. **45** exhibited a higher hole mobility because of its shorter π-π stacking distance. The photovoltaic performance of these polymers followed the same trend as well. In a blend with $PC_{71}BM$, **45** demonstrated a PCE of 1.13% when processed with chloronapthalene as an additive. As opposed to **44**, the higher hole mobility of **45** produced a higher J_{SC}, resulting in a higher efficiency.

1.5.3 Isoindigo-based n-type Polymers

The majority of isoindigo-based polymers reported to date are p-type semiconductors; however, there have been a few n-type materials as well. The homopolymer of isoindigo (**46**) and the copolymer of isoindigo with benzothiadiazole (**47**) were the first two isoindigo-based n-type polymers. Reynolds and co-workers again were the pioneers in developing isoindigo-based n-type semiconductors.[116] The electrochemical reduction of **46** was more stable and reversible compared to **47**. The homopolymer **46** also had a deeper LUMO (-3.9 eV), which matched well with the commonly used n-type material $PC_{61}BM$ (-4.2 eV). Based on the electrochemical reversibility of **46** and because its LUMO energy was a closer match to $PC_{61}BM$, it was incorporated in solar cells with the prototypical p-type material P3HT. Although **46** had an onset of absorption over 700 nm, the photovoltaic performance was poor, producing a maximum PCE of 0.47% because of the low J_{SC} (1.91 $mA{\cdot}cm^{-2}$). The poor electron mobility caused by a high torsion angle between neighboring isoindigo units was thought to limit the photocurrent of the devices. This report motivated Grenier et al. to synthesize a series of polymers (**48-50**) using isoindigo and three different electron deficient units: 5-octylthieno[3,4-c]pyrrole-4,6-dione, 5,5′-dioctyl-1,1′-4H-bithieno[3,4-c]pyrrole-4,4′,6,6′ (5H,5′H)-tetrone (BTPD), and 3,6-bis(thiophen-2-yl)-2,5-bis(2-octyldodecyl)pyrrolo[3,4-c]-pyrrole-1,4-dione.[117] All of the polymers had a LUMO energy between -4.0 and -4.2 eV. Although this was on par with the fullerene derivatives, the photovoltaic performance of these polymers was not explored in this work. Instead, the field-effect electron mobility was measured. The polymer with the centrosymmetric BTPD comonomer (**49**) afforded a better packing in the solid state, which resulted in the highest electron mobility (3.5×10^{-3} cm^2/V·s) among the three polymers studied.

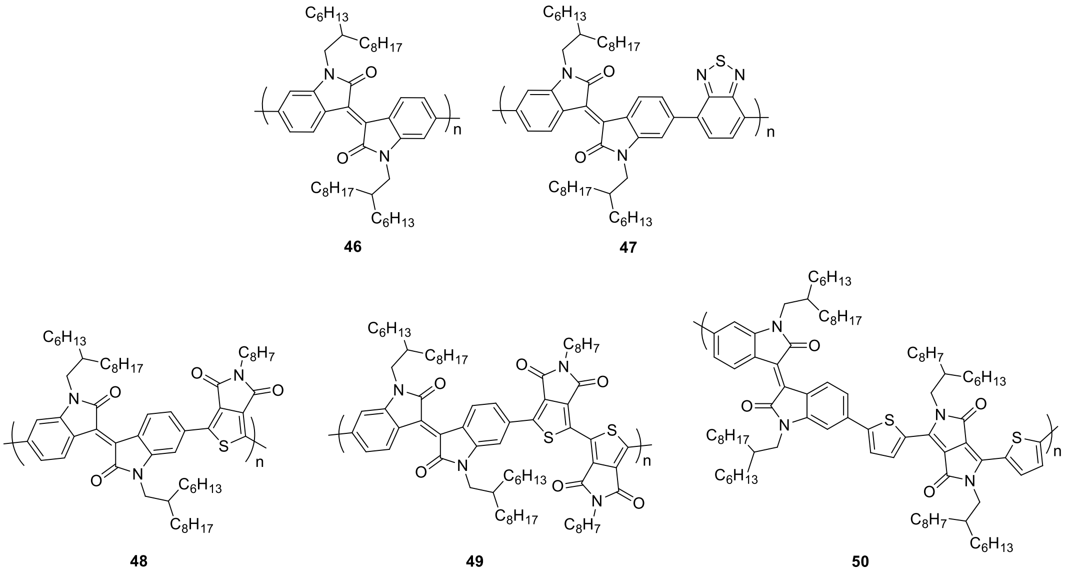

Chart 1.15 Isoindigo-based n-type polymers (**46-50**).

Table 1.3 Optoelectronic properties, electron mobility, and OPV performance of isoindigo-based n-type polymer semiconductors **46-50**.

Polymer	HOMO[a] (eV)	LUMO[a] (eV)	$E_{g,elec}$ (eV)	$E_{g,opt}$ (eV)	μ_e[b] cm^2/V·s	V_{OC}[b] (V)	J_{SC}[b] mA·cm^{-2}	FF[b] (%)	PCE[b] (%)	Ref.
46	-5.54[e]	-3.84	-	1.70	3.7[c,d] × 10^{-7}	0.62	1.91	41	0.47	116
47	-5.67[e]	-3.90	-	1.77	-	-	-	-	-	116
48	-6.0	-4.2	1.80	1.72	3.0×10^{-4}	-	-	-	-	117
49	-6.1	-4.2	1.90	1.75	3.5×10^{-3}	-	-	-	-	117
50	-5.3	-4.0	1.30	1.35	2.7×10^{-4}	-	-	-	-	117

[a]HOMO/LUMO energies estimated from the onset of oxidation/reduction in voltammetry experiments, calibrated against Fc$^+$/Fc. [b]Device parameters of best performing devices. [c]Average performance. [d]Hole mobilities measured using the single carrier devices based on SCLC method, all others are measured by incorporating the semiconductor in OFETs. [e]HOMO energy estimated from $E_{HOMO} = E_{LUMO} - E_{g,opt}$.

1.6 Semiconductors with Modified Isoindigo Structures

In the early research on isoindigo, briefly discussed in section 1.5, isoindigo was always combined with readily available donor units; however, the primary isoindigo structure was not modified. Since 2012, numerous efforts have been made to modify the structure of isoindigo. These modified isoindigo derivatives can be classified into four different sections - halogenated isoindigos, isoindigos substituted with heterocycles, peripherally ring-fused isoindigos, and isoindigos with expanded cores.

1.6.1 Halogenated Isoindigos

In halogenated isoindigos, hydrogen atoms on the isoindigo unit are substituted by halogen atoms such as fluorine and chlorine. Despite having a low lying LUMO level, the majority of isoindigo-based semiconductors described in section 1.5 exhibited p-type behavior. The isoindigo unit was halogenated to further lower the LUMO level, which can introduce n-type or ambipolar behaviour in the semiconductor. In 2012, Lei and coworkers replaced two hydrogen atoms on isoindigo with fluorine atoms, which was the first attempt to modify the core structure of isoindigo.[118] This fluoroisoindigo monomer was copolymerized with bithiophene to yield polymer **52** (Chart 1.16). The LUMO of **52** (-3.88 eV) was lowered by 0.18 eV relative to the non-fluorinated analog **51** (-3.70 eV) (Table 1.4). **52** also demonstrated ambipolar transport behavior when incorporated in OFETs with the top-gate/bottom-contact architecture. Devices fabricated in ambient atmosphere showed a high hole mobility of 1.85 $cm^2/V{\cdot}s$ compared to 10^{-2} $cm^2/V{\cdot}s$ shown by the reference polymer **51** (Table 1.4). The lowered LUMO level in **52** significantly increased the electron mobility up to 0.43 $cm^2/V{\cdot}s$. The introduction of fluorine atoms assisted the polymer to pack more densely, and also functioned as a barrier to oxygen and water, stabilizing electron transport under ambient conditions.

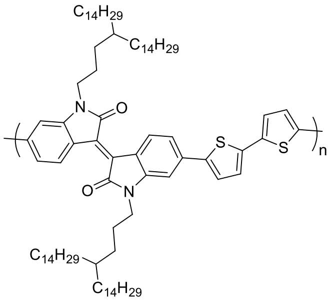

51

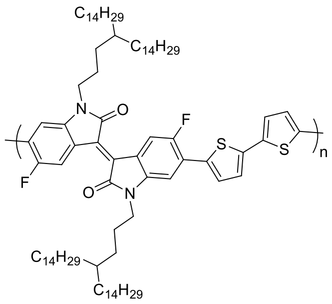

52

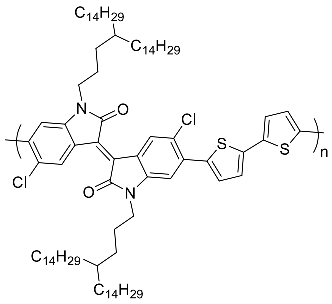

53

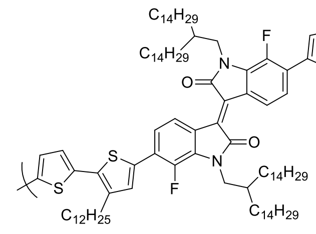

54

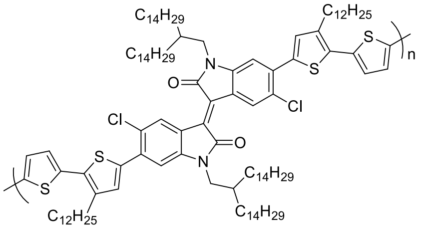

55

Chart 1.16 Halogenated isoindigo based polymer semiconductors (**51 - 55**).

Table 1.4 Optoelectronic properties, charge carrier mobilities, and OPV performance of semiconductors (**51**- **65**) based on halogenated and heterocycle-substituted isoindigos.

Semiconductor	HOMO[a] (eV)	LUMO[a] (eV)	$E_{g,opt}$ (eV)	μ_h[b] $cm^2/V \cdot s$	μ_e[b] $cm^2/V \cdot s$	V_{OC}[b] (V)	J_{SC}[b] $mA \cdot cm^{-2}$	*FF*[b] (%)	PCE[b] (%)	Ref.
51	-5.31[e]	-3.70	1.57	1.27	0.01	-	-	-	-	118
52	-5.46[e]	-3.88	1.50	1.85	0.43	-	-	-	-	118
53	-5.64	-3.86	1.53	0.50	0.62					119
54	-5.51	-3.92	1.45	0.75	-	0.63	4.26	44	1.19	120
55	-5.53	-3.85	1.50	0.10	-	0.75	10.0	61	4.60	120
56	-4.80[e]	-3.73	0.92	0.16	0.14	-	-	-	-	121
57	-5.12	-3.49	1.36	14.4	0.092	-	-	-	-	122
58	-5.64	-3.86	1.78	-	-	0.66[c]	2.7[c]	31[c]	0.6[b]	123
59	-5.23	-3.95	1.28	-	-	0.67[c]	2.5[c]	40[c]	0.7[b]	123
60	-5.68	-3.92	1.76	-	-	0.28[c]	0.22[c]	28[c]	0.02[b]	123
61	-5.25	-3.92	1.33	-	-	0.3[c]	0.6[c]	22[c]	0.04[b]	123
63	-5.67	-3.64	1.54	7.28	0.78	-	-	-	-	124
64	-5.8[e]	-4.1[d]	1.70	-	1.0	-	-	-	-	125
65	-5.6[e]	-4.0[d]	1.60	0.20	0.50	-	-	-	-	125

[a] HOMO/LUMO energies estimated from the onset of oxidation/reduction in voltammetry experiments, calibrated against Fc^+/Fc. [b] Device parameters of best performing devices. [c] Average device parameters. [d] LUMO energy estimated from $E_{LUMO} = E_{HOMO} + E_{g,opt}$. [e] HOMO energy determined by photoelectron spectroscopy.

This initial success with fluorination motivated Lei et al. to synthesize chloroisoindigo and develop polymer **53**.[119] The chlorine substitution followed the same trend as fluorinaton in lowering the LUMO level (-3.86 eV) by 0.16 eV as compared to the parent polymer **51** (-3.70 eV). Similar to the fluorinated analogue (**52**), polymer **53** exhibited ambipolar behavior when incorporated in OFETs. As compared to the parent polymer **51**, the electron mobility of **53** increased to 0.62 $cm^2/V \cdot s$ because of the lowered LUMO level; however, the hole mobility decreased to 0.50 $cm^2/V \cdot s$ (1.27 $cm^2/V \cdot s$ for **51**). This unexpected decrease in hole mobility was attributed to a change in polymer packing. The isoindigo-bithiophene parent polymer (**51**) had a face-on π-π stacking orientation, while polymer **53** had a combination of both edge-on and face-on π-π stacking. The edge-on and face-on orientations refer to the direction of π-π stacking relative to the substrate.[126] In the edge-on orientation, the π-π stacking direction is parallel to the substrate which is desired in OFETs as the charge moves laterally from the source to the drain electrodes.

In the face-on orientation, the π-π stacking direction is perpendicular to the substrate, which is beneficial for OPVs as the layers are stacked vertically in the device.

Following these two reports, Zhang et al. compared the performance of fluoroisoindigo and chloroisoindigo based polymers in both OFETs and OPVs.[120] They used halogenated isoindigos as the acceptor unit and quaterthiophene as the donor unit to synthesize polymer **54** and **55**. The hole mobility of the fluorinated polymer **54** (0.75 $cm^2/V{\cdot}s$) was again higher than its chlorinated counterpart **55** (0.10 $cm^2/V{\cdot}s$) (Table 1.4). Surprisingly, the photovoltaic performance of the chloroisoindigo derivative (**55**, PCE = 4.60%) in a blend with $PC_{71}BM$ was significantly higher than devices made using **54**:$PC_{71}BM$ (PCE = 1.19%). This unexpected difference in performance was ascribed to the contrast in the planarity of the two macromolecules. The torsion angle of the phenyl-thienyl connection was shown to increase from 19° to 40° when the F-atom was substituted by a larger Cl-atom. The increased torsion angle in **55** reduced the planarity of the polymer backbone relative to **54**. The more planar backbone in **54** helped to form highly crystalline films, which resulted in a higher hole mobility in OFETs; however, this planarity produced larger domains when **54** was blended with $PC_{71}BM$ in OPV active layers. These larger domains resulted in inefficient exciton dissociation, producing a poor J_{SC}; hence, **54** exhibited poor efficiencies in OPV applications. In contrast, the reduced planarity in polymer **55** weakened the π-π stacking; therefore, the polymer could not achieve the required crystallinity to obtain a high hole mobility. However, this weakened intermolecular interaction helped **55** to blend well with $PC_{71}BM$ in the OPV active layer. The improved interaction with $PC_{71}BM$ resulted in a favorable morphology, with smaller domains that provided an efficient exciton dissociation pathway, generating a higher J_{SC}. This report is a good example where the torsion angle between neighboring units of a polymer played an important role in determining the charge carrier mobility in OFETs, and helped inspire the work in chapter 3 of this thesis.

1.6.2 Isoindigos Substituted with Heterocycles

To reduce the steric repulsion between the hydrogen atoms at the 4 and 4′-positions and the lactam oxygen on the isoindigo unit, the benzene rings of isoindigo were replaced with thiophenes to develop thienoisoindigo. This was the first heterocycle-substituted isoindigo derivative. It was first synthesized by Ashraf and coworkers and combined with benzothiadiazole to synthesize polymer **56** (Chart 1.17).[121] Owing to its extremely low band gap (0.92 eV), **55** absorbed efficiently in the NIR region. When incorporated in OFETs, the polymer demonstrated ambipolar behavior, with both hole and electron mobilities of ~0.1 $cm^2/V \cdot s$ (Table 1.4). A favorable intramolecular interaction between the sulfur of thiophene and the carbonyl oxygen of the lactam ring further planarizes the system, which afforded a high charge carrier mobility. Following this report, thienoisoindigo was extensively used as the acceptor unit in several donor-acceptor copolymers.[102-104, 127] Among these polymers, the thienoisoindigo-napthalene copolymer **57**, synthesized by Kim et al., exhibited p-type behavior with a record hole mobility of 14.4 $cm^2/V \cdot s$ when incorporated in OFETs (Table 1.4).[122] The increased planarity of the polymer backbone from the incorporation of thienoisoindigo was the primary reason for this extraordinary hole mobility.

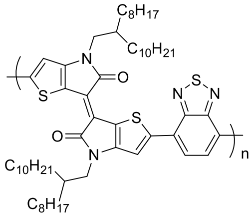

56

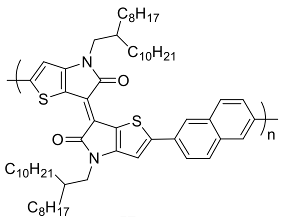

57

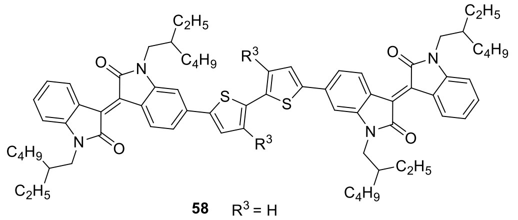

58 R^3 = H

59 R^3 = $OC_{12}H_{25}$

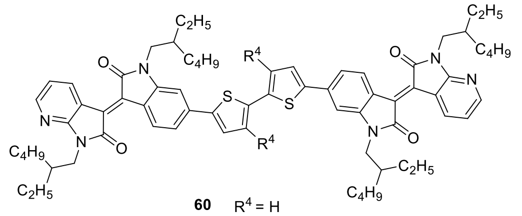

60 R^4 = H

61 R^4 = $OC_{12}H_{25}$

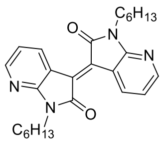

62

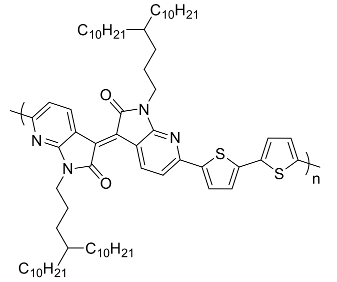

63

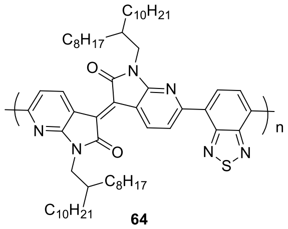

64

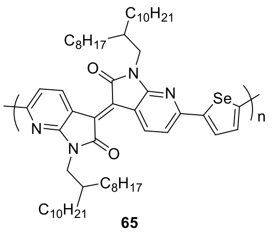

65

Chart 1.17 Organic semiconductors based on heterocycle substituted isoindigo building blocks, (**56-65**).

The next heterocycle substituted building block was azaisoindigo, where one benzene ring of the isoindigo unit was replaced with a pyridine unit. Randell et al. synthesized 7-azaisoindigo and coupled it with substituted bithiophenes to develop D-A molecular semiconductors **60** and **61** (Chart 1.17).[123] The electron deficient nitrogen atom was expected to lower the LUMO of these semiconductors (**60** and **61**) relative to reference molecules (**58** and **59**). However, in comparison to reference molecules **58** and **59**, the pyridine substitution had little effect on the frontier orbital energies and drastically reduced the OPV performance when used with $PC_{61}BM$. The introduction of the nitrogen atom was thought to lower the hole mobility of the semiconductor, thus limiting the PCE. Following this work, Miguel et al. synthesized 7,7′-diazaisoindigo (**62**), a new acceptor unit for organic semiconductors (Chart 1.17). With insights provided by theoretical calculations, this new building block was found to be more planar than isoindigo because of an enhanced electrostatic attraction between the carbonyl group and the H atom at position 4.[128] Since this report was published, several research groups have used 7,7′-diazaisoindigo to synthesize copolymers for OFET applications. Huang et al. developed the diazaisoindigo-bithiophene copolymer **63**, which was shown to have a high crystallinity in thin-films and exhibit an exceptionally high hole mobility of over 7 $cm^2/V \cdot s$(Table 1.4).[124] Following this work, Yue et al. employed benzothiadiazole and selenophene to develop the copolymers **64** and **65**.[125] Owing to its donor-acceptor structure, **65** exhibited ambipolar behavior with high hole/electron mobilities when incorporated in OFETs. Polymer **64** demonstrated a unipolar electron mobility because of its acceptor-acceptor structure.

1.6.3 Peripherally Ring-fused Isoindigos

The last two types of structurally-modified isoindigos include a more advanced transformation of the molecular structure. In peripherally ring-fused isoindigo derivatives, new aromatic rings are fused on the outside of the isoindigo unit. The advantages of a peripherally ring fused system are as follows. Ring-fusion has been shown to increase coplanarity along the polymer or molecular backbone, providing increased π-conjugation, which is favorable for intramolecular charge transport. Moreover, this longer conjugation length extends the optical absorption further into the NIR region. Ring-fusion also provides a larger π-overlap, which leads to better π-π stacking between these conjugated cores, facilitating intermolecular charge hopping. This increased intermolecular π-overlap also makes these aromatic systems less sensitive to positional disorder, which can help charge transport despite a lack of crystallinity. Extending on the idea of thienoisoindigo, [121] Meager et al. developed a thieno[3,2- b]thiophene flanked isoindigo unit (**66**) where thiophene rings were peripherally fused on either side of thienoisoindigo (Chart 1.18).[129] The monomer **66** was copolymerized with benzothiadiazole, thiophene and bithiophene, resulting in polymers **67**-**69**, respectively (Chart 1.18). Thin-films of all polymers exhibited broad absorption spectra having absorption maxima between 875-926 nm. The $E_{g,opt}$ of the polymers were also quite low, varying between 1.05-1.19 eV (Table 1.5). When incorporated in top-gate/bottom-contact OFETs, all of the polymers demonstrated ambipolar behaviour with improvements in mobility observed at high annealing temperature. **67** exhibited higher electron mobilities (0.7 $cm^2/V \cdot s$ at 300 ºC), while **69** had higher hole mobilities (0.4 $cm^2/V \cdot s$ at 300 ºC) (Table 1.5). **68** demonstrated balanced hole and electron mobilities (0.2 $cm^2/V \cdot s$ at 300 ºC). The electron deficient nature of the benzothiadiazole unit lowered the LUMO (-3.9 eV) of **67** and facilitated electron injection from the electrode, which contributed to the higher electron mobility. When the electron deficient benzothiadiazole unit was replaced by an electron rich thiophene unit, the polymer (**68**) showed balanced hole and electron transport. When the thiophene unit was replaced by the more electron rich bithiophene unit, the polymer (**69**) showed a higher hole mobility. All of the polymers showed a large increase in crystallinity at higher annealing temperatures, which is in line with the higher charge carrier mobilities observed post-annealing. These results encouraged McCulloch and coworkers to develop an eight-ring fused isoindigo monomer incorporating thieno[2,3-b]benzothiophene (**70**) (Chart 1.18). This was copolymerized with thiophene to synthesize **71**.[130] The extended conjugation redshifted the lowest energy transition to 665 nm and the polymer had an optical band gap of 1.6 eV (Table 1.5). The polymer was used in the active layer of solar cells alongside $PC_{71}BM$ and exhibited a maximum PCE of 9.1%, the highest efficiency of an OPV made using an isoindigo-based material. This high PCE was mainly because of the high absorption coefficient and hole mobility, which produced a high J_{SC} (17.7 mA·cm^{-2}). Notably, this performance was achieved without using any solvent additives or annealing. Recently, Neophytou et al. synthesized a series of polymers using this thieno[2,3-b]benzothiophene fused isoindigo monomer unit (**70**), although the photovoltaic performance of these polymers was limited to 5.6% because of a substantially lower J_{SC} compared to **71**.[131]

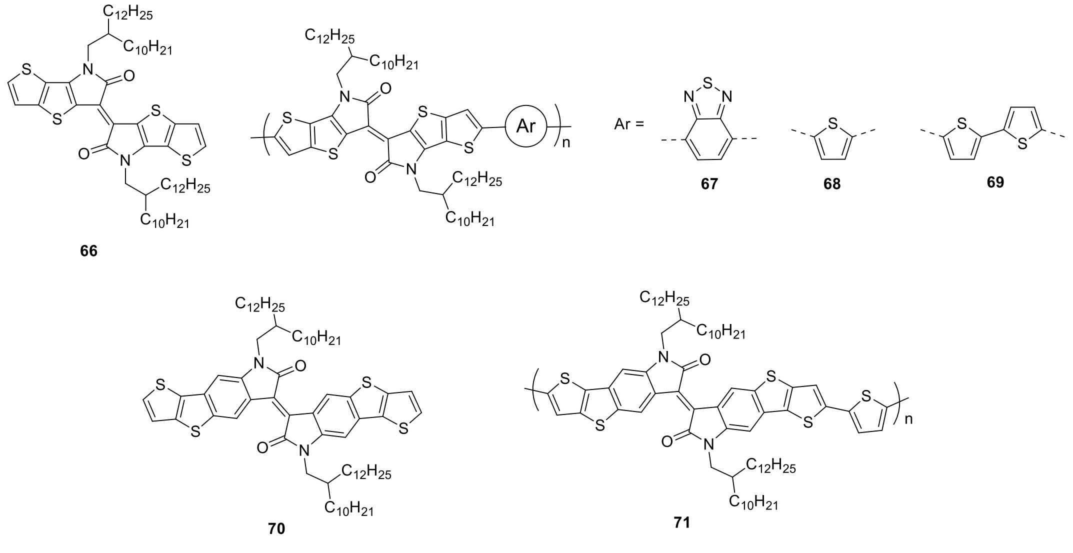

Chart 1.18 Peripherally ring fused isoindigo building block (**66** and **70**) and corresponding copolymers, (**66-69**, **71**).

Table 1.5 Optoelectronic properties, charge carrier mobilities, and OPV performance of semiconductors (**67-85**) based on peripherally ring-fused and core-expanded isoindigos.

Semiconductor	HOMO^{a} (eV)	LUMO^{a} (eV)	$E_{g,opt}$ (eV)	μ_h^{b} cm^2/V·s	μ_e^{b} cm^2/V·s	V_{OC}^{b} (V)	J_{SC}^{b} mA·cm^{-2}	FF^{b} (%)	PCE^{b} (%)	Ref.
67	-4.90	-3.90	1.05	0.40	0.70	-	-	-	-	[129]
68	-4.80	-3.70	1.13	0.20	0.20	-	-	-	-	[129]
69	-4.80	-3.60	1.19	0.40	0.10	-	-	-	-	[129]
71	-5.10^{e}	-3.50^{d}	1.60	0.31^{c}	-	0.72^{c}	17.7^{c}	71^{c}	9.1^{c}	[130]
73	-5.83^{e}	-4.41^{d}	1.42	0.84^{c}	1.1^{c}	-	-	-	-	[132]
75	-5.32^{e}	-4.05^{d}	1.27	1.92^{c}	-	-	-	-	-	[133]
76	-5.71	-3.70	1.22	0.10^{c}	0.075^{c}	-	-	-	-	[134]
78	-5.60	-4.2	1.27	-	-	0.59^{c}	1.28^{c}	30^{c}	0.23^{c}	[135]
79	-5.16	-3.66	1.29	1.1×10^{-3}	6.2×10^{-3}	-	-	-	-	[136]
80	-5.16	-3.58	1.31	1.55	0.021	-	-	-	-	[136]
81	-5.24	-3.58	1.29	1.79	0.087	-	-	-	-	[136]
82	-5.20^{e}	-4.2^{d}	1.01	-	0.03	-	-	-	-	[137]
83	-5.14	-3.96	1.19	1.1×10^{-5}	8.4×10^{-4}	-	-	-	-	[138]
84	-5.85	-3.97	1.60	1.6×10^{-3}	1.3×10^{-3}	0.86	4.2	50	1.8	[139]
85	-5.65	-3.92	1.54	9×10^{-4}	2.3×10^{-3}	0.77	5.9	61	2.8	[139]
86	-5.51	-3.75	1.22	0.19^{b}	$1.5^{c} \times 10^{-2}$	-	-	-	-	[140]
87	-5.40	-3.73	1.26	1.1^{b}	$6.6^{c} \times 10^{-3}$	-	-	-	-	[140]

[a]HOMO/LUMO energies estimated from the onset of oxidation/reduction in voltammetry experiments, calibrated against Fc^{+}/Fc. [b]Average device parameters. [c]Device parameters of best performing devices. [d]LUMO energy estimated from $E_{LUMO} = E_{HOMO} + E_{g,opt}$. [e]HOMO energy determined by photoelectron spectroscopy.

Modifying the isoindigo unit by ring-fusion at the periphery is clearly an interesting approach; however, there have been only a few reports of peripherally modified isoindigo skeletons. Benzoisoindigo was developed by fusing a benzene ring on either side of the isoindigo unit in work described in chapter 2.[141] A series of benzoisoindigo-based semiconductors were synthesized and the effect of linear and cross-conjugation on the optoelectronic properties of these molecules was studied in detail. These results will be discussed in chapter 2.

1.6.4 Isoindigos with Expanded Cores

Isoindigo derivatives with expanded cores have been developed by incorporating conjugated units between the lactam rings of isoindigo. Lei et al. first expanded the core of isoindigo by inserting a benzodifurandione unit between the lactam rings of isoindigo (**72**) (Chart 1.19).[132] As mentioned in section 1.4, early success in organic electronics came with PPVs and Lei et al. carefully analyzed the limitation of these materials. The poor charge carrier mobilities of PPVs were caused by the following. The double bonds in PPVs readily undergo *trans* to *cis* isomerization under UV irradiation, which increases the steric burden between aromatic cores and lowers the π-orbital overlap, inhibiting charge transport (Figure 1.18 a). Even in all-*trans* backbones, the single bonds in PPVs can rotate freely at room temperature, generating many conformational isomers; this again impedes intrachain charge transport (Figure 1.18 b). Because of the limited conjugated area, π-π stacking is also weak in PPVs. Compared to PPVs, the core-expanded monomer **72** was conformationally locked where the vinylene units of PPVs are replaced by lactam rings connected to furanone units via exocyclic double bonds (Figure 1.18 c). The copolymer **73** exhibited a strong absorption in the NIR region with a low $E_{g,opt}$ of 1.42 eV (Table 1.5). Owing to the electron deficient carbonyl groups, the polymer had a very low LUMO level of -4.41 eV. When incorporated in OFETs, **73** exhibited electron mobility up to 1.1 $cm^2/V{\cdot}s$. The higher electron mobility was ascribed to the low lying LUMO level, conformationally locked geometry, and increased planarity because of a non-bonding interaction between the carbonyl oxygen and the hydrogen atom on the aromatic unit (Figure 1.18c). In addition, the low LUMO level increased the stability of OFETs in ambient condition and the devices were shown to be stable over 30 days.

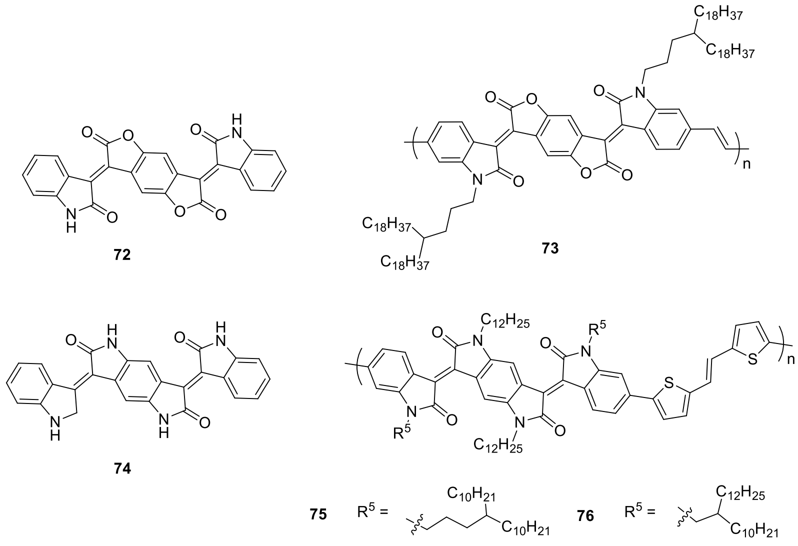

Chart 1.19 Copolymers (**73**, **75**, and **76**) based on core expanded isoindigo building blocks. (**72** and **74**).

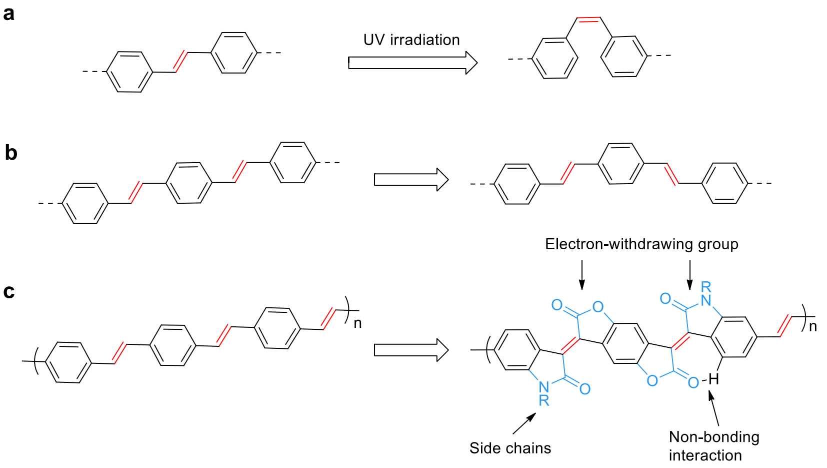

Figure 1.18 (a) Isomerization of PPV derivatives under UV irradiation, (b) Formation of conformational isomer of PPV derivatives because of single bond rotation, (c) Design strategy to modify conformationally labile PPV backbone into a geometrically locked structure.

Following this work, the benzodifurandione unit of **72** was substituted by benzodipyrroledione to produce **74** by the concurrent efforts of the Pei research group[133] and Li research group (Chart 1.19).[134] The monomer **72** only had two nitrogen atoms available for alkylation. Therefore, extremely large alkyl chains such as 4-octadecyldocosyl (40 carbon atoms) were required to impart sufficient solubility to the polymer. These large alkyl chains are not readily available and difficult to synthesize in good yield. Replacing the benzodifurandione unit by benzodipyrroledione introduced two more nitrogen sites for alkylation which afforded sufficient solubility even with shorter alkyl chains. **74** was copolymerized with 1,2-bis(thiophen-2-yl)ethene to yield polymers **75** and **76**. Both of these polymers had an optical band gap below 1.3 eV (Table 1.5). When incorporated in OFETs, **75** exhibited an extremely high hole mobility of 1.92 $cm^2/V{\cdot}s$ while **76** demonstrated hole (0.10 $cm^2/V{\cdot}s$) dominated ambipolar behavior. Despite having similar polymer backbones, the different electronic behavior can be ascribed to the nature of the side chain interactions. The branching point of the alkyl chains in **75** was separated by three methylene groups from the polymer backbone, while the branch point in **76** was separated by only a single methylene group. The close proximity of the branch point in **76** hindered the π-π stacking, thus lowering the hole mobility. In contrast, the distant branching point in polymer **75** helped to maintain the planarity of the backbone, leading to stronger π-π stacking.

Randell et al. developed isoindigo[7,6-g]isoindigo or bisisoindigo (**77**) where a ring-fused dimer of isatin is inserted between isoindigo lactam rings (Chart 1.20).[135] The *N*-alkylated building block was coupled with 5-hexyl-2,2′-bithiophene to produce the molecular semiconductor **78** (Chart 1.20). **78** absorbed across the entire visible region and had an optical bandgap of 1.27 eV (Table 1.5). In contrast to its excellent optical absorption, **78**:$PC_{71}BM$ OPVs had a poor J_{SC} of 1.88 $mA{\cdot}cm^{-2}$, which limited the PCE (0.23%). The poor solubility of this material resulted in an unfavourable blend morphology and larger domain size inhibiting exciton dissociation. Owing to the strong electron deficient nature imparted by the four lactam rings, **78** possessed a LUMO comparable to $PC_{71}BM$. Therefore, semiconductor **78** was also evaluated as an n-type material in a blend with PTB7-Th,[142-143] a commercially available p-type material. The poor OPV performance of those devices was ascribed to large domain sizes and poor film morphologies because of insufficient solubility of **78** in processing solvents. Jiang et al. also copolymerized **78** with a set of thiophene oligomers, resulting in three different polymers (**79-81**) (Chart 1.20).[136] In keeping with their lower band gaps (ranging between 1.50-1.67 eV), all of these polymers exhibited ambipolar behaviour when incorporated in OFETs (Table 1.5). Both the highest hole mobility (1.79 $cm^2/V{\cdot}s$) and the highest electron mobility (0.087 $cm^2/V{\cdot}s$) were achieved with polymer **81**. This was ascribed to the denser packing and higher molecular weight of **81**. To exclude the energetic disorder rising from the free rotation along the polymer backbone, Onwubiko et al. synthesized polymer **82** where double bonds lock-in a rigid backbone.[137] This locked geometry facilitated extensive delocalization along the polymer backbone and shifted the lowest energy transition into the NIR region (927 nm). When incorporated in OFETs, **82** exhibited a high electron mobility of 0.03 $cm^2/V \cdot s$. While the extended conjugation in the locked conformation enhanced the intra-chain electron transport, the promoted π-stacking resulted in a higher inter-chain electronic coupling which provided more facile electron hopping. The extended delocalization also deepened the LUMO (-4.2) which helped to achieve air-stable electron transport. Jiang et al. synthesized **83**, an oligomer of **77**.[138] Owing to its extended conjugation, the lowest energy transition maxima (890 nm) was centered in the NIR region and the oligomer had a low $E_{g,opt}$ of 1.19 eV. **83** demonstrated ambipolar behaviour in OFETs with electron and hole mobilities of 8.4×10^{-4} and 1.1×10^{-5} $cm^2/V \cdot s$ The poor charge carrier mobilities of **83** were attributed to its weak intermolecular attraction because of bulky and branched alkyl side chains. These promising results suggested that further research on bisisoindigo-based systems was warranted and bisisoindigo (**77**) has also been used in the work discussed in chapter 3 of this thesis.

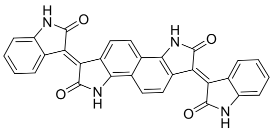

77

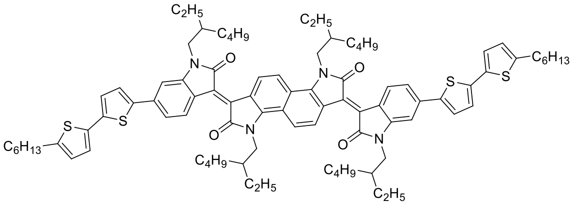

78

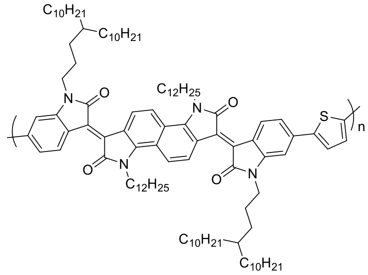

79

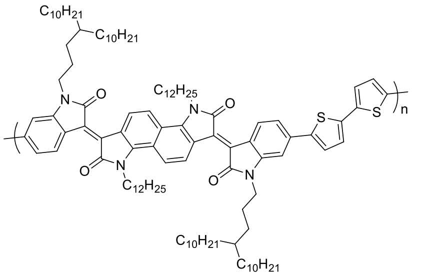

80

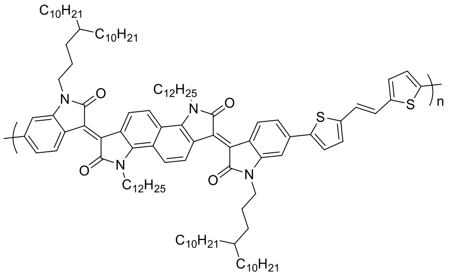

81

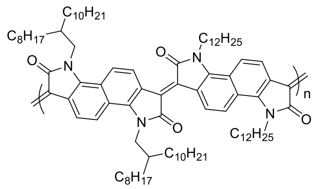

82

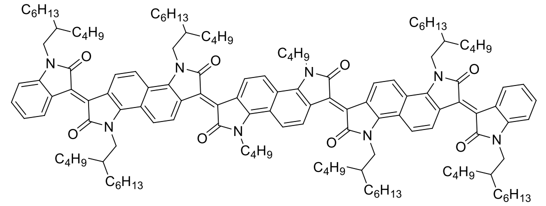

83

Chart 1.20 Semiconductors (**78-83**) based on core expanded isoindigo building block **77**.

Dimers of isoindigo have also been used to develop more complex polymer structures. Randell et al. also synthesized a dimer of isoindigo where two isoindigo units were covalently connected at the 6,6′ position by a single bond.[139] When combined with thiophene and terthiophene to produce polymers **84** and **85** (Chart 1.21, Table 1.5), the LUMO energies were lower and the electron mobilities were higher compared to their isoindigo analogues. James et al. used a dimer where the benzene ring on one indolinone unit was replaced by a thiophene ring on either side of the dimer.[144] This dimer unit was copolymerized with thiophene and bithiophene to synthesize donor-acceptor-acceptor type polymers **86** and **87**, respectively (Chart 1.21).[140] This donor-acceptor-acceptor structure resulted in lower LUMO energies. Both of these polymers exhibited balanced hole/electron mobility, with a highest hole mobility of 1.1 cm^2/V·s for **87** (Table 1.5).

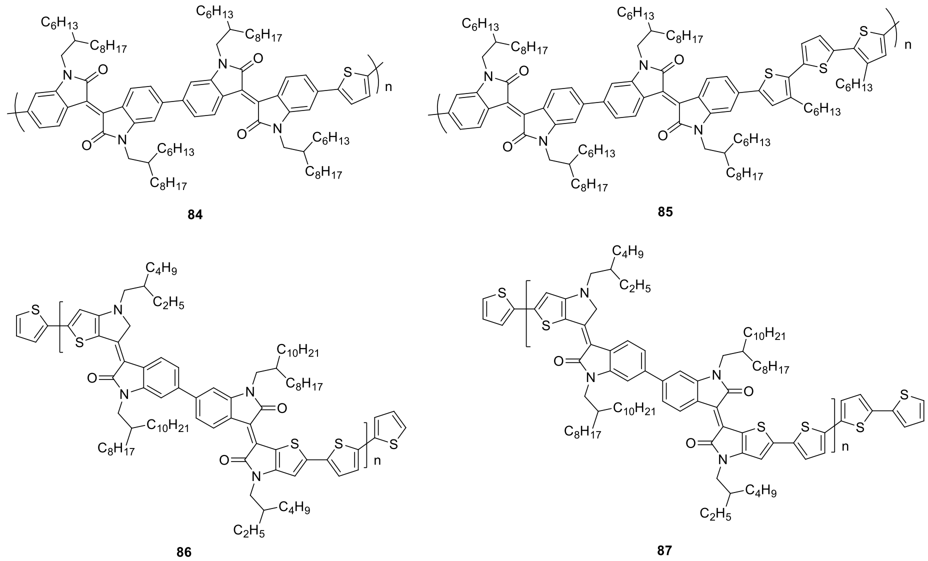

Chart 1.21 Polymers **84-87** which are based on dimerized isoindigo derivatives.

Although numerous examples of modified isoindigo building blocks have been developed over the last six years and proven to be successful in improving device performance, there is room to bring more variation to the isoindigo structure. A clear understanding of structure-property relationships in these new systems is also critically important to move the field forward. Therefore, the work presented in this thesis focuses on modifying the isoindigo structure and understanding the impact of these modifications on OPV and OFET performance.

1.7 Thesis Objectives

This thesis presents the synthesis of novel organic semiconductors and aims to develop a fundamental understanding of the effect of structural changes on optoelectronic properties. Isoindigo based semiconductors have been used to accomplish the work presented in this thesis. Over the course of two major projects, this thesis describes the synthesis of two new modified isoindigo units and their incorporation into a series of molecular and polymeric semiconductors. The thesis also represents a detailed characterization of optoelectronic properties such as the oscillator strength, optical band gap, energy of the HOMO and LUMO, and the charge carrier mobilities. For the work presented here, charge carrier mobilities have been measured by testing the organic semiconductor in OFETs. The semiconductors were also used to fabricate organic solar cells to evaluate their photovoltaic performance.

In chapter 2, the synthesis and characterization of benzoisoindigo based molecular semiconductors is discussed. Benzoisoindigo is a ring-fused isoindigo derivative which was paired with the 5-hexyl-2,2′-bithiophene unit to develop a new donor-acceptor semiconductor. The objective of developing benzoisoindigo was to extend the conjugation length of the isoindigo unit and determine how the substitution pattern on this extended isoindigo unit affects the optoelectronic properties of the resulting donor-acceptor materials. The substitution of donor units on benzoisoindigo can produce either cross or linearly conjugated semiconductors depending on the position of substitution. This study provided a comprehensive understanding of how cross-conjugation affects the optical properties and electronic structure of benzoisoindigo-based semiconductors relative to linearly-conjugated analogues. The extended conjugation length of benzoisoindigo substantially red-shifted the absorption maximum of the lowest energy transition; however, the cross-conjugation significantly reduced the oscillator strength, which limited the photocurrent in OPVs.

Chapter 3 describes synthetic efforts to reduce the torsional strain and conserve the planarity in isoindigo-based polymers. Two new polymers, polyethynylisoindigo and polybisisoindigo, were synthesized. Polyisoindigo, the control polymer in this project, exhibited a poor electron mobility because of a lack of planarity in its backbone. In polyethynylisoindigo, ethynyl spacers were incorporated between neighboring isoindigo units. Polybisisoindigo was synthesized using bisisoindigo, a ring-fused isoindigo derivative. The objective of this study was to determine whether the structural modifications of isoindigo can reduce the torsional strain in the polymer backbone and increase the charge carrier mobility. The study showed that the introduction of an ethynyl spacer in polyethynylisoindigo led to a higher electron mobility compared to the control polymer. In the case of polybisisoindigo, the ring fusion extended the conjugation along the polymer backbone which enhanced the electron mobility. The larger overlap because of ring fusion also made the polymer packing less sensitive to positional disorder which helped to maintain a higher electron mobility.

Finally, the thesis will collect the results from chapters 2 and 3 and draw broader conclusions about structure-property relationships in isoindigo-based systems. While these results were obtained on isoindigo derivatives, a general conclusion will be drawn about the effect of substitution patterns and torsional strain on the optoelectronic properties of the materials which can be applied to other building blocks as well. Ultimately, the research presented in this thesis enhances our understanding of the effect of molecular structure on optoelectronic properties.

1.8 Statement of Co-authorship

A single crystal x-ray diffraction pattern was obtained and the molecular structure of **91** (presented in chapter 2) was determined by Dr. Jianfeng Zhu of the Saskatchewan Structural Sciences Centre, University of Saskatchewan. OFET measurements (presented in chapter 3) were done by Dr. Arthur D. Hendsbee under the supervision of Professor Yuning Li at the University of Waterloo. GIWAXS data (presented in chapter 3) was obtained by Dr. Maged Abdelsamie under the supervision of Dr. Michael F. Toney at the Stanford Synchrotron Radiation Lightsource. Both of the collaborators significantly contributed to the analysis of the OFET and GIWAXS data.

Chapter 2 - Effect of Cross-Conjugation on Derivatives of Benzoisoindigo, an Isoindigo Analogue with an Extended π-System[*]

2.1 Introduction

The emergence of isoindigo as an electron deficient building block in conjugated systems was discussed briefly in section 1.5, which focused on the reports where isoindigo was paired with readily available donors to synthesize new donor-acceptor materials.[102, 104] In a majority of those materials, extended conjugation led to an improvement in their device performance. The research presented in this chapter was designed to further explore the potential of extending the conjugation length of isoindigo. As discussed in section 1.5, when thiophenes on isoindigo-thiophene materials were replaced with oligothiophenes, the increased conjugation length enhanced the planarity. This resulted in a higher charge carrier mobility.[109] McCulloch and coworkers modified the isoindigo core structure by fusing thienothiophene to the periphery of the isoindigo unit to increase its conjugation length (section 1.6). A thienothiophene-fused isoindigo based polymer exhibited a PCE of 9.1% when incorporated in OPVs. The rigid backbone of the ring-fused building block resulted in a high hole mobility which generated a high photocurrent of 17.7 $mA\cdot cm^{-2}$.[130] Using a similar ring-fusion approach, I developed benzoisoindigo by fusing benzene rings on either side of the isoindigo unit (Figure 2.1 a, b). In this ring-fused benzoisoindigo unit, the π-conjugation is extended relative to isoindigo. Therefore, semiconductors based on the benzoisoindigo unit are expected to have a narrower bandgap, leading to efficient absorption in the NIR region. Moreover, the ring-fused system of benzoisoindigo introduces additional rigidity in the system, which helps maintain planarity in the molecular backbone. The synthesis and optoelectronic characterization of benzoisoindigo-based molecular semiconductors will be discussed and compared with isoindigo analogues in this chapter.

---

[*] A version of this chapter has been published before. Reproduced with permission from Ganguly, A.; Zhu, J.; Kelly, T. L. Effect of cross-conjugation on derivatives of benzoisoindigo, an isoindigo analogue with an extended π-system. *J. Phys. Chem. C* **2017**, *121*, 9110-9119.

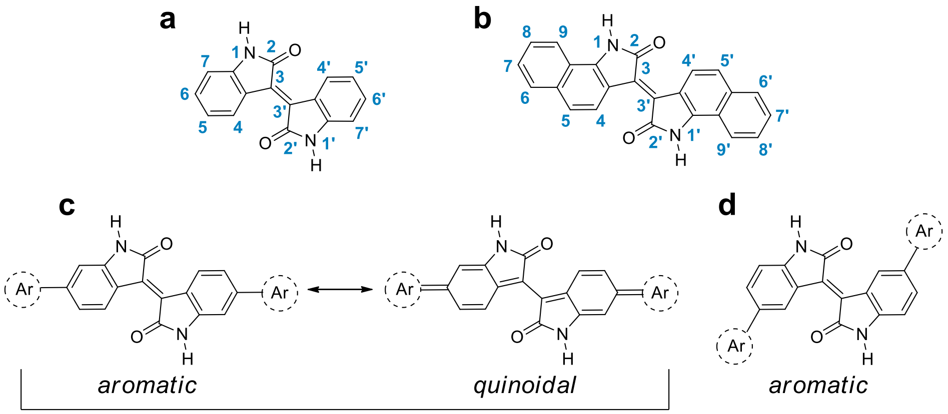

Figure 2.1 The structure and numbering scheme of (a) isoindigo and (b) benzoisoindigo; isoindigo-based D-A compounds with (c) a linearly-conjugated 6,6′-linkage, and (d) a cross-conjugated 5,5′-linkage.

In the preparation of D-A semiconductors, the donor unit and the acceptor unit are often synthesized separately, followed by Pd-catalyzed cross-coupling reactions to covalently connect the two units. In these cross-coupling reactions, the substitution pattern of the donor and acceptor can greatly influence the optoelectronic properties of the resulting materials. When isoindigo is used as the acceptor unit, there are two common substitution patterns – substitution at the 5,5′ or the 6,6′ positions of isoindigo (Figure 2.1 c). All of the isoindigo-based semiconductors reviewed in section 1.5 and section 1.6 were synthesized following an identical substitution pattern. In those examples, isoindigo was always substituted at the 6,6′ positions, producing linearly-conjugated systems. In a linearly conjugated system the π-electrons are effectively delocalized over the entire molecule; however, substitution at the 5,5′ positions generates cross-conjugated isomers because of the lack of a quinoidal form (Figure 2.1 d). In a cross-conjugated system, the conjugation is therefore broken at the linkage of the donor and acceptor, which dramatically affects the properties of the D-A material. There are only a few studies comparing these cross-conjugated systems with their linearly-conjugated analogues. Estrada et al. studied isoindigo-based oligomers with different substituents and substitution patterns. They concluded that the transition dipole moment is more influenced by the pattern of substitution (6,6′ or 5,5′) than the functional groups attached to the system.[145] Pruissen et al. carried out another study on the effect of cross-conjugation on two different D-A copolymers, with similar results.[146]

Similar to isoindigo, benzoisoindigo can be substituted in such a way that both linearly-conjugated and cross-conjugated derivatives can be prepared. For example, substitution at the 7,7′ position (Figure 2.1 d) will afford linearly-conjugated materials, while 5,5′ linkage will produce cross-conjugated isomers. Although there are a few reports on isoindigo-based systems where the substitution pattern was systematically varied, the impact of cross-conjugation on more extended π-systems such as benzoisoindigo has not yet been explored. The longer conjugation length of benzoisoindigo derivatives, even when the system is cross-conjugated, may have a substantial impact on the overall optical and electronic properties. Hence, this chapter includes a comparative discussion on the effect of substitution pattern on isoindigo and benzoisoindigo-based semiconductors. Therefore, in addition to synthesizing benzoisoindigo, the intention was to develop both linearly-conjugated and cross-conjugated semiconductors and accomplish a comparative study of their optoelectronic properties. The compounds included in this study are shown in Chart 2.1. They include isoindigo (**88**) and benzoisoindigo (**89**), as well as D-A small molecules **1, 90-92**. Compound **91** is a new cross-conjugated D-A material based on benzoisoindigo, while **92** is the linearly-conjugated analogue. **91** was successfully synthesized; **92** was synthetically inaccessible, and therefore density functional theory (DFT) was used to compare the properties of all six compounds. For comparison, the analogous isoindigo-based systems (**1**, **90**) were also synthesized. The optoelectronic properties of compounds **1**, **88-91** are characterized by both UV-vis spectroscopy and cyclic voltammetry. The impact of cross-conjugation on device performance was evaluated by the fabrication and testing of prototype OPV devices.

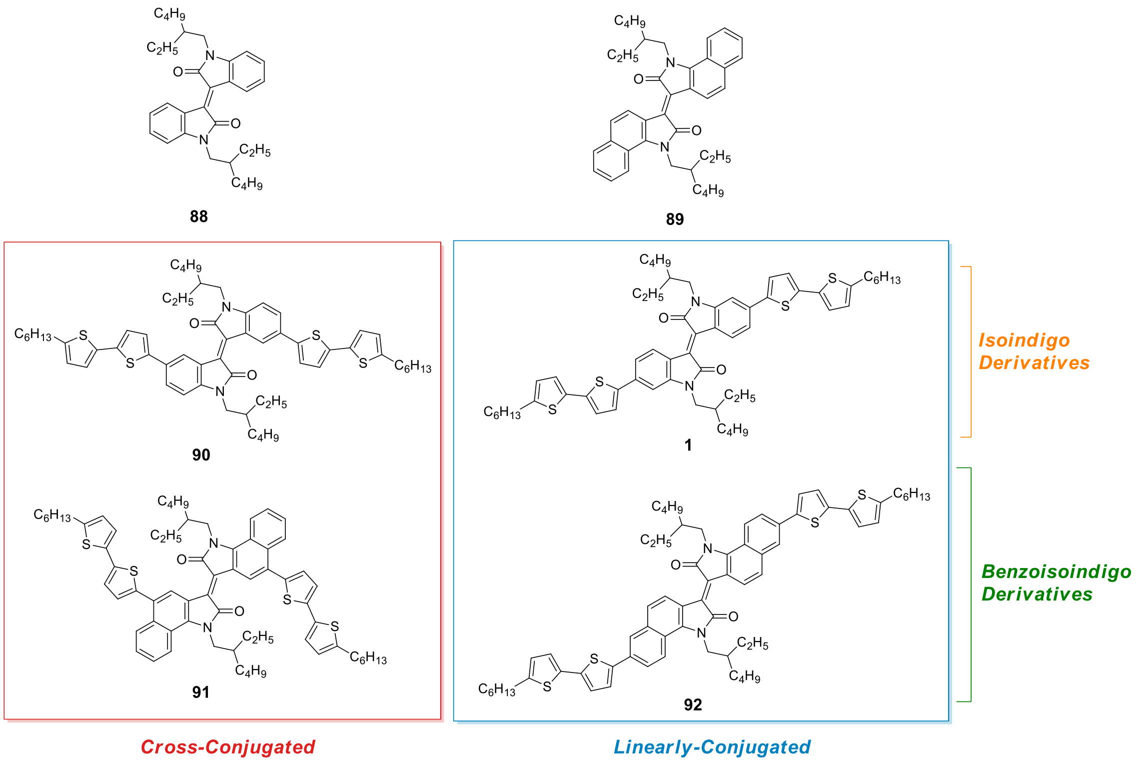

Chart 2.1 Structure of isoindigo (**88**), benzoisoindigo (**89**), and the D-A materials (**1, 90–92**).

2.2 Results and Discussion

2.2.1 Synthesis

The synthesis of compound **89** was accomplished in four steps, as presented in Scheme 2.1. The Martinet isatin synthesis was first used to prepare compound **94** starting from commercially available 1-aminonaphthalene (**93**).[135, 147] The Sandmeyer isatin synthesis is commonly employed to prepare isatins and their derivatives and it requires the use of water as a solvent;[148-149] however, the complete insolubility of **93** in water precludes its use. As a consequence, the Martinet synthesis (carried out in glacial acetic acid) was used.[150] In order to reduce the corresponding isatin derivative (**94**), a Wolff-Kishner reduction was employed.[151] The acid-catalysed aldol condensation of **94** and **95** subsequently afforded benzoisoindigo (**96**) in moderate yield.[150] Owing to extended intermolecular π-π interactions, this ring-fused isoindigo derivative is completely insoluble, even when compared to the isoindigo analogue. To increase the solubility, compound

96 was *N*-alkylated using 2-ethylhexyl bromide and potassium carbonate to yield *N*,*N*′-bis(2-ethylhexyl)benzoisoindigo (**89**), which was highly soluble in both dichloromethane and chloroform.

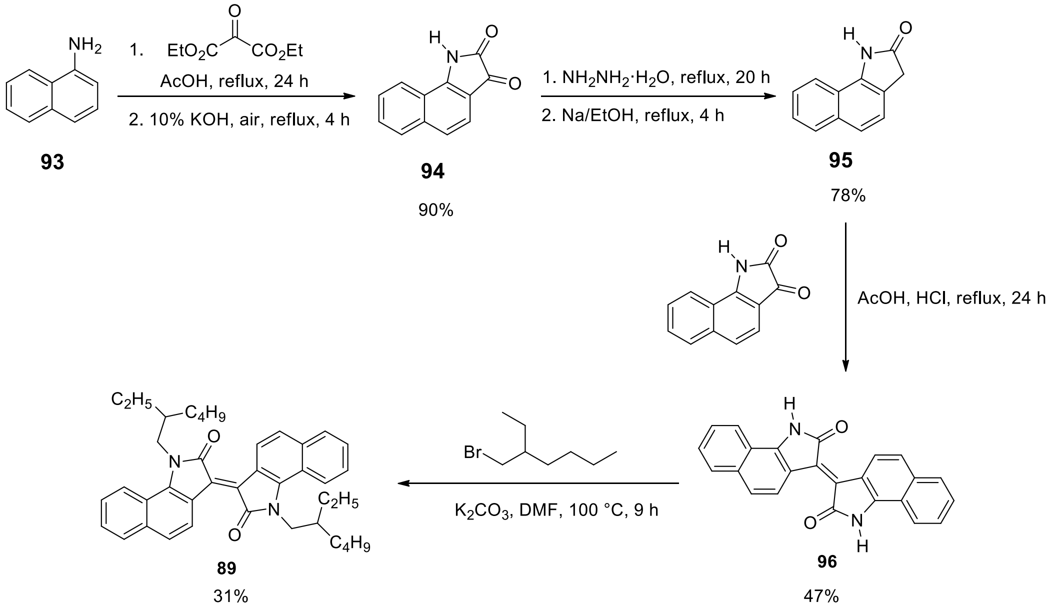

Scheme 2.1 Synthesis of *N*,*N*′-bis(2-ethylhexyl)benzoisoindigo (**89**).

The synthesis of **91** started from 1-amino-4-bromonapthalene (**97**) (Scheme 2.2). In the first three steps, 5,5′-dibromobenzoisoindigo (**100**) was synthesized in a similar fashion to **89**. However, in addition to **100**, the acid-catalysed aldol condensation of **98** and **99** produced a monobrominated byproduct (5-bromobenzoisoindigo, **101**) in a nearly 1:1 mole ratio. The poor separation of the dibrominated (**100**) and monobrominated (**101**) products further complicated the synthesis; however, the formation of this side product could be avoided by instead carrying out a deoxygenation reaction[152] on the corresponding isatin. The alkylated 5,5′-dibromobenzoisoindigo (**102**) was then reacted with 5-trimethylstannyl-5′-hexyl-2,2′-bithiophene (**103**) to form the D-A compound **91** via Stille cross-coupling.

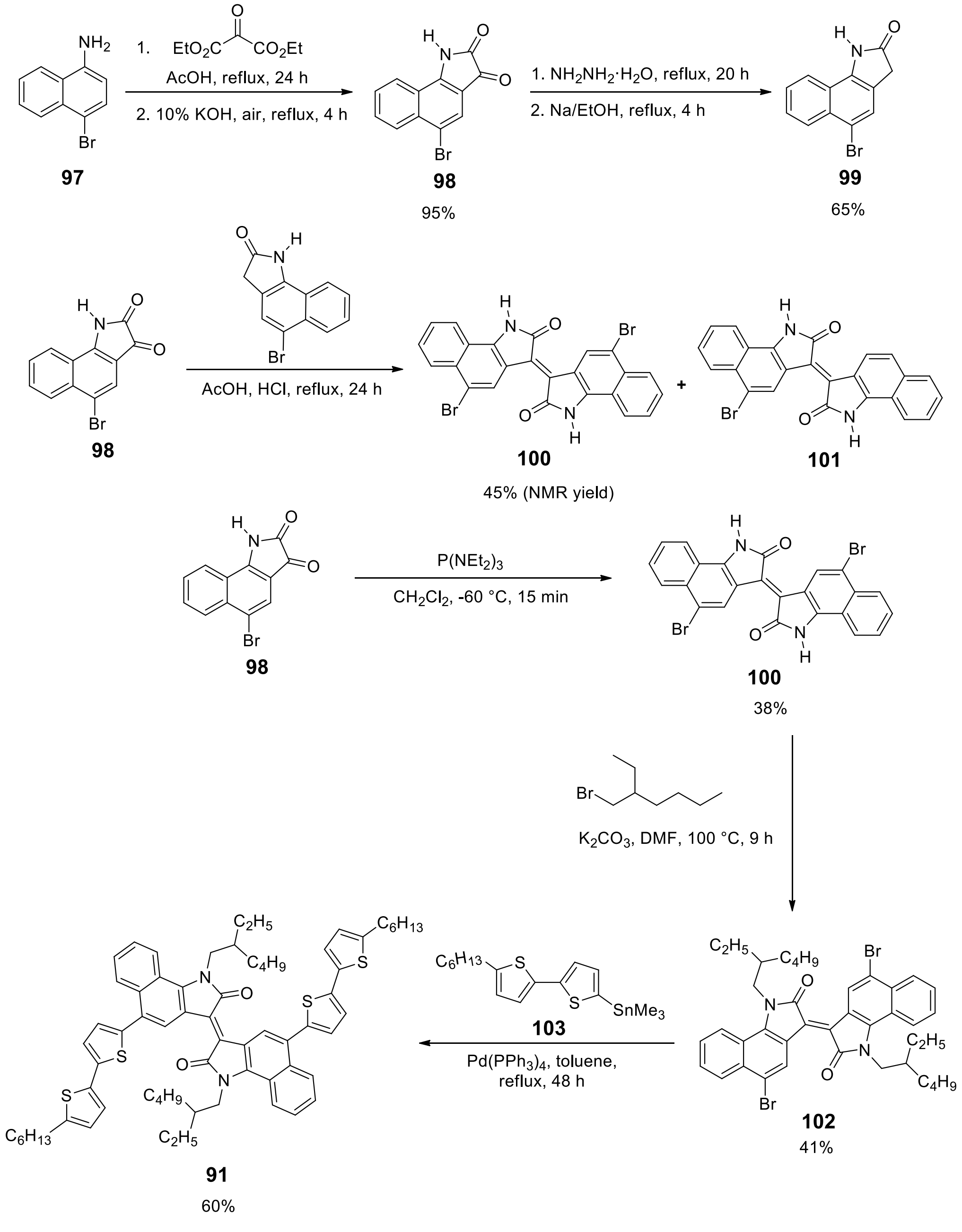

Scheme 2.2 Synthesis of Donor–Acceptor−Donor Compound **91**.

Compounds **88** and **1** are known compounds and were synthesized according to previously reported procedures.[150] Compound **90** is an isomer of **1** and has not been previously reported; **90** was synthesized in a similar fashion to **91**. The synthetic details of **1**, **88-91** are given in Chapter 0. Unfortunately, the linearly-conjugated isomer (**92**) was not synthetically accessible, owing to difficulty accessing the requisite 1-amino-6-bromonaphthalene starting material. An attempt to synthesize another linearly conjugated isomer, starting from 6-bromo-2-napthol (**104**) is presented in Scheme 2.3. In practice, it did not afford the desired isomer of the isatin (**107**), making it impossible to produce a linearly-conjugated benzoisoindigo derivative. Zhao et al. also reported synthetic difficulties with the same isomer of benzoisoindigo; the yield in their final step (4%) was far too low to be a viable route to the desired product.[153] Therefore, a detailed theoretical treatment of all compounds was also carried out, including the linearly-conjugated isomer (**92**).

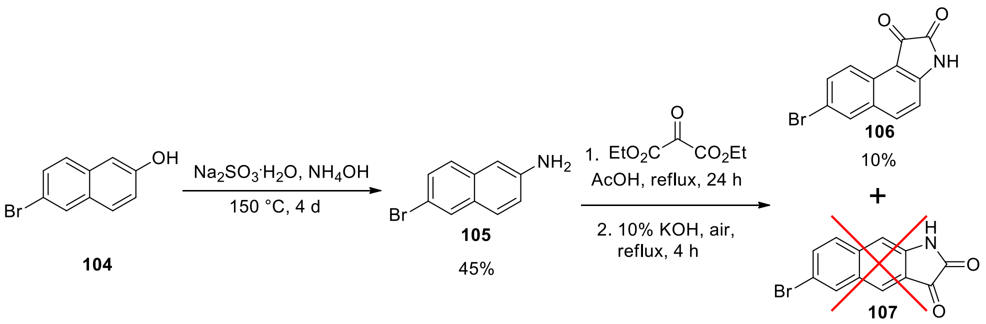

Scheme 2.3 Attempted reactions to synthesize linearly-conjugates isomer starting from 6-bromo-2-napthol.

2.2.2 Density Functional Theory Calculations

In order to compare the effect of cross-conjugation and extended conjugation on the optoelectronic properties of these semiconductors, the electronic structure of compounds **88-90**, **1**, and **91-92** was calculated using density functional theory at the B3LYP/6-31G(d,p) level of theory. After optimization of the molecular geometry, the vertical excited-state transitions were calculated using time-dependent density functional theory to determine their theoretical oscillator strengths (f_{osc}). The long 2-ethylhexyl alkyl chains were replaced by methyl groups in all calculations to reduce the computing cost. The FMO energies, HOMO-LUMO gaps (ΔE), and the oscillator strength for the lowest-energy electronic transition are summarized in Table 2.1.

Table 2.1 Experimental and calculated electronic spectroscopic data and frontier orbital energy levels for compounds **88-90, 1,** and **91-92**.

Compound	λ_{max}^{a} (soln) (nm)	$\varepsilon/10^{4a}$ (soln) ($M^{-1}\cdot cm^{-1}$)	f_{osc}^{a} (exp.)	E_{HOMO}^{b} (exp.) (eV)	E_{LUMO}^{b} (exp.) (eV)	ΔE^{b} (exp.) (eV)	f_{osc}^{c} (cal.)	E_{HOMO}^{c} (cal.) (eV)	E_{LUMO}^{c} (cal.) (eV)	ΔE^{c} (cal.) (eV)
88	499	0.41	0.06	-	–3.82	-	0.12	–5.71	–2.94	2.77
89	625	0.86	0.19	–5.75	–4.01	1.74	0.27	–5.25	–3.02	2.23
90	560	0.25	0.05	–5.49	–3.89	1.60	0.02	–5.11	–2.93	2.18
1	591	3.20	0.34	–5.61	–3.87	1.70	1.55	–5.12	–2.94	2.18
91	654	0.67	0.14	–5.57	–4.08	1.49	0.08	–5.06	–3.10	1.96
92	-	-	-	-	-	-	1.17	–5.03	–3.07	1.96

[a]Measured in chloroform solution for the lowest energy electronic transition. [b]Measured electrochemically. Cyclic voltammograms were referenced to a ferrocenium/ferrocene (Fc^{+}/Fc) external standard, which is –5.1 eV with respect to vacuum. The HOMO and LUMO energies were determined from the onset of oxidation and reduction, respectively.[154] [c]Calculated using DFT at the B3LYP/6-31G(d,p) level of theory, using a polarizable continuum model with a dielectric constant equal to that of dichloromethane.

The calculated HOMO/LUMO levels (-5.71/-2.94 eV) of isoindigo (**88**) are in reasonable agreement with those calculated by Estrada et al. for *N*,*N'*-dimethylisoindigo (–5.91 and –3.06 eV, respectively).[145] Relative to isoindigo (**88**), benzoisoindigo (**89**) has a substantially reduced (ca. 500 meV) HOMO-LUMO gap since it has a longer conjugation length. The HOMO of **89** is substantially higher in energy than that of **88** (–5.25 vs. –5.71 eV), while the LUMO is only slightly deeper (–3.02 vs. –2.94 eV). This suggests the impact of the additional fused benzene ring on the LUMO is relatively small, which is in agreement with the idea that the electron-withdrawing amide groups of the isoindigo molecule are primarily responsible for controlling the LUMO energy (Figure 2.2).[145] As per the calculated data, these changes in the FMO energy levels are predicted to result in a pronounced red-shift (152 nm) in the lowest energy (HOMO → LUMO) electronic transition (Figure 2.3a). Owing to the extended conjugation length of benzoisoindigo, the oscillator strength of this transition is also anticipated to substantially increase from 0.12 to 0.27. The HOMO–2 → LUMO transition is also predicted to exhibit a similar red-shift (47 nm) from 402 to 449 nm.

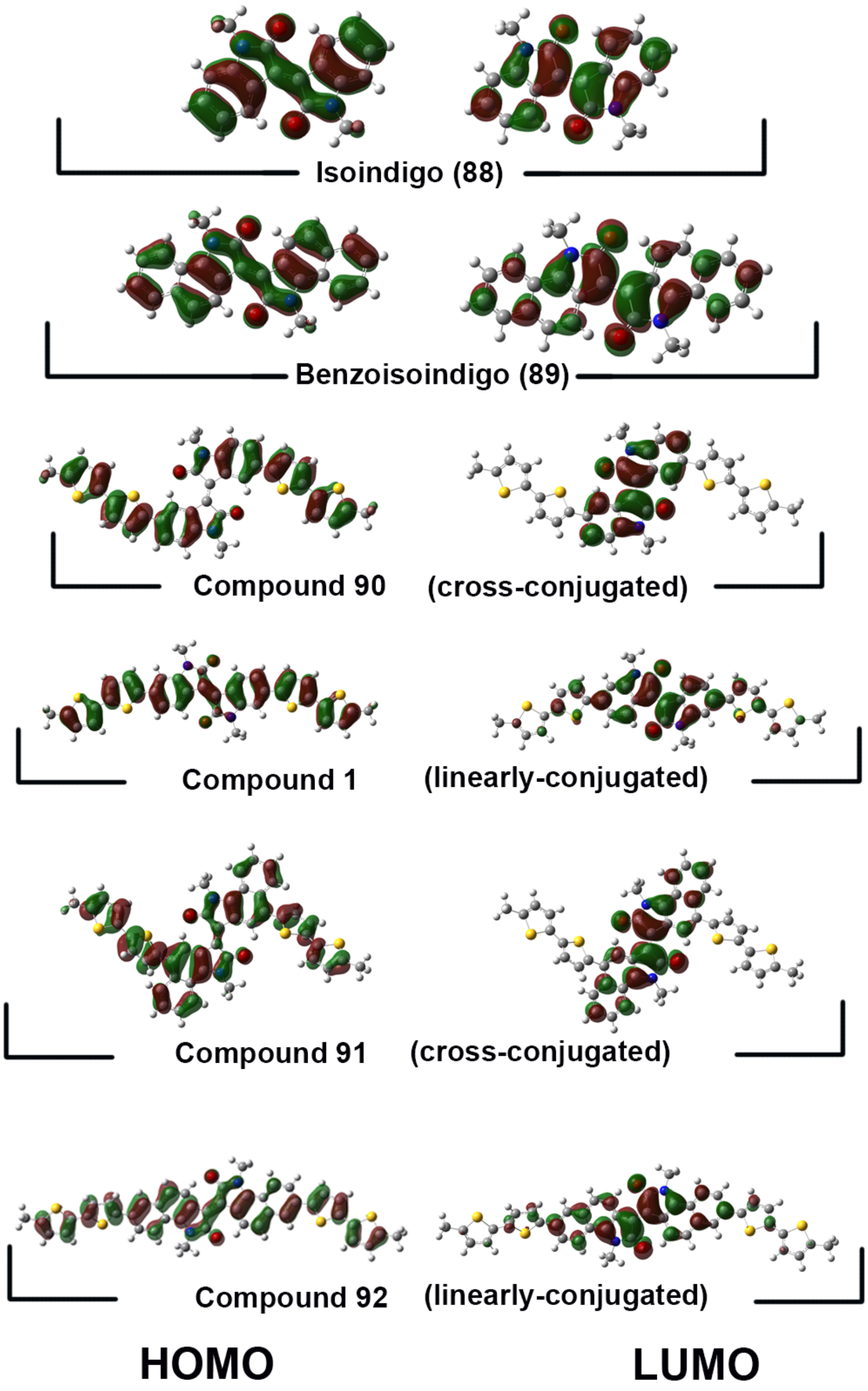

Figure 2.2 Frontier molecular orbital isosurfaces of compound **88-90**, **1**, and **91-92**.

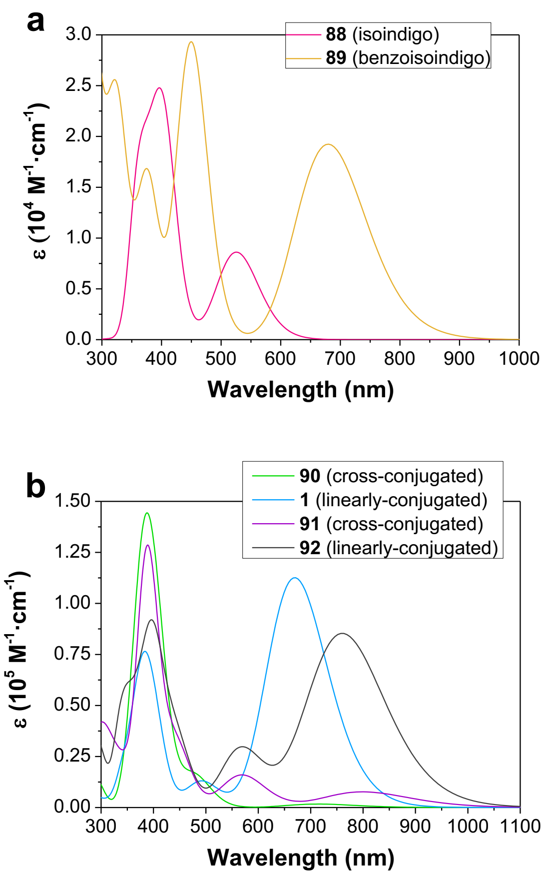

Figure 2.3 Predicted UV-vis spectra, calculated using time-dependent density functional theory (TDDFT), for: (a) isoindigo (**88**) and benzoisoindigo (**89**); (b) D-A compounds **1**, and **90-92**.

In the case of the cross-conjugated and linearly-conjugated bithiophene-isoindigo semiconductors (**90** and **1**, respectively), the substitution pattern on isoindigo appears to have little impact on the HOMO and LUMO levels. Hence, the HOMO (–5.11 vs. –5.12 eV) and the LUMO (–2.93 vs. –2.94 eV) energies are not significantly changed (Table 2.1). In comparison to isoindigo (**88**), the addition of the electron rich 2,2'-bithiophene groups substantially raises the HOMO energy (by ca. 600 meV), but the LUMO energy is essentially identical. In contrast to the FMO energies, both the relative contributions to the FMOs and the oscillator strength of the HOMO → LUMO transition are affected by the substitution pattern on isoindigo. While the HOMO of **90** is primarily localized on the oxindole and pendant bithiophene groups, the HOMO of **1** has a substantial contribution from the exocyclic double bond (Figure 2.2). Furthermore, the LUMO of

1 also has a notable contribution from the bithiophene groups; this is in contrast to **90**, where it is strictly centered on the isoindigo core. These differences resulted in a much higher oscillator strength in **1**; f_{osc} of the linearly-conjugated **1** is nearly 80-fold higher than that of the cross-conjugated **90**. Since the LUMO of both molecules is primarily centered on the 3,3′-bipyrrolidine-2,2′-dione core, the spatial overlap of the initial and final wavefunctions will be much higher in **1** than in **90**, leading to a larger overall f_{osc}.

For the bithiophene-benzoisoindigo derivatives **91** and **92**, the same trends are observed. Following the same trend, the HOMO-LUMO gap in **91** and **92** is narrowed by ca. 300 meV relative to the parent benzoisoindigo (**89**), mostly because of the higher HOMO energies (Table 2.1). Again, the FMO energies of **91** and **92** are essentially unchanged, while the f_{osc} of the HOMO → LUMO transition in **92** is over an order of magnitude (15-fold) larger than in **91**. The effect of ring fusion on the FMOs and the lowest energy electronic transition is substantial. The HOMO of **91** again has substantial contributions from both the pendant bithiophene groups and the central oxindole units; however, in contrast to **90**, there is now a significant contribution from the exocyclic double bond (Figure 2.2). Since the LUMO of **91** is still predominantly centered on the 3,3′-bipyrrolidine-2,2′-dione core (as in **90**), this enhances the spatial overlap of the initial and final wavefunctions in **91** for the HOMO → LUMO transition. As a result, the difference in f_{osc} (15-fold) is substantially lower in the bithiophene-benzoisoindigo derivatives (**91** and **92**) than in the bithiophene-isoindigo derivatives (**90** and **1**, 80-fold difference in f_{osc}).

In keeping with the extended conjugation in the benzoisoindigo-based systems, most of the electronic transitions for the benzoisoindigo-bithiophene derivatives are associated with a red-shift compared to the isoindigo-bithiophene analogues. The HOMO → LUMO transition is red-shifted by ca. 90 nm when comparing both **90** and **91** (cross-conjugated) and **1** and **92** (linearly conjugated). The HOMO–2 → LUMO transitions, located between 475 and 575 nm, are also red-shifted in a similar fashion (Figure 2.3b). Since the higher energy $\pi \rightarrow \pi^*$ transitions (between 375 - 400 nm) are more localized in nature and mostly centered on either the pendant bithiophene groups or napthalene backbone, these transitions do not shift as a function of substitution pattern.

2.2.3 Optical Properties

To evaluate the impact of cross-conjugation on benzoisoindigo and its derivatives and validate the calculated optical properties, the absorbance spectra were measured in solution for compounds **88-90**, **1**, and **91-92**. The absorption maximum (λ_{max}), molar extinction coefficient and experimentally-determined oscillator strength ($f_{osc(exp)}$) for each compound are listed in Table 2.1. $f_{osc(exp)}$ was calculated according to Equation 2.1.[145] Where, ε_{max} is the molar absorptivity at the maximum of the lowest energy transition, $\bar{\nu}$ is peak maximum in cm^{-1}, $\Delta\bar{\nu}_{1/2}$ is the full-width at half-maximum (FWHM) in cm^{-1}. Isoindigo (**88**) exhibits a reasonably strong absorption band in the middle of the visible region ($\lambda_{max} \approx 500$ nm), with a molar absorption coefficient of 4.1×10^3 $M^{-1}\cdot cm^{-1}$ (Figure 2.4 a), along with several higher energy absorption bands between 300 and 400 nm ($\varepsilon \approx 1 \times 10^4$ $M^{-1}\cdot cm^{-1}$). Based on the predictions by TDDFT (Figure 2.3 a), the band at 500 nm can be ascribed to the HOMO → LUMO transition, whereas the bands at 300 – 400 nm emerge because of the HOMO–2 → LUMO and HOMO–3 → LUMO transitions. The benzoisoindigo (**89**) displays similar features in its absorption spectrum (Figure 2.4 a), only red-shifted relative to isoindigo. The red-shift, along with the increase in oscillator strength for the HOMO → LUMO transition, are entirely consistent with the theoretical TDDFT results.

$$f_{osc(exp)} = \frac{\varepsilon_{max}\Delta\bar{\nu}_{1/2}}{2.5 \times 10^8} \qquad \text{Equation 2.1}$$

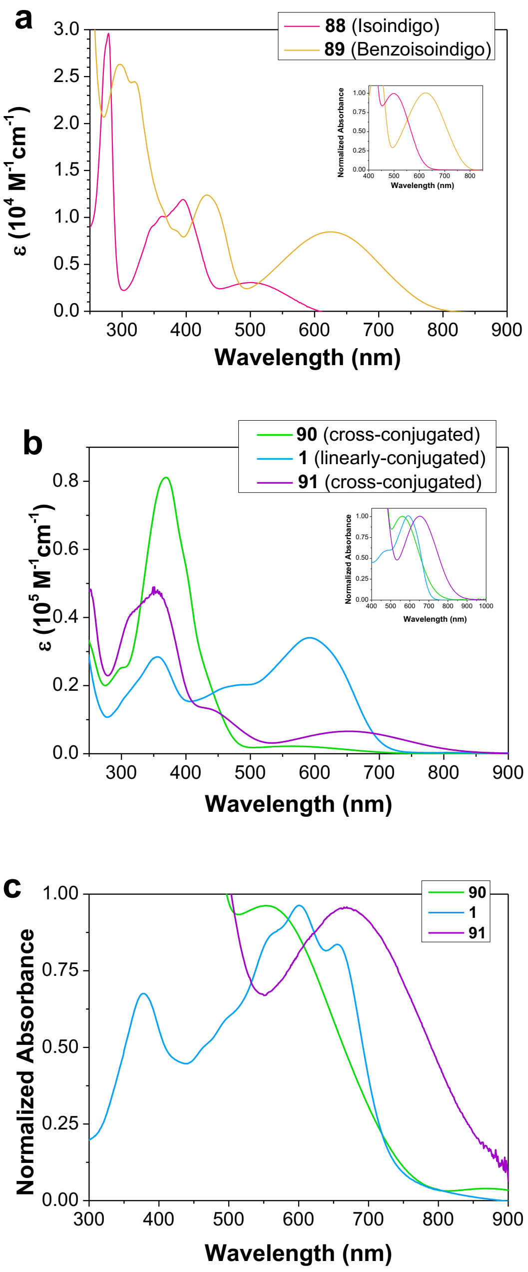

Figure 2.4 UV-vis spectra of (a) isoindigo (**88**) and benzoisoindigo (**89**) in $CHCl_3$; (b) compounds **90**, **1** and **91** in $CHCl_3$; (c) compounds **90**, **1**, and **91** as thin films. An expanded view of the lowest energy absorption bands (normalized to the peak maxima) is shown separately in the inset of (a) and (b).

Most of the features in the absorption spectra of any D-A material stem from π→π* transitions; however, the high energy transitions are typically localized on either the donor or acceptor, while the lowest energy transition usually possesses intramolecular charge transfer (ICT) character.[155] Both of these two distinct features are observed in compounds **90**, **1**, and **91** with the transitions from 300 – 400 nm being primarily localized on the pendant bithiophene groups, while those in the 400 – 500 nm (HOMO–2 → LUMO) and > 500 nm (HOMO → LUMO) ranges have more ICT character.

The absorption maxima in the low energy region for the isoindigo-based D-A materials (**90** and **1**) reside at 592 and 650 nm, respectively (Figure 2.4 b). As these low energy transitions involve transition from a HOMO with a large degree of bithiophene character to a LUMO largely centered on the isoindigo core, they have the most ICT character. This affords a large transition dipole moment, which in turn should increase the oscillator strength and extinction coefficient. Hence, both the oscillator strength and molar extinction coefficient are enhanced by an order of 10 for the linearly conjugated compound **1** compared to isoindigo (**88)**. However, the cross-conjugation in isomer **90** effectively negates the increase in transition dipole moment; the molar absorptivity of **90** is actually lower than that of isoindigo (**88**) (Table 2.1). A similar trend is observed when comparing benzoisoindigo (**89**) to its cross-conjugated bithiophene derivative (**91**). Although the λ_{max} of the HOMO → LUMO transition red-shifts slightly, the same decrease in oscillator strength is observed because of cross-conjugation.

The solid-state absorption spectra of **90**, **1**, and **91** are depicted in (Figure 2.4 c). In general, strong π-π interactions in the solid state results in broadening and/or the emergence of shoulder peaks in the solid-state spectra of conjugated systems. This is reflected in the solid state spectrum of the linearly-conjugated compound **1**; however, in the cross-conjugated systems **90** and **91**, there is a much less substantial red-shift observed in the HOMO → LUMO transition. Clearly, the substitution pattern is affecting the strength of the electronic π-interactions in the solid state. The $E_{g,opt}$ of **91**, measured from the onset of absorption, was found to be 1.23 eV.

2.2.4 Structure of Compound 91

Optoelectronic properties, such as charge carrier mobility, can greatly be impacted by the torsion angle between the pendant bithiophene groups and the isoindigo or benzoisoindigo core. As per the DFT results, the calculated torsion angle in **91** is much higher than it is in either **90**, **1**, or **92**. In order to experimentally verify this data, single crystals of **91** were grown by slow evaporation of a chloroform solution of the compound, and analyzed by single crystal X-ray diffraction. As depicted in Figure 2.5 a, the crystal structure of **91** belongs to the triclinic space group *P*-1. Crystal and structural refinement data, bond lengths and angles are provided in Table 5.1, Table 5.2, and Table 5.3 (Chapter 5), respectively. The additional data related to anisotropic displacement parameters, hydrogen coordinates, and isotropic displacement parameters are presented in Table 5.4 and Table 5.5 (Chapter 5). All of these data sets are also available at the Cambridge Crystallographic Data Centre (CCDC 1542137). The experimentally measured benzoisoindigo-bithiophene torsion angle (57.43˚) (Figure 2.5 a) is in close agreement with the geometry optimized by DFT (ca. 50°), while this same torsion angle for compounds **90**, **1** and **92** is calculated to lie between 20° and 26°. Therefore, the bithiophene groups in **91** are no longer coplanar with the benzoisoindigo core because of the additional steric strain supplied by the larger napthalene backbone. In compound **92**, this additional torsional strain is effectively eliminated by the substitution pattern. Hence, the reduced coplanarity owing to the orthogonality of the bithiophene and benzoisoindigo π-systems in compound **91** further limits the oscillator strength of the HOMO → LUMO transition. In spite of this increased torsion, the benzoisoindigo core is nonetheless able to π-stack in a slipped stack packing motif, with an interlayer spacing of 3.44 Å (Figure 2.5 c). This is in keeping with the reported interlayer spacing of 1,1′-dimethylisoindigo[156] (3.47 Å) and slightly longer than the interlayer spacing of cyanated isoindigo derivatives[157] (3.22 Å).

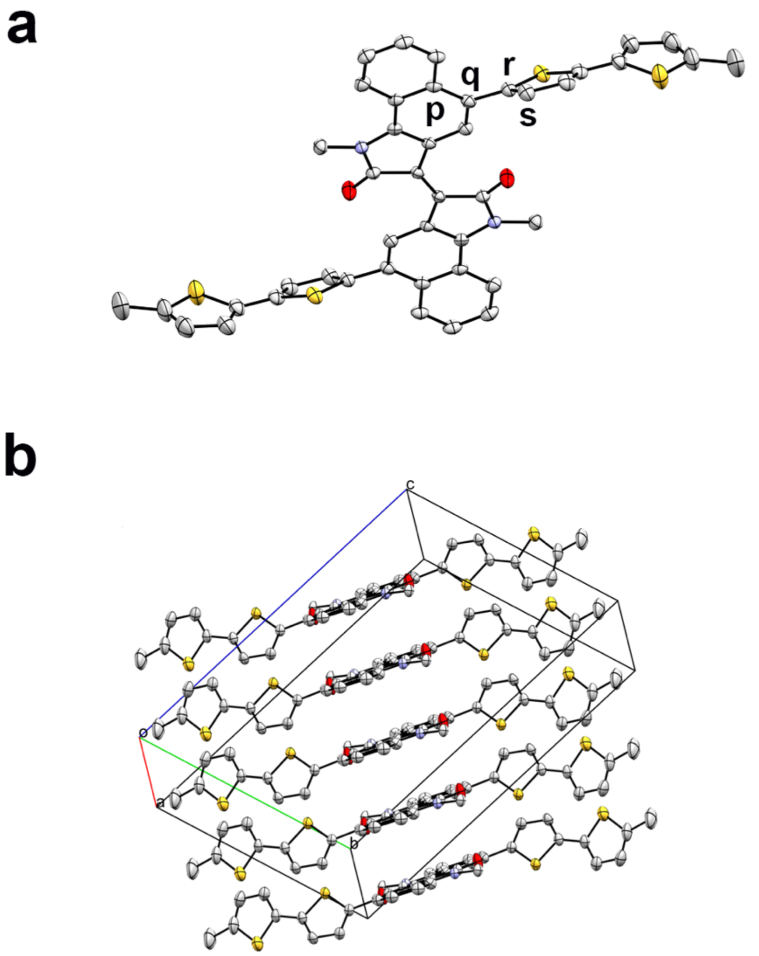

Figure 2.5 (a) Molecular structure of **91** with thermal ellipsoids drawn at the 50% probability level. Hydrogen atoms are omitted for clarity. Both the 2-ethylhexyl and hexyl chains have been truncated to methylene groups. Carbon, sulphur, oxygen and nitrogen atoms are shown in grey, yellow, red, and blue, respectively. The measured dihedral angle (C_p-C_q-C_r-C_s) between the plane of benzoisoindigo and the plane of the adjacent bithiophene ring is 57.43°. (b) View of **91** showing the π-π stacking of benzoisoindigo units along the a-axis.

2.2.5 Electrochemical Properties

Electrochemical behaviours of organic semiconductors can be explored by voltammetry experiments. In voltammetry, a specified voltage profile is applied to a working electrode as a function of time and the current produced by a redox system is measured. There are several voltammetry methods; however, cyclic voltammetry[158-159] and differential pulse voltammetry[159] (DPV) are commonly used to characterize organic semiconductors. In cyclic voltammetry, a linear potential is swept back and forth in a cycle between a specified initial and final value at a fixed rate. In DPV, the potential is changed using pulses of increasing amplitude and the difference in output current before and after each pulse is measured. Owing to its differential nature, DPV is a highly sensitive technique and often preferred over cyclic voltammetry for more accurate determination of redox potentials.

The extraction of E_{HOMO} and E_{LUMO} from a voltammogram is based on several assumptions. Ideally, the ionization potential and the electron affinity are extracted from the onset of oxidation and reduction of a cyclic voltammogram, respectively. IP and EA are assumed to be identical to E_{HOMO} and E_{LUMO}, respectively. This is based on the approximation that both of these frontier orbital energies are not affected by the removal of an electron from the HOMO or the addition of an electron to the LUMO, which is not true in reality.[160] Hence, E_{HOMO} and E_{LUMO} derived from the voltammogram should be taken as estimates. On the timescale of a voltammetry experiment, an organic semiconductor can undergo nuclear reorganization after oxidation or reduction, in contrast to spectroscopic transitions which are too fast for nuclear movement.[160] Therefore, the HOMO-LUMO gap measured electrochemically is always different than $E_{\mathrm{g,opt}}$, which is measured from the onset of the UV-vis spectrum.

The redox behaviour of the synthesized compounds (**1**, **88-91**) was explored by cyclic voltammetry and the frontier orbital levels were extracted from the onset of oxidation and reduction (Figure 2.6). The E_{HOMO} and E_{LUMO} values are tabulated in Table 2.1. All potentials are calibrated against $\mathrm{Fc^+/Fc}$. Equation 2.2 and Equation 2.3 were used to reference the E_{HOMO} and E_{LUMO} to vacuum. Where, $\mathrm{E_{[onset,\ ox\ vs.\ Fc+/Fc]}}$ and $\mathrm{E_{[onset,\ red\ vs.\ Fc+/Fc]}}$ are energies estimated from the onset of oxidation and reduction potentials, respectively. $\mathrm{Fc^+/Fc}$ redox standard is +0.380 V *vs.*

saturated calomel electrode which is at 4.7 eV *vs.* vacuum. Therefore, Fc^+/Fc redox standard is at -5.1 eV *vs.* vacuum.[154]

The electrochemistry of isoindigo (**88**) is straight-forward, with only one quasi-reversible reduction peak at $E_{1/2}^{red} = –1.37$ V, and no obvious oxidation features. This is in good agreement with previous reports, differing by only ca. 30 mV.[145] Benzoisoindigo (**89**) shows a similar quasi-reversible reduction peak, only shifted slightly to more positive potentials ($E_{1/2}^{red} = –1.30$ V), consistent with the slightly lower LUMO level predicted by DFT. A second small, quasi-reversible reduction wave is also observed at $E_{1/2}^{red} = –1.71$ V. In contrast to isoindigo (**88**), benzoisoindigo (**89**) shows three quasi-reversible oxidation peaks with $E_{1/2}^{ox}$ of 0.71, 0.97 and 1.29 V. As predicted by DFT, the addition of the fused benzene ring to each half of the isoindigo molecule substantially increases the HOMO level, making oxidation much more facile in this system.

$$E_{\mathrm{HOMO}} = -\,[e(\mathrm{E}_{[\text{onset, ox vs. Fc+/Fc}]} + 5.1)](\mathrm{eV}) \qquad \text{Equation 2.2}$$

$$E_{\mathrm{LUMO}} = -\,[e(\mathrm{E}_{[\text{onset, red vs. Fc+/Fc}]} + 5.1)](\mathrm{eV}) \qquad \text{Equation 2.3}$$

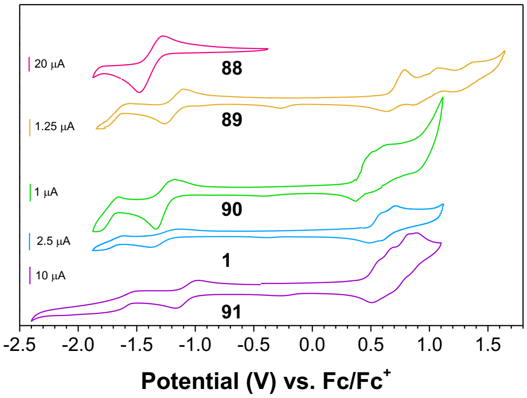

Figure 2.6 Cyclic voltammograms (scan rate 50 mV/s) of compounds **88-90**, **1**, and **91** dissolved in a dichloromethane solution of 0.05 M^{-1} tetrabutylammonium hexafluorophosphate.

Both the isoindigo-based D-A compounds, the cross-conjugated isomer (**90**) and the linearly-conjugated isomer (**1**), show two quasi-reversible reduction waves with exactly the same $E_{1/2}^{red}$ of –1.25 and –1.74 V.[145, 150] Both systems also show two very similar, irreversible oxidation waves at 0.51 and 0.61 V for **90**, and 0.59 and 0.70 V for **1**. Given the similarity in HOMO and LUMO energy levels predicted by DFT, this similarity in the electrochemistry of **90** and **1** is not surprising. The electrochemical behaviour of the benzoisoindigo-based cross-conjugated compound **91** also follows the trends predicted by DFT. The two quasi-reversible reduction peaks ($E_{1/2}^{\text{red}} = -1.07$ and -1.51 V) closely resemble those of benzoisoindigo (**89**), although shifted to slightly more positive potentials. Similarly, the onset of oxidation is similar for compounds **90**, **1**, and **91** again indicating that the position of the HOMO is governed almost entirely by the bithiophene donor groups. Of the four irreversible oxidation waves (0.56, 0.67, 0.82, and 0.88 V), only the two peaks at higher potentials are not observed in the isoindigo analogues (**90**). This suggests that these latter two oxidation processes arise from the benzoisoindigo core, in keeping with the voltammogram of **89**.

In general, the electrochemical data supports the general trends predicted by DFT. As can be seen in Table 2.1, for all of the compounds, the position of the LUMO is almost entirely dictated by whether isoindigo or benzoisoindigo is used as the electron-deficient acceptor. Similarly, the position of the HOMO varies by no more than 100 meV for the bithiophene-containing compounds, suggesting that the electron-rich donor effectively controls the HOMO energy. Thus, the HOMO-LUMO gaps are virtually independent of the substitution pattern (linearly or cross-conjugated); only the intensity of the HOMO → LUMO transition varies between the regioisomers.

2.2.6 OPV Performance

In order to examine the effect of these variations in substitution pattern on OPV performance, bulk heterojunction solar cells were fabricated with a regular device architecture: ITO/PEDOT:PSS/Donor:PCBM/LiF/Al. Each of the three synthesized D-A compounds (**90**, **1**, and **91**) were used as the p-type semiconductor in the active layer, alongside either $PC_{61}BM$ (for **90** and **1**) or $PC_{71}BM$ (for **91**) as their n-type counterpart. Device performance was optimized using different solvents such as chloroform, chlorobenzene, *o*-dichlorobenzene and a 1:1 (v/v) mixture of chlorobenzene and chloroform, to make the active layer solution. Two semiconductors (p-type and n-type) were mixed in a blend ratio of 1:1 in case of each solvent used, with a total solution concentration of 18 mg/mL. In addition to the systematic variations in casting solvent, a batch of devices were annealed in each case to screen if annealing leads to better morphology compared to pristine devices. All of the devices fabricated with **90**:$PC_{61}BM$ system were non-functional and did not exhibit any PCE because of the extremely low J_{SC} and V_{OC} (Table 2.2). The representative *J-V* characteristics are shown in Figure 2.7 a. The devices based on the linearly conjugated bithiophene-isoindigo compound (**1**:$PC_{61}BM$) exhibited the best performance when the active layer was cast from chloroform and annealed at 100 ˚C for 15 min, with the champion device producing a PCE of 1.25% (Table 2.3). The J_{SC} for this cell was 4.84 $mA{\cdot}cm^{-2}$ with a V_{OC} as high as 0.81 V. The J_{SC} was also calculated from the incident photon-to-current efficiency (IPCE) spectrum for a OPV device. The IPCE is defined as the ratio of the number of carriers collected by the solar cell to the number of photons of a given energy incident on the solar cell. The fraction of photons that are used by the device at a given wavelength can be calculated from an IPCE spectrum. It depends on the extinction coefficient of the active material at that wavelength, charge transport within the active layer and interfacial charge transport. The calculated J_{SC} (6.14 $mA{\cdot}cm^{-2}$) from the IPCE curve of the active layer **1**:$PC_{61}BM$ was similar (although slightly higher) to that obtained from OPV devices (Figure 2.7 b). Similar to **90**, the benzoisoindigo-based semiconductor (**91**) did not produce any functional devices when used in OPVs in a blend with $PC_{61}BM$. This was because of an insufficient driving force to split the photogenerated excitons as the LUMO level of **91** is almost identical to that of $PC_{61}BM$.[161] In order to achieve a higher energy offset, compound **91** was paired with $PC_{71}BM$, which has a lower LUMO. However, only a few barely-functional devices were obtained (Table 2.4), irrespective of the fabrication conditions used. These displayed diodic behaviour, but had extremely low short-circuit current densities.

Table 2.2 Optimization of **90**:PC$_{61}$BM devices. The casting solvent chloroform (CF), chlorobenzene (CB) and annealing conditions (100 ˚C for 15 min or non-annealed) were systematically varied. For average data, the number of cells tested (*N*) is reported, along with the standard deviation. In all cases, the cells were non-functional.

Solvent	**Annealed**	***N***	**J_{sc} (mA/cm^2)**	**V_{oc} (V)**	**FF (%)**	**PCE (%)**
CF	Yes	28	0.02 ± 0.01	0.004 ± 0.0002	-	-
		Champion	0.03	0.003	-	-
	No	12	0.0001	0.00006 ± 0	-	-
		Champion	0.01	0.0001	-	-
CB:CF (1:1)	Yes	28	0.02 ± 0.01	0.0003 ± 0.0002	-	-
		Champion	0.04	0.0003	-	-
	No	6	0.0010 ± 0.0007	0.06 ± 0.06	-	-
		Champion	0.002	0.06	-	-

Table 2.3 Optimization of **1**:$PC_{61}BM$ devices. The casting solvent (chloroform (CF), chlorobenzene (CB), or *o*-dichlorobenzene (ODCB)) and annealing conditions (100 ˚C for 15 min or non-annealed) were systematically varied. For average data, the number of cells tested (*N*) is reported, along with the standard deviation.

Solvent	Annealed	*N*	J_{sc} (mA/cm^2)	V_{oc} (V)	FF (%)	PCE (%)
ODCB	Yes	5	0.67 ± 0.08	0.06 ± 0.01	25 ± 1	0.010 ± 0.004
		Champion	0.76	0.07	26	0.01
	No	19	0.6 ± 0.1	0.22 ± 0.09	30 ± 4	0.04 ± 0.02
		Champion	0.57	0.35	34	0.07
CB	Yes	19	4.8 ± 0.5	0.5 ± 0.1	34 ± 2	0.8 ± 0.3
		Champion	5.28	0.62	37	1.23
	No	15	4 ± 1	0.5 ± 0.1	31 ± 2	0.6 ± 0.2
		Champion	3.96	0.76	31	0.92
CF	Yes	27	4.0 ± 0.7	0.6 ± 0.2	31 ± 2	0.8 ± 0.3
		Champion	4.84	0.79	33	1.25
	No	25	3.3 ± 0.9	0.6 ± 0.2	29 ± 1	0.6 ± 0.3
		Champion	4.37	0.79	29	1.01
CB:CF (1:1)	Yes	21	4 ± 1	0.6 ± 0.2	31 ± 3	0.8 ± 0.3
		Champion	4.46	0.81	34	1.25
	No	19	3.4 ± 0.8	0.6 ± 0.2	27 ± 3	0.6 ± 0.3
		Champion	4.37	0.82	27	0.97

Table 2.4 Optimization of **91**:$PC_{71}BM$ devices. The casting solvent (chloroform (CF), chlorobenzene (CB)) and annealing conditions (100 ˚C for 15 min or non-annealed) were systematically varied. For average data, the number of cells tested (*N*) is reported, along with the standard deviation.

Solvent	Annealed	*N*	J_{sc} (mA/cm^2)	V_{oc} (V)	FF (%)	PCE (%)
CF	Yes	5	0.006 ± 0.002	0.22 ± 0.08	28 ± 4	0.0004 ± 2
		Champion	0.01	0.21	29	0.006
	No	13	0.0077 ± 0.0005	0.4 ± 0.2	29 ± 3	0.0009 ± 0.0005
		Champion	0.007	0.72	32	0.0018
CB:CF (1:1)	Yes	9	0.016 ± 0.001	0.03 ± 0.02	-	-
		Champion	0.018	0.03	-	-
	No	17	0.0143 ± 0.0009	0.5 ± 0.2	28 ± 2	0.002 ± 0.0007
		Champion	0.016	0.64	28	0.003

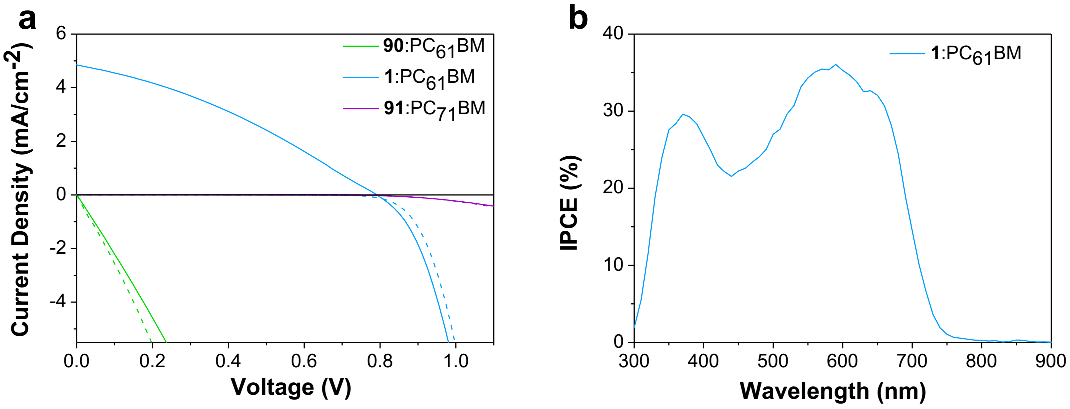

Figure 2.7 (**a**) *J-V* curves in the light (solid lines) and the dark (dashed lines) for OPV devices with **90**:$PC_{61}BM$, **1**:$PC_{61}BM$, and **91**:$PC_{71}BM$ active layers; (**b**) IPCE spectrum for the champion **1**:$PC_{61}BM$ cell.

Figure 2.8 presents the solid state spectra of a **91**:$PC_{71}BM$ thin film cast from chloroform; in part, it explains the poor device performance observed for the cross-conjugated molecules. The spectrum does not show any features of **91**; it only displays the features of $PC_{71}BM$.[162] This is in agreement with the low oscillator strength (and molar extinction coefficient) of the cross-conjugated isomer. Moreover, an absorbance of 0.1 – 0.3 is too meager to absorb enough photons to produce meaningful photocurrents. Therefore, cross-conjugated compounds such as **90** and **91** have limited utility for photovoltaic applications.

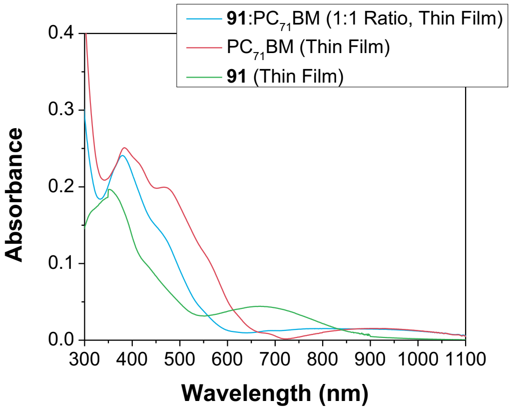

Figure 2.8 UV-vis thin film absorption spectra of $PC_{71}BM$, **91**, and the **91**:$PC_{71}BM$ blend used in OPV fabrication.

The low extinction coefficient of **91** is one of the primary reasons for its poor device performance; however, the efficiency of these devices is 100-times smaller than those fabricated with **1**, while the oscillator strengths differ only by a factor of 10. This suggests there are other factors possibly contributing to the poor performance of **91**. After carefully examining the images of **91**:$PC_{71}BM$ active layers taken by atomic force microscopy (AFM) and the structure of **91** determined by single crystal x-ray diffraction, a sub-optimal film morphology and a low hole mobility are hypothesized to further lower the PCE. While neither strongly intermixed phases nor large crystallites are beneficial for efficient photocurrent generation, the **90**:$PC_{61}BM$ film appears to have strongly intermixed phases and the **91**:$PC_{71}BM$ film is shown to form larger aggregates (0.9 – 1 µm, measured along XY direction) compared to the blend of **1**:$PC_{61}BM$ (Figure 2.9).[163-164] In addition, the slipped-stack packing motif of **91** does not offer a good overlap between adjacent bithiophene sub-units (Figure 2.10). This is likely to limit the device performance since this intermolecular overlap between donor subunits in a D-A system is essential for hole transport.

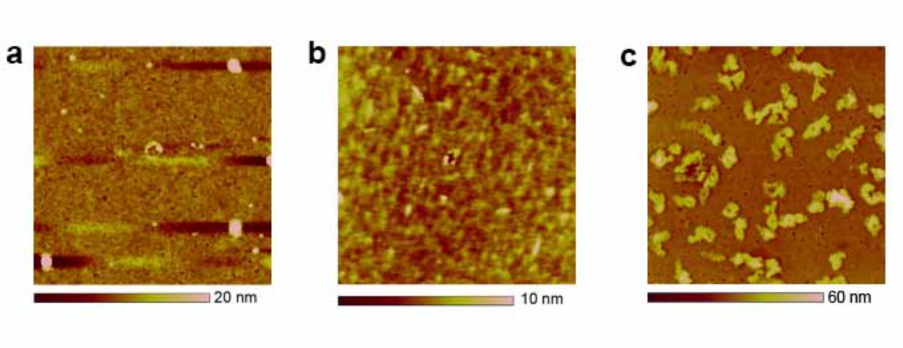

Figure 2.9 AFM images (10 × 10 μm) of active layer blends: (a) **90**:$PC_{61}BM$, cast from chloroform and annealed; (b) **1**: $PC_{61}BM$, cast from chloroform and annealed; and (c) **91**:$PC_{71}BM$, cast from a 1:1 mixture of chloroform/chlorobenzene.

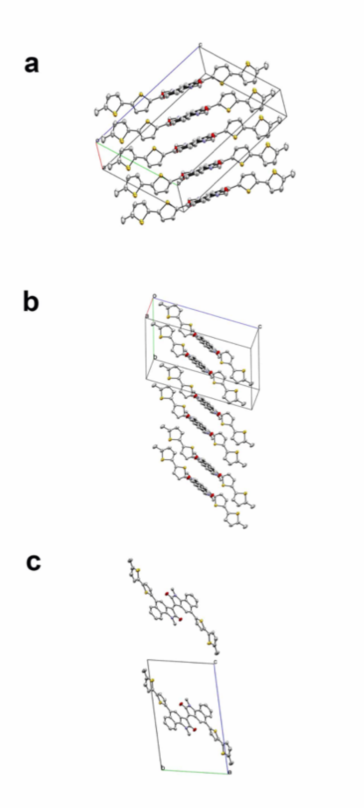

Figure 2.10 Multiple views of **91**, showing the molecular packing: (a) along the a-axis, (b) along the b-axis, and (c) along the c-axis.

2.3 Conclusions

In this chapter, the synthesis of a new electron-deficient building block (benzoisoindigo) was described, which can be used to prepare new conjugated organic semiconductors. Extending the conjugation length of isoindigo by the fusion of a benzene ring was shown to reduce the HOMO-LUMO gap and red-shift the absorption bands in the UV-vis spectra, primarily by raising the position of the HOMO. The impact of substitution pattern (linearly vs. cross-conjugated) on D-A compounds based on both benzoisoindigo and isoindigo was evaluated by a combined theoretical and experimental study. The results show that in these D-A systems, the HOMO and LUMO positions are mostly independent of the substitution pattern, and depend only on the particular choice of donor and acceptor. In contrast, the oscillator strength of the HOMO → LUMO transition depends strongly on the substitution pattern; cross-conjugated systems lack efficient overlap of the initial and final-state wavefunctions, leading to extremely low oscillator strengths and molar extinction coefficients. These results, therefore, suggest that if derivatives of benzoisoindigo can be prepared, with linkages at the linearly conjugated 7,7′-positions, they may be highly suitable for optoelectronic applications.

Note: The work presented in 'Chapter 2' was published and adapted from the following reference-

J. Phys. Chem. C **2017**, *121*, 9110−9119.

Chapter 3 - Effect of Torsion Angle on the Electron Mobilities of Isoindigo-based Polymers

3.1 Introduction

In the second chapter of this thesis, the development of benzoisoindigo was described along with its application in photovoltaic devices. The findings revealed two key facts. First, linear conjugation is essential to achieve a high oscillator strength for electronic transitions. Second, molecular semiconductors, especially those with large π-systems such as benzoisoindigo, tend to π-stack and over-crystallize. Based on these findings, polymer semiconductors were developed using linearly-conjugated building blocks, and the results are presented in chapter 3. As mentioned in section 1.5.2, polymer semiconductors often exhibit a semi-crystalline microstructure with separate crystalline and amorphous regions, which prevents over-crystallization. Moreover, polymers with ultrahigh charge carrier mobilities have been shown to have crystalline domains interconnected by amorphous polymer chains that ensure fast charge transport.[165]

The majority of isoindigo-based semiconductors are p-type.[102-105] There are only a few isoindigo-based unipolar n-type semiconductors and much needs to be done to develop new n-type materials. Among these handful of examples, polyisoindigo (**46**) was the first isoindigo-based n-type semiconductor.[116] It exhibited an extremely low electron mobility because of a lack of planarity in the polymer backbone. The planarity was not maintained because of a large torsion angle between neighboring isoindigo units. This work aims to improve the electron mobility of polyisoindigo (**46**) by structural modification. Two new polymers, polyethynylisoindigo (**108**) and polybisisoindigo (**109**), are synthesized (Figure 3.1). In polyethynylisoindigo (**108**), linearly conjugated 6,6′-substituted isoindigo units are connected *via* ethynyl spacers. The spacer increases the distance between adjacent isoindigo units which is expected to lower the torsion angle. This will planarize the polymer backbone leading to an increased effective conjugation length. The other polymer, polybisisoindigo (**109**), is based on the building block isoindigo[7,6-g]isoindigo (bisisoindigo, **77**).[135-136] Bisisoindigo (**77**) is a core-expanded isoindigo unit where a ring-fused dimer of isatin is inserted between isoindigo lactam rings. Polybisisoindigo (**109**) will have the same torsional strain present in polyisoindigo (**46**); however, the structural repeat unit is now twice as large as in polyisoindigo (**46**), leading to an overall increase in conjugation length. Effectively, the ring-fusion will result in fewer single bonds along the polybisisoindigo (**109**) backbone relative to a polyisoindigo (**46**) chain with the same molecular weight.

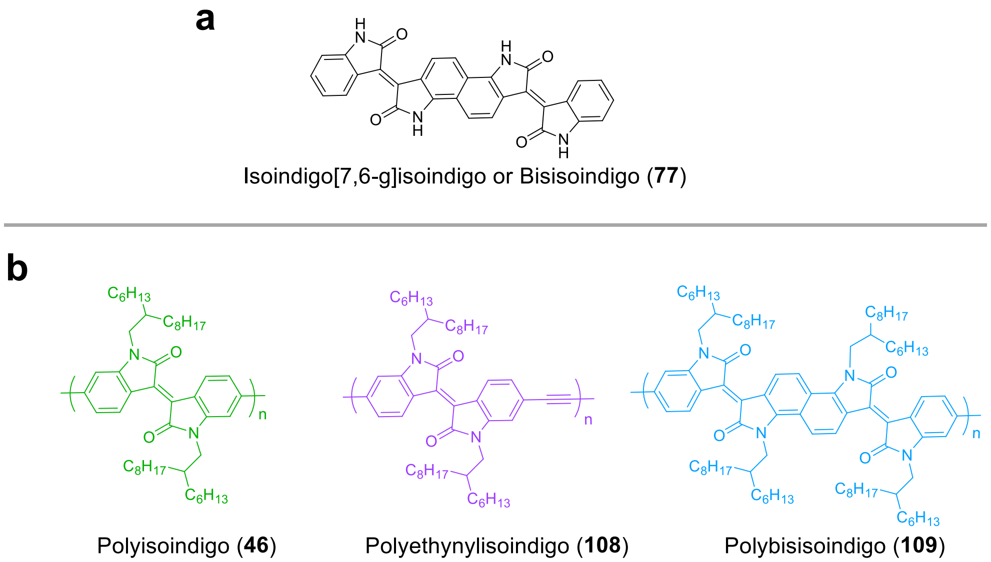

Figure 3.1 Structure of bisisoindigo (**77**). (b) polymers studied: polyisoindigo (**46**), polyethynylisoindigo (**108**), and polybisisoindigo (**109**).

This chapter focuses on the synthesis of two new polymers (**108**, **109**) and explores their structure-property relationships using a combined theoretical and experimental study. Polyisoindigo (**46**) is also synthesized as a control polymer. The optimized geometry of the polymer backbone is calculated using DFT. The optical and electrochemical properties of the three polymers are characterized by UV-vis spectroscopy and differential pulse voltammetry, respectively. To measure the electron mobilities, the polymers were incorporated in OFETs. The packing patterns of the polymers in the solid-state were probed by grazing-incidence wide angle x-ray scattering (GIWAXS), and the results were used to explain the observed trends in electron mobility.

3.2 Results and Discussion

3.2.1 Synthesis

Polyisoindigo (**46**) was synthesized according to the previously reported procedure shown in Scheme 3.1.[116] First, 6-bromoisatin (**110**) was reduced to 6-bromooxindole (**111**) using a Wolff-Kishner reduction. An acid-catalyzed aldol condensation of an equimolar mixture of **110** and **111** afforded 6,6′-dibromoisoindigo (**112**). In order to increase the solubility of **112**, 6,6′-dibromoisoindigo was *N*-alkylated using 2-hexyldecylbromide and potassium carbonate, yielding **113**. The alkylated isoindigo (**113**) was subjected to a Miyaura borylation producing a pinacol ester (**114**). This was coupled with an equimolar amount of **113** using a Suzuki coupling reaction to synthesize the homopolymer of isoindigo (**46**).

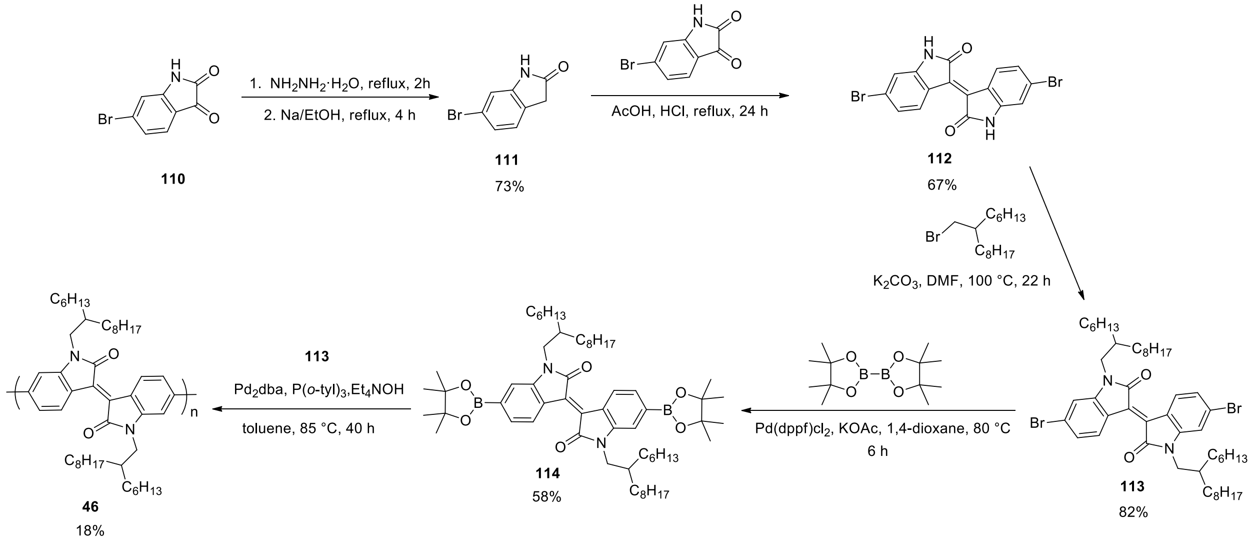

Scheme 3.1 Synthesis of the polyisoindigo (**46**)

To synthesize polyethynylisoindigo (**108**), **113** was first synthesized as shown in Scheme 3.1. In order to couple the ethynyl spacer to the isoindigo unit, **113** was reacted with ethynyltrimethylsilane using a Pd-catalyzed Sonogashira cross-coupling to yield **115** (Scheme 3.2). The trimethylsilyl groups were removed in the following step using potassium carbonate in a 1:1 mixture of MeOH/CH_2Cl_2. Sonogashira cross-coupling was employed again to copolymerize an equimolar mixture of **116** and **113,** affording polyethynylisoindigo (**108**).

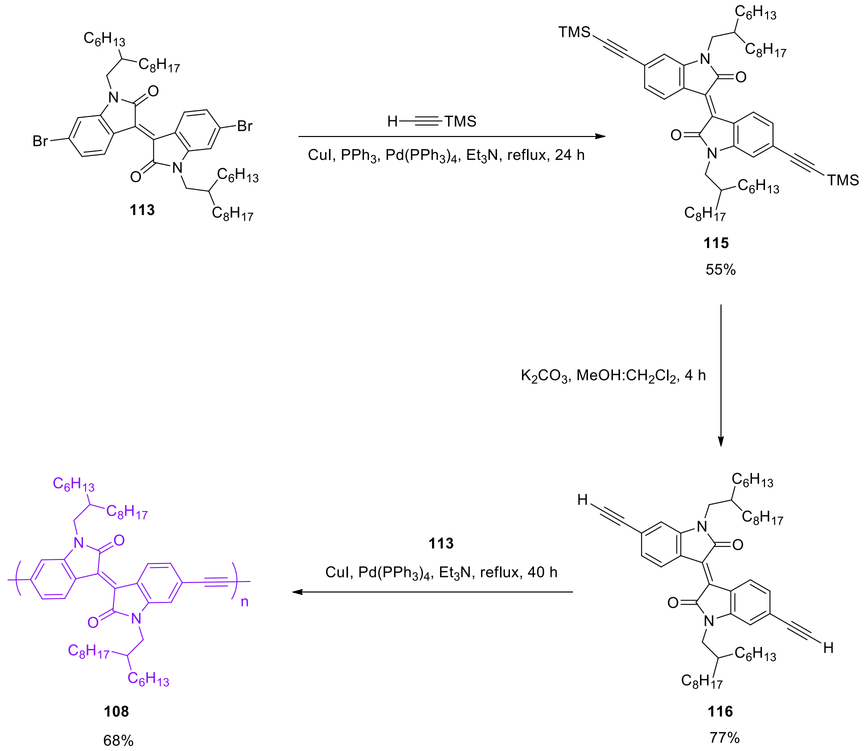

Scheme 3.2 Synthesis of n-type polymer polyethynylisoindigo (**108**).

A first attempt was made to synthesize polybisisoindigo (**109**) using traditional metal-catalyzed cross-coupling methods (Scheme 3.3), as was employed for polyisoindigo (**46**) and polyethynylisoindigo (**108**). The synthesis started with *N*-alkylation of 1,5-diaminonapthalene (**117**) which was done in two steps. First, **117** was subjected to *N*-acylation followed by a reduction of the acyl group to produce **118** using $LiAlH_4$ in THF. This was followed by a double Martinet isatin synthesis on **119** to yield *N*-alkylated bisisatin (**119**), a ring-fused dimer of isatin. In the following step, **120** was reacted with alkylated 6-bromooxindole (**122**) in an acid-catalyzed aldol condensation reaction to produce dibromobisisoindigo (**123**). In order to use Pd-catalyzed Stille coupling reaction to produce the homopolymer of bisisoindigo, **123** was treated with n-BuLi and trimethyltin chloride. Unfortunately, the stannylated product (**124**) readily underwent protodestannylation in the reaction medium to produce **125** along with only a minor amount of **124** (X = $-SnMe_3$). When **123** was treated with bis(pinacolato)diboron, the resulting pinacol ester (**124**, X = -Bpin) also suffered from protodeboronation which precluded the use of a Suzuki coupling in the synthesis of polybisisoindigo.

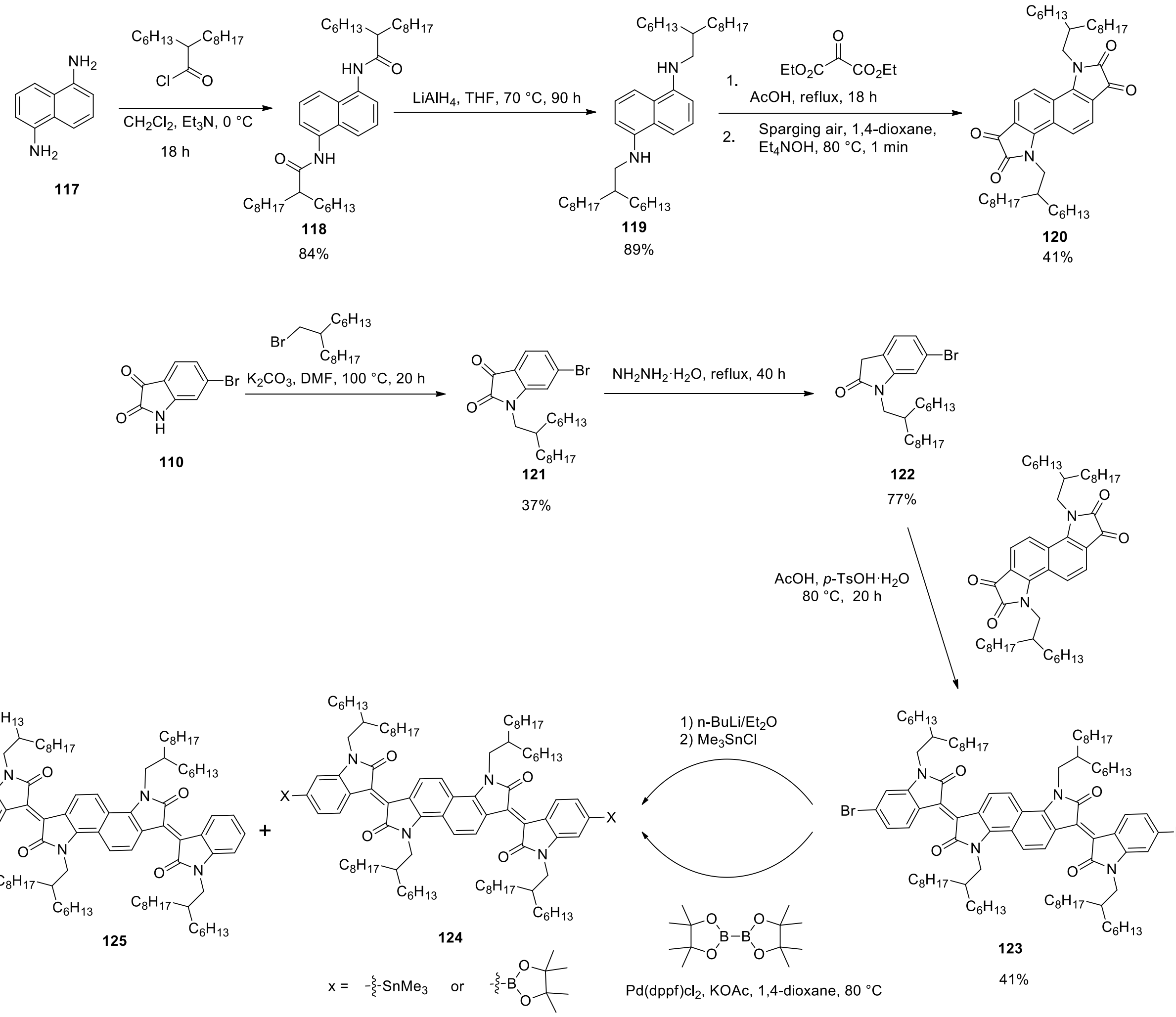

Scheme 3.3 Synthetic attempts to access n-type polymer polybisisoindigo (**109**) *via* metal-catalyzed cross-coupling methods.

To produce polybisisoindigo, new synthetic methodologies were required. In this new approach, the polymer was designed to be accessible *via* an acid-catalyzed aldol polymerization (Scheme 3.4). First, *N*-alkylated 6-bromoisatin (**121**) underwent a Miayura coupling to generate the boronic ester-functionalized isatin (**126**). A Suzuki coupling between **126** with an equimolar amount of **121** produced the 6,6′-diisatin dimer (**127**). In the following step, compound **127** was reduced to 6,6′-dioxindole (**128**) by refluxing in neat hydrazine hydrate over 40 h. In the final step, an equimolar mixture of bifunctional isatin (**127**) and oxindole (**128**) co-monomers were refluxed in toluene using *p*-TsOH as the catalyst. The initial aldol reaction was immediately followed by the elimination of water to form the new exocyclic carbon-carbon bond, affording polybisisoindigo (**109**).

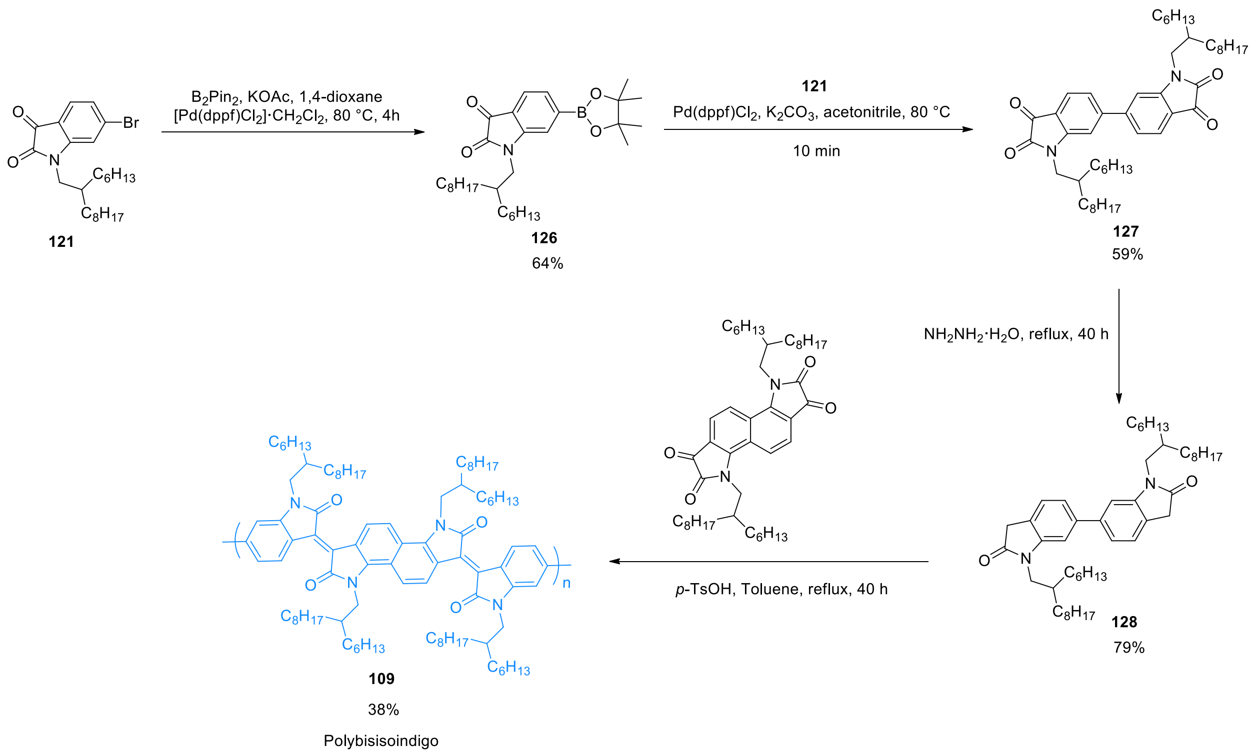

Scheme 3.4 Synthesis of polybisisoindigo (**109**) *via* aldol polymerization methodology.

Besides affording access to polymers that are not otherwise synthetically accessible using conventional coupling methods, aldol polymerization has several other advantages. It only produces water as a byproduct and does not involve transition metal catalysts. In contrast, Stille couplings involve highly toxic organotin reagents, the byproducts of which must be carefully removed after synthesis. Even more environmentally-benign methods like Suzuki and Sonogashira couplings require basic conditions, which are not compatible with all monomers or functional groups, and all of these cross-couplings make use of expensive metal catalysts.[138] Finally, any trace metal ions from the residual catalyst must be rigorously removed, as they have been shown to lead to trap states that attenuate carrier transport in polymer films.[166] Therefore, the synthesis of polybisisoindigo (**109**) in this work highlights the versatility of the aldol polymerization methodology. With no organometallic reagents involved in the polymerization, this methodology is also much more amenable to scale-up than conventional Stille coupling methods, where reagent toxicity remains a limiting factor. In addition, all three polymers have comparable number-average molecular weights (ranging from 15 to 22 kDa) and dispersities (2.0 to 2.6), showing that the aldol polymerization is capable of producing materials with chain lengths equal to that of conventional cross-coupling methods (Table 3.1).

Table 3.1 Molecular weight, optical bandgap, and electrochemical data of polymer (**46**, **108**, and **109**).

Polymer	**M_n**[a] **(kDa)**	**M_w**[a] **(kDa)**	***Đ***[a]	***E_g***[c] **(Opt) (eV)**	***E_{HOMO}***[d] **(exp.) (eV)**	***E_{LUMO}***[d] **(exp.) (eV)**	**Δ*E***[d] **(exp.) (eV)**
46	21.9	43.9	2.0	1.69	-6.22	-3.79	2.43
108	15.4	40.4	2.6	1.73	-6.22	-3.90	2.32
109	15.5	38.0	2.4	1.32	-6.03	-3.94	2.09

[a] Measured in 1,2,4-trichlorobenzene at 130 °C by size exclusion chromatography. [b] Measured in chloroform solution for the lowest energy electronic transition. [c] Measured from the absorption onset of thin film UV-vis spectra. [d] Estimated from the first anodic/cathodic peak ($E_{\text{HOMO}}/E_{\text{LUMO}}$) in the differential pulse voltammogram; voltammograms were referenced to the Fc^+/Fc redox couple, which was assumed to be −5.1 eV relative to vacuum.[154]

3.2.2 Optical Properties

The UV-vis absorption spectra of all three polymers were measured as both chloroform solutions and thin films (Figure 3.2). All polymers absorb well across the visible region, as expected from their blue-green to green color. Polyisoindigo (**46**) exhibits three main absorption bands, with the lowest energy transition centered at 684 nm. Compared to polyisoindigo (**46**), polyethynylisoindigo (**108**) is expected to have a lower torsion angle along the polymer backbone (and therefore red-shifted absorption bands), owing to the lack of steric constraints provided by the ethynyl spacer. This is supported by geometry optimizations calculated for trimers at the B3LYP/6-31G(d,p) level of theory. The calculated torsion angle between the ethynyl and isoindigo sub-units (3°) is significantly reduced in comparison to the torsion angle between isoindigo repeat units (34°) in polyisoindigo (Figure 3.3). However, the UV-vis spectrum of polyethynylisoindigo (**108**) is actually blue-shifted relative to that of polyisoindigo (**46**) ($\lambda_{\max}$ of the lowest energy transition is 597 nm) (Table 3.1). This can be explained based on the conformational flexibility of the ethynyl spacer. In solution, there is effectively free rotation of the isoindigo units about the ethynyl linker, leading to larger average torsion angles and a reduction in effective conjugation length. This is manifested as both a blue-shift and a loss of vibronic fine structure in the UV-vis spectrum (Figure 3.2). In the solid-state UV-vis spectra (Figure 3.2), there is a red-shift of the polyethynylisoindigo (**108**) spectrum relative to solution, as the polymer locks into a more planar conformation in the thin film. No such shift is observed for polyisoindigo (**46**), where there is little ability for the conformationally-restricted polymer backbone to planarize further. In contrast, the UV-vis spectrum of the polybisisoindigo (**109**) is dramatically red-shifted relative to polyisoindigo (**46**) (λ_{max} of the lowest energy transition is 768 nm, with a shoulder at 856 nm). Polybisisoindigo (**109**) suffers from the same torsional strain present in polyisoindigo (**46**) (Figure 3.3, Table 3.1), with a torsion angle of 34° between adjacent bisisoindigo units; however, the structural repeat unit is now twice as large as in polyisoindigo (**46**), leading to an overall increase in conjugation length. Effectively, the ring-fusion results in fewer single bonds along the polybisisoindigo (**109**) backbone relative to a polyisoindigo (**46**) chain with the same molecular weight. When combined with the slightly more electron-rich naphthalene core (which imparts more charge transfer character to the $S_0 \rightarrow S_1$ transition), the $E_{\mathrm{g,opt}}$ of polybisisoindigo (**109**) is reduced by 370 meV compared to that of polyisoindigo (**46**) (Table 3.1).

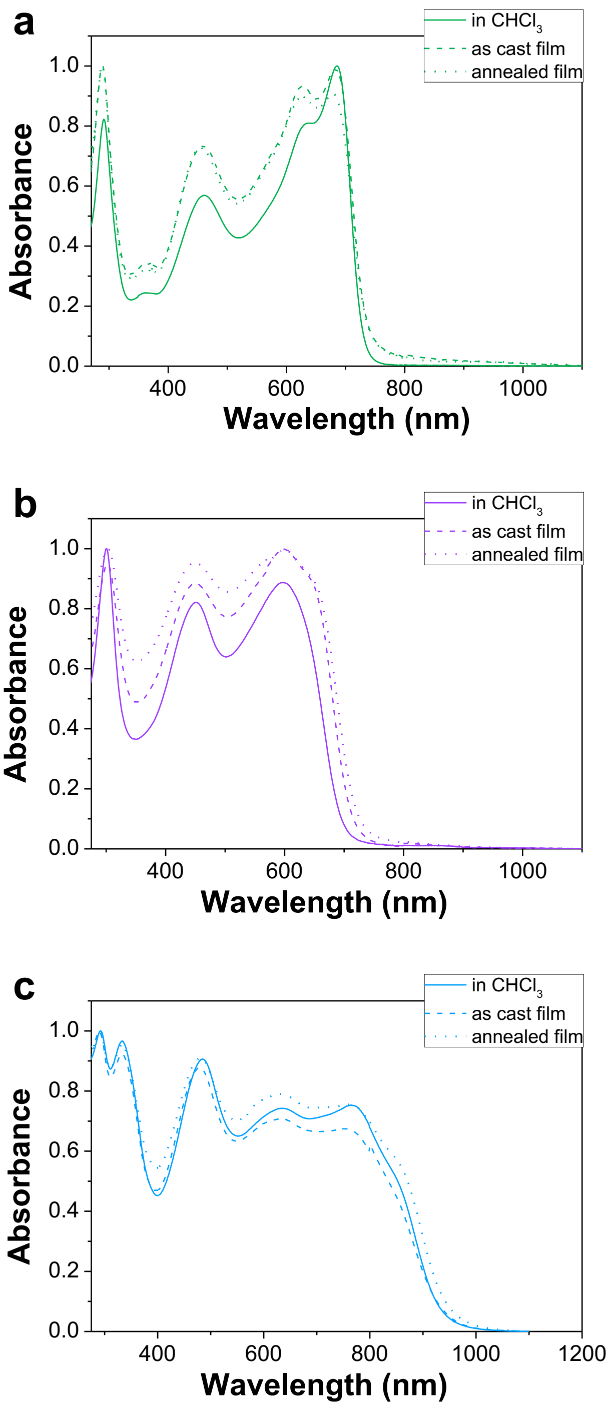

Figure 3.2 UV-vis spectra of: (a) polyisoindigo (**46**), (b) polyethynylisoindigo (**108**), and (c) polybisisoindigo (**109**). Thin films were drop cast from chloroform solutions (as-cast) and annealed for 15 minutes at 100 °C (annealed).

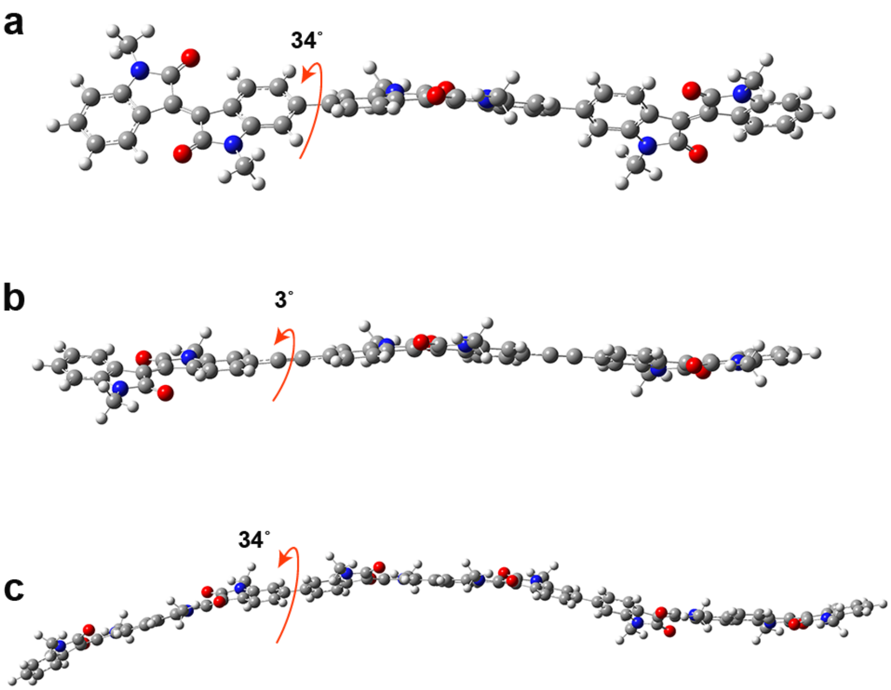

Figure 3.3 Optimized geometries (B3LYP/6-31G(d,p)) of: (a) polyisoindigo (**46**), (b) polyethynylisoindigo (**108**), and (c) polybisisoindigo (**109**). The torsion angles between adjacent sub-units are indicated.

3.2.3 Electrochemical Properties

The oxidation and reduction potentials of the polymers were measured by differential pulse voltammetry, using thin films of each material (Figure 3.4). As mentioned in section 2.2.5, differential measurements in DPV result in peaked output rather than the wave-like response in cyclic voltammetry.[159] E_{HOMO} and E_{LUMO} were estimated from the peak maxima of oxidation and reduction (Table 3.1). The voltammograms presented in this section were also calibrated against the $\mathrm{Fc}^+/\mathrm{Fc}$ redox couple and referenced to vacuum as done in chapter 2 (Equation 2.2 and Equation 2.3). All three polymers show one anodic peak, which is shifted slightly (190 mV) toward less positive potentials in polybisisoindigo (**109**). This reflects both the extended conjugation and the more electron-rich naphthalene core of the bisisoindigo polymer. The reduction of the polymers is more varied. Polyisoindigo (**46**) displays two reduction peaks (at −1.31 and −1.87 V vs. $\mathrm{Fc}^+/\mathrm{Fc}$), while polyethynylisoindigo (**108**) has three (−1.19, −1.61, and −1.78 V), and polybisisoindigo

(**109**) has multiple overlapping peaks between −1.13 and −2.12 V. With more functional groups such as ethynyl spacer in polyethynylisoindigo or additional lactam rings in polybisisoindigo, higher number reduction peaks were obseved compared to polyisoindigo. The more positive reduction potentials in polyethynylisoindigo (**108**) and polybisisoindigo (**109**) support the idea of extended conjugation in these systems, particularly in the solid state. The LUMO of polybisisoindigo (**109**) is quite low-lying ($E_{\mathrm{LUMO}} = -3.94$ eV), and is close to the −4.0 eV needed for air-stable electron transport.

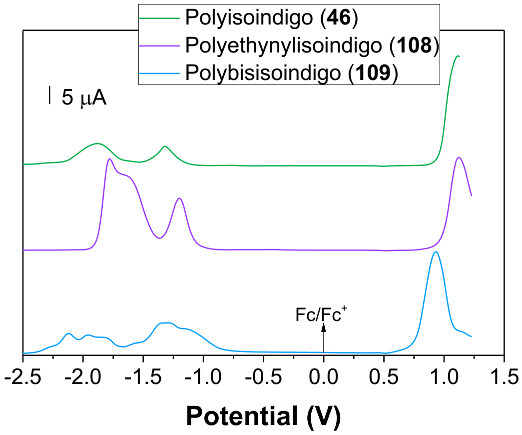

Figure 3.4 Differential pulse voltammograms of polymers (**46**, **108**, and **109**) thin films measured in a 0.05 M^{-1} acetonitrile solution of tetrabutylammonium hexafluorophosphate.

3.2.4 OFET Measurements

Polymers were next used to prepare OFETs with a bottom-gate bottom-contact architecture. The devices were fabricated on a dodecyltrichlorosilane-modified SiO_2/Si wafer with a pair of Au electrodes as the source and drain contacts. After spin-coating the polymer films from a chloroform solution, they were annealed at different temperatures (50, 100, 150, and 200 °C) under an inert atmosphere. Table 3.2 presents a summary of the OFET performances of the three polymers.

Table 3.2 Summary of OFET performance characteristics of polymer **46**, **108**, and **109**.

Polymer	$T_{\text{annealing}}$[a] (°C)	N	μ_e (cm^2/V·s)	$I_{\text{ON}}/I_{\text{OFF}}$	V_{TH} (V)
46	room temperature	5	$3.2 \times 10^{-5} \pm 4.8 \times 10^{-6}$	4600	71 ± 5
		Best	3.9×10^{-5}	10000	79
	50	5	$3.5 \times 10^{-5} \pm 1.8 \times 10^{-6}$	4600	45 ± 1
		Best	3.8×10^{-5}	1000	46
	100	5	$4.7 \times 10^{-5} \pm 1.5 \times 10^{-5}$	8200	44 ± 1
		Best	7.4×10^{-5}	10000	45
	150	5	$5.0 \times 10^{-5} \pm 7.3 \times 10^{-6}$	8200	42 ± 4
		Best	5.9×10^{-5}	1000	42
	200	5	$7.6 \times 10^{-5} \pm 2.1 \times 10^{-5}$	26000	50.7 ± 5.0
		Best	1.0×10^{-4}	10000	48.2
108	room temperature	5	$7.0 \times 10^{-5} \pm 3.8 \times 10^{-5}$	1000	87 ± 2
		Best	1.3×10^{-4}	1000	88
	50	5	$1.6 \times 10^{-4} \pm 1.0 \times 10^{-4}$	4600	85 ± 3
		Best	3.2×10^{-4}	1000	87
	100	5	$2.8 \times 10^{-4} \pm 9.5 \times 10^{-5}$	46000	56 ± 2
		Best	4.0×10^{-4}	100000	57
	150	5	$2.4 \times 10^{-4} \pm 6.9 \times 10^{-5}$	82000	57 ± 2
		Best	3.0×10^{-4}	10000	58
	200	5	$1.9 \times 10^{-4} \pm 1.3 \times 10^{-4}$	8200	63.1 ± 2.0
		Best	4.2×10^{-4}	10000	61.4
109	room temperature	5	$2.4 \times 10^{-4} \pm 2.0 \times 10^{-4}$	8200	47 ± 5
		Best	5.2×10^{-4}	10000	51
	50	5	$2.9 \times 10^{-4} \pm 1.2 \times 10^{-4}$	10000	49 ± 3
		Best	4.3×10^{-4}	10000	50
	100	5	$5.8 \times 10^{-4} \pm 4.5 \times 10^{-4}$	46000	42 ± 3
		Best	1.2×10^{-3}	100000	46
	150	5	$6.3 \times 10^{-4} \pm 4.9 \times 10^{-4}$	10000	44.9 ± 1.4
		Best	1.3×10^{-3}	10000	43.7
	200	5	$3.7 \times 10^{-4} \pm 1.8 \times 10^{-4}$	1000	44 ± 5
		Best	5.2×10^{-4}	1000	48

[a] Devices were annealed for 30 min at each specified temperature.

The working principles of OFETs were discussed in section 1.3.1. As described in this section, the application of a positive gate voltage with respect to the source ($V_{GS} > 0$) results in an accumulation of negative charge in the conduction channel. According to the transfer curves shown in Figure 3.5, positive gate voltages result in charge transport, indicating unipolar n-type charge transport characteristics. μ_e was calculated from the slope of the linear part of the $\sqrt{I_{DS}}$ vs V_{GS} curve (i.e., the saturation regime). The electron mobility of polyisoindigo (**46**) was found to be low, as expected from the literature;[116] the average mobility was only 7.6 × 10^{-5} $cm^2/V \cdot s$, and the best device yielded an electron mobility of 1.0 × 10^{-4} $cm^2/V \cdot s$. This is most likely because of the large torsion angle between adjacent monomer units, which forces the polymer backbone into a twisted conformation. The electron mobility of polyisoindigo rose with increase in temperature, indicating enhanced crystallinity with annealing temperature. Polyethynylisoindigo (**108**) had a higher average electron mobility of 1.9 × 10^{-4} $cm^2/V \cdot s$, and the best mobility was 4.2 × 10^{-4} $cm^2/V \cdot s$. The improvements may be because of higher intra-chain mobility, owing to a more planar backbone; or, they may be because of a higher inter-chain mobility, because of tighter π-π stacking. Given that the conformational flexibility of the ethynyl spacer was shown to disrupt the conjugation in solution (Figure 3.2), and the smaller *d*-spacing of the polyethynylisoindigo (**108**) π-stack (vide infra), the improved mobility was ascribed to better inter-chain carrier transport. Of the three polymers, polybisisoindigo (**109**) had the highest electron mobility of 1.26 × 10^{-3} $cm^2/V \cdot s$, with an average value of 6.26 × 10^{-4} $cm^2/V \cdot s$. The extensive ring fusion in the polymer backbone would be expected to facilitate intra-chain charge transport, explaining the higher mobility observed for polybisisoindigo (**109**). The average electron mobility of both polyethynylisoindigo and polybisisoindigo initially increased with increase in temperature; however, they exhibited a decrease at 200 °C, which is possibly due to unfavourable morphology at higher annealing temperature.

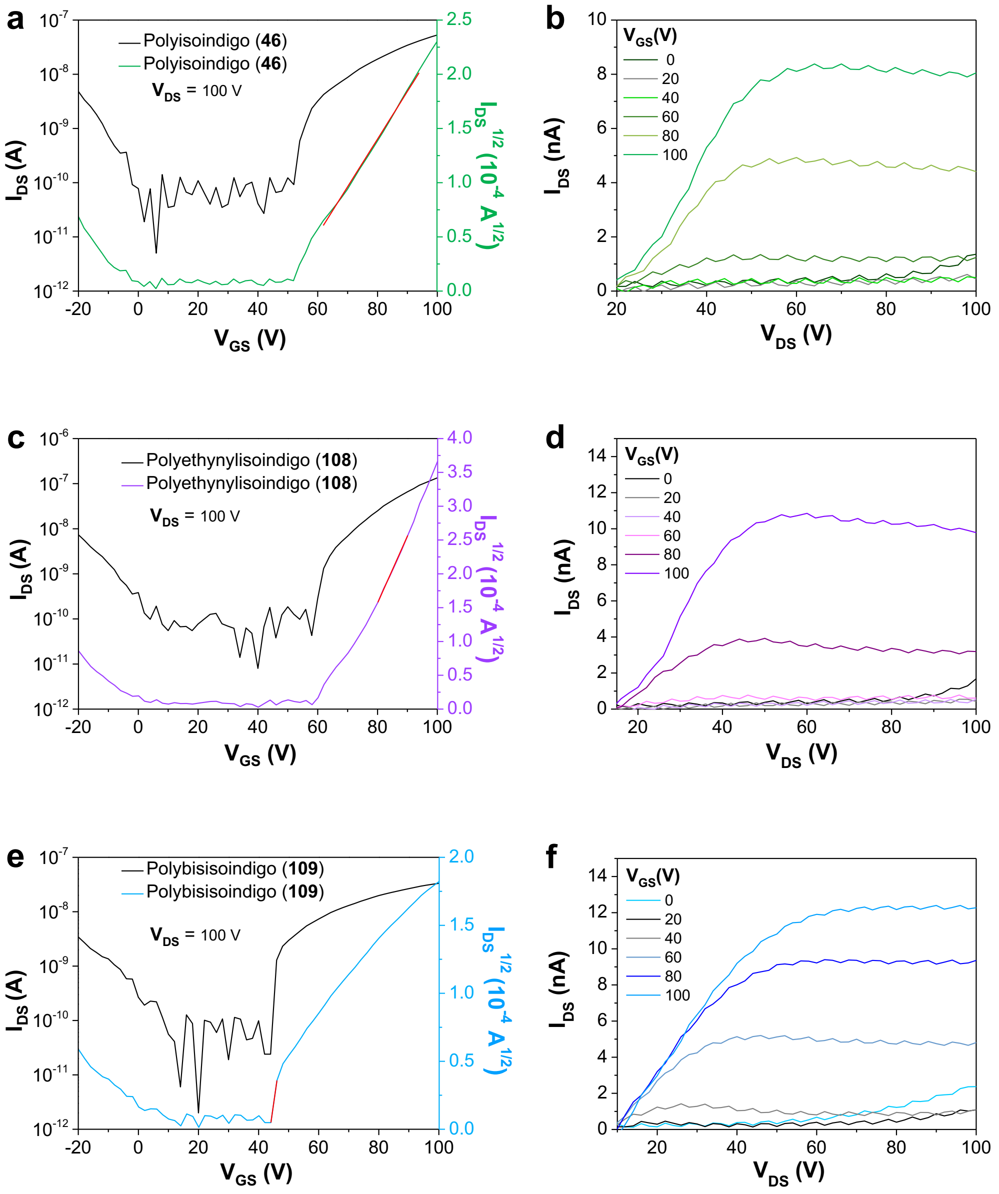

Figure 3.5 Transfer (left) and output (right) characteristics of the best performing OFETs fabricated using: (a,b) polyisoindigo (**46**), (c,d) polyethynylisoindigo (**108**), and (e,f) polybisisoindigo (**109**). The observed spikes with in 0 - 40 V in transfer curves are because of low signal to noise ratio. Extremely low drain current caused the current oscillation in output curves.

3.2.5 Thin-film Microstructure

The complex microstructure of conjugated polymers greatly influences their optoelectronic properties and functionality in organic electronic devices. The characterization of this microstructure is often done by employing the GIWAXS technique.[126, 167] In the GIWAXS technique, the X-ray beam impinges onto the sample surface at an extremely shallow incident angle (< 1°) which makes the x-ray scattering surface sensitive. In order to correlate the observed changes in electron mobility with changes in film microstructure, GIWAXS patterns of polymers (**46**, **108**, and **109**) were collected to analyze the degree of order in the polymer films. GIWAXS patterns of the polymer films, both before and after annealing, are shown in Figure 3.6. The pristine films of all three polymers show scattering from lamellar stacking, centered at q ~0.27-0.33 $Å^{-1}$, and scattering from π-π stacking centered at q ~1.6-1.8 $Å^{-1}$; these peaks are assigned to the (100) and (010) reflections, respectively (Figure 3.6, Table 3.3). For polyisoindigo (**46**), the lamellar stacking of the as-cast film has a spacing of 20.9 Å that decreases slightly to 20.3 Å upon thermal annealing, whereas the spacing of the π-π stack is ~ 3.7 Å for both as-cast and annealed films (**Error! Reference source not found.**, Table 3.3). The incorporation of the ethynyl spacer in polyethynylisoindigo (**108**) increases the lamellar spacing to 22.4-23.3 Å, but decreases the π-π separation to ~ 3.5 Å, giving rise to better π-π overlap along the [010] direction. This is consistent with the higher electron mobility of polyethynylisoindigo (**108**) relative to polyisoindigo (**46**). Conversely, the incorporation of the ring-fused monomer unit in polybisisoindigo (**109**) decreases the lamellar spacing to 19.0-19.6 Å, but marginally increases the π-π separation to ~ 3.8 Å. Moreover, the scattering features from the π-π stack become broader and less pronounced in polybisisoindigo (**109**) than in polyisoindigo (**46**). This finding excludes the possibility that the improvements in electron mobility observed for polybisisoindigo (**109**) are because of closer inter-chain interactions along the [010] direction. Instead, better co-planarity along the polymer backbone likely improves the intra-chain π-π overlap and carrier transport. Another possibility is that the larger surface area of the bisisoindigo π-system makes the polymer less sensitive to positional disorder. This leads to sufficient π-orbital overlap between adjacent polymer chains, even when long-range order is lacking, and has been observed in other materials with large, ring-fused systems.[165] It is worth noting that there is uncertainty in defining the π-π stacking spacing because of the presence of an amorphous scattering ring centered at $q \sim 1.4\text{-}1.5$ Å^{-1} that overlaps with the π-π stacking scattering for most of the samples.

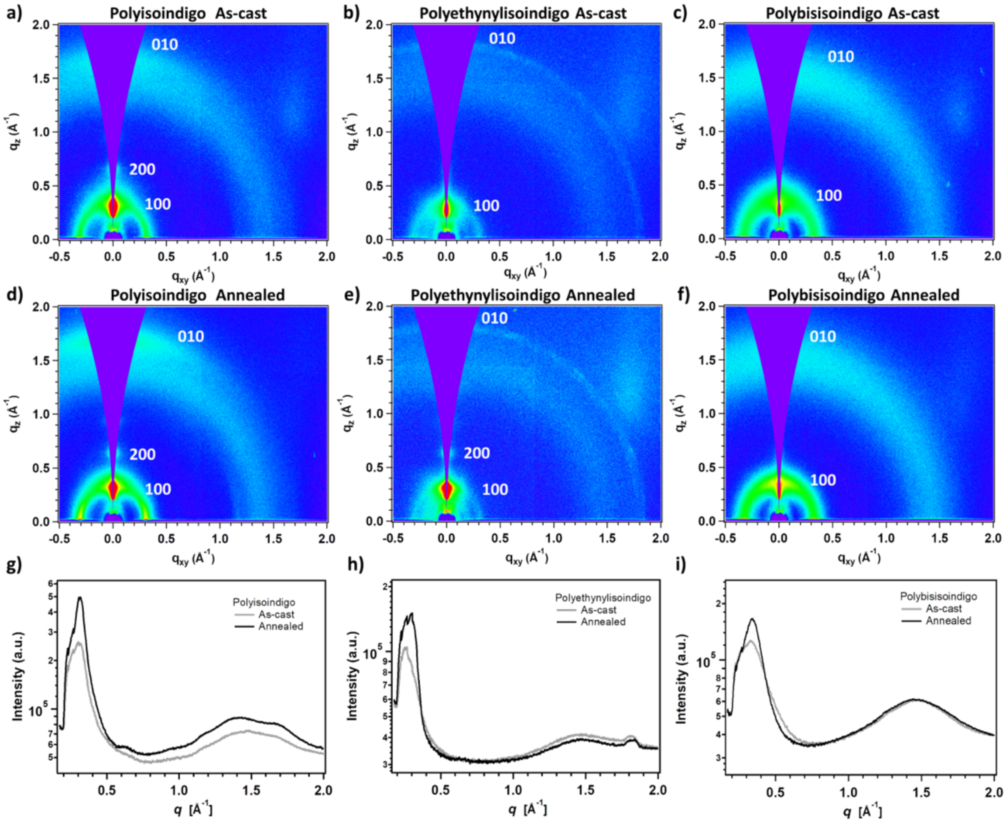

Figure 3.6 (a-c) GIWAXS patterns of the as-cast polymer thin films on Si wafers: (a) polyisoindigo (**46**), (b) polyethynylisoindigo (**108**), and (c) polybisisoindigo (**109**). (d-f) GIWAXS patterns of polymer thin films annealed at 100 ˚C for 30 min: (d) polyisoindigo (**46**), (e) polyethynylisoindigo (**108**), and (f) polybisisoindigo (**109**). (g-i) The azimuthally-integrated intensities corresponding to the GIWAXS patterns of the annealed (black lines) and the as-cast (gray lines) polymer thin films: (g) polyisoindigo (**46**), (h) polyethynylisoindigo (**108**), and (i) polybisisoindigo (**109**). The thicknesses of the films were 82 ± 8 nm, 36 ± 4 nm, and 60 ± 5 nm for polyisoindigo, polyethynylisoindigo, and polybisisoindigo (**46**, **108**, and **109**), respectively.

Table 3.3 Summary of structural parameters and crystalline correlation length for the lamellar stacking of polymers'.

Polymer	$q_{(100)}$ ($Å^{-1}$)		$d_{(100)}$ (Å)		$FWHM_{(100)}$ ($Å^{-1}$)		$CCL_{(100)}$ (nm)	
	As-cast	Annealed	As-cast	Annealed	As-cast	Annealed	As-cast	Annealed
46	0.3	0.31	20.9	20.3	0.08	0.068	7.9	9.2
108	0.27	0.28	23.3	22.4	0.082	0.075	7.7	8.4
109	0.32	0.33	19.6	19.0	0.12	0.1	5.2	6.3

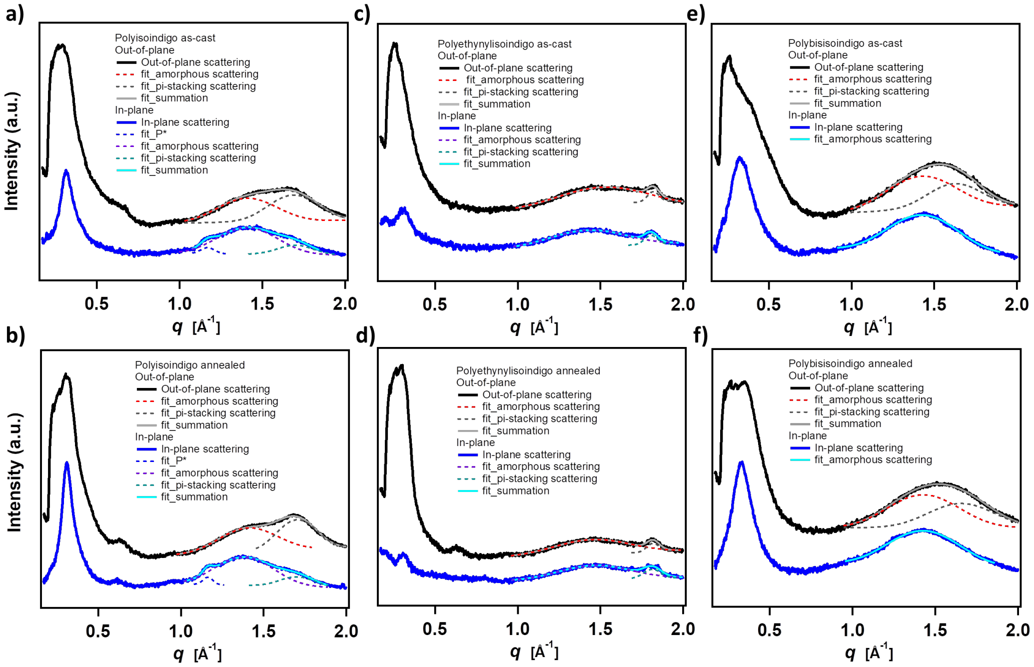

Figure 3.7 Fitting of the scattering peaks between $q \sim 1\text{-}2$ $Å^{-1}$ for the GIWAXS patterns of polymer thin films: (a) as-cast polyisoindigo, (b) annealed polyisoindigo, (c) as-cast polyethynylisoindigo, (d) annealed polyethynylisoindigo, (e) as-cast polybisisoindigo, and (f) annealed polybisisoindigo. An amorphous scattering peak appears around $q \sim 1.4\text{-}1.5$ $Å^{-1}$ for all samples, whereas the π-π stacking scattering peak appears at $q \sim 1.7 \pm 0.1$ $Å^{-1}$, $q \sim 1.8 \pm 0.1$ $Å^{-1}$, and $q \sim 1.64 \pm 0.1$ $Å^{-1}$ for polyisoindigo (46), polyethynylisoindigo (108), and polybisisoindigo

Figure 3.7 (continued) (109), respectively. It is worth noting that there is a large uncertainty in the peak position of the π-π stacking feature in polybisisoindigo (108) because of the large overlap with amorphous scattering. This was attributed to very weak ordering of the π-π stack in polybisisoindigo films. An additional scattering peak at $q \sim 1.17$ Å^{-1} appears in-plane for polyisoindigo films (fits marked as P*). All polymers exhibit reorganization in the solid state after thermal annealing, leading to an increase in the polymer order as revealed by an increase in the GIWAXS-integrated intensities (Figure 3.6g-i). This is consistent with the highest OFET performances being observed for annealed devices (Table 3.2).

The fractional amount of the crystalline phase in a polymer film is called the degree of crystallinity. However, this parameter is difficult to measure. As an alternative, the crystallinity in a film can be quantified relative to a reference film of the same material, which is known as the relative degree of crystallinity (RDC). RDC is determined by integrating the scattering intensity across all orientation angles (χ) from 0° to 90° as per Equation 3.1.

$$RDC \propto \int_0^{\frac{\pi}{2}} \sin(\chi)\, I(\chi) dx \qquad \text{Equation 3.1}$$

Here, $I(\chi)$ presents the scattering intensity at a given orientation angle. $\sin(\chi)$ is a geometrical correction factor which accounts for the change in the observed intensity with the orientation angle in the grazing incidence geometry.[168] The relative degree of crystallinity was calculated using the (100) peak for the annealed films as compared to as-cast films (Figure 3.8). The RDC increases by ~ 92%, 85%, and 44% for polyisoindigo (**46**), polyethynylisoindigo (**108**), and polybisisoindigo (**109**), respectively. Clearly, polybisisoindigo (**109**), having the most rigid polymer chains, exhibits the least reorganization upon thermal annealing. Overall, the GIWAXS data reveal two different origins for the observed improvements in electron mobility: closer inter-chain interactions along the π-π stacking direction for polyethynylisoindigo (**108**), and better intra-chain co-planarity along the polymer backbone for polybisisoindigo.

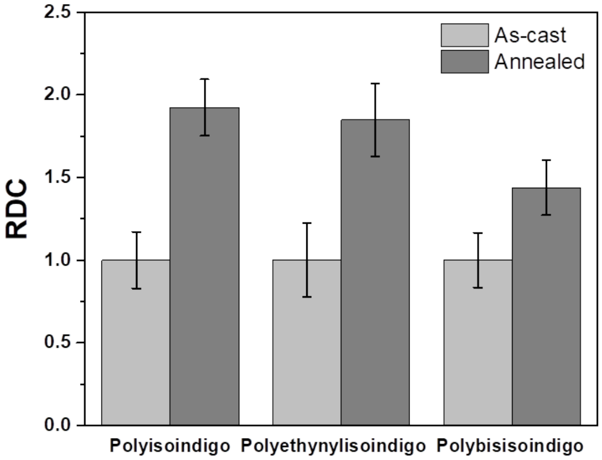

Figure 3.8 Relative degree of crystallinity calculated from the lamellar stacking of polyisoindigo (**46**), polyethynylisoindigo (**108**), and polybisisoindigo (**109**), for annealed vs. as-cast films. The error bars correspond to the uncertainty in the measured materials' volume. To isolate the π-π stacking scattering from the amorphous scattering, the in-plane and out-of-plane scattering profiles were fitted separately (**Error! Reference source not found.**), relying on the fact that amorphous scattering is isotropic in both the in-plane and out-of-plane orientations.

The conjugation length and the crystal size of these π-conjugated systems strongly affect their optoelectronic properties, which was also observed for the organic semiconductors discussed in this thesis. The average size of ordered regions can be estimated from the crystalline correlation length (CCL).[169-170] Owing to the anisotropy in the crystal dimensions, CCL is assigned to a specific crystallographic plane. For polymers **46**, **108** and **109**, the CCL was determined along the (100) lamellar stacking direction. As-cast polyisoindigo films exhibited the highest CCL among the three polymers, while polybisisoindigo had the lowest CCL. This again showed that polybisisoindigo was the most disordered of three polymers. Annealing at higher temperatures increased the CCL for every polymer, although the value was still highest for polyisoindigo and lowest for polybisisoindigo, as seen in the as-cast films.

3.3 Conclusions

In conclusion, the electron mobility of polyisoindigo (**46**) has been improved by modifying the structure of the repeating unit. Two new polymers, polyethynylisoindigo (**108**) and polybisisoindigo (**109**), were synthesized with an aim to improve the planarity of the polymer backbone. In polyethynylisoindigo (**108**), an ethynyl spacer was incorporated between neighboring isoindigo units to reduce the torsional strain observed in polyisoindigo (**46**). Polyethynylisoindigo (**108**) exhibited a higher electron mobility relative to polyisoindigo. Based on the GIWAXS analysis, the incorporation of the ethynyl spacer shortened the π-π stacking distance, which improved the inter-chain electron mobility. The synthesis of polybisisoindigo (**109**) demonstrates that the acid-catalyzed aldol polycondensation reaction can be a viable alternative to toxic Stille couplings in the synthesis of n-type conjugated polymers. The resulting homopolymer of bisisoindigo has a broad absorption spectrum and a low-lying LUMO, consistent with extensive co-planarity and conjugation along the polymer backbone. GIWAXS and OFET data show that this improved co-planarity leads to better intra-chain charge transport and therefore a higher electron mobility than either polyethynylisoindigo (**108**) or polyisoindigo (**46**).

Chapter 4 - General Conclusions and Outlook

4.1 General Conclusions

The primary goal of this thesis was to explore the effect of molecular structure on the optoelectronic properties of isoindigo-based organic semiconductors. This was achieved by synthesizing new acceptor building blocks and incorporating them into new donor-acceptor materials. The molecular structure of these new materials was varied in a number of ways. A set of structural isomers was developed by changing the substitution pattern when they were coupled to donors. The molecular structure was also altered by incorporating isoindigo-based building blocks with varying degrees of torsional strain. The effects of these structural changes were first predicted by using density functional theory to calculate optimized geometries, oscillator strengths, and absorption spectra. These findings were supported by experimentally determined crystal structure, optical and electrochemical properties. These studies were accomplished over the course of two major projects, presented in this thesis.

In the first project, the core structure of isoindigo was modified by ring-fusion to develop a new building block, benzoisoindigo. Benzoisoindigo was used as the acceptor in D-A materials to study the effect of substitution pattern in donor-acceptor semiconductors. Relative to isoindigo analogues, the extended conjugation length in benzoisoindigo reduced the band gap of the D-A material. Therefore, it was concluded that the conjugation length plays a crucial role in tuning the band gap of D-A semiconductors. The comparison between D-A materials with different substitution patterns demonstrated that the substitution pattern did not greatly affect the frontier molecular orbital levels; hence, the band gaps of cross-conjugated materials remain unaltered with respect to their linearly conjugated analogues. However, the cross-conjugation dramatically reduced the oscillator strength of the $S_0 \rightarrow S_1$ transition. DFT calculations showed that cross-conjugation leads to localization of the LUMO on the acceptor unit, without any contribution from the donor. This greatly reduces the HOMO → LUMO transition probability, leading to a low oscillator strength. When incorporated in OPVs, the cross-conjugated materials were barely functional, because of an extremely low photocurrent. As the oscillator strength was low, the cross-conjugated materials were not capable of absorbing enough photons to produce a reasonable photocurrent for photovoltaic applications. Therefore, linear conjugation is essential for organic electronic applications. This work also revealed valuable findings on the morphology of benzoisoindigo-based semiconductors in OPV active layers. AFM images showed that the larger π-system of benzoisoindigo led to over-crystallization, which hindered charge separation in OPV active layers.

Based on the findings of the first project, a set of polymer semiconductors was synthesized in the second project. The polymers were used to study the effect of torsional strain on the charge carrier mobility of organic semiconductors. Polyisoindigo was chosen as a control polymer where a large torsion angle between neighboring isoindigo units caused a low electron mobility. Two new polymers (polyethynylisoindigo and polybisisoindigo) were synthesized with varying degrees of torsional strain in their backbones. In polyethynylisoindigo, the torsion angle was lowered because of the lack of steric constraints provided by the ethynyl spacers. The ring-fused bisisoindigo unit in polybisisoindigo was twice as large as the isoindigo unit in polyisoindigo. This resulted in an overall increase in conjugation length. Ring fusion reduced the number of single bonds, leading to an overall torsional strain lower than in polyisoindigo chains of similar molecular weight. When incorporated in OFETs, polyethynylisoindigo exhibited a higher electron mobility compared to polyisoindigo. GIWAXS analysis showed the reduced torsion angle in polyethynylisoindigo shortened the π-π stacking distance, and improved the inter-chain electron mobility. Interestingly, polybisisoindigo was the most disordered of the three polymers, although it exhibited an electron mobility even higher than polyethynylisoindigo. Based on the GIWAXS analysis, there could be two plausible reasons for this improvement. Either the intrachain electron mobility was increased because of the extended conjugation of the ring-fused monomer unit, or the larger π-system of the bisisoindigo unit made the polymer less sensitive towards positional disorder. It therefore produced a high electron mobility in spite of its amorphous nature. The extended conjugation length was also reflected in the optical absorption spectrum which tailed out to 1000 nm. This result is also in line with the findings of the first chapter, where benzoisoindigo derivatives showed a red-shift in their optical absorption spectra. Because of ring-fusion, bisisoindigo has four lactam rings, which lowered the LUMO level to -3.94 eV. Therefore, ring-fusion with electron deficient functional groups is an interesting approach to attain low LUMO energies, which is necessary for achieving air-stable electron transport.

Another aspect of this thesis is developing new synthetic methodologies for synthesizing conjugated polymers for organic electronics. The third chapter of this thesis discussed the versatility of aldol polymerization. Aldol polycondensation was used to prepare polybisisoindigo, which could not be accessed *via* traditional metal-catalyzed cross coupling methods. Aldol methodology does not involve any organometallic reagent and is much more amenable to scale-up than conventional Stille coupling methods which involve highly toxic reagents.

As a whole, this thesis concludes that ring-fusion is a useful approach to promote planarity and increase the effective conjugation length in D-A materials. When it comes to designing new D-A semiconductors, linear conjugation is an utmost requirement. Cross-conjugation greatly reduces the oscillator strength of the materials. A high torsion angle undermines charge transport along the polymer backbone. Incorporating spacers between repeating units lowers the torsion angle, resulting in a substantial increase in charge carrier mobilities. Using a larger ring-fused repeat unit is another approach which reduces the overall torsional constraint on polymer chains and extends the effective conjugation length, therefore leading to high charge carrier mobilities.

4.2 Future Work

The overarching goal of this thesis was to establish a deeper understanding of the effect of molecular structure on the performance of organic semiconductors in OPVs and OFETs. Based on the findings of this thesis, I propose a set of future projects to further advance these technologies. In addition to exploring the photovoltaic performance of polyethynylisoindigo and polybisisoindigo, the remaining projects are primarily designed to further modify the structure of bisisoindigo derivatives, tailored for OPV and OFET applications.

4.2.1 Photovoltaic Applications of Polyethynylisoindigo and Polybisisoindigo

OPV research was previously dominated by p-type polymer and n-type fullerene-based molecular materials. The disadvantages of fullerene-based OPVs were discussed in section 1.4.2. As mentioned in the previous section, non-fullerene n-type semiconductors are revolutionizing the field of OPVs and have led to a PCE over 15%.[89] Another promising approach to build OPVs is using polymers as both the p and n-type materials, known as all-polymer solar cells. Progress on all-polymer solar cells have been slow, primarily because of poor polymer-polymer miscibility, leading to unfavorable phase separation in the BHJ active layers. The excessive phase separation results in charge recombination, which lowers the photocurrent leading to poor PCEs. However, the PCE of all-polymer solar cells has recently exceeded 10%.[171] All-polymer solar cells also have several unique advantages. They have been shown to be more stable than OPVs based on non-fullerene molecular semiconductors.[172-174] The PCEs of all-polymer solar cells have also been shown to be less sensitive to the ratio of p-type and n-type material.[174] All-polymer solar cells are also more resistant towards mechanical fracture in comparison to their molecular counterparts, making them more useful for flexible applications.[175]

To further advance the field of all-polymer solar cells, I propose to study and optimize the photovoltaic performance of polyethynylisoindigo (**108**) and polybisisoindigo (**109**) as n-type semiconductors. The LUMO of polyethynylisoindigo (-3.90 eV) and polybisisoindigo (-3.94 eV) lie between $PC_{61}BM$ (-3.8 eV) and $PC_{71}BM$ (-4.3 eV).[26] Therefore, both of these polymers (**108** and **109**) can possibly serve as n-type semiconductor in OPVs. Moreover, OFET measurements showed polybisisoindigo (~10^{-3} $cm^2/V{\cdot}s$) has an electron mobility on par with $PC_{71}BM$.[176] The

LUMO of P3HT and PTB7 reside at -3.0 and -3.31 eV, respectively.[26] When used as p-type semiconductors, both of these polymers would have an energy offset higher than 0.3 eV relative to LUMO of either polyisoindigo (**108**) or polybisisoindigo (**109**), which is required to break an electron-hole pair.[16-17] These polymers are also completely soluble in chloroform, chlorobenzene and dichlorobenzene, which are the common processing solvents to deposit active layer in OPVs. Moreover, GIWAXS data showed each polymer exhibited an increased crystallinity with annealing at a higher temperature (100 °C). The optimization of OPV parameters will be done with varying p-type materials (P3HT or PTB7), changing processing solvents, ratio of p and n-type materials and annealing temperatures. All of these parameters will be systematically varied with both regular (ITO/PEDOT:PSS/ P3HT or PTB7:**polymer**/LiF/Al) and inverted (ITO/ZnO/ P3HT or PTB7:**polymer**/MoO_3/Ag) architectures.

4.2.2 Further Exploiting Aldol Polycondensation to Synthesize Polymers with Core-expanded Isoindigo Structures

As discussed in section 1.6.4, Lei et al. incorporated a benzodifurandione unit between the lactam rings of isoindigo to develop compound **72**. Polymer **73** had a conjugated structure similar to PPVs; however, the conformational flexibility was eliminated as vinylene units of PPVs were replaced by lactam rings connected to furanone units via exocyclic double bonds.[132] In OFET applications, this rigid structure of **73** resulted in a high electron mobility of 1.1 $cm^2/V{\cdot}s$. Zheng et al. developed a fluorinated derivative (**129**) and used it to synthesize D-A copolymer **130**. Electron deficient F-atoms lowered the LUMO (-4.32 eV) of polymer **130** which exhibited air-stable and extremely high electron mobility of 14.9 $cm^2/V{\cdot}s$ (Chart 4.2).[177]

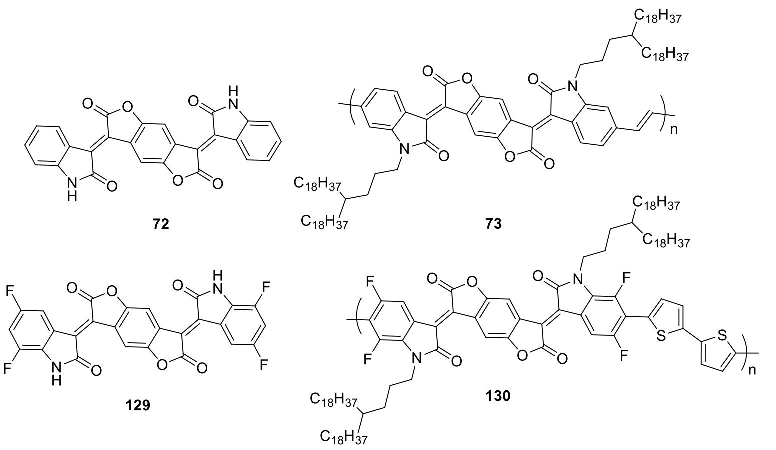

Chart 4.1 Structure of polymer **73** and **130** based on building block **72** and **129**, respectively.

The potential of building block **72** can be explored further, and the homopolymer of **72** is an ideal candidate for aldol polycondensation. Therefore, I propose to develop polymers **131-133** (Chart 4.2). The synthesis of all of three polymers can be performed *via* the aldol polycondensation reaction given in Scheme 4.1. This project will again highlight the versatility of the scalable and metal-free aldol polymerization. Compared to the homopolymer (**131**) of **72**, the F-atoms in **132** are expected to produce a lower LUMO, which is required for air-stable electron transport. Polymer **133** should have a lower torsion angle relative to **131,** as the peripheral benzene rings of the repeat units are replaced by thiophenes. This will make the polymer backbone more planar and rigid. Following the synthesis of these three polymers, their photovoltaic and OFET performance will be estimated.

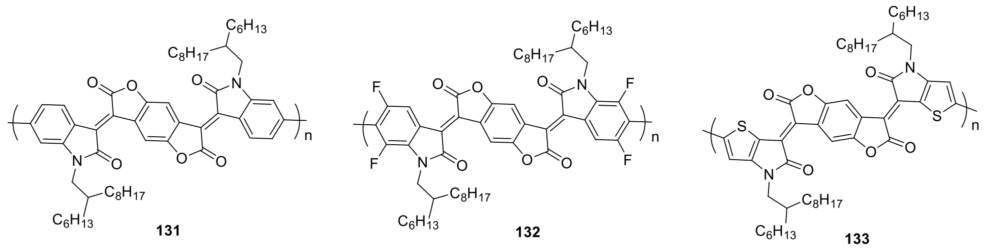

Chart 4.2 Structure of the proposed polymer **131-133**.

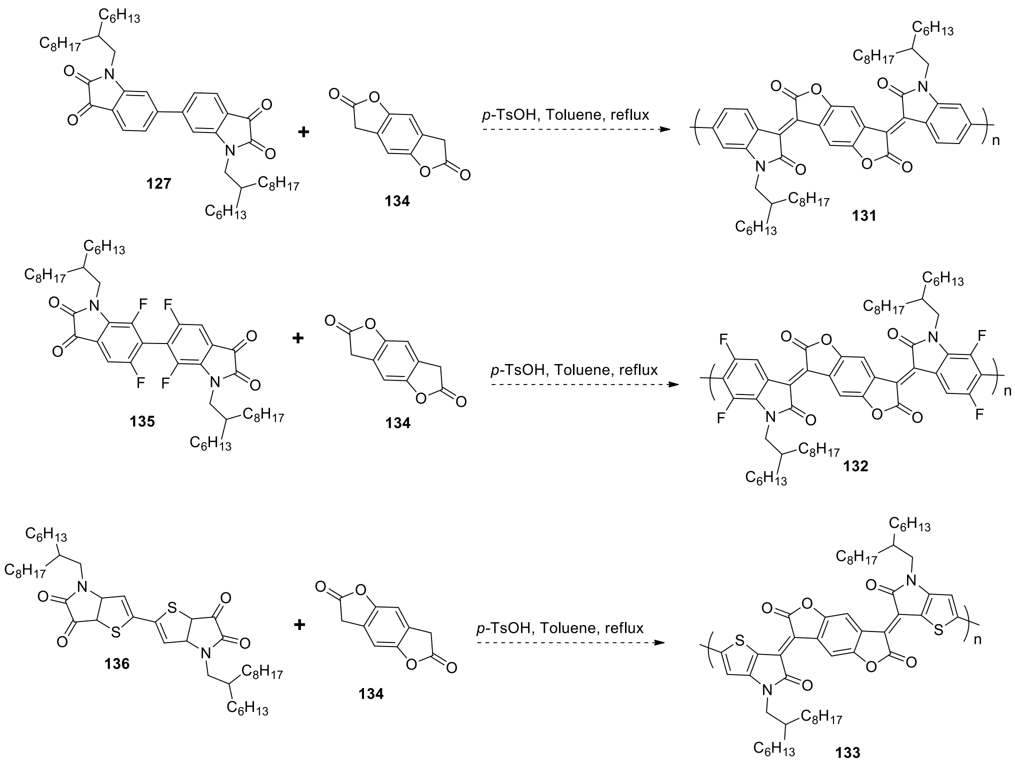

Scheme 4.1 Synthesis of **131-133** *via* aldol polycondensation.

Bisisoindigo-based polymers have also shown promising electron mobility when incorporated in OFETs.[136-137, 139] By combining alkylated bisisatin and benzodifurandione units, polymers with larger π-systems and low LUMO energies can result in stable electron transport with high charge carrier mobility. Therefore, I propose to synthesize polymer **137** and **138** (Chart 4.3) according to Scheme 4.2. Both of these conjugated polymers are conformationally locked as the monomers are connected *via* double bonds. The lactam rings in polymer **137** will be alkylated with branched side chains while polymer **138** will have linear side chains. This set of polymers will be a good example to study the effect of alkyl side chains on the optoelectronic properties of conformationally-locked polymers.

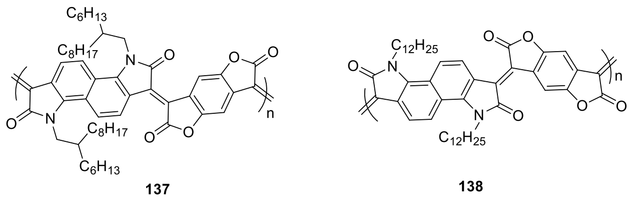

Chart 4.3 Structure of proposed polymer **137-138**.

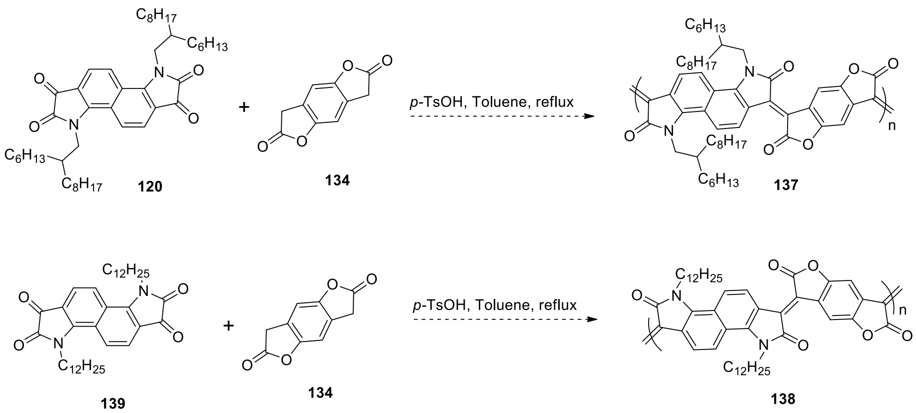

Scheme 4.2 Synthesis of **137-138** *via* aldol polycondensation.

Compound **74**, where the benzodifurandione unit is replaced by benzodipyrroledione, has additional *N*-atoms for alkylation, as compared to **72** (Chart 4.4). As discussed in 1.6.4, polymer **75** exhibited a high hole mobility of 1.92 cm^2/V·s.[134] Hence, I propose to develop another set of analogous polymers (**140-142**) where the benzodifurandione unit will be replaced by benzodipyrroledione (Chart 4.5). Aldol polycondensation will again be used to synthesize these polymers, as per Scheme 4.3. This set of polymers is expected to be more processable, compared to the benzodifurandione-based analogues, which is expected to impact the film morphology. The synthesis of these polymers will be followed by their testing in OPV and OFET applications.

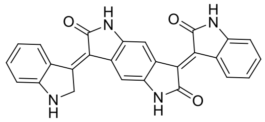

74

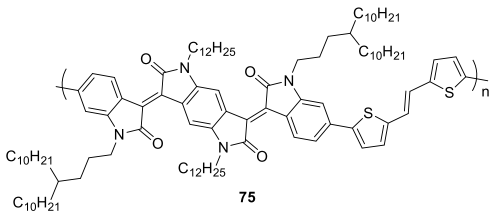

75

Chart 4.4 Structure of building block **74** and polymer **75**.

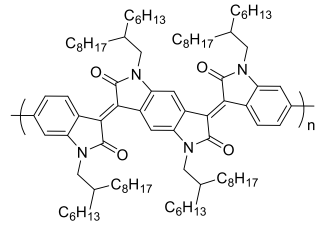

140

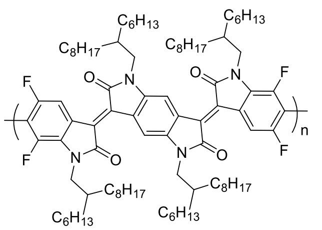

141

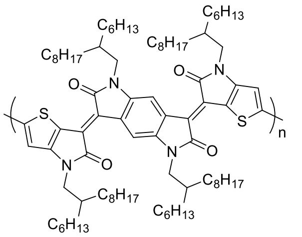

142

Chart 4.5 Structure of proposed polymer **140-142**.

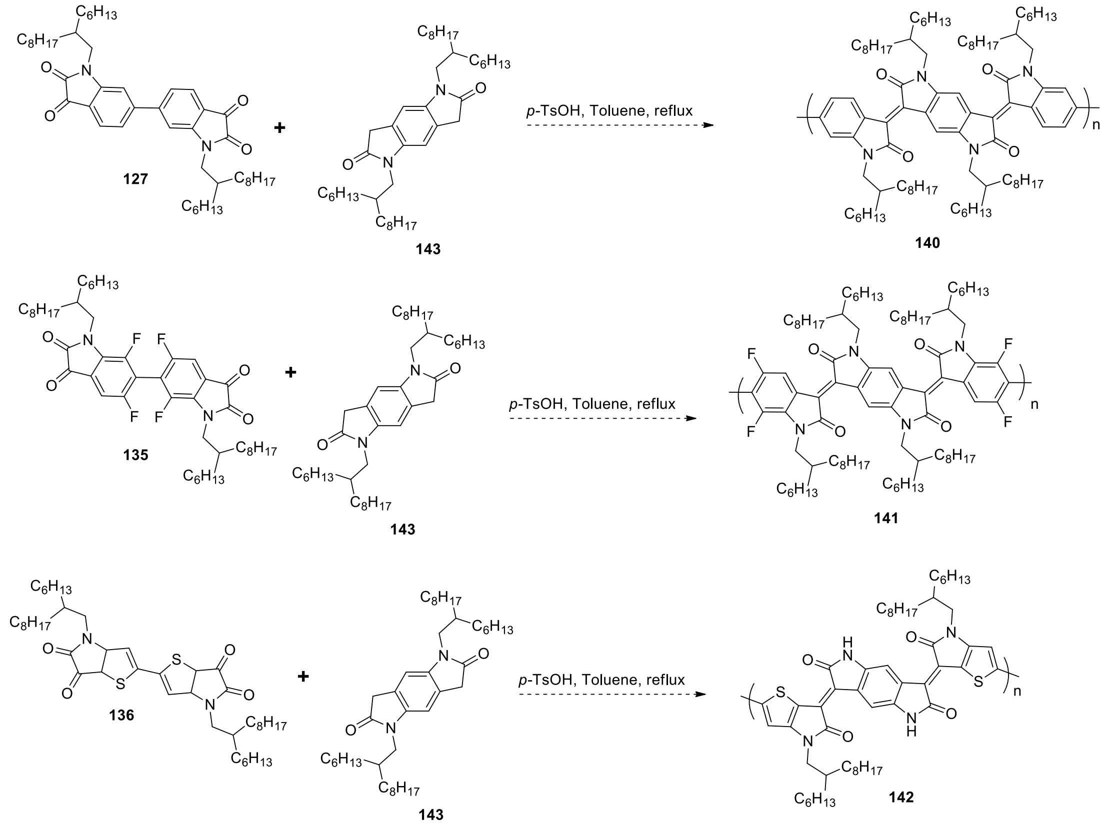

Scheme 4.3 Synthesis of **140-142** *via* aldol polycondensation.

I also propose to couple alkylated bisisatin units to alkylated benzodipyrroledione to synthesize polymers **144** and **145** (Chart 4.6) using aldol polycondensation (Scheme 4.4). These materials would enable me to compare the benzodipyrroledione based polymers (**144** and **145**) (Chart 4.6) to the benzodifurandione based polymers (**137** and **138**) (Chart 4.3). Polymers **144** and **145** will have twice as many alkyl side chains as in polymers **137** and **138.** These additional alkyl side chains will influence the thin-film microstructure, which might result in interesting structure-property relationships.

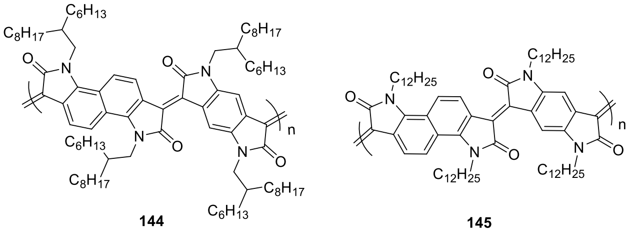

144

145

Chart 4.6 Structure of proposed polymer **144-145**.

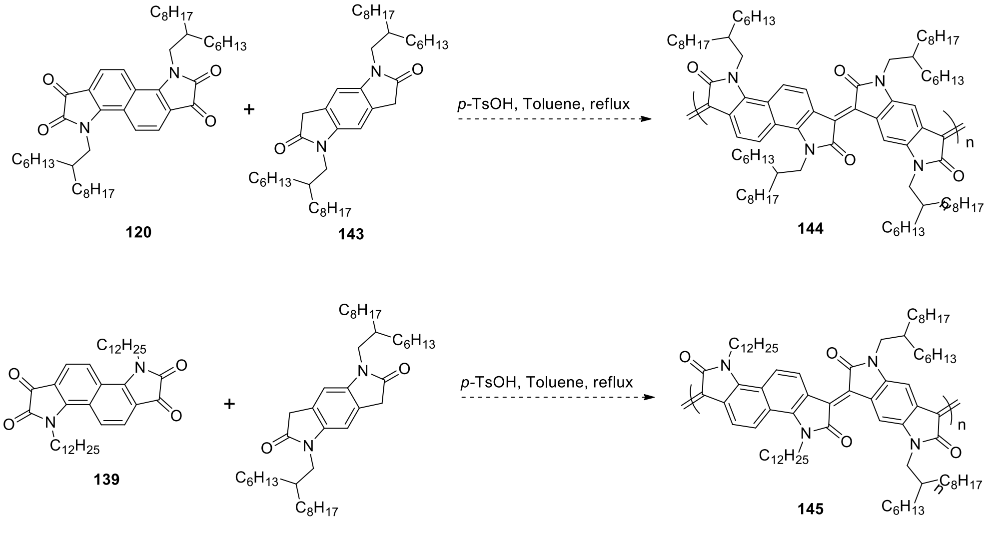

120

143

144

139

143

145

Scheme 4.4 Synthesis of **144-145** *via* aldol polycondensation.

4.2.3 Developing Thienyl Derivative of Polybisisoindigo

The emergence of thienoisoindigo and its application in OPVs and OFETs was discussed in section 1.6.2. As mentioned earlier, the thienoisoindigo-napthalene copolymer **57** demonstrated p-type behavior in OFETs with a record hole mobility of 14.4 cm^2/V·s.[121-122]The increased planarity of the polymer backbone from the incorporation of thienoisoindigo was the primary reason for this extraordinary hole mobility. As discussed in chapter 3, polybisisoindigo (**109**) has an increased electron mobility relative to polyisoindigo[116] (**46**) because of the extended conjugation of the ring-fused bisisoindigo unit (Chart 4.7). Polybisisoindigo nonetheless has a torsion angle as high as in polyisoindigo. Therefore, a reduction in torsion angle can further increase its electron mobility.

Hence, I propose to synthesize polymer **147** as per Scheme 4.5, incorporating **146** as the repeat unit (Chart 4.8). This modification will replace six-membered benzene rings by five-membered thiophene rings at the periphery of the repeat unit, which would possibly reduce the torsion angle in the resulting polymer. The electron rich thiophene unit is also expected to raise the HOMO of the resulting polymer, which may result in ambipolar carrier transport. GIWAXS analysis showed that polybisisoindigo (**109**) was amorphous in nature and that the π-stacking was too weak to transport electrons efficiently *via* charge hopping (discussed in chapter 3). The reduced torsional strain in this thienyl-bisisoindigo derivative (**147**) will strengthen the π-stacking, hence, it should lead to an improved electron mobility.

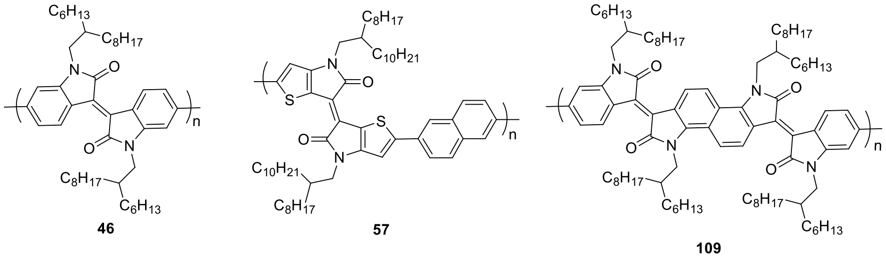

Chart 4.7 Structure of polymer **46**,[116] **57**[122] and **109**.

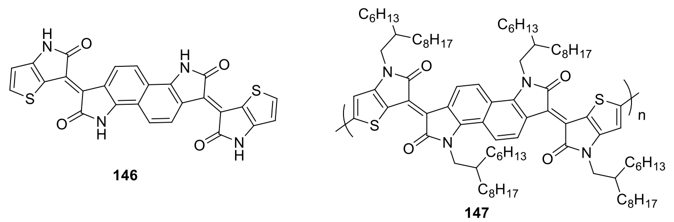

Chart 4.8 Structure of proposed polymer **147** based on the building block **146**.

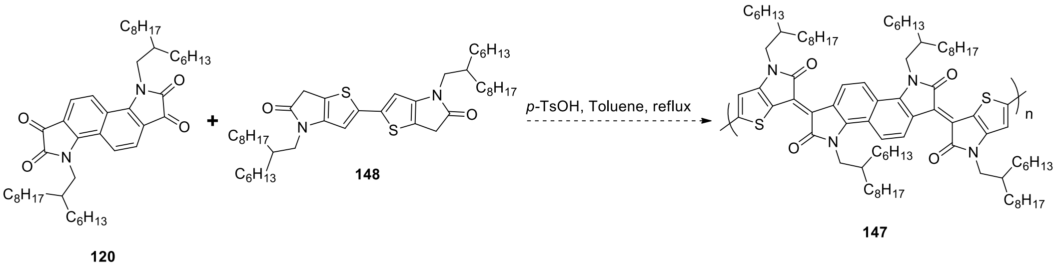

Scheme 4.5 Synthesis of **147** *via* aldol polycondensation.

4.2.4 Effect of Locked Geometry *vs.* Alkyl Chain Branching on the Microstructure of Polybisisoindigo

Onwubiko et al. synthesized two polybisisoindigo derivatives (**82**, **150**) with a conformationally-locked geometry, where the repeat units were connected *via* double bonds (Chart 4.9).[137] Polymer **149** was *N*-alkylated with branched side chains, while polymer **82** had linear and branched side chains on alternate bisisatin units. When incorporated in OFETs, polymer **82** showed an electron mobility one order of magnitude higher than that of **149**. Since both polymers had a locked geometry, the higher electron mobility of **82** was ascribed to better π-π stacking because of the arrangement of alternating linear and branched side chains. I synthesized polybisisoindigo (**109**, presented in Chapter 3), which is structurally similar to **82** and **149**. However, the structure of **109** is conformationally flexible, as the repeating units are connected *via* single bonds. Surprisingly, polybisisoindigo (**109**) exhibited an electron mobility of a similar order of magnitude as **149**. Polybisisoindigo (**109**) and polymer **149** both had branched side chains, while **82** had a conformationally locked geometry; however, polybisisoindigo (**109**) had the monomer units connected through single bonds. This poses a question on the relevance of the locked geometry of polybisisoindigo derivatives. Is the locked geometry in **82** and **149** critically important for uninterrupted electron transport? Or does the larger π-system of bisisoindigo make the locked geometry optional? Is the role of side chains more important than a geometrically locked polymer backbone? To answer these questions, I propose to investigate the structure-property relationship of polymers **109** and **150-152** (Figure 4.1). Polymers **150** and **151** have a conformationally locked polymer backbone with different alkyl side chain orientation. All alkyl chains in polymer **150** will be branched, while polymer **151** will have alternating branched and linear side chains. Polymers **109** and **152** are also varied in their alkyl side chain orientation in a similar fashion; however, both of these polymers will have more rotational freedom around the single bonds connecting the monomers. These polymers will be incorporated in OFETs to measure their charge carrier mobilities and thin-film microstructures will be explored by GIWAXS. Based on the measured charge carrier mobilities and observed microstructure, an unequivocal conclusion can be drawn on the role of the locked geometry and alkyl-chain branching for these bisisoindigo-based systems.

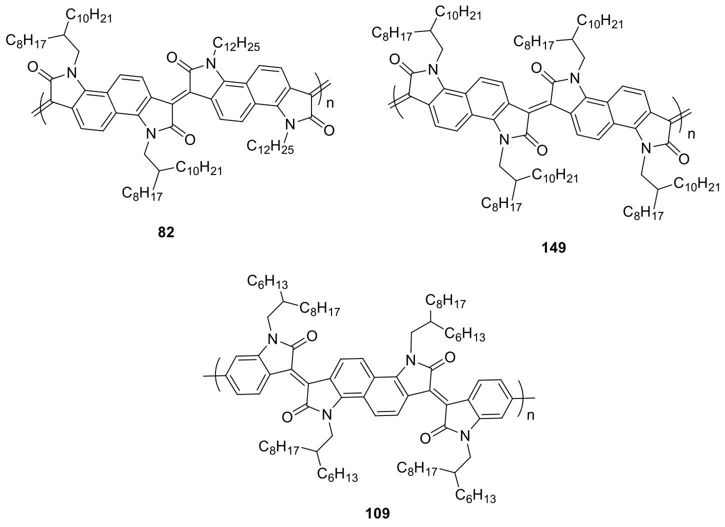

Chart 4.9 Structure polymer **82**,[137] **109**, and **149**.[137]

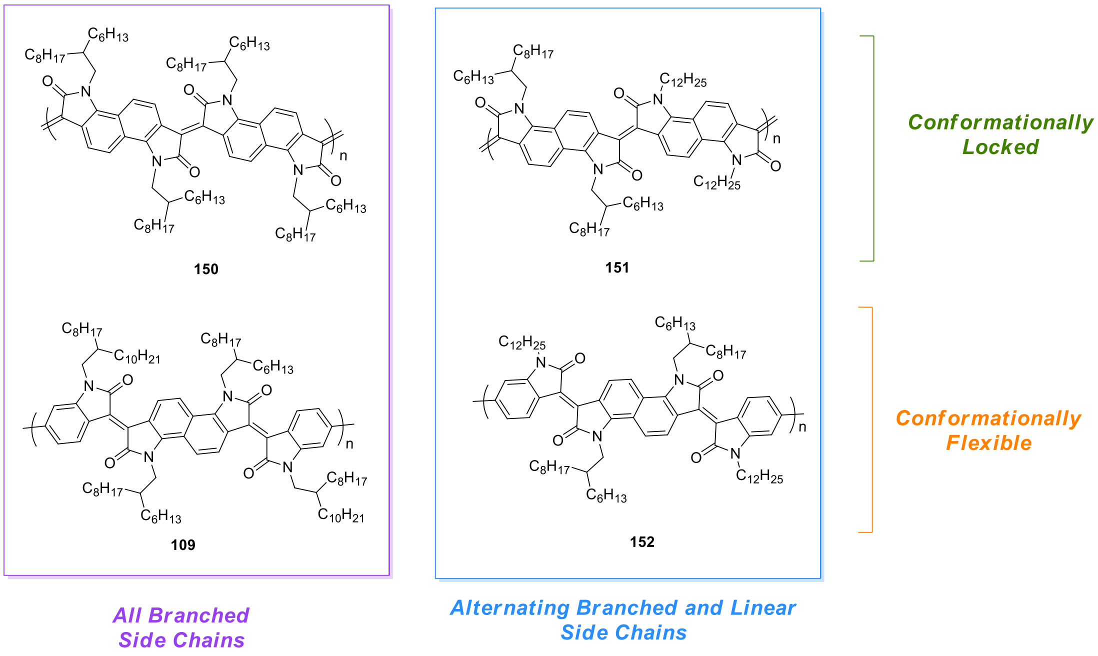

Figure 4.1 Structure of the proposed polymer **109**, **150-152**.

Chapter 5 - Experimental Details

5.1 Materials and Methods

All starting materials were purchased from commercial suppliers and used as received. *N*,*N*-Dimethylformamide, toluene, dichloromethane, triethylamine, 1,4-dioxane, methanol, chloroform and chlorobenzene were dried over activated 3 Å molecular sieves and stored under nitrogen prior to use. NMR spectra were acquired on either a Bruker Avance 500 or 600 MHz spectrometer. Mass spectra were obtained on a JEOL AccuToF 4GGCv mass spectrometer with an EiFi field desorption ionization source. Elemental analysis was done on a 2400 CHN Elemental analyzer (Perkin Elmer). UV-vis spectra were recorded either in $CHCl_3$ or as thin films on glass substrates using a Cary 6000 UV-vis spectrophotometer. Cyclic voltammetry was carried out in CH_2Cl_2 using tetrabutylammonium hexafluorophosphate (0.05 M) as the supporting electrolyte. To perform differential pulse voltammetry, a solution of tetrabutylammonium hexafluorophosphate (0.05 M) in acetonitrile was used as the supporting electrolyte. For all voltammetry experiments, a glassy carbon electrode was used as the working electrode, a Pt wire was used as the counter electrode, and a Ag wire was used as the reference electrode. All voltammograms were calibrated to a ferrocenium/ferrocene external standard. For polymers, differential pulse voltammetry was done on thin films deposited on glassy carbon working electrodes (films were prepared by drop casting from a chloroform solution). AFM images were obtained using a Dimensions Hybrid Nanoscope system (Veeco Metrology Group).

5.2 Computational Details

DFT and TDDFT calculations were carried out using the Gaussian09 and Gaussview suites of software,[178] at a B3LYP/6-31G(d,p) level of theory. Geometries were optimized and vibrational frequencies were calculated. Once the frequency analysis confirmed there were no imaginary frequencies, single point energy calculations were carried out using a polarizable continuum model (PCM) with a dielectric constant equal to that of dichloromethane. TDDFT calculations were carried out using the same PCM, but with a dielectric constant equal to that of chloroform. The calculated UV-vis spectra were processed using the SWizard program, revision 5.0, using the Gaussian/Lorentzian/pseudo-Voigt model.[179-180]

5.3 Single Crystal X-ray Diffraction

A single crystal of Compound **91** (CCDC 1542137) was coated with Paratone-N oil and then mounted using a Micromount™ (*MiTeGen*). The crystal was frozen to –100 °C in the cold stream of N_2, controlled by the Oxford Cryojet attached to the diffractometer. Crystal data were collected on a Bruker APEX II diffractometer, using monochromated Mo Kα radiation (λ = 0.71073 Å). First, the orientation matrix and unit cell were determined by ω scans, and then the X-ray data were measured using ϕ and ω scans.[181] Frame integration and data reduction was performed with the Bruker SAINT software package.[182] Data were then corrected for absorption effects using the multi-scan method (SADABS).[182] The structure was solved by the Intrinsic Phasing method implemented with SHELXT and refined using the Bruker SHELXTL software package.[183-184] Non-hydrogen atoms were refined with independent anisotropic displacement parameters (except atoms involved in disorder). Hydrogen atoms were refined with the riding model – they were placed at geometrically idealized positions with respect to the attached non-hydrogen atoms and their displacement parameters were fixed to be 20-50 % larger than those of the attached non-hydrogen atoms. Ellipsoid plots were prepared using Mercury (CCDC).[185]

5.4 GIWAXS Measurements

GIWAXS measurements were performed at the Stanford Synchrotron Radiation Lightsource (SSRL) beamline 11-3 in a helium-filled chamber. An X-ray beam with a wavelength of 0.9752 Å and a beam size of 50 µm vertical and 150 µm horizontal dimensions was used. GIWAXS images were recorded using a Rayonix MX225 X-ray detector at a sample to detector distance of 29.84 cm. Data processing was performed using the Nika software package for Wavemetrics Igor,[186] in combination with WAXStools,[187] with a custom written Igor script.

5.5 OPV Fabrication and Testing

ITO-coated glass substrates (Delta Technologies, $R_s \sim 6\ \Omega/\square$) were cleaned by successive sonication for 15 min in each of 10% (v/v) Extran 300 detergent solution, Millipore water, acetone, and isopropanol. Clean substrates were stored under isopropanol, and they were blown dry with compressed air immediately prior to use and UV-ozone cleaned for 15 min. PEDOT:PSS (Clevios P VP AI 4083) solution was filtered through a 0.45 μm filter. This solution was spin coated onto the clean ITO substrates and annealed at 150 °C for 15 min before being placed in a N_2-atmosphere glove box. The active layer solution (18 $mg\cdot mL^{-1}$) was prepared by dissolving the organic semiconductor (compound **90**, **1**, and **91**) and either $PC_{61}BM$ or $PC_{71}BM$ in a 1:1 donor/acceptor ratio by mass in the solvent chosen and stirred overnight at room temperature. The solution was filtered through a 0.45 μm filter and spin coated onto the PEDOT:PSS-coated substrate. After drying, LiF (0.8 nm) and Al (100 nm) were thermally evaporated onto the substrate at a base pressure of 2×10^{-6} mbar.

J-V curves were acquired inside a N_2-atmosphere glovebox using a Keithley 2400 source-measure unit. The cells were irradiated by a 450 W Class AAA solar simulator in conjunction with an AM1.5G filter (Sol3A, Oriel instruments) at a calibrated intensity of 100 $mW\cdot cm^{-2}$ which was determined by a standard silicon reference cell (91150 V, Oriel Instruments). The cell area was masked by a non-reflective anodized aluminium mask to be 0.101 cm^2. IPCE was measured for the highest efficiency devices in an ambient atmosphere using a QE-PV-SI system (Oriel Instruments) consisting of a 300 W Xe arc lamp, monochromator, chopper, lock-in amplifier and certified silicon reference cell. Measurements were performed with a 30 Hz chop frequency.

5.6 OFET Fabrication and Testing

5.6.1 Wafer Preparation

A bottom-gate bottom-contact configuration was used for all of the OFET devices. A heavily n^+-doped SiO_2/Si wafer with a 300 nm thick SiO_2 dielectric layer was patterned with a gold source and drain pairs by conventional photolithography and thermal deposition techniques. The wafers were cleaned via oxygen plasma treatment with $C_{18}H_{37}SH$ for 2 minutes, followed by sonication in acetone and isopropanol. Subsequently, the wafers were treated with acid (aq.) and dodecyltrichlorosilane was deposited as a monolayer in toluene. The prepared wafers were dried on a hotplate at 120 °C for 30 minutes before spin-coating of the polymer films.

5.6.2 Spin-Coating

Each of the compounds was spin-coated from a solution (6 mg/mL) in chloroform at 2000 rpm for 60 s. All devices were dried on a hotplate at 30 °C for 20 minutes before being brought into the glove-box for testing. Devices were tested as-cast, and annealed at 50 °C, 100 °C, 150 °C, and 200 °C for 30 minutes at each temperature. The annealed devices were re-tested after each annealing cycle. The data presented in this report relate to the best performing condition for each polymer.

5.6.3 Device Testing

Device testing was performed in the glovebox, in the dark, under an argon atmosphere using an Agilent B2912A source/measure unit. All the OFET devices have a channel length (L) of 30 μm and a channel width (W) of 1000 μm.

5.7 Detailed Synthetic Procedures

5.7.1 Synthesis of 94

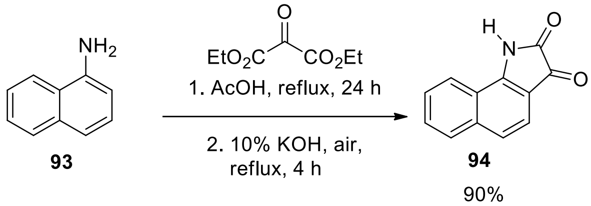

1-Aminonaphthalene (**93**) (5.0 g, 35 mmol) was dissolved in 50.0 mL of AcOH and heated to reflux under an argon atmosphere. Diethylketomalonate (10.0 mL, 65.8 mmol) was dissolved in 30 mL of AcOH in a Schlenk flask under an argon atmosphere and added to the refluxing solution of 1-aminonaphthalene over 0.75 h. The resulting solution was refluxed for 24 h. The solvent was then removed under reduced pressure and 1 M KOH was added to the resibecause of raise the pH to 11.0. Then the solution was heated to reflux and portions of 1 M KOH were added to maintain the pH. The solution was refluxed and sparged with air for 4 h. Then the solution was cooled to room temperature and acidified with 6 M HCl to a pH of 1.0. The brown precipitate was isolated by filtration, washed well with water, and finally dried under high vacuum to yield a brown solid. The dark brown solid (**94**) was used directly for the next step without any further purification because of its poor solubility in common organic solvents (6.05 g, 90%). ^{1}H NMR (DMSO-d_6, 500 MHz, δ) 11.68 (s, 1H), 8.19 (d, J = 8.35 Hz, 1H), 7.98 (d, J = 8.25 Hz, 1H), 7.75 (t, J = 7.55 Hz, 1H), 7.64 (t, J = 7.35 Hz, 1H), 7.55 (d, J = 8.35 Hz, 1H), 7.48 (d, J = 8.35 Hz, 1H).

5.7.2 Synthesis of 95

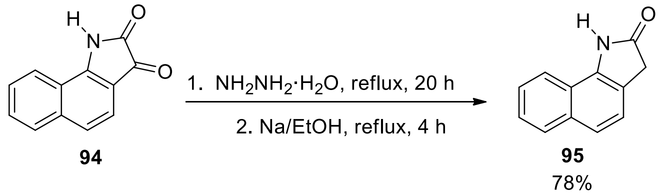

Compound **94** (2.50 g, 12.8 mmol) was suspended in 30.0 mL of hydrazine hydrate and refluxed under a N_2 atmosphere for 20 h. The hydrazine hydrate was removed under reduced pressure to afford a yellow-orange residue. In a separate flask, metallic sodium (4.0 g, 0.17 mol) was dissolved in 30.0 mL of anhydrous ethanol. When the sodium was completely dissolved, the residue from the last step was dissolved in anhydrous ethanol (10 mL) and added portion-wise, with stirring, at 60-70 °C over a 10 min interval. Then the solution was refluxed for 4 h under a N_2 atmosphere. The dark brown solution was then poured onto 200 mL of ice-water and acidified to pH 1.0 with 6 M HCl solution. The resulting gray-brown precipitate was isolated by filtration, washed well with water and finally dried under high vacuum. The gray-brown solid (**95**) was used directly for the next step without any further purification because of its poor solubility in common organic solvents (1.7 g, 78%). ^{1}H NMR (DMSO-d_6, 500 MHz, δ) 11.14 (s, 1H), 8.06 (d, J = 7.85 Hz, 1H), 7.90 (d, J = 7.45 Hz, 1H), 7.54 (d, J = 8.15 Hz, 2H), 7.50-7.46 (m, 2H), 7.41 (d, J = 8.20 Hz, 1H), 3.68 (s, 2H).

5.7.3 Synthesis of 96

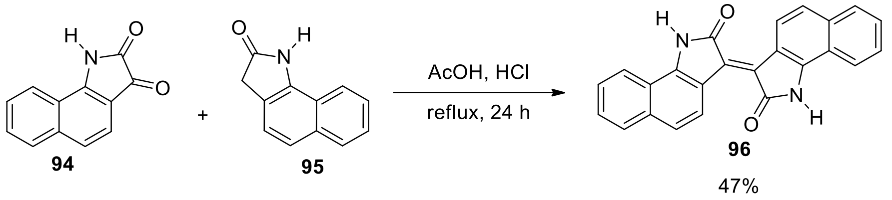

To a mixture of **94** (670 mg, 3.45 mmol) and **95** (628 mg, 3.42 mmol) in glacial acetic acid (50.0 mL), concentrated HCl (0.30 µL) was added, and the resulting solution was refluxed for 24 h under an argon atmosphere. The reaction mixture was poured onto ~100 mL of ice-water and filtered. The resulting bluish-green solid was washed with water, ethyl alcohol and ethyl acetate. It was finally dried under vacuum to yield a bluish green solid (**96**) (573.0 mg, 47%). ^{1}H NMR (DMSO-d_6, 500 MHz, δ) 11.64 (s, 1H), 8.96 (d, *J* = 8.75 Hz, 1H), 8.17 (d, *J* = 8.10 Hz, 1H), 7.88 (d, *J* = 8.10 Hz, 1H), 7.58-7.53 (m, 2H), 7.45 (d, *J* = 8.65 Hz, 1H).

5.7.4 Synthesis of 89

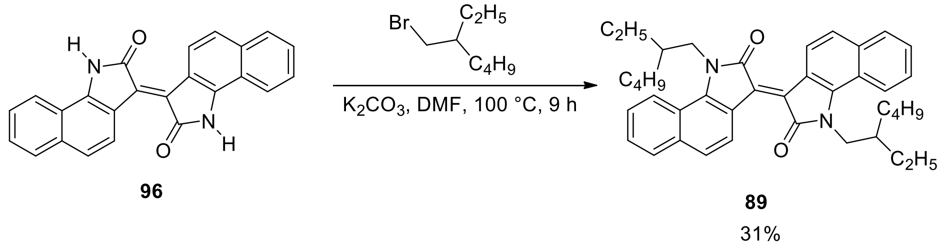

96 (471 mg, 1.30 mmol) was dissolved in dry DMF (30.0 mL) under an argon atmosphere, followed by the addition of K_2CO_3 (922 mg, 6.67 mmol) and 2-ethylhexylbromide (0.50 mL, 2.81 mmol). The solution was stirred at 100 °C for 9 h. After cooling the solution to room temperature, it was poured onto ~100 mL of ice-water. The product was extracted with CH_2Cl_2 (2 × 50 mL), and 1 M HCl was used to break the resulting emulsion. The organic layer was washed with water (6 × 100 mL) and brine (1 × 100 mL), and dried over Na_2SO_4. The solvent was removed under reduced pressure to yield a dark-green solid (**89**), which was purified by flash column chromatography on silica gel, eluting with a gradient of CH_2Cl_2:hexanes (10% CH_2Cl_2 to 35% CH_2Cl_2) (271 mg, 31%). ^{1}H NMR ($CDCl_3$, 500 MHz, δ) 8.67 (d, *J* = 8.80 Hz, 1H), 8.19 (d, *J* =

8.55 Hz, 1H), 7.79 (d, *J* = 8.80 Hz, 1H), 7.48-7.40 (m, 3H), 4.30-4.17 (m, 2H), 2.01-1.98 (m, 1H), 1.46-1.28 (m, 8H), 0.94-0.86 (m, 6H). ^{13}C NMR ($CDCl_3$, 125 MHz, δ): 169.81, 142.47, 137.57, 132.85, 129.62, 127.52, 125.79, 124.39, 123.68, 122.17, 120.71, 119.01, 46.50, 38.88, 30.44, 28.63, 23.71, 23.25, 14.22, 10.72. HRMS (*m/z*): ($M^{\bullet+}$) Cal. ($C_{40}H_{46}N_2O_2$): 586.35593 found: 586.35703. Anal. Calcd. for $C_{40}H_{46}N_2O_2$: C, 81.87; H, 7.90; N, 4.77; found: C, 81.90; H, 8.11; N, 4.72.

5.7.5 Synthesis of 98

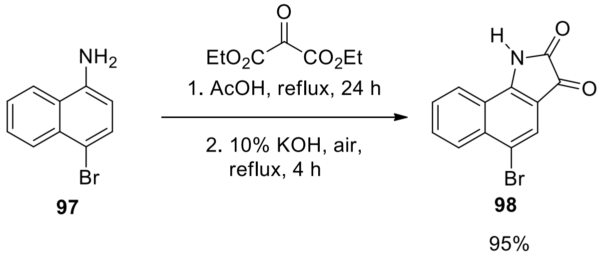

The synthesis of **98** was carried out using the same procedure as for **94**, starting with compound **97** (2.0 g, 9.1 mmol). This yielded a brown solid (**98**) (2.4 g, 95%). ^{1}H NMR (DMSO-*d*$_6$, 500 MHz, δ) 11.83 (s, 1H), 8.27 (d, *J* = 8.25 Hz, 1H), 8.18 (d, *J* = 8.50 Hz, 1H), 7.93 (t, *J* = 7.65 Hz, 1H), 7.81 (s, 1H), 7.77 (t, *J* = 7.57 Hz, 1H).

5.7.6 Synthesis of 99

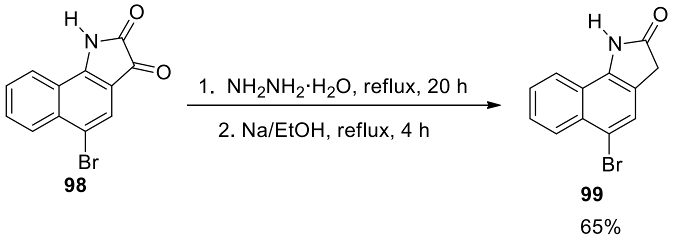

The synthesis of **99** was carried out using the same procedure as for **95**, starting with compound **98** (3.10 g, 11.2 mmol). This yielded a gray-brown solid (**99**) (1.8 g, 65%). ^{1}H NMR (DMSO-*d*$_6$, 500 MHz, δ) 11.30 (s, 1H), 8.11 (t, *J* = 7.85 Hz, 2H), 7.78 (s, 1H), 7.66-7.59 (m, 2H), 3.71 (s, 2H).

5.7.7 Synthesis of 100

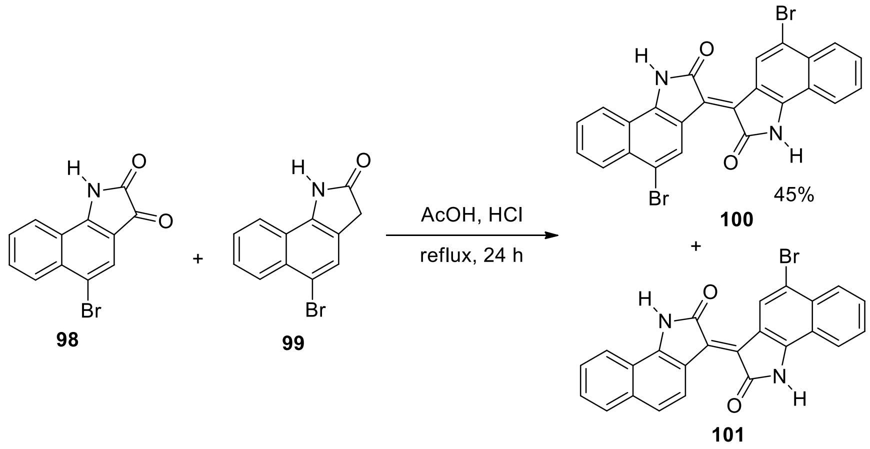

To a mixture of **98** (2.49 g, 9.03 mmol) and **99** (2.30 g, 8.78 mmol) in glacial acetic acid (50.0 mL), concentrated HCl (2.0 mL) was added, and the resulting solution was refluxed for 24 h under an argon atmosphere. The reaction mixture was poured onto ~200 mL of ice-water and filtered. The resulting bluish-green solid was washed with water, ethyl alcohol and ethyl acetate. It was finally dried under vacuum to yield a bluish green solid (**100**, 2.05 g, ~45%, based on NMR spectra). ^{1}H NMR (DMSO-d_6, 500 MHz, δ) 11.83 (m, 2H), 11.66 (s, 2H), 9.42 (s, 1H), 8.96 (d, J = 8.90 Hz, 2H), 8.26-7.44 (m, 13 H). HRMS (*m/z*): (M$^{\bullet+}$) Cal. ($C_{24}H_{13}BrN_2O_2$): 440.01604 found: 440.01893, Cal. ($C_{24}H_{12}Br_2N_2O_2$): 517.92655 found: 517.92603.

In addition to the desired product (**100**), the above aldol condensation produced a side product (**101**). The mixture (**100** and **101** in a ~ 1:1 ratio) was insoluble in most organic solvents and was therefore carried forward to the next step without any further purification.

5.7.8 Synthesis of 102

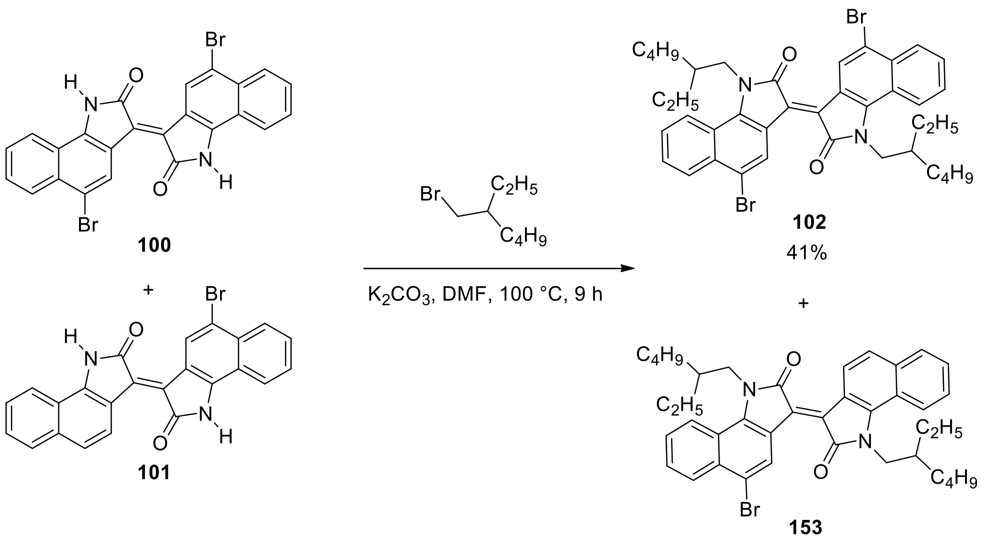

The mixture of compounds **100** and **101** (507 mg, 0.976 mmol) was dissolved in dry DMF (30.0 mL) under an argon atmosphere, followed by the addition of K_2CO_3 (426 mg, 3.16 mmol) and 2-ethylhexylbromide (0.50 mL, 2.81 mmol). The solution was stirred at 100 °C for 9 h. After cooling the solution to room temperature, it was poured onto ~40 mL of ice-water. The product was extracted with CH_2Cl_2 (2 × 50 mL), and 1 M HCl was used to break the resulting emulsion. The organic layer was washed with water (6 × 100 mL) and brine (1 × 100 mL), and dried over Na_2SO_4. The solvent was removed under reduced pressure to yield a dark-green solid (**102**), which was purified by flash column chromatography on silica gel, eluting with a gradient of CH_2Cl_2:hexanes (10% CH_2Cl_2 to 35% CH_2Cl_2) (290 mg, 41%). ^{1}H NMR ($CDCl_3$, 500 MHz, δ) 9.30 (s, 1H), 8.27 (d, J = 8.00 Hz, 1H), 8.22 (d, J = 9.00 Hz, 1H), 7.60 (t, J = 7.20 Hz, 1H), 7.50 (t, J = 7.52 Hz, 1H), 4.25 (m, 2H), 1.94 (s, 1H), 1.25-1.43 (m, 6H), 0.86-0.94 (m, 8H). ^{13}C NMR ($CDCl_3$, 125 MHz, δ): 169.44, 142.50, 134.98, 132.06, 129.10, 129.04, 128.25, 126.49, 124.11, 121.74, 119.26, 115.63, 46.72, 38.75, 29.84, 28.59, 23.76, 23.23, 14.21, 10.77. HRMS (*m/z*): ($M^{\bullet+}$) Cal. ($C_{40}H_{44}Br_2N_2O_2$): 744.17695 found: 744.17458. Anal. Calcd. for $C_{40}H_{44}Br_2N_2O_2$: C, 64.52; H, 5.96; N, 3.76; found: C, 64.31; H, 5.87; N, 3.68.

Compound **153**: ^{1}H NMR ($CDCl_3$, 500 MHz, δ) 9.26 (s, 1H), 8.85 (d, *J* = 8.80 Hz, 1H), 8.26 (d, *J* = 8.50 Hz, 1H), 8.03 (brs, 2H), 7.77 (d, *J* = 8.15 Hz, 1H), 7.56 (t, *J* = 7.62 Hz, 1H), 7.47-7.37 (m, 4H), 4.14-4.00 (m, 4H), 1.86 (brs, 2H), 1.37-1.25 (m, 15H), 0.88-0.85 (m, 13H). HRMS (*m/z*): ($M^{\bullet+}$) Cal. ($C_{40}H_{45}BrN_2O_2$): 664.26644 found: 664.25968.

5.7.9 Synthesis of 100 *via* deoxygenation reaction

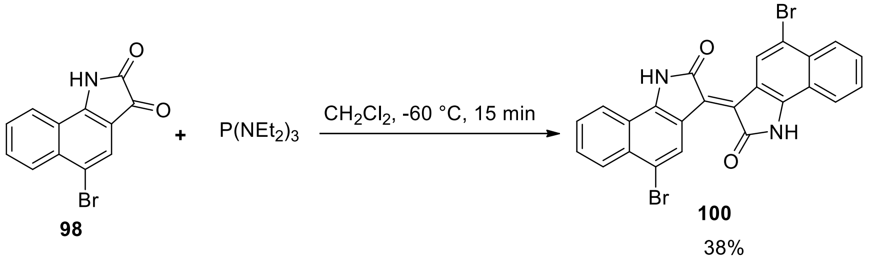

The formation of monobrominated compound (**153**) could be avoided by using a deoxygenation reaction of the corresponding isatin (**98**). $P(NEt_2)_3$ (497 mg, 2.01 mmol) was added drop-wise to a degassed suspension of **98** (479 mg, 1.74 mmol) in CH_2Cl_2 (10.0 mL) at –60 °C and stirred for 15 min. The reaction mixture was then slowly warmed to room temperature and stirred for another hour. The solvent was removed under reduced pressure and the solid was washed with EtOAc, CH_2Cl_2 and acetone and dried under high vacuum to yield a bluish-green solid (**100**, 174 mg, 38%). ^{1}H NMR (DMSO-d_6, 500 MHz, δ) 11.87 (s, 1H), 9.45 (s, 1H), 8.20 (d, *J* = 8.50 Hz, 1H), 8.12 (d, *J* = 8.40 Hz, 1H), 7.93 (t, *J* = 7.30 Hz, 1H), 7.66 (t, *J* = 7.72 Hz, 1H).

5.7.10 Synthesis of 154

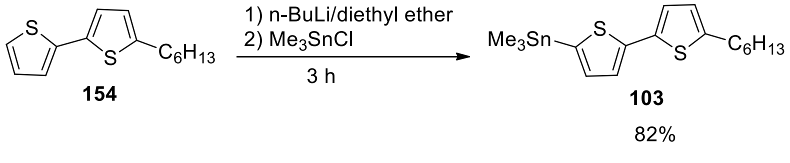

This procedure was adapted from a previous report.$^{188-189}$ To a solution of 5-hexyl-2,2′-bithiophene (**154**) (148 mg, 0.593 mmol) in 5 mL of anhydrous diethyl ether, a 2.09 M solution of *n*-BuLi in hexanes (0.32 mL, 0.67 mmol) was added drop-wise at room temperature. It was then stirred for 30 min and trimethyltin chloride (0.22 g, 0.67 mmol) was added drop-wise. The solution became turbid and yellow immediately after the addition was completed. The solution was then stirred for 2 h, and quenched with water. The product was extracted with diethyl ether, dried over Na_2SO_4, and concentrated under high vacuum to yield **103** as a viscous yellow liquid (184 mg, 82%). ^{1}H NMR ($CDCl_3$, 500 MHz, δ) 7.19 (d, *J* = 3.35 Hz, 1H), 7.05 (d, *J* = 3.30 Hz, 1H), 6.96 (d, *J* = 3.50 Hz, 1H), 6.66 (d, *J* = 3.50 Hz, 1H), 2.77 (t, *J* = 7.50 Hz, 2H), 1.40-1.28 (m, 8H), 0.88 (t, *J* = 7.20 Hz, 3H), 0.37 (s, 9H).

5.7.11 Synthesis of 91

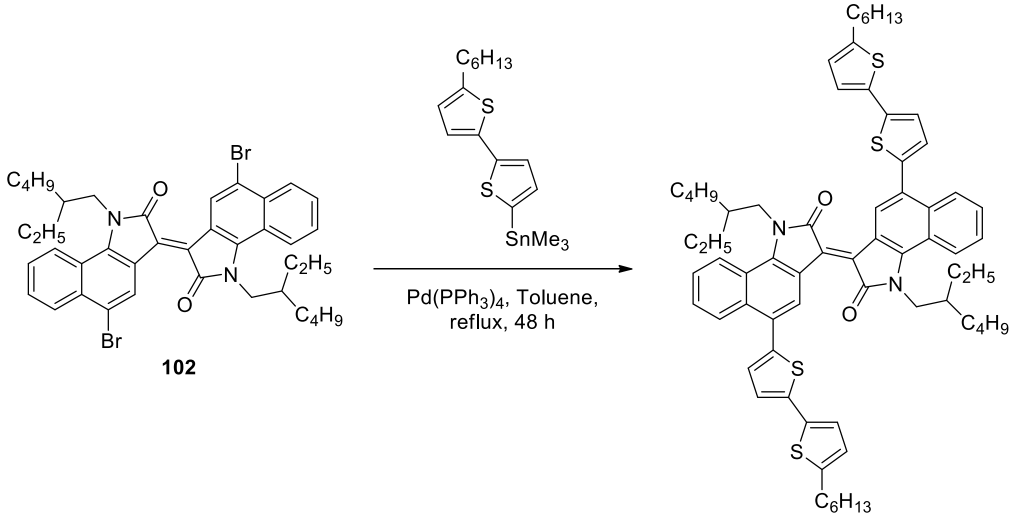

91

60%

To a solution of compound **102** (154 mg, 0.207 mmol) in 10 mL of freshly degassed (3× freeze-pump-thaw cycles), dry toluene, compound **103** (242 mg, 0.450 mmol) and $Pd(PPh_3)_4$ (31 mg, 0.026 mmol) were added under a N_2 atmosphere. The solution was then refluxed for ~48 h. The solvent was removed under reduced pressure and the crude product (**91**) was purified by column chromatography on silica gel, eluting with a gradient of CH_2Cl_2:hexanes (10% CH_2Cl_2 to 35% CH_2Cl_2) (135 mg, 60%). ^{1}H NMR (CD_2Cl_2, 600 MHz, δ) 9.05 (s, 1H), 8.28-8.23 (m, 2H), 7.52-7.46 (m, 2H), 7.16 (d, *J* = 3.60 Hz, 1H), 7.11 (d, *J* = 3.50 Hz, 1H) 7.03 (d, *J* = 3.6 Hz, 1H), 6.72 (d, *J* = 3.6 Hz, 1H), 4.25-4.22 (m, 2H), 2.80 (t, *J* = 7.57 Hz, 2H), 1.99 (brs, 1H), 1.71-1.65 (m, 2H), 1.38-1.23 (m, 14H), 0.93-0.81 (m, 9H). ^{13}C NMR (CD_2Cl_2, 125 MHz, δ): 169.64, 145.68, 142.82, 140.54, 137.93, 135.65, 134.71, 132.54, 128.15, 127.28, 126.53, 125.91, 125.43, 124.92, 124.13, 123.35, 123.23, 120.96, 118.25, 46.45, 38.81, 31.70, 31.66, 30.29, 30.20, 28.85, 28.53, 23.57, 23.17, 22.68, 13.93, 13.88, 10.36. HRMS (*m/z*): ($M^{\bullet +}$) Cal. ($C_{68}H_{78}N_2O_2S_4$): 1082.49461 found: 1082.49705. Anal. Calcd. for $C_{68}H_{78}N_2O_2S_4$: C, 75.37; H, 7.26; N, 2.59; found: C, 75.18; H, 6.99; N, 2.48.

5.7.12 Synthesis of 105

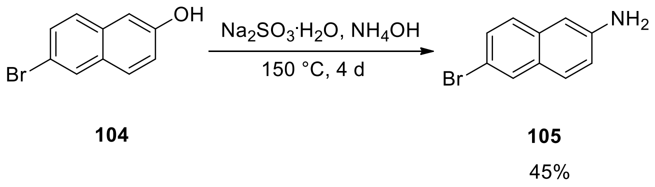

This procedure was adapted from a patent.[190] 6-Bromo-2-napthol (**104**) (2.05 g, 9.18 mmol) and sodium sulfite monohydrate (4.35 g, 34.5 mmol) were placed in a sealed tube followed by the addition of 15 mL of concentrated ammonium hydroxide. The reaction was stirred at 150 ºC for 4 days. After cooling to room temperature, the reaction mixture was extracted with ethyl acetate and washed with 1 M NaOH (3 × 100 mL) and brine (1 × 100 mL). Finally, it was dried over $MgSO_4$ and concentrated under high vacuum to yield **105** as a brown solid (920 mg, 45%). ^1H NMR ($CDCl_3$, 500 MHz, δ) 7.85 (s, 1H), 7.57 (d, *J* = 10.1 Hz, 1H), 7.46 (d, *J* = 8.7 Hz, 1H), 7.34 (d, *J* = 8.0 Hz, 1H), 6.94 (d, *J* = 8.5 Hz, 1H), 6.79 (s, 1H), 5.51 (s, 2H).

5.7.13 Synthesis of 106

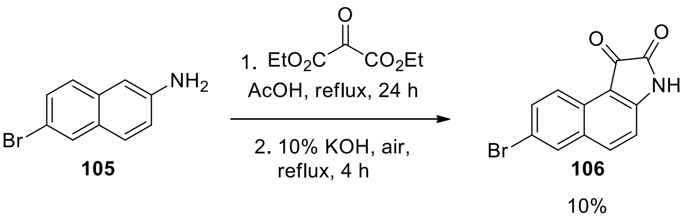

The synthesis of **106** was carried out using the same procedure as for **94**, starting with compound **105** (1.0 g, 4.5 mmol). The crude product was purified by column chromatography on silica gel, eluting with a mixture of EtOAc:hexanes (1:1) to yield an orange solid (124 mg, 10%). ^1H NMR (DMSO-d_6, 500 MHz, δ) 11.43 (s, 1H), 8.33 (d, *J* = 9 Hz, 1H), 8.26 (s, 1H), 8.22 (d, *J* = 8.5 Hz, 1H), 7.81 (d, *J* = 5.0 Hz, 1H), 7.25 (d, *J* = 9.0 Hz, 1H). ^{13}C NMR (DMSO-d_6, 125 MHz, δ):182.96, 159.94, 154.98, 139.60, 133.62, 131.18, 130.72, 127.13, 124.05, 117.39, 114.66, 108.68.

5.7.14 Synthesis of 156

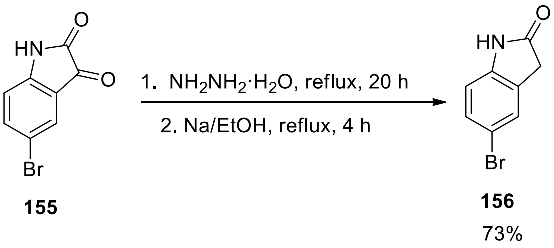

The synthesis of 4-bromooxindole (**156**) was carried out using the same procedure as for **95**, starting with compound **155** (2.0 g, 8.8 mmol). This afforded **156** as a dark brown solid (1.47 g, 73%). ^{1}H NMR (DMSO-d_6, 500 MHz, δ) 10.5 (s, 1H), 7.37 (s, 1H), 7.33 (d, *J* = 6.15 Hz, 1H), 6.75 (d, *J* = 8.25 Hz, 2H), 3.50 (s, 2H).

5.7.15 Synthesis of 157

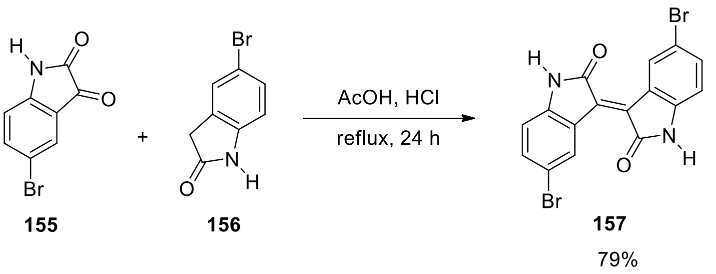

The synthesis of 5,5′-dibromoisoindigo (**157**) was carried out using the same procedure as for **96**, starting with compound **155** (1.57 g, 6.93 mmol) and **156** (1.47 g, 6.93 mmol). This afforded **157** as a brownish-violet solid (2.31 g, 79%). ^{1}H NMR (DMSO-d_6, 500 MHz, δ) 10.7 (s, 1H), 9.32 (s, 1H), 7.57 (d, *J* = 8.05 Hz, 1H), 6.84 (d, *J* = 8.45 Hz, 1H).

5.7.16 Synthesis of 158

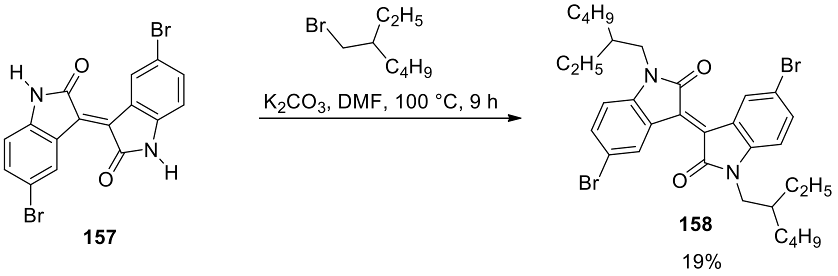

The synthesis of **158** was carried out using the same procedure as for **89**, starting with compound **157** (511 mg, 1.22 mmol). The crude product was purified by column chromatography on silica gel, eluting with a gradient of CH_2Cl_2:hexanes (10% CH_2Cl_2 to 30% CH_2Cl_2) to yield **158** as a brownish-violet solid (151 mg, 19%). ^{1}H NMR ($CDCl_3$, 500 MHz, δ) 9.37 (s, 1H), 7.47 (d, *J* = 10.45 Hz, 1H), 6.66 (d, *J* = 8.35 Hz, 1H), 3.69-3.60 (m, 2H), 1.83-1.80 (m, 1H), 1.38-1.29 (m, 8H), 0.94-0.87 (m, 6H). ^{13}C NMR ($CDCl_3$, 125 MHz, δ): 167.74, 144.36, 135.30, 133.50, 132.66, 123.07, 115.04, 109.71, 44.46, 37.60, 30.79, 28.81, 24.19, 23.21, 14.23, 10.91. HRMS (*m/z*): ($M^{\bullet+}$) Cal. ($C_{32}H_{40}Br_2N_2O_2$): 642.14565 found: 642.14716. Anal. Calcd. for $C_{32}H_{40}Br_2N_2O_2$: C, 59.64; H, 6.26; N, 4.35; found: C, 59.65; H, 6.35; N, 4.27.

5.7.17 Synthesis of 90

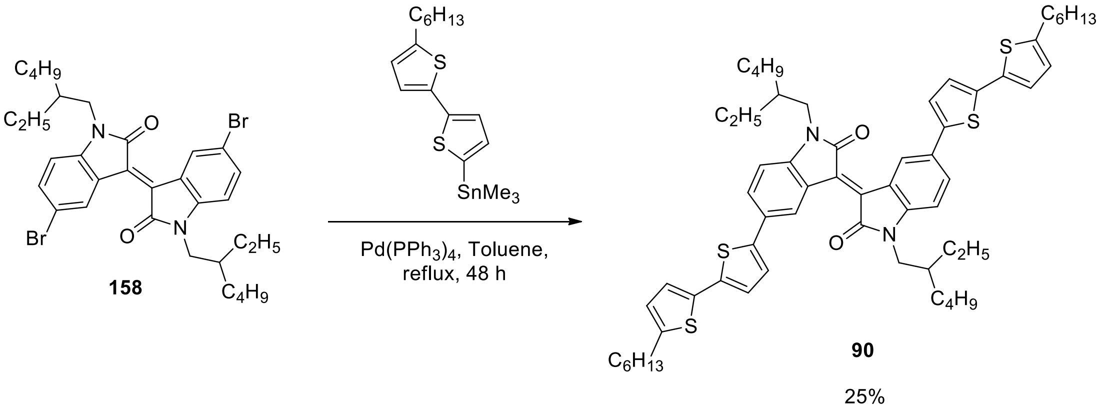

The synthesis of **90** was carried out using the same procedure as for **91**, starting with compound **158** (511 mg, 1.22 mmol). The crude product was purified by column chromatography on silica gel, eluting with a gradient of CH_2Cl_2:hexanes (10% CH_2Cl_2 to 30% CH_2Cl_2) to afford

90 as a yellowish-brown solid (151 mg, 25%). ^{1}H NMR (CDCl$_3$, 500 MHz, δ) 9.54 (s, 1H), 7.57 (dd, J_1 = 8.12 Hz, J_2 = 1.82 Hz, 1H), 7.21 (d, J = 3.70 Hz, 1H), 7.06 (d, J = 3.70 Hz, 1H), 7.01(d, J = 3.50 Hz, 1H), 6.78 (d, J = 8.15 Hz, 1H), 6.69 (d, J = 3.55 Hz, 1H), 3.74-3.69 (m, 2H), 2.80 (t, J = 7.60 Hz, 2H), 1.89-1.86 (m, 1H), 1.72-1.66 (m, 2H), 1.41-1.30 (m, 14H), 0.97-0.88 (m, 9H). ^{13}C NMR (CDCl$_3$, 125 MHz, δ): 168.24, 145.37, 144.58, 142.77, 136.60, 135.10, 133.95, 129.73, 128.72, 127.21, 124.88, 124.04, 123.26, 122.24, 108.56, 44.33, 37.22, 31.73, 30.81, 30.35, 28.91, 28.86, 24.18, 23.24, 22.73, 14.28, 14.25, 10.89. HRMS (*m/z*): ($M^{\bullet+}$) Cal. ($C_{60}H_{74}N_2O_2S_4$): 982.46331 found: 982.46554. Anal. Calcd. for $C_{60}H_{74}N_2O_2S_4$: C, 73.27; H, 7.58; N, 2.85; found: C, 73.26; H, 7.46; N, 2.86.

5.7.18 Synthesis of 112

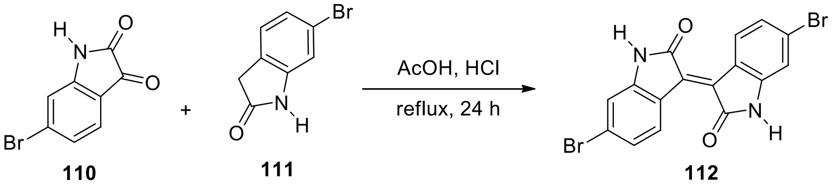

110 **111** **112**

67%

The synthesis of **112** was carried out using the same procedure as for **96**, starting with compound **110** (667 mg, 2.95 mmol) and **111** (627 mg, 2.95 mmol). This afforded **112** as a brown solid (842 mg, 67%). ^{1}H NMR (DMSO-d_6, 500 MHz, δ) 11.9 (s, 1H), 9.01 (d, J = 8.65 Hz, 1H), 7.19 (d, J = 10.45 Hz, 1H), 7.01 (s, 1H).

5.7.19 Synthesis of 159[93]

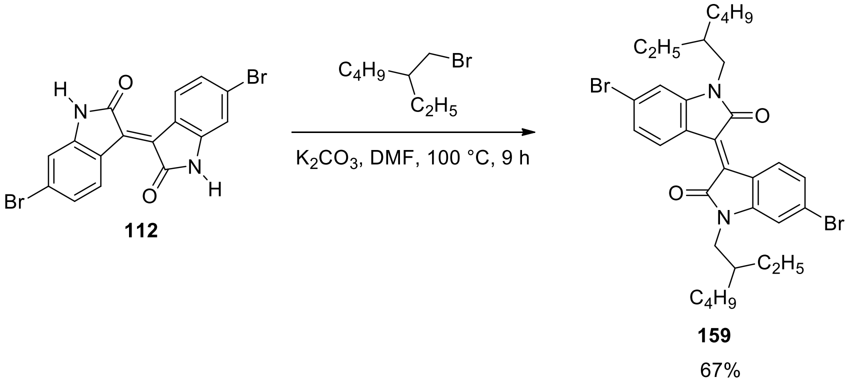

The synthesis of **159** was carried out using the same procedure as for **89**, starting with compound **112** (509 mg, 1.22 mmol). The crude product was purified by column chromatography on silica gel, eluting with a gradient of CH_2Cl_2:hexanes (20% CH_2Cl_2 to 30% CH_2Cl_2) to yield **159** as a brown solid (527 mg, 67%). ^1H NMR ($CDCl_3$, 500 MHz, δ) 9.05 (d, *J* = 8.55 Hz, 1H), 7.16 (d, *J* = 8.60 Hz, 1H), 6.90 (s, 1H), 3.65-3.61 (m, 2H), 1.87-1.81 (m, 1H), 1.39-1.29 (m, 8H), 0.94-0.88 (m, 6H).

5.7.20 Synthesis of 1[93]

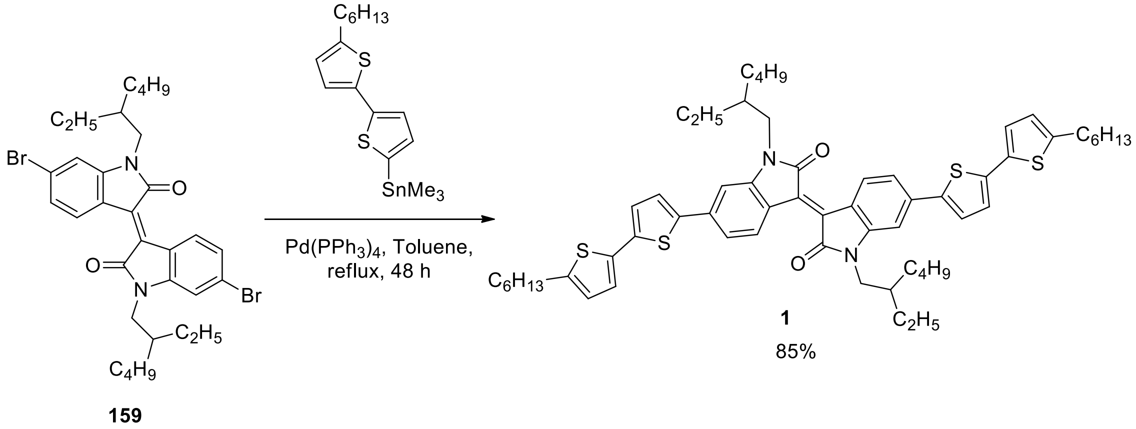

The synthesis of **1** was carried out using the same procedure as for **91**, starting with compound **159** (81 mg, 0.13 mmol). The crude product was purified by column chromatography on silica gel, eluting with 50% CH_2Cl_2 in hexanes to afford **1** as a bluish-violet solid (110 mg, 85%).[93] ^1H NMR (CD_2Cl_2, 500 MHz, δ) 9.14 (d, *J* = 8.40 Hz, 1H), 7.34 (d, *J* = 3.75 Hz, 1H), 7.25

(d, *J* = 8.40 Hz, 1H), 7.10 (d, *J* = 3.80 Hz, 1H), 7.05 (d, *J* = 3.50 Hz, 1H), 6.97 (s, 1H), 6.71 (d, *J* = 3.55 Hz, 1H), 3.76-3.64 (m, 2H), 2.79 (t, *J* = 7.60 Hz, 2H), 1.89-1.87 (m, 1H), 1.70-1.64 (m, 2H), 1.44-1.29 (m, 14H), 0.97-0.86 (m, 9H). ^{13}C NMR (CD_2Cl_2, 125 MHz, δ) 168.61, 146.45, 145.90, 141.89, 138.77, 137.35, 134.39, 131.67, 130.18, 125.18, 125.12, 124.06, 123.86, 121.12, 118.48, 104.55, 44.00, 37.83, 31.66, 31.63, 30.85, 30.21, 28.94, 28.82, 24.30, 23.19, 22.66, 14.00, 13.91, 10.62.

5.7.21 Synthesis of 113

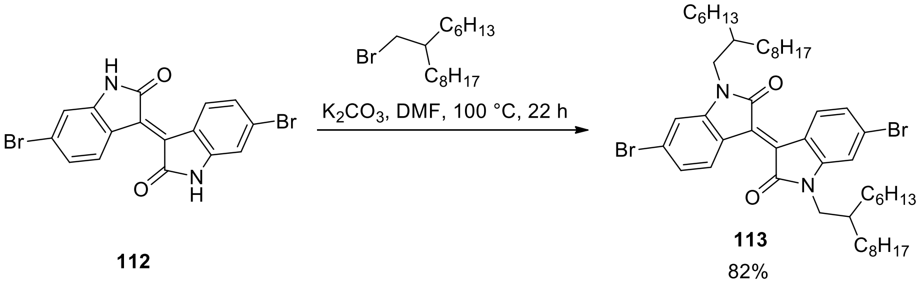

This procedure was adapted from a previous report on the alkylation of isoindigo.[191] **112** (1.02 mg, 2.43 mmol) was dissolved in dry DMF (50.0 mL) under an argon atmosphere, followed by the addition of K_2CO_3 (1.67 g, 12.0 mmol) and 2-hexyldecylbromide (2.20 mL, 7.18 mmol). The solution was stirred at 100 °C for 22 h. After cooling the solution to room temperature, it was poured onto ~100 mL of ice-water. The product was extracted with Et_2O (2 × 70 mL), and the organic layer was washed with water (6 × 100 mL) and brine (1 × 100 mL), and dried over Na_2SO_4. The solvent was removed under reduced pressure to yield a dark red solid (**113**), which was purified by flash column chromatography on silica gel, eluting with 20% CH_2Cl_2 in hexanes. The collected pure fraction was condensed to yield a red solid which was thoroughly washed with MeOH (1.7 g, 82%). ^{1}H NMR ($CDCl_3$, 500 MHz, δ) 9.06 (d, *J* = 8.6 Hz, 2H), 7.16 (d, *J* = 8.7 Hz, 2H), 6.90 (s, 1H), 3.62 (d, *J* = 7.5 Hz, 4H), 1.84-1.92 (m, 2H), 1.17-1.42 (m, 46 H), 0.85 (t, *J* = 3.6 Hz, 12H).

5.7.22 Synthesis of 114

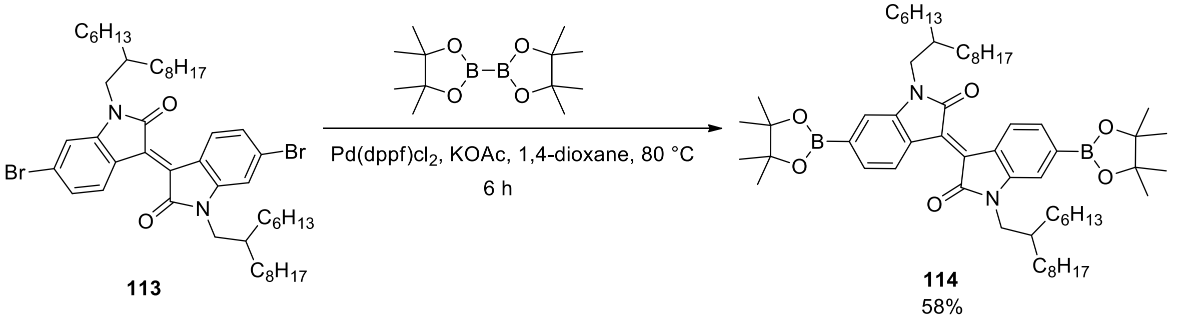

The synthesis of **114** was reproduced from a previous report.[116] Compound **113** (520 mg, 0.598 mmol) was dissolved in 12 mL dry 1,4-dioxane. This was followed by an addition of bis(pinacolato)diboron (413 mg, 1.62 mmol), Pd(dppf)Cl_2 (56.0 mg, 0.06 mmol), and KOAc (396.0 mg, 4.034 mmol). The resulting reaction mixture was then heated to 80 °C for 6 h. After the reaction mixture was cooled down to room temperature, the solution was filtered through a short silica-pad with a mixture of 50% CH_2Cl_2 in hexanes. The filtrate was condensed to yield a brown-red solid (**114**) which was re-precipitated twice in MeOH (340 mg, 58%). ^{1}H-NMR ($CDCl_3$, 500 MHz, δ) 9.15 (d, J = 7.2 Hz, 2H), 7.48 (d, J_1 = 8.1Hz, J_2 = 0.6 Hz, 2H), 7.15 (d, J = 0.6 Hz, 2H), 3.69 (d, J = 7.5 Hz, 2H), 1.95 (bs, 2H), 1.59-1.19 (m, 72H), 0.85 (t, J = 6.6 Hz, 6H); ^{13}C-NMR ($CDCl_3$, 125 MHz, δ) 168.3, 144.7, 134.5, 129.0, 128.9, 124.4, 113.7, 84.2, 44.6, 36.3, 32.1, 32.0, 31.8, 31.2, 29.8, 29.78, 29.5, 26.6, 25.1, 22.9, 22.8, 14.32, 14.30.

5.7.23 Synthesis of 46

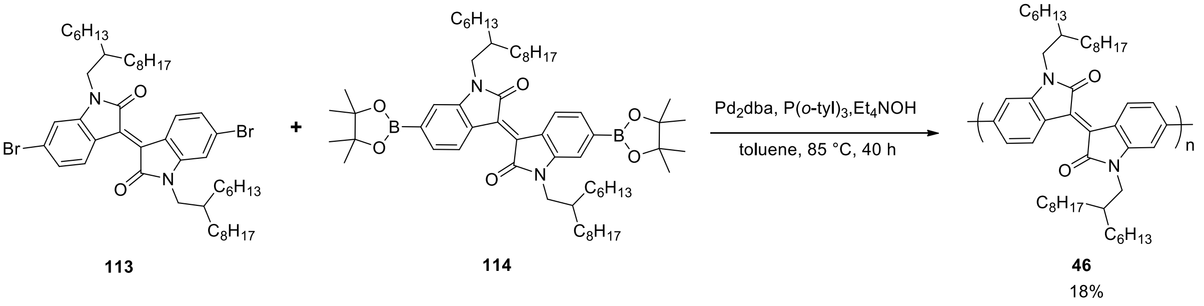

The synthesis of polyisoindigo (**46**) was reproduced from a previous report.[116] Compounds **113** (448 mg, 0.515 mmol) and **114** (495 mg, 0.515 mmol) were dissolved in dry toluene under argon and the solution was degassed for 30 minutes. It was followed by the addition of $Pd_2(dba)_3$ (47.3 mg, 0.051 mmol), $P(o\text{-tolyl})_3$ (22.4 mg, 0.072 mmol), and tetraethylammonium hydroxide (3.12 mmol, 25% in H_2O). After heating the resulting solution at 85 ˚C for 40 h, it was cooled to room temperature. Diethylammonium diethyldithiocarbamate (20.0 mg, 0.089 mmol) was subsequently added and stirred at room temperature for 2 h to scavenge the residual palladium in the solution. The resulting solution was then slowly precipitated in methanol and the crude polymer was collected by filtration. This was purified by sequential Soxhlet extraction with methanol (24 h), acetone (24 h), and hexanes (24 h). The remaining insoluble fraction was extracted into chloroform and precipitated from methanol. The resulting dark bluish-green solid (**46**) was isolated by vacuum filtration and dried under high vacuum (131 mg, 18%). M_w = 43.9 kDa, M_n = 21.9 kDa, $Đ$ = 2.0. ^{1}H-NMR ($CDCl_3$, 500 MHz, δ) 8.98-8.70 (br), 7.40-6.80 (br), 4.25-3.61 (br), 2.07-0.81 (br). Anal. Calcd. for $C_{50}H_{72}N_2O_2$: C, 81.3; H, 10.2; N, 4.0; found: C, 81.1; H, 10.4; N, 3.8.

5.7.24 Synthesis of 115

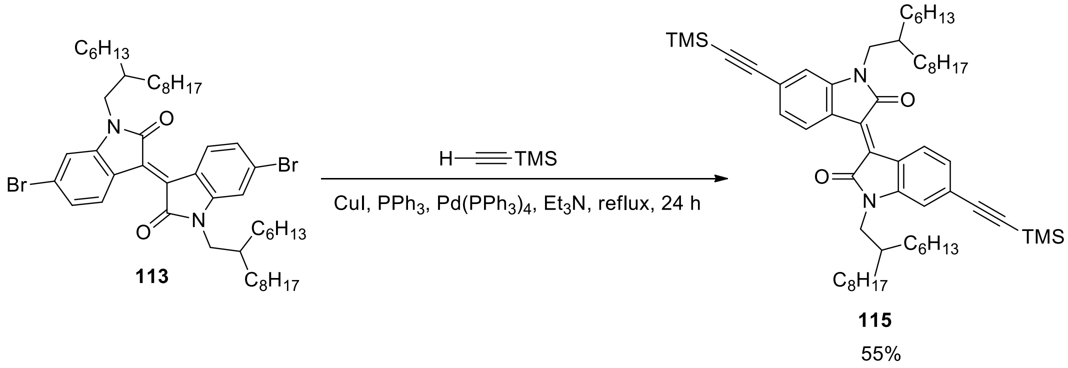

To a solution of **113** (509 mg, 0.585 mmol) in 15 mL of dry triethylamine, CuI (340 mg, 1.78 mmol) and trimethylsilylacetylene (0.28 mg, 2.88 mmol) were added. The solution was then sparged with argon for 30 min. It was followed by an addition of $Pd(PPh_3)_4$ (113 mg, 0.0978 mmol). After refluxing the solution for 24 h, the solvent was removed using a rotary evaporator to yield a brown slurry. This was dissolved in diethyl ether and washed with water (2 × 30 mL), brine (1 × 30 mL), and dried over anhydrous Na_2SO_4. After removal of the solvent, the crude was purified by flash column chromatography on silica gel, eluting with 20% CH_2Cl_2 in hexanes to yield **115** as a brown crystalline solid (290 mg, 55%). ^{1}H NMR ($CDCl_3$, 500 MHz, δ) 9.10 (d, *J* = 8.30 Hz, 1H), 7.11 (d, *J* = 8.30 Hz, 1H), 6.79 (s, 1H), 3.64 (d, *J* = 7.60 Hz, 2H), 1.92-1.90 (m, 1H), 1.33-1.25 (m, 24H), 0.88-0.84 (m, 6H), 0.27 (s, 9H). ^{13}C NMR ($CDCl_3$, 125 MHz, δ) 168.33, 145.13, 133.09, 129.62, 126.85, 126.28, 120.06, 111.17, 105.40, 97.95, 44.75, 36.20, 32.01, 31.95, 31.63, 30.15, 29.80, 29.69, 29.43, 26.52, 26.48, 22.81, 22.76, 22.81, 16.04, 14.23, 0.03. HRMS (*m/z*): ($M^{\bullet +}$) Cal. ($C_{58}H_{90}N_2O_2Si_2$): 902.65408 found: 902.65380. Anal. Calcd. for $C_{58}H_{90}N_2O_2Si_2$: C, 77.1; H, 10.1; N, 3.1; found: C, 76.4; H, 10.8; N, 3.1.

5.7.25 Synthesis of 116

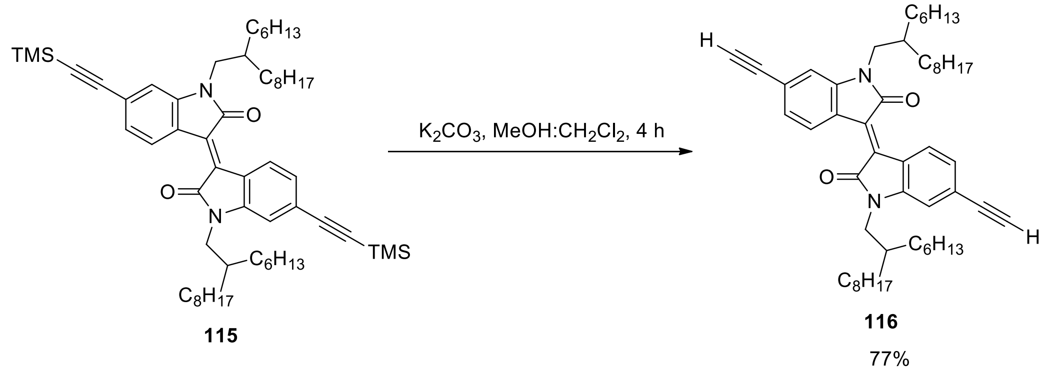

To a solution of **115** (100 mg, 0.1 mmol) in a mixture of dry CH_2Cl_2 and MeOH (1:1), K_2CO_3 (42 mg, 0.30 mmol) was added. After stirring the solution at room temperature for 4 h, the organic layer was extracted with ether (20 mL). This organic layer was washed with water (2 × 30 mL) and brine (1 × 30 mL) and dried over Na_2SO_4. The solvent was removed under reduced pressure to yield a dark-brown solid (**116**), which was dissolved in a mixture of 50% CH_2Cl_2 in hexanes and filtered through a short silica-gel pad. The solvent was removed by evaporation under reduced pressure to yield **116** as a brown solid (65 mg, 77%). ^{1}H NMR (CD_2Cl_2, 500 MHz, δ) 9.13 (d, *J* = 8.25 Hz, 1H), 7.12 (d, *J* = 8.30 Hz, 1H), 6.86 (s, 1H), 3.61 (d, *J* = 7.50 Hz, 2H), 3.30 (s, 1H), 1.90-1.87 (s, 1H), 1.31-1.23 (m, 24H), 0.84-0.82 (m, 6H). ^{13}C NMR ($CDCl_3$, 125 MHz, δ): 168.23, 145.25, 133.25, 129.81, 126.39, 125.86, 122.21, 111.39, 84.03, 80.14, 44.82, 36.25, 32.01, 31.95, 31.66, 30.14, 29.81, 29.69, 29.43, 26.53, 26.50, 22.81, 22.78, 16.16, 14.26, 14.23. HRMS (*m/z*): ($M^{\bullet +}$) Cal. ($C_{52}H_{74}N_2O_2$): 758.57503 found: 758.57474. Anal. Calcd. for $C_{52}H_{74}N_2O_2$: C, 82.3; H, 9.8; N, 3.7; found: C, 82.2; H, 10.1; N, 3.8.

5.7.26 Synthesis of 108

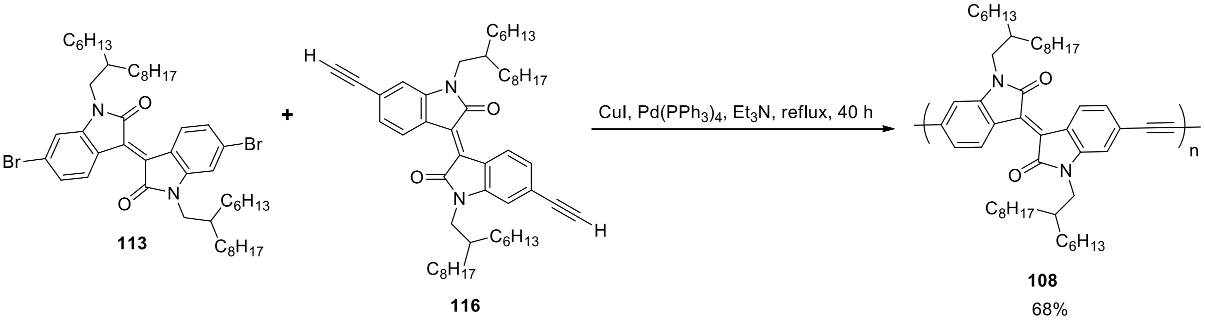

Compound **116** (112.0 mg, 0.128 mmol) and **113** (96.1 mg, 0.128 mmol) were dissolved in dry triethylamine (12.0 mL), followed by the addition of CuI (91.2 mg, 0.478 mmol). The solution was degassed by sparging argon for 30 min and further followed by the addition of Pd(PPh$_3$)$_4$ (18.0 mg, 0.015 mmol). After refluxing the solution for 40 h, it was allowed to cool to room temperature. Diethylammonium diethyldithiocarbamate (10.0 mg, 0.045 mmol) was then added and the mixture was stirred for 3 h to remove any residual catalyst. It was then precipitated in methanol (100 mL) and filtered to yield a green solid. This was purified via Soxhlet extraction consecutively with methanol, acetone, and hexanes for 24 h for each solvent. The remaining insoluble fraction was extracted into chloroform and precipitated from methanol. The precipitate was isolated by vacuum filtration and dried under high vacuum to yield polyethynylisoindigo (**108**) as a dark green solid (130 mg, 68%). $M_w = 40.4$ kDa, $M_n = 15.4$ kDa, $Đ = 2.6$. ^{1}H NMR (CDCl$_3$, 500 MHz, δ) 9.18-8.99 (br), 7.00-6.54 (br), 3.69-3.67 (br), 1.96-0.85 (br). $M_w = 40.4$ kDa, $M_n = 15.4$ kDa, $Đ = 2.6$. Anal. Calcd. for $C_{50}H_{72}N_2O_2$: C, 81.92; H, 9.90; N, 3.82; found: C, 72.02; H, 9.22; N, 3.40.

5.7.27 Synthesis of 118

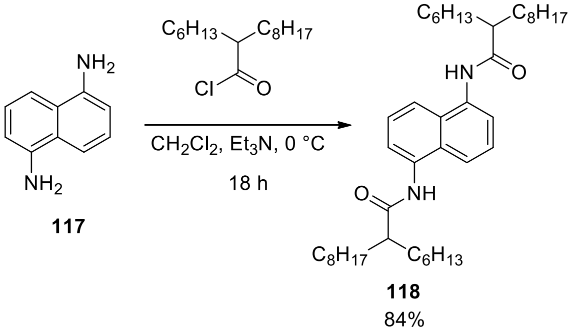

The synthesis of **118** was reproduced from a previous report.[139] In a flame dried flask, 2-hexyldecanoic (10.0 mL, 34.08 mmol) acid was stirred at 60 °C in thionyl chloride (20.0 mL) for 2.5 h under argon atmosphere. After cooling the mixture, excess thionyl chloride was removed under high vacuum. The isolated 2-hexyldecanoyl chloride was dissolved in dry CH_2Cl_2 (20.0 mL). In another flame dried flask, 1,5-diaminonapthalene (**117**) (2.67 g, 16.9 mmol) was suspended in dry CH_2Cl_2 (60.0 mL) under argon atmosphere, followed by an addition of triethylamine (5.50 mL, 39.4 mmol). The mixture was then cooled to 0 °C and the solution of 2-hexyldecanoyl chloride in CH_2Cl_2 was added dropwise. A yellow-white solid started precipitating out with addition of 2-hexyldecanoyl chloride. The mixture was slowly brought to room temperature and stirred for 18 h. The resulting white sludge was filtered using suction filtration and washed with minimal ethanol. The collected solid was dried under high vacuum to obtain the product (**118**) as a white powder (9.02 g, 84%). ^{1}H NMR ($CDCl_3$, 500 MHz, δ) 7.88 (d, J = 6.85 Hz, 2H), 7.68 (s, 2H), 7.57 (d, J = 8.15 Hz, 2H), 7.38 (t, J = 7.60 Hz, 2H), 2.35-2.45 (m, 2H), 1.74-1.85 (m, 4H), 1.19-1.50 (m, 48H), 0.82-0.93 (m, 12H). ^{13}C NMR ($CDCl_3$, 125 MHz, δ) 175.22, 132.96, 128.00, 126.04, 121.41, 118.04, 49.18, 33.57, 32.02, 31.93, 29.93, 29.69, 29.59, 29.45, 28.03, 28.00, 22.81, 22.78, 14.24. HRMS (m/z): ($M^{\bullet+}$) Cal. ($C_{42}H_{70}N_2O_2$): 634.54373 found: 634.54256. Anal. Calcd. for $C_{42}H_{70}N_2O_2$: C, 79.44; H, 11.11; N, 4.41; found: C, 79.03; H, 11.36; N, 4.51.

5.7.28 Synthesis of 119

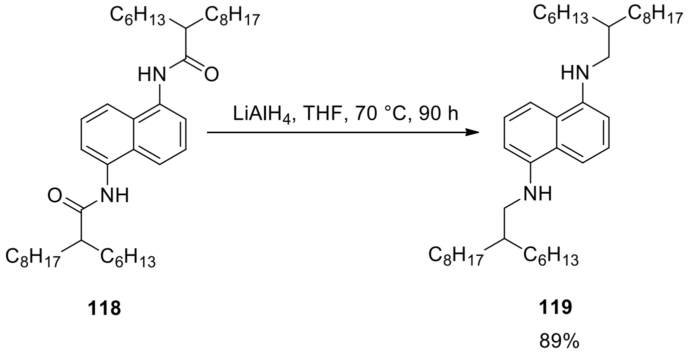

The synthesis of **119** was reproduced from a previous report.[139] To a suspension of compound **118** (4.62 g, 7.27 mmol), dry THF (75.0 mL), a solution of lithium aluminium hydride (2 M in THF) (14.9 mL, 29.8 mmol) was added dropwise. The reaction mixture was slowly brought to room temperature and refluxed for 90 h. After cooling the resulting mixture to 0 °C, an aqueous NaOH (0.3 M, 46 mL) solution was added dropwise to the solution. The crude sludge was filtered and washed with water. The solid was then dissolved in CH_2Cl_2, washed with 5% HCl, dried over Na_2SO_4. The solvent was removed under reduced pressure to yield the crude product which was purified by column chromatography on silica gel, eluting with a mixture of 30% EtOAc in hexanes to yield a yellow-red oil (**119**, 3.89 g, 89%). ^{1}H NMR ($CDCl_3$, 500 MHz, δ) 7.30 (t, *J* = 8.0 Hz, 2H), 7.12 (d, *J* = 8.4 Hz, 2H), 6.59 (d, *J* = 7.6 Hz, 2H), 4.39 (br, 2H), 3.16 (d, *J* = 6.1 Hz, 4H), 1.77 (sep, *J* = 6.0 Hz, 2H), 1.39-1.46 (m, 8H), 1.34-1.39 (m, 8H), 1.21-1.33 (m, 32H), 0.85-0.90 (m, 12H). ^{13}C NMR ($CDCl_3$, 125 MHz, δ) 144.56, 125.58, 124.09, 108.37, 104.20, 47.90, 37.75, 32.62, 32.05, 32.02, 30.22, 29.89, 29.75, 29.48, 26.95, 26.93, 22.83, 14.25. HRMS (m/z): ($M^{\bullet+}$) Cal. ($C_{42}H_{74}N_2$): 606.58520 found: 606.58473. Anal. Calcd. for $C_{42}H_{74}N_2$: C, 83.10; H, 12.29; N, 4.61; found: C, 83.31; H, 12.31; N, 4.41.

5.7.29 Synthesis of 120

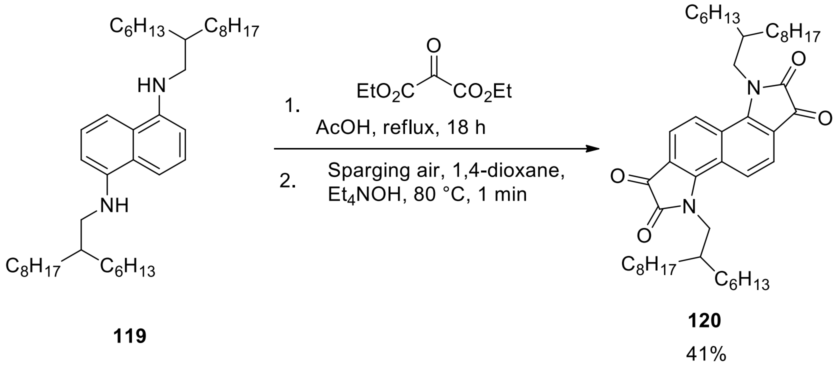

The synthesis of **120** was reproduced from a previous report.[139] Compound **119** (1.41 g, 2.22 mmol) was suspended in 50.0 mL of AcOH and heated to reflux under an argon atmosphere. In another Schlenk flask, diethylketomalonate (1.6 mL, 10.5 mmol) was dissolved in 20 mL of AcOH under an argon atmosphere and the resulting solution was added to the refluxing solution of **119** over 0.75 h. The resulting reaction mixture was degassed for 20 min. The mixture was then refluxed for 18 h. After cooling the reaction mixture, the solvent was removed using rotary evaporator to yield a brown sludge. This was dissolved in EtOAc and filtered through a silica pad. The filtrate was condensed and dissolved in 1,4-dioxane (50 mL); the resulting solution was left to stir vigorously in air. To this solution, 1.5 M tetraethylammonium hydroxide solution in methanol (7.50 mL, 11.3 mmol) was added quickly. Immediately followed by this addition, the reaction mixture was placed in an 80 °C oil bath. The reaction was monitored by TLC (30% EtOAc in hexanes) until (~1 min) the isolated intermediate was completely consumed. The reaction mixture was then quickly quenched with cold HCl (10% v/v, 50.0 mL) The resulting product is unstable in basic conditions, therefore, it must not be left in a basic solution longer than required. The organic layer was extracted with EtOAc (3 × 30 mL). The organic layers were combined, washed with water, and dried over Na_2SO_4. The solvent was removed and the resulting crude was purified by column chromatography on silica gel, eluting with a mixture of 30% EtOAc in hexanes to yield a dark-blue solid (**120**) (670 mg, 41%). ^1H NMR ($CDCl_3$, 500 MHz, δ) 7.99 (d, *J* = 8.66 Hz, 2H), 7.66 (d, *J* = 8.66 Hz, 2H), 4.16 (d, *J* = 7.40 Hz, 4H), 1.87-1.94 (m, 2H), 1.31-142 (m, 8H), 1.16-1.31 (m, 40H), 0.80-0.92 (m, 12H). ^{13}C NMR ($CDCl_3$, 125 MHz, δ) 182.89, 159.41, 152.50, 127.55, 120.22, 120.10, 116.45, 47.70, 37.68, 31.98, 31.84, 31.17, 30.09, 29.85, 29.75, 29.61, 29.39, 26.31, 26.26, 22.80, 22.74, 14.26, 14.21. HRMS (m/z): ($M^{\bullet+}$) Cal. ($C_{46}H_{70}N_2O_4$): 714.53356 found: 714.53246. Anal. Calcd. for $C_{46}H_{70}N_2O_4$: C, 77.27; H, 9.89; N, 3.92; found: C, 77.21; H, 10.04; N, 3.90.

5.7.30 Synthesis of 121

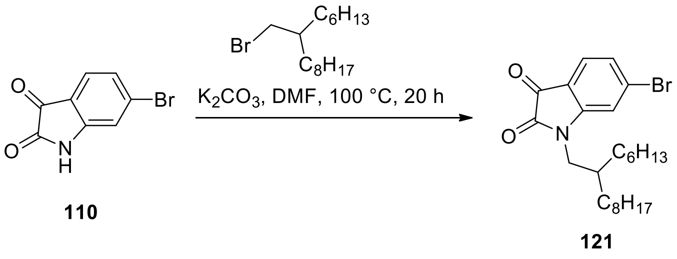

110

121

37%

The synthesis of **121** was reproduced from a previous report.[139] Compound **110** (3.02 g, 13.3 mmol) was dissolved in 50.0 mL of dry DMF which was followed by an addition of 2-hexyldecyl bromide (4.15 g, 13.6 mmol) and anhydrous potassium carbonate (2.12 g, 15.3 mmol). The resulting mixture was stirred at 100 °C for 20 h. The reaction mixture was then collected over 50.0 mL ice-water. The organic layer was extracted with 100 mL Et_2O, washed with water (5 × 50 mL) and brine (1 × 50 mL), dried over Na_2SO_4. The solvent was then removed under reduced pressure to yield a brown sludge which was purified by column chromatography on silica gel, eluting with a mixture of 10% EtOAc in hexanes to yield a dark-red solid (**121**) (2.28 g, 37%). ^{1}H NMR ($CDCl_3$, 500 MHz, δ) 7.46 (d, J = 8.0 Hz, 1H), 7.27 (d, J = 8.0 Hz, 1H), 7.02 (s, 1H), 3.57 (d, J = 3.57, 2H), 1.80-1.88 (m, 1H), 1.52-1.61 (m, 1H), 1.20-1.40 (m, 25H), 0.87 (t, J = 6.9 Hz, 6H). ^{13}C NMR ($CDCl_3$, 125 MHz, δ) 182.47, 158.46, 152.46, 133.63, 126.92, 126.47, 116.42, 114.14, 45.06, 36.11, 32.00, 31.91, 31.57, 30.07, 29.74, 29.66, 29.41, 26.43, 26.39, 22.81, 22.78, 14.25, 14.22. HRMS (m/z) ($M^{\bullet+}$): Cal. ($C_{24}H_{36}BrNO_2$): 449.19294 found: 449.19246. Anal. Calcd. for $C_{24}H_{36}NO_2Br$: C, 73.07; H, 9.20; N, 3.55; found: C, 73.29; H, 9.37; N, 3.63.

5.7.31 Synthesis of 122

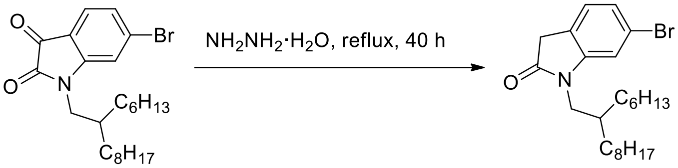

121

122
77%

The synthesis of **122** was reproduced from a previous report.[139] Compound **121** (940 mg, 2.22 mmol) was suspended in 10 mL of hydrazine hydrate and refluxed under a N_2 atmosphere for 40 h. The resulting mixture was collected over ice-water and the organic layer was extracted with CH_2Cl_2 (2 × 30 mL). The organic layers were combined, washed with water, and dried over Na_2SO_4. The solvent was removed under reduced pressure to yield a viscous brown oil (**122**, 689 mg, 77%) which was further dried under high vacuum. The obtained product was used without any further purification. ^{1}H NMR ($CDCl_3$, 500 MHz, δ) 7.15 (d, *J* = 7.8 Hz, 1H), 7.09 (d, *J* = 7.8 Hz, 1H), 6.92 (s, 1H), 3.55 (d, *J* = 7.5 Hz, 2H), 3.46 (s, 2H), 1.80-1.88 (m, 1H), 1.20-1.44 (m, 34H), 0.88 (t, *J* = 7.2 Hz, 8H). ^{13}C NMR ($CDCl_3$, 125 MHz, δ) 175.19, 171.31, 146.62, 125.71, 124.93, 123.53, 121.43, 112.43, 65.91, 60.54, 44.78, 40.69, 36.03, 35.46, 32.02, 31.94, 31.09, 30.12, 29.79, 29.67, 29.43, 26.51, 26.47, 14.25. HRMS (m/z) ($M^{\bullet+}$): Cal. ($C_{24}H_{38}BrNO$): 435.21368 found: 435.21485.

5.7.32 Synthesis of 123

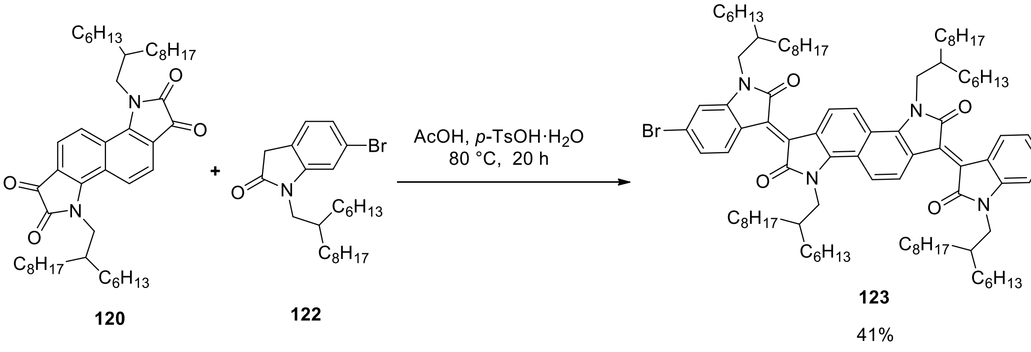

The synthesis of **123** was reproduced from a previous report.[139] Compound **120** (150 mg, 0.209 mmol) and compound **122** (201 mg, 0.461 mmol) were suspended in 15.0 mL of glacial acetic acid under argon atmosphere. To the resulting mixture, *p*-toluene sulfonic acid monohydrate (10.0 mg) was added and the mixture was then heated to 80 °C and stirred for 20 h. The reaction mixture was cooled and poured onto ice-water (50 mL). The aqueous mixture was filtered by suction, washed with water and acetone. The obtained product was dried under high vacuum to yield the desired product as a waxy brown solid (**123**,135 mg, 41%). ^{1}H NMR ($CDCl_3$, 500 MHz, δ) 8.94-9.01 (m, 4H) 7.84 (d, *J* = 9.3 Hz, 2H), 7.17 (d, *J* = 8.5 Hz, 2H), 6.91 (s, 2H), 4.23 (d, *J* = 7.20 Hz, 4H), 3.65 (d, *J* = 7.40 Hz, 4H), 1.99-2.09 (m, 2H), 1.86-1.96 (m, 2H), 1.08-1.45 (m, 96H), 0.77-0.93 (m, 24H). ^{13}C NMR ($CDCl_3$, 125 MHz, δ) 170.03, 168.06, 146.47, 143.53, 132.73, 132.70, 130.50, 127.03, 125.23, 124.51, 123.51, 120.97, 120.24, 117.41, 111.80, 47.47, 44.93, 37.50, 36.29, 32.02, 31.95, 31.90, 31.70, 31.19, 30.22, 30.14, 29.86, 29.80, 29.70, 29.65, 29.43, 26.59, 26.53, 26.24, 22.81, 22.78, 22.74, 14.23. HRMS (m/z): ($M^{\bullet+}$) Cal. ($C_{94}H_{142}Br_2N_4O_4$): 1548.93978 found: 1548.94600. Anal. Calcd. for $C_{94}H_{142}N_4O_4Br_2$: C, 72.75; H, 9.22; N, 3.61; found: C, 60.19; H, 8.41; N, 3.12.

5.7.33 Synthesis of 126

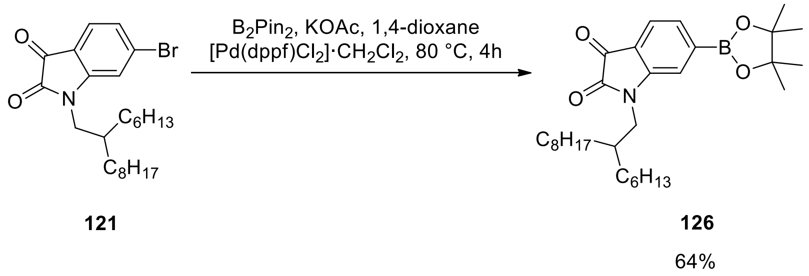

The synthesis of **126** was reproduced from a previous report.[139] Compound **121** (316 mg, 0.701 mmol) was dissolved in 5.0 mL 1,4-dioxane. To the resulting mixture, bis(pinacolato)diboron (216 mg, 0.858 mmol), [Pd(dppf)Cl_2]·CH_2Cl_2 (54.0 mg, 0.060 mmol), and KOAc (213 mg, 2.15 mmol) were added. The mixture was then heated to 80 °C and stirred for 4 h. The solution was cooled and poured onto ice-water (20 mL). The organic layer was extracted with EtOAC, washed with water, dried over Na_2SO_4 and condensed to yield brown-orange solid (**126**), which was dried under high vacuum (223 mg, 64%). ^{1}H NMR ($CDCl_3$, 500 MHz, δ) 7.55 (q, *J* = 6.7 Hz, 2H), 7.24 (s, 1H), 3.61 (d, *J* = 7.4 Hz, 2H), 1.85-1.93 (m, 1H), 1.56-1.60 (m, 1H), 1.18-1.43 (m, 40H), 0.87 (t, *J* = 6.8Hz, 8H). ^{13}C NMR ($CDCl_3$, 125 MHz, δ) 184.36, 158.54, 150.59, 130.15, 124.20, 119.47, 115.72, 84.76, 83.60, 44.75, 36.01, 31.99, 31.90, 31.64, 31.62, 30.03, 24.98, 14.20. HRMS (m/z) ($M^{\bullet+}$): Cal. ($C_{30}H_{48}BNO_4$): 497.36764 found: 497.36780. Anal. Calcd. for $C_{30}H_{48}NO_4B$: C, 72.42; H, 9.72; N, 2.82; found: C, 70.23; H, 10.19; N, 2.35.

5.7.34 Synthesis of 127

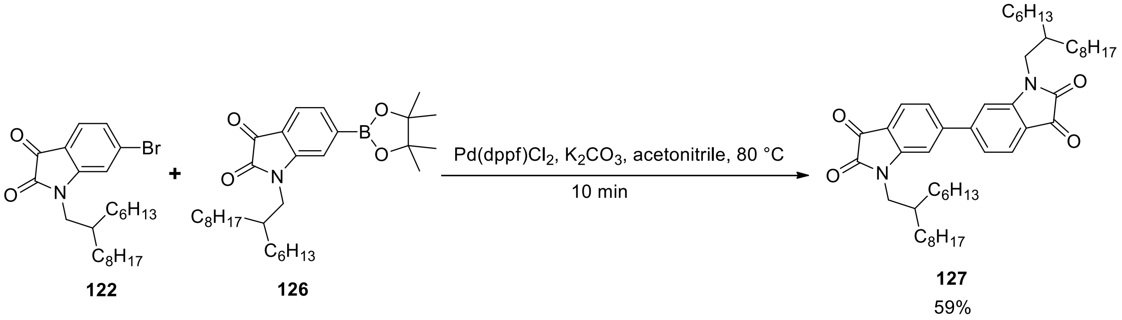

The synthesis of **127** was reproduced from a previous report.[139] Compound **122** (206 mg, 0.457 mmol) and **126** (223 mg, 0.448 mmol) were dissolved in acetonitrile (10.0 mL). K_2CO_3 (124 mg, 0.897 mmol) was dissolved in minimal H_2O, and the solution was degassed for 15 min. The aqueous solution of K_2CO_3 was added to the previous solution in acetonitrile and the resulting solution was degassed again for 30 min. After adding $[Pd(dppf)Cl_2]\cdot CH_2Cl_2$ (25 mg, 0.031 mmol), the reaction mixture was heated to 80 °C and stirred for 10 min. After cooling the reaction mixture, the organic layer was extracted with EtOAC, washed with water and brine, and dried over Na_2SO_4. The solvent was removed under reduced pressure to yield a brown crude which was purified by column chromatography on silica gel, eluting with a mixture of 25% EtOAc in hexanes. The collected pure fractions were condensed under reduced pressure and dried under high vacuum to obtain the desired product as an orange solid (**127**) (194 mg, 59%). ^{1}H NMR ($CDCl_3$, 500 MHz, δ) 7.72 (d, *J* = 7.7 Hz, 2H,), 7.30 (d, *J* = 7.7 Hz, 2H), 7.00 (s, 2H), 3.66 (d, *J* = 7.4 Hz, 4H), 1.84-1.93 (m, 2H), 1.18-1.42 (m, 57 H), 0.81-0.90, (m, 14 H). ^{13}C NMR ($CDCl_3$, 125 MHz, δ) 182.93, 158.59, 152.22, 149.65, 126.09, 122.78, 117.68, 109.20, 77.42, 77.16, 76.91, 44.90, 36.34, 31.96, 31.89, 31.87, 31.63, 30.10, 29.76, 29.66, 29.41, 26.55, 26.51, 22.80, 22.75, 22.72, 14.21, 14.18. HRMS (m/z) ($M^{\bullet+}$): Cal. ($C_{48}H_{72}N_2O_4$): 740.54921 found: 740.55050. Anal. Calcd. for $C_{48}H_{72}N_2O_4$: C, 77.79; H, 9.79; N, 3.78; found: C, 77.23; H, 9.95; N, 3.57.

5.7.35 Synthesis of 128

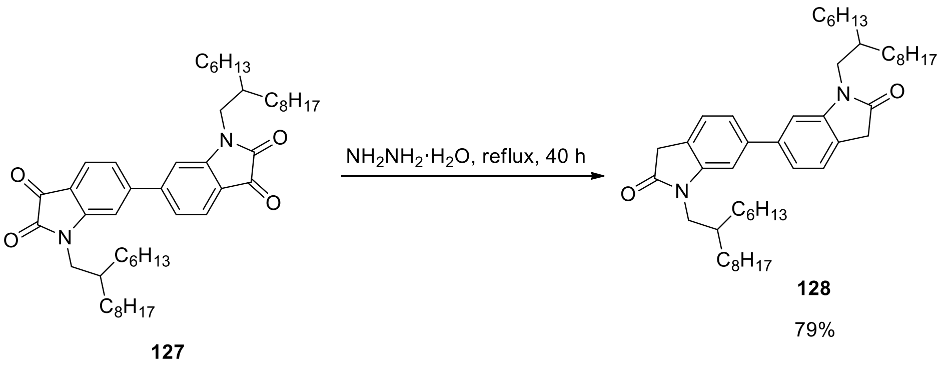

127

128

79%

Compound **127** (1.21 g, 1.63 mmol) was suspended in 50 mL of hydrazine monohydrate and heated to reflux for 40 h. After cooling the mixture down to room temperature, the organic layer was extracted with dichloromethane (2 × 40 mL). The organic layer was washed with water (5 × 50 mL) and brine (1 × 50 mL), dried over anhydrous $MgSO_4$, and finally condensed to yield a brown oil. The oil was precipitated in a mixture 25% hexanes in isopropanol to yield a gray solid. This was isolated by vacuum filtration to yield **128** (921 mg, 79%). ^{1}H NMR ($CDCl_3$, 600 MHz, δ) 7.32 (d, *J* = 7.68 Hz, 1H), 7.21 (d, *J* = 7.23 Hz, 1H), 6.96 (s, 1H), 3.64 (d, *J* = 7.44 Hz, 2H), 3.57 (s, 1H), 1.91-1.89 (s, 1H), 1.32-1.21 (m, 24H), 0.86-0.83 (m, 6H). ^{13}C NMR ($CDCl_3$, 150 MHz, δ): 175.56, 145.90, 141.52, 147.76, 124.09, 121.10, 107.61, 44.67, 36.30, 35.70, 32.01, 31.97, 31.76, 30.20, 29.87, 29.72, 29.47, 27.23, 26.69, 26.64, 22.81, 16.04, 14.26, 14.23. HRMS (*m/z*): ($M^{\bullet+}$) Cal. ($C_{48}H_{76}N_2O_2$): 712.59068 found: 712.59158. Anal. Calcd. for $C_{48}H_{76}N_2O_2$: C, 80.8; H, 10.7; N, 3.9; found: C, 80.2; H, 10.4; N, 4.4.

5.7.36 Synthesis of 109

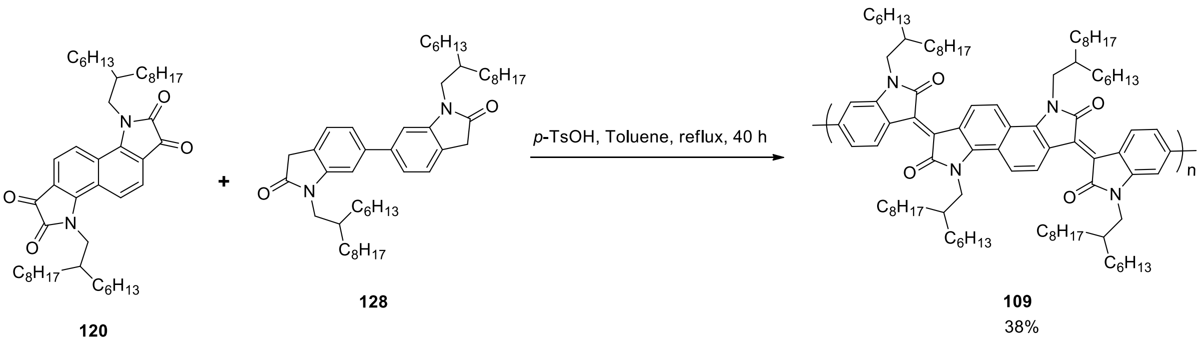

To a solution of **120** (60.9 mg, 0.0853), and **128** (61.1 mg, 0.0853 mmol) in 10.0 mL dry toluene, *p*-toluene sulfonic acid was added (5 mg, 0.03 mmol). The solution was refluxed for 40 h with a Dean-Stark apparatus to distill out the water generated over the course of reaction. The resulting suspension was cooled to room temperature and precipitated in cold methanol (50.0 mL). The precipitate was filtered off and then washed by sequential Soxhlet extraction with methanol (24 h), acetone (24 h), and hexanes (12 h). The remaining insoluble fraction was extracted in chloroform and precipitated from methanol. The precipitate was isolated by vacuum filtration and dried under high vacuum to yield polybisisoindigo as a dark green solid (**109**, 45 mg, 38%). M_w = 38.0 kDa, M_n = 15.5 kDa, *Đ* = 2.4. ^{1}H NMR ($CDCl_3$, 500 MHz, δ) 9.16 (brs), 8.89-8.79 (brd), 7.67 (brs), 7.08-6.90 (br), 5.14-5.12 (brs), 4.72-3.63 (br), 1.99-0.67 (br). M_w = 38.0 kDa, M_n = 15.5 kDa, *Đ* = 2.4. Anal. Calcd. for $C_{50}H_{72}N_2O_2$: C, 81.10; H, 10.28; N, 4.02; found: C, 80.88; H, 9.97; N, 4.14.

5.8 Crystallographic Data of 91

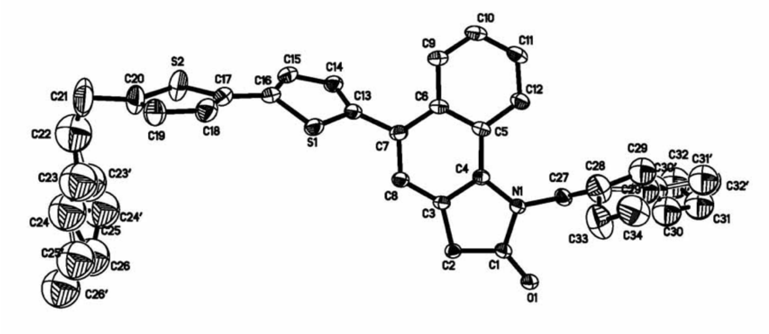

Figure 5.1(b) Structure and numbering of atoms of **91** for crystal and structural refinement data. The one half of the molecule is presented as the structure is centrosymmetric.

Table 5.1 Crystal and Structural Refinement Data for Compound **91**.

	Compound **91**	
Empirical formula	$C_{68}H_{78}N_2O_2S_4$	
Formula weight	1083.56	
Temperature / K	173(2)	
Wavelength / Å	0.71073	
Crystal system	Triclinic	
Space group	*P*-1	
Unit cell dimensions	*a* / Å = 6.0240(2)	α / ° = 78.658(2)
	b / Å = 12.4238(4)	β / ° = 86.669(2)
	c / Å = 20.2310(6)	γ /° = 78.084(2)
Volume / $Å^3$	1452.31(8)	
Z	1	
Density (calculated) / mg m^{-3}	1.239	
Absorption coefficient / mm^{-1}	0.211	
Crystal size	0.420 × 0.210 × 0.120 mm^3	
Theta range for data collection / °	1.706 to 27.543	
Reflections collected	33415	
Independent reflections	6642 [R(int) = 0.0316]	
Completeness to theta = 25.242°	99.5 %	
Absorption correction	Multi-scan	
Refinement method	Full-matrix least-squares on F^2	

Table 5.1 (continued).

Data / restraints / parameters	6642 / 113 / 342	
Goodness-of-fit on F^2	1.039	
R_1 [$I > 2\sigma(I)$][a]	0.0956	
wR_2 (all data)	= 0.2978	
Extinction coefficient	n/a	
Largest diff. peak and hole, $\Delta\rho_{elect}$ / e Å^{-3}	1.736 and -0.821	

[a] $R_1 = [\Sigma||F_o|-|F_c||]/[\Sigma|F_o|]$ for $[F_o^2 > 2\sigma(F_o^2)]$, $wR_2 = \{[\Sigma w(F_o^2 - F_c^2)^2]/[\Sigma w(F_o^2 - F_c^2)^2]/[\Sigma w(F_o^2)^2]\}^{1/2}$ [all data].

Table 5.2 Atomic coordinates ($\times 10^4$) and equivalent isotropic displacement parameters ($Å^2 \times 10^3$) for compound **91**. U(eq) is defined as one third of the trace of the orthogonalized U^{ij} tensor.

	x	y	z	U(eq)
S(1)	5808(1)	8876(1)	6144(1)	32(1)
S(2)	4330(3)	9682(1)	8129(1)	59(1)
O(1)	9675(5)	4213(2)	3864(1)	42(1)
N(1)	6390(4)	5452(2)	3965(1)	24(1)
C(1)	8525(5)	4876(3)	4178(2)	26(1)
C(2)	9026(5)	5231(2)	4816(2)	21(1)
C(3)	7021(5)	6096(2)	4912(2)	21(1)
C(4)	5480(5)	6196(2)	4397(2)	23(1)
C(5)	3365(5)	6973(3)	4348(2)	24(1)
C(6)	2827(5)	7648(3)	4855(2)	25(1)
C(7)	4390(5)	7523(3)	5383(2)	26(1)
C(8)	6442(5)	6782(3)	5397(2)	24(1)
C(9)	748(6)	8440(3)	4817(2)	30(1)
C(10)	-751(6)	8566(3)	4317(2)	33(1)
C(11)	-257(6)	7902(3)	3825(2)	34(1)
C(12)	1739(6)	7132(3)	3833(2)	30(1)
C(13)	3863(5)	8145(3)	5948(2)	27(1)
C(14)	2097(6)	8166(3)	6406(2)	32(1)
C(15)	2333(6)	8761(3)	6918(2)	34(1)
C(16)	4248(6)	9195(3)	6852(2)	32(1)
C(17)	5169(7)	9800(3)	7289(2)	36(1)
C(18)	6828(8)	10405(4)	7148(2)	45(1)
C(19)	7473(9)	10778(4)	7716(3)	54(1)
C(20)	6289(10)	10451(5)	8284(3)	61(1)
C(21)	6483(15)	10681(6)	8984(3)	92(2)
C(22)	7390(17)	9625(9)	9466(5)	122(2)
C(23)	9750(30)	9100(20)	9305(15)	124(2)
C(23')	9400(20)	8764(12)	9341(10)	124(2)
C(24)	10480(50)	8070(20)	9820(17)	127(2)

Table 5.2 (continued).

	x	y	z	U(eq)
C(24')	10320(30)	7864(15)	9912(10)	127(2)
C(25)	9290(40)	7149(19)	9791(15)	131(3)
C(25')	12640(30)	7356(15)	9701(9)	132(3)
C(26)	11510(40)	6409(18)	9987(14)	133(3)
C(26')	13580(30)	6524(16)	10183(9)	136(4)
C(27)	5380(6)	5127(3)	3415(2)	30(1)
C(28)	5627(10)	5860(5)	2717(3)	63(1)
C(29)	4141(18)	5552(9)	2219(5)	66(2)
C(29')	4910(20)	5237(10)	2205(6)	70(2)
C(30)	5330(20)	4445(9)	2016(7)	77(2)
C(30')	3740(20)	4228(10)	2325(6)	76(2)
C(31)	4030(20)	3705(12)	1726(6)	82(2)
C(31')	2940(30)	4144(12)	1634(5)	84(2)
C(32)	2230(20)	3321(12)	2237(7)	95(3)
C(32')	1760(30)	3053(14)	1824(9)	91(3)
C(33)	7861(11)	6107(6)	2532(3)	75(2)
C(34)	8047(11)	6927(6)	1891(3)	77(2)

Table 5.3 Bond lengths [Å] and angles [°] compound **91**.

S(1)-C(13)	1.729(3)
S(1)-C(16)	1.733(4)
S(2)-C(17)	1.730(4)
S(2)-C(20)	1.741(5)
O(1)-C(1)	1.218(4)
N(1)-C(1)	1.384(4)
N(1)-C(4)	1.404(4)
N(1)-C(27)	1.460(4)
C(1)-C(2)	1.508(4)
C(2)-C(2)#1	1.385(6)
C(2)-C(3)	1.473(4)
C(3)-C(8)	1.406(4)
C(3)-C(4)	1.406(4)
C(4)-C(5)	1.427(4)
C(5)-C(12)	1.429(5)
C(5)-C(6)	1.430(5)
C(6)-C(9)	1.419(4)
C(6)-C(7)	1.430(5)
C(7)-C(8)	1.379(4)
C(7)-C(13)	1.486(5)
C(8)-H(8)	0.95
C(9)-C(10)	1.359(5)
C(9)-H(9)	0.95
C(10)-C(11)	1.396(6)
C(10)-H(10)	0.95

Table 5.3 (continued).

C(11)-C(12)	1.372(5)
C(11)-H(11)	0.95
C(12)-H(12)	0.95
C(13)-C(14)	1.369(5)
C(14)-C(15)	1.416(5)
C(14)-H(14)	0.95
C(15)-C(16)	1.361(5)
C(15)-H(15)	0.95
C(16)-C(17)	1.465(5)
C(17)-C(18)	1.356(6)
C(18)-C(19)	1.421(6)
C(18)-H(18)	0.95
C(19)-C(20)	1.354(8)
C(19)-H(19)	0.95
C(20)-C(21)	1.515(7)
C(21)-C(22)	1.494(12)
C(21)-H(21A)	0.99
C(21)-H(21B)	0.99
C(22)-C(23)	1.485(9)
C(22)-C(23')	1.486(8)
C(22)-H(22A)	0.99
C(22)-H(22B)	0.99
C(22)-H(22C)	0.99
C(22)-H(22D)	0.99
C(23)-C(24)	1.485(9)

Table 5.3 (continued).

C(23)-H(23A)	0.99
C(23)-H(23B)	0.99
C(23')-C(24')	1.485(8)
C(23')-H(23C)	0.99
C(23')-H(23D)	0.99
C(24)-C(25)	1.485(9)
C(24)-H(24A)	0.99
C(24)-H(24B)	0.99
C(24')-C(25')	1.485(9)
C(24')-H(24C)	0.99
C(24')-H(24D)	0.99
C(25)-C(26)	1.484(9)
C(25)-H(25A)	0.99
C(25)-H(25B)	0.99
C(25')-C(26')	1.33(2)
C(25')-H(25C)	0.99
C(25')-H(25D)	0.99
C(26)-H(26A)	0.98
C(26)-H(26B)	0.98
C(26)-H(26C)	0.98
C(26')-H(26D)	0.98
C(26')-H(26E)	0.98
C(26')-H(26F)	0.98
C(27)-C(28)	1.539(7)
C(27)-H(27A)	0.99

Table 5.3 (continued).

C(27)-H(27B)	0.99
C(28)-C(33)	1.454(8)
C(28)-C(29)	1.535(6)
C(28)-C(29')	1.538(6)
C(28)-H(28A)	1
C(28)-H(28B)	1
C(29)-C(30)	1.536(6)
C(29)-H(29A)	0.99
C(29)-H(29B)	0.99
C(29')-C(30')	1.533(6)
C(29')-H(29C)	0.99
C(29')-H(29D)	0.99
C(30)-C(31)	1.539(6)
C(30)-H(30A)	0.99
C(30)-H(30B)	0.99
C(30')-C(31')	1.535(6)
C(30')-H(30C)	0.99
C(30')-H(30D)	0.99
C(31)-C(32)	1.536(6)
C(31)-H(31A)	0.99
C(31)-H(31B)	0.99
C(31')-C(32')	1.630(19)
C(31')-H(31C)	0.99
C(31')-H(31D)	0.99
C(32)-H(32A)	0.98

Table 5.3 (continued).

C(32)-H(32B)	0.98
C(32)-H(32C)	0.98
C(32')-H(32D)	0.98
C(32')-H(32E)	0.98
C(32')-H(32F)	0.98
C(33)-C(34)	1.498(8)
C(33)-H(33A)	0.99
C(33)-H(33B)	0.99
C(34)-H(34A)	0.98
C(34)-H(34B)	0.98
C(34)-H(34C)	0.98
C(13)-S(1)-C(16)	92.11(17)
C(17)-S(2)-C(20)	91.5(2)
C(1)-N(1)-C(4)	109.7(3)
C(1)-N(1)-C(27)	118.6(3)
C(4)-N(1)-C(27)	131.2(3)
O(1)-C(1)-N(1)	121.3(3)
O(1)-C(1)-C(2)	130.3(3)
N(1)-C(1)-C(2)	108.4(3)
C(2)#1-C(2)-C(3)	133.0(4)
C(2)#1-C(2)-C(1)	123.5(3)
C(3)-C(2)-C(1)	103.5(2)
C(8)-C(3)-C(4)	118.6(3)
C(8)-C(3)-C(2)	132.7(3)
C(4)-C(3)-C(2)	108.7(3)

Table 5.3 (continued).

N(1)-C(4)-C(3)	109.5(3)
N(1)-C(4)-C(5)	128.2(3)
C(3)-C(4)-C(5)	122.2(3)
C(4)-C(5)-C(12)	125.2(3)
C(4)-C(5)-C(6)	117.5(3)
C(12)-C(5)-C(6)	117.3(3)
C(9)-C(6)-C(7)	121.3(3)
C(9)-C(6)-C(5)	118.9(3)
C(7)-C(6)-C(5)	119.7(3)
C(8)-C(7)-C(6)	120.5(3)
C(8)-C(7)-C(13)	117.2(3)
C(6)-C(7)-C(13)	122.2(3)
C(7)-C(8)-C(3)	121.4(3)
C(7)-C(8)-H(8)	119.3
C(3)-C(8)-H(8)	119.3
C(10)-C(9)-C(6)	121.9(3)
C(10)-C(9)-H(9)	119.1
C(6)-C(9)-H(9)	119.1
C(9)-C(10)-C(11)	119.7(3)
C(9)-C(10)-H(10)	120.1
C(11)-C(10)-H(10)	120.1
C(12)-C(11)-C(10)	120.8(3)
C(12)-C(11)-H(11)	119.6
C(10)-C(11)-H(11)	119.6
C(11)-C(12)-C(5)	121.3(3)

Table 5.3 (continued).

C(11)-C(12)-H(12)	119.4
C(5)-C(12)-H(12)	119.4
C(14)-C(13)-C(7)	129.8(3)
C(14)-C(13)-S(1)	110.9(3)
C(7)-C(13)-S(1)	119.0(2)
C(13)-C(14)-C(15)	112.7(3)
C(13)-C(14)-H(14)	123.6
C(15)-C(14)-H(14)	123.6
C(16)-C(15)-C(14)	113.7(3)
C(16)-C(15)-H(15)	123.1
C(14)-C(15)-H(15)	123.1
C(15)-C(16)-C(17)	130.6(4)
C(15)-C(16)-S(1)	110.5(3)
C(17)-C(16)-S(1)	118.8(3)
C(18)-C(17)-C(16)	128.6(4)
C(18)-C(17)-S(2)	111.0(3)
C(16)-C(17)-S(2)	120.1(3)
C(17)-C(18)-C(19)	113.5(4)
C(17)-C(18)-H(18)	123.2
C(19)-C(18)-H(18)	123.2
C(20)-C(19)-C(18)	112.8(4)
C(20)-C(19)-H(19)	123.6
C(18)-C(19)-H(19)	123.6
C(19)-C(20)-C(21)	128.5(6)
C(19)-C(20)-S(2)	111.2(3)

Table 5.3 (continued).

C(21)-C(20)-S(2)	120.3(5)
C(22)-C(21)-C(20)	111.0(6)
C(22)-C(21)-H(21A)	109.4
C(20)-C(21)-H(21A)	109.4
C(22)-C(21)-H(21B)	109.4
C(20)-C(21)-H(21B)	109.4
H(21A)-C(21)-H(21B)	108
C(23)-C(22)-C(21)	113.5(13)
C(23')-C(22)-C(21)	125.5(10)
C(23)-C(22)-H(22A)	108.9
C(21)-C(22)-H(22A)	108.9
C(23)-C(22)-H(22B)	108.9
C(21)-C(22)-H(22B)	108.9
H(22A)-C(22)-H(22B)	107.7
C(23')-C(22)-H(22C)	105.9
C(21)-C(22)-H(22C)	105.9
C(23')-C(22)-H(22D)	105.9
C(21)-C(22)-H(22D)	105.9
H(22C)-C(22)-H(22D)	106.3
C(22)-C(23)-C(24)	108.7(19)
C(22)-C(23)-H(23A)	109.9
C(24)-C(23)-H(23A)	109.9
C(22)-C(23)-H(23B)	109.9
C(24)-C(23)-H(23B)	109.9
H(23A)-C(23)-H(23B)	108.3

Table 5.3 (continued).

C(24')-C(23')-C(22)	118.8(14)
C(24')-C(23')-H(23C)	107.6
C(22)-C(23')-H(23C)	107.6
C(24')-C(23')-H(23D)	107.6
C(22)-C(23')-H(23D)	107.6
H(23C)-C(23')-H(23D)	107
C(25)-C(24)-C(23)	114(2)
C(25)-C(24)-H(24A)	108.7
C(23)-C(24)-H(24A)	108.7
C(25)-C(24)-H(24B)	108.7
C(23)-C(24)-H(24B)	108.7
H(24A)-C(24)-H(24B)	107.6
C(25')-C(24')-C(23')	106.6(15)
C(25')-C(24')-H(24C)	110.4
C(23')-C(24')-H(24C)	110.4
C(25')-C(24')-H(24D)	110.4
C(23')-C(24')-H(24D)	110.4
H(24C)-C(24')-H(24D)	108.6
C(26)-C(25)-C(24)	84.6(17)
C(26)-C(25)-H(25A)	114.5
C(24)-C(25)-H(25A)	114.5
C(26)-C(25)-H(25B)	114.5
C(24)-C(25)-H(25B)	114.5
H(25A)-C(25)-H(25B)	111.7
C(26')-C(25')-C(24')	110.2(16)

Table 5.3 (continued).

C(26')-C(25')-H(25C)	109.6
C(24')-C(25')-H(25C)	109.6
C(26')-C(25')-H(25D)	109.6
C(24')-C(25')-H(25D)	109.6
H(25C)-C(25')-H(25D)	108.1
C(25)-C(26)-H(26A)	109.5
C(25)-C(26)-H(26B)	109.5
H(26A)-C(26)-H(26B)	109.5
C(25)-C(26)-H(26C)	109.5
H(26A)-C(26)-H(26C)	109.5
H(26B)-C(26)-H(26C)	109.5
C(25')-C(26')-H(26D)	109.5
C(25')-C(26')-H(26E)	109.5
H(26D)-C(26')-H(26E)	109.5
C(25')-C(26')-H(26F)	109.5
H(26D)-C(26')-H(26F)	109.5
H(26E)-C(26')-H(26F)	109.5
N(1)-C(27)-C(28)	114.7(3)
N(1)-C(27)-H(27A)	108.6
C(28)-C(27)-H(27A)	108.6
N(1)-C(27)-H(27B)	108.6
C(28)-C(27)-H(27B)	108.6
H(27A)-C(27)-H(27B)	107.6
C(33)-C(28)-C(29)	122.5(7)
C(33)-C(28)-C(29')	109.7(7)

Table 5.3 (continued).

C(33)-C(28)-C(27)	116.7(5)
C(29)-C(28)-C(27)	108.5(6)
C(29')-C(28)-C(27)	105.8(6)
C(33)-C(28)-H(28A)	101.8
C(29)-C(28)-H(28A)	101.8
C(27)-C(28)-H(28A)	101.8
C(33)-C(28)-H(28B)	108.1
C(29')-C(28)-H(28B)	108.1
C(27)-C(28)-H(28B)	108.1
C(28)-C(29)-C(30)	109.2(8)
C(28)-C(29)-H(29A)	109.8
C(30)-C(29)-H(29A)	109.8
C(28)-C(29)-H(29B)	109.8
C(30)-C(29)-H(29B)	109.8
H(29A)-C(29)-H(29B)	108.3
C(30')-C(29')-C(28)	129.6(10)
C(30')-C(29')-H(29C)	104.9
C(28)-C(29')-H(29C)	104.9
C(30')-C(29')-H(29D)	104.9
C(28)-C(29')-H(29D)	104.9
H(29C)-C(29')-H(29D)	105.8
C(29)-C(30)-C(31)	122.1(10)
C(29)-C(30)-H(30A)	106.8
C(31)-C(30)-H(30A)	106.8
C(29)-C(30)-H(30B)	106.8

Table 5.3 (continued).

C(31)-C(30)-H(30B)	106.8
H(30A)-C(30)-H(30B)	106.7
C(29')-C(30')-C(31')	106.3(9)
C(29')-C(30')-H(30C)	110.5
C(31')-C(30')-H(30C)	110.5
C(29')-C(30')-H(30D)	110.5
C(31')-C(30')-H(30D)	110.5
H(30C)-C(30')-H(30D)	108.7
C(32)-C(31)-C(30)	110.3(11)
C(32)-C(31)-H(31A)	109.6
C(30)-C(31)-H(31A)	109.6
C(32)-C(31)-H(31B)	109.6
C(30)-C(31)-H(31B)	109.6
H(31A)-C(31)-H(31B)	108.1
C(30')-C(31')-C(32')	101.7(9)
C(30')-C(31')-H(31C)	111.4
C(32')-C(31')-H(31C)	111.4
C(30')-C(31')-H(31D)	111.4
C(32')-C(31')-H(31D)	111.4
H(31C)-C(31')-H(31D)	109.3
C(31)-C(32)-H(32A)	109.5
C(31)-C(32)-H(32B)	109.5
H(32A)-C(32)-H(32B)	109.5
C(31)-C(32)-H(32C)	109.5
H(32A)-C(32)-H(32C)	109.5

Table 5.3 (continued).

H(32B)-C(32)-H(32C)	109.5
C(31')-C(32')-H(32D)	109.5
C(31')-C(32')-H(32E)	109.5
H(32D)-C(32')-H(32E)	109.5
C(31')-C(32')-H(32F)	109.5
H(32D)-C(32')-H(32F)	109.5
H(32E)-C(32')-H(32F)	109.5
C(28)-C(33)-C(34)	116.8(5)
C(28)-C(33)-H(33A)	108.1
C(34)-C(33)-H(33A)	108.1
C(28)-C(33)-H(33B)	108.1
C(34)-C(33)-H(33B)	108.1
H(33A)-C(33)-H(33B)	107.3
C(33)-C(34)-H(34A)	109.5
C(33)-C(34)-H(34B)	109.5
H(34A)-C(34)-H(34B)	109.5
C(33)-C(34)-H(34C)	109.5
H(34A)-C(34)-H(34C)	109.5
H(34B)-C(34)-H(34C)	109.5

Note: Symmetry transformations used to generate equivalent atoms- #1 -x+2, -y+, -z+1

Table 5.4 Anisotropic displacement parameters (Å^2 × 10^3) for compound **91**. The anisotropic displacement factor exponent takes the form: $-2\pi^2[h^2 a^{*2}U^{11} + ... + 2\,h\,k\,a^*\,b^*\,U^{12}]$

	U^{11}	U^{22}	U^{33}	U^{23}	U^{13}	U^{12}
S(1)	23(1)	34(1)	41(1)	-16(1)	0(1)	-3(1)
S(2)	73(1)	70(1)	46(1)	-30(1)	6(1)	-28(1)
O(1)	34(1)	48(2)	43(2)	-26(1)	-16(1)	18(1)
N(1)	22(1)	24(1)	27(1)	-7(1)	-5(1)	1(1)
C(1)	24(2)	24(2)	28(2)	-6(1)	-6(1)	2(1)
C(2)	20(1)	18(1)	25(2)	-5(1)	-1(1)	-2(1)
C(3)	17(1)	19(1)	27(2)	-4(1)	-2(1)	-2(1)
C(4)	22(2)	20(1)	25(2)	-2(1)	-1(1)	-3(1)
C(5)	18(1)	22(1)	30(2)	-1(1)	-4(1)	-2(1)
C(6)	18(1)	23(2)	31(2)	-3(1)	0(1)	-2(1)
C(7)	22(2)	23(2)	31(2)	-7(1)	-1(1)	-1(1)
C(8)	20(2)	25(2)	28(2)	-6(1)	-2(1)	-2(1)
C(9)	24(2)	26(2)	35(2)	-5(1)	0(1)	2(1)
C(10)	22(2)	32(2)	40(2)	-1(2)	-3(1)	4(1)
C(11)	23(2)	39(2)	37(2)	-1(2)	-9(1)	-1(1)
C(12)	23(2)	32(2)	33(2)	-4(1)	-5(1)	-2(1)
C(13)	21(2)	27(2)	33(2)	-10(1)	-5(1)	0(1)
C(14)	22(2)	35(2)	42(2)	-15(2)	-2(1)	-3(1)
C(15)	27(2)	35(2)	39(2)	-13(2)	3(1)	2(1)
C(16)	27(2)	30(2)	37(2)	-11(1)	-3(1)	4(1)
C(17)	34(2)	33(2)	42(2)	-16(2)	-3(2)	0(2)
C(18)	45(2)	41(2)	54(3)	-20(2)	-2(2)	-8(2)
C(19)	53(3)	50(3)	68(3)	-25(2)	-12(2)	-15(2)

Table 5.4 (continued).

	U^{11}	U^{22}	U^{33}	U^{23}	U^{13}	U^{12}
C(20)	76(4)	58(3)	59(3)	-32(2)	-18(3)	-12(3)
C(21)	136(7)	83(4)	72(4)	-41(4)	-25(4)	-28(4)
C(22)	124(3)	126(3)	119(3)	-27(2)	-3(2)	-24(2)
C(27)	29(2)	31(2)	33(2)	-10(1)	-10(1)	-3(1)
C(28)	63(2)	73(2)	55(2)	-9(2)	-6(2)	-20(2)
C(33)	78(4)	97(5)	54(3)	0(3)	-10(3)	-38(4)
C(34)	66(4)	90(4)	62(3)	17(3)	7(3)	-19(3)

Table 5.5 Hydrogen coordinates (× 10^4) and isotropic displacement parameters (Å^2 × 10^3) for compound **91**.

	x	y	z	U(eq)
H(8)	7485	6733	5741	29
H(9)	396	8895	5150	36
H(10)	-2130	9103	4304	40
H(11)	-1316	7985	3479	41
H(12)	2045	6695	3490	36
H(14)	847	7818	6382	39
H(15)	1255	8848	7275	41
H(18)	7496	10564	6712	54
H(19)	8612	11210	7699	65
H(21A)	7504	11217	8967	110
H(21B)	4970	11027	9145	110
H(22A)	7337	9791	9926	147
H(22B)	6395	9083	9465	147
H(22C)	7701	9858	9886	147
H(22D)	6113	9226	9573	147
H(23A)	10773	9630	9305	149
H(23B)	9827	8905	8851	149
H(23C)	9002	8401	8983	149
H(23D)	10635	9159	9158	149
H(24A)	12129	7799	9762	153
H(24B)	10222	8270	10273	153
H(24C)	10381	8179	10322	152
H(24D)	9359	7294	10010	152

Table 5.5 (continued).

	x	y	z	U(eq)
H(25A)	8058	7072	10133	157
H(25B)	8788	7135	9336	157
H(25C)	12567	7068	9282	158
H(25D)	13592	7933	9608	158
H(26A)	12597	6496	9610	200
H(26B)	11323	5628	10098	200
H(26C)	12071	6614	10380	200
H(26D)	13808	6825	10581	205
H(26E)	15040	6148	10021	205
H(26F)	12569	5986	10303	205
H(27A)	3745	5155	3519	36
H(27B)	6090	4341	3393	36
H(28A)	4742	6607	2784	76
H(28B)	4522	6586	2697	76
H(29A)	3887	6154	1814	80
H(29B)	2647	5473	2433	80
H(29C)	3912	5824	1889	84
H(29D)	6307	5007	1945	84
H(30A)	6121	3972	2421	93
H(30B)	6531	4624	1680	93
H(30C)	2431	4339	2641	91
H(30D)	4815	3535	2518	91
H(31A)	3287	4133	1304	98
H(31B)	5108	3042	1617	98

Table 5.5 (continued).

	x	y	z	U(eq)
H(31C)	4231	4023	1313	101
H(31D)	1832	4825	1439	101
H(32A)	1217	3977	2361	143
H(32B)	2984	2848	2641	143
H(32C)	1354	2891	2035	143
H(32D)	2870	2404	2037	136
H(32E)	1210	2896	1412	136
H(32F)	474	3202	2136	136
H(33A)	8917	5395	2496	90
H(33B)	8388	6397	2905	90
H(34A)	7639	6631	1510	115
H(34B)	9609	7047	1827	115
H(34C)	7014	7640	1915	115

Chapter 6 - References

1. Shirakawa, H.; Louis, E. J.; MacDiarmid, A. G.; Chiang, C. K.; Heeger, A. J. Synthesis of electrically conducting organic polymers: Halogen derivatives of polyacetylene. *J. Chem. Soc., Chem. Commun.* **1977**, 578-580.
2. Chiang, C. K.; Fincher, C. R.; Park, Y. W.; Heeger, A. J.; Shirakawa, H.; Louis, E. J.; Gau, S. C.; MacDiarmid, A. G. Electrical conductivity in doped polyacetylene. *Phys. Rev. Lett.* **1977**, *39*, 1098-1101.
3. Rice, M. J. Organic linear conductors as systems for the study of electron-phonon interactions in the organic solid state. *Phys. Rev. Lett.* **1976**, *37*, 36-39.
4. Sirringhaus, H. Device physics of solution-processed organic field-effect transistors. *Adv. Mater.* **2005**, *17*, 2411-2425.
5. Vissenberg, M. C. J. M. Opto-electronic properties of disordered organic semiconductors. PhD thesis, Leiden University, Leiden, Netherlands, 1999.
6. Randell, N. M. Tuning the properties of isoindigo-based organic semiconductors through structural engineering. PhD Thesis, University of Saskatchewan, Saskatoon, Canada, 2017.
7. Capuano, L., International energy outlook 2018 (ieo2018). U.S. Energy Information Administration https://csis-prod.s3.amazonaws.com/s3fs-public/event/180725_International_Energy_Outlook_Final.pdf?KIx4oqkE81Mc.45kXH76otNYksQDdluG, Accessed August 3, 2018.
8. Hansen, J.; Ruedy, R.; Sato, M.; Lo, K. Global surface temperature change. *Reviews of Geophysics* **2010**, *48*, DOI:10.1029/2010RG000345.
9. Gavin Schmidt, R. R., Avi Persin, 2018:GISS surface temperature analysis (GISTEMP). NASA Goddard Institute for Space Studies https://data.giss.nasa.gov/gistemp/, Accessed Jan 16, 2019.
10. U. S. Department of Energy, The Histroy of Solar https://www1.eere.energy.gov/solar/pdfs/solar_timeline.pdf, Accessed Jan 16, 2019.
11. Kurtz, S.; Haegel, N.; Sinton, R.; Margolis, R. A new era for solar. *Nat. Photon.* **2017**, *11*, 3-5.

12. Li, C.; Liu, M.; Pschirer, N. G.; Baumgarten, M.; Müllen, K. Polyphenylene-based materials for organic photovoltaics. *Chem. Rev.* **2010**, *110*, 6817-6855.
13. Servaites, J. D.; Ratner, M. A.; Marks, T. J. Organic solar cells: A new look at traditional models. *Energy Environ. Sci.* **2011**, *4*, 4410-4422.
14. Nelson, J., *The physics of solar cells*, First ed.; Imperial College Press: London, 2003.
15. Hains, A. W.; Liang, Z.; Woodhouse, M. A.; Gregg, B. A. Molecular semiconductors in organic photovoltaic cells. *Chem. Rev.* **2010**, *110*, 6689-6735.
16. Kippelen, B.; Bredas, J. L. Organic photovoltaics. *Energy Environ. Sci.* **2009**, *2*, 251-261.
17. Mazzio, K. A.; Luscombe, C. K. The future of organic photovoltaics. *Chem. Soc. Rev.* **2015**, *44*, 78-90.
18. Tang, C. W. Two-layer organic photovoltaic cell. *Appl. Phys. Lett.* **1986**, *48*, 183-185.
19. Sariciftci, N. S.; Smilowitz, L.; Heeger, A. J.; Wudl, F. Photoinduced electron transfer from a conducting polymer to buckminsterfullerene. *Science* **1992**, *258*, 1474-1476.
20. Sariciftci, N. S.; Braun, D.; Zhang, C.; Srdanov, V. I.; Heeger, A. J.; Stucky, G.; Wudl, F. Semiconducting polymer-buckminsterfullerene heterojunctions: Diodes, photodiodes, and photovoltaic cells. *Appl. Phys. Lett.* **1993**, *62*, 585-587.
21. Yu, G.; Gao, J.; Hummelen, J. C.; Wudl, F.; Heeger, A. J. Polymer photovoltaic cells: Enhanced efficiencies via a network of internal donor-acceptor heterojunctions. *Science* **1995**, *270*, 1789-1791.
22. Rand, B. R., H., *Organic solar cells: Fundamentals, devices, and upscaling*, First ed.; Pan Stanford Publishing: Singapore, 2014.
23. Yang, Y.; Li, G., *Progress in high-efficient solution process organic photovoltaic devices*, First ed.; Springer: Berlin and Heidelberg, 2015.
24. Ma, H.; Yip, H. L.; Huang, F.; Jen, A. K. Y. Interface engineering for organic electronics. *Adv. Funct. Mater.* **2010**, *20*, 1371-1388.
25. Chen, L. M.; Xu, Z.; Hong, Z.; Yang, Y. Interface investigation and engineering – achieving high performance polymer photovoltaic devices. *J. Mater. Chem.* **2010**, *20*, 2575-2598.
26. Yip, H.-L.; Jen, A. K. Y. Recent advances in solution-processed interfacial materials for efficient and stable polymer solar cells. *Energy Environ. Sci.* **2012**, *5*, 5994-6011.

27. Steim, R.; Kogler, F. R.; Brabec, C. J. Interface materials for organic solar cells. *J. Mater. Chem.* **2010**, *20*, 2499-2512.

28. Groenendaal, L.; Jonas, F.; Freitag, D.; Pielartzik, H.; Reynolds, J. R. Poly(3,4-ethylenedioxythiophene) and its derivatives: Past, present, and future. *Adv. Mater.* **2000**, *12*, 481-494.

29. Brabec, C. J.; Shaheen, S. E.; Winder, C.; Sariciftci, N. S.; Denk, P. Effect of lif/metal electrodes on the performance of plastic solar cells. *Appl. Phys. Lett.* **2002**, *80*, 1288-1290.

30. Hung, L. S.; Tang, C. W.; Mason, M. G. Enhanced electron injection in organic electroluminescence devices using an Al/LiF electrode. *Appl. Phys. Lett.* **1997**, *70*, 152-154.

31. Jong, M. P. d.; IJzendoorn, L. J. v.; Voigt, M. J. A. d. Stability of the interface between indium-tin-oxide and poly(3,4-ethylenedioxythiophene)/poly(styrenesulfonate) in polymer light-emitting diodes. *Appl. Phys. Lett.* **2000**, *77*, 2255-2257.

32. John Bardeen; Brattain, W. Three-electrode circuit element utilizing semiconductivematerials. US2524035, June 17, 1948.

33. Horowitz, G. Organic thin film transistors: From theory to real devices. *J. Mater. Res.* **2011**, *19*, 1946-1962.

34. Zschieschang, U.; Yamamoto, T.; Takimiya, K.; Kuwabara, H.; Ikeda, M.; Sekitani, T.; Someya, T.; Klauk, H. Organic electronics on banknotes. *Adv. Mater.* **2011**, *23*, 654-658.

35. Sokolov, A. N.; Tee, B. C. K.; Bettinger, C. J.; Tok, J. B. H.; Bao, Z. Chemical and engineering approaches to enable organic field-effect transistors for electronic skin applications. *Acc. Chem. Res.* **2012**, *45*, 361-371.

36. Edgar, L. J. Method and apparatus for controlling electric currents. US1745175A, Jan 28, 1930.

37. Dawon, K. Electric field controlled semiconductor device. US3206670A, March 8, 1960.

38. Klauk, H. Organic thin-film transistors. *Chem. Soc. Rev.* **2010**, *39*, 2643-2666.

39. Bao, Z.; Locklin, J., *Organic field-effect transistors*, First ed.; CRC Press, Inc.: Boka Raton, USA, 2007.

40. Neamen, D. A., *Semiconductor physics and devices : Basic principles*, Third ed.: London, United States, 2002.

41. Newman, C. R.; Frisbie, C. D.; da Silva Filho, D. A.; Bredas, J.-L.; Ewbank, P. C.; Mann, K. R. Introduction to organic thin film transistors and design of n-channel organic semiconductors. *Chem. Mater.* **2004**, *16*, 4436-4451.
42. Roncali, J. Conjugated poly(thiophenes): Synthesis, functionalization, and applications. *Chem. Rev.* **1992**, *92*, 711-738.
43. McCullough, R. D.; Lowe, R. D.; Jayaraman, M.; Anderson, D. L. Design, synthesis, and control of conducting polymer architectures: Structurally homogeneous poly(3-alkylthiophenes). *J. Org. Chem.* **1993**, *58*, 904-912.
44. Padinger, F.; Rittberger, R. S.; Sariciftci, N. S. Effects of postproduction treatment on plastic solar cells. *Adv. Funct. Mater.* **2003**, *13*, 85-88.
45. Kim, Y.; Cook, S.; Tuladhar, S. M.; Choulis, S. A., et al. A strong regioregularity effect in self-organizing conjugated polymer films and high-efficiency polythiophene:Fullerene solar cells. *Nat. Mater.* **2006**, *5*, 197-203.
46. He, Y.; Li, Y. Fullerene derivative acceptors for high performance polymer solar cells. *Phys. Chem. Chem. Phys.* **2011**, *13*, 1970-1983.
47. Ma, W.; Yang, C.; Gong, X.; Lee, K.; Heeger, A. J. Thermally stable, efficient polymer solar cells with nanoscale control of the interpenetrating network morphology. *Adv. Funct. Mater.* **2005**, *15*, 1617-1622.
48. Gundlach, D. J.; Lin, Y. Y.; Jackson, T. N.; Nelson, S. F.; Schlom, D. G. Pentacene organic thin-film transistors-molecular ordering and mobility. *IEEE Electron Device Lett.* **1997**, *18*, 87-89.
49. Mei, J.; Diao, Y.; Appleton, A. L.; Fang, L.; Bao, Z. Integrated materials design of organic semiconductors for field-effect transistors. *J. Am. Chem. Soc.* **2013**, *135*, 6724-6746.
50. Zhang, W.; Liu, Y.; Yu, G. Heteroatom substituted organic/polymeric semiconductors and their applications in field-effect transistors. *Adv. Mater.* **2014**, *26*, 6898-6904.
51. Mei, J.; Diao, Y.; Appleton, A. L.; Fang, L.; Bao, Z. Integrated materials design of organic semiconductors for field-effect transistors. *J. Am. Chem. Soc.* **2013**, *135*, 6724-6746.
52. Bao, Z.; Dodabalapur, A.; Lovinger, A. J. Soluble and processable regioregular poly(3-hexylthiophene) for thin film field-effect transistor applications with high mobility. *Appl. Phys. Lett.* **1996**, *69*, 4108-4110.

53. McCulloch, I.; Heeney, M.; Chabinyc, M. L.; DeLongchamp, D., et al. Semiconducting thienothiophene copolymers: Design, synthesis, morphology, and performance in thin-film organic transistors. *Adv. Mater.* **2009**, *21*, 1091-1109.

54. McCulloch, I.; Heeney, M.; Bailey, C.; Genevicius, K., et al. Liquid-crystalline semiconducting polymers with high charge-carrier mobility. *Nat. Mater.* **2006**, *5*, 328-333.

55. Bao, Z.; Lovinger, A. J.; Brown, J. New air-stable n-channel organic thin film transistors. *J. Am. Chem. Soc.* **1998**, *120*, 207-208.

56. Jones, B. A.; Ahrens, M. J.; Yoon, M.-H.; Facchetti, A.; Marks, T. J.; Wasielewski, M. R. High-mobility air-stable n-type semiconductors with processing versatility: Dicyanoperylene-3,4:9,10-bis(dicarboximides). *Angew. Chem. Int. Ed.* **2004**, *43*, 6363-6366.

57. Babel, A.; Jenekhe, S. A. Electron transport in thin-film transistors from an n-type conjugated polymer. *Adv. Mater.* **2002**, *14*, 371-374.

58. Babel, A.; Jenekhe, S. A. High electron mobility in ladder polymer field-effect transistors. *J. Am. Chem. Soc.* **2003**, *125*, 13656-13657.

59. Yan, H.; Chen, Z.; Zheng, Y.; Newman, C.; Quinn, J. R.; Dötz, F.; Kastler, M.; Facchetti, A. A high-mobility electron-transporting polymer for printed transistors. *Nature* **2009**, *457*, 679-686.

60. Murphy, A. R.; Fréchet, J. M. J. Organic semiconducting oligomers for use in thin film transistors. *Chem. Rev.* **2007**, *107*, 1066-1096.

61. Guo, X.; Facchetti, A.; Marks, T. J. Imide- and amide-functionalized polymer semiconductors. *Chem. Rev.* **2014**, *114*, 8943-9021.

62. Sirringhaus, H. 25th anniversary article: Organic field-effect transistors: The path beyond amorphous silicon. *Adv. Mater.* **2014**, *26*, 1319-1335.

63. Heeger, A. J. Semiconducting polymers: The third generation. *Chem. Soc. Rev.* **2010**, *39*, 2354-2371.

64. Steinmann, V.; Kronenberg, N. M.; Lenze, M. R.; Graf, S. M.; Hertel, D.; Meerholz, K.; Bürckstümmer, H.; Tulyakova, E. V.; Würthner, F. Simple, highly efficient vacuum-processed bulk heterojunction solar cells based on merocyanine dyes. *Adv. Energy Mater.* **2011**, *1*, 888-893.

65. Zhang, Q. T.; Tour, J. M. Low optical bandgap polythiophenes by an alternating donor/acceptor repeat unit strategy. *J. Am. Chem. Soc.* **1997**, *119*, 5065-5066.

66. Mühlbacher, D.; Scharber, M.; Morana, M.; Zhu, Z.; Waller, D.; Gaudiana, R.; Brabec, C. High photovoltaic performance of a low-bandgap polymer. *Adv. Mater.* **2006**, *18*, 2884-2889.

67. Blouin, N.; Michaud, A.; Leclerc, M. A low-bandgap poly(2,7-carbazole) derivative for use in high-performance solar cells. *Adv. Mater.* **2007**, *19*, 2295-2300.

68. Park, S. H.; Roy, A.; Beaupré, S.; Cho, S.; Coates, N.; Moon, J. S.; Moses, D.; Leclerc, M.; Lee, K.; Heeger, A. J. Bulk heterojunction solar cells with internal quantum efficiency approaching 100%. *Nat. Photon.* **2009**, *3*, 297-303.

69. Hou, J.; Chen, H.-Y.; Zhang, S.; Li, G.; Yang, Y. Synthesis, characterization, and photovoltaic properties of a low band gap polymer based on silole-containing polythiophenes and 2,1,3-benzothiadiazole. *J. Am. Chem. Soc.* **2008**, *130*, 16144-16145.

70. Schulz, G. L.; Fischer, F. S. U.; Trefz, D.; Melnyk, A.; Hamidi-Sakr, A.; Brinkmann, M.; Andrienko, D.; Ludwigs, S. The PCPDTBT family: Correlations between chemical structure, polymorphism, and device performance. *Macromolecules* **2017**, *50*, 1402-1414.

71. Li, Y.; Sonar, P.; Murphy, L.; Hong, W. High mobility diketopyrrolopyrrole-based organic semiconductor materials for organic thin film transistors and photovoltaics. *Energy Environ. Sci.* **2013**, *6*, 1684-1710.

72. Li, W.; Hendriks, K. H.; Wienk, M. M.; Janssen, R. A. J. Diketopyrrolopyrrole polymers for organic solar cells. *Acc. Chem. Res.* **2016**, *49*, 78-85.

73. Qu, S.; Tian, H. Diketopyrrolopyrrole based materials for organic photovoltaics. *Chem. Commun.* **2012**, *48*, 3039-3051.

74. Naik, M. A.; Patil, S. Diketopyrrolopyrrole-based conjugated polymers and small molecules for organic ambipolar transistors and solar cells. *J. Polym. Sci ., Part A: Polym. Chem.* **2013**, *51*, 4241-4260.

75. Nielsen, C. B.; Turbiez, M.; McCulloch, I. Recent advances in the development of semiconducting containing polymers for transistor applications. *Adv. Mater.* **2013**, *25*, 1859-1880.

76. Yi, Z.; Wang, S.; Liu, Y. Design of high-mobility diketopyrrolopyrrole-based π-conjugated copolymers for organic thin-film transistors. *Adv. Mater.* **2015**, *27*, 3589-3606.

77. Yao, H.; Ye, L.; Zhang, H.; Li, S.; Zhang, S.; Hou, J. Molecular design of benzodithiophene-based organic photovoltaic materials. *Chem. Rev.* **2016**, *116*, 7397-7457.

78. Li, C.; Wonneberger, H. Perylene imides for organic photovoltaics: Yesterday, today, and tomorrow. *Adv. Mater.* **2012**, *24*, 613-636.

79. Nowak-Krol, A.; Shoyama, K.; Stolte, M.; Würthner, F. Naphthalene and perylene diimides – better alternatives to fullerenes for organic electronics? *Chem. Commun.* **2018**, *54*, 13763-13772.

80. Chua, M. H.; Zhu, Q.; Tang, T.; Shah, K. W.; Xu, J. Diversity of electron acceptor groups in donor–acceptor type electrochromic conjugated polymers. *Sol. Energy Mater. Sol. Cells* **2019**, *197*, 32-75.

81. Zhao, J.; Li, Y.; Yang, G.; Jiang, K.; Lin, H.; Ade, H.; Ma, W.; Yan, H. Efficient organic solar cells processed from hydrocarbon solvents. *Nat. Energy* **2016**, *1*, 15027-15033.

82. Zhan, X.; Tan, Z. a.; Domercq, B.; An, Z.; Zhang, X.; Barlow, S.; Li, Y.; Zhu, D.; Kippelen, B.; Marder, S. R. A high-mobility electron-transport polymer with broad absorption and its use in field-effect transistors and all-polymer solar cells. *J. Am. Chem. Soc.* **2007**, *129*, 7246-7247.

83. Few, S.; Frost, J. M.; Kirkpatrick, J.; Nelson, J. Influence of chemical structure on the charge transfer state spectrum of a polymer:fullerene complex. *J Phys. Chem. C* **2014**, *118*, 8253-8261.

84. Jørgensen, M.; Norrman, K.; Gevorgyan, S. A.; Tromholt, T.; Andreasen, B.; Krebs, F. C. Stability of polymer solar cells. *Adv. Mater.* **2012**, *24*, 580-612.

85. Yang, X.; van Duren, J. K. J.; Janssen, R. A. J.; Michels, M. A. J.; Loos, J. Morphology and thermal stability of the active layer in poly(p-phenylenevinylene)/methanofullerene plastic photovoltaic devices. *Macromolecules* **2004**, *37*, 2151-2158.

86. Cheng, P.; Li, G.; Zhan, X.; Yang, Y. Next-generation organic photovoltaics based on non-fullerene acceptors. *Nat. Photon.* **2018**, *12*, 131-142.

87. Hou, J.; Inganäs, O.; Friend, R. H.; Gao, F. Organic solar cells based on non-fullerene acceptors. *Nat. Mater.* **2018**, *17*, 119-128.

88. Li, S.; Ye, L.; Zhao, W.; Yan, H.; Yang, B.; Liu, D.; Li, W.; Ade, H.; Hou, J. A wide band gap polymer with a deep highest occupied molecular orbital level enables 14.2% efficiency in polymer solar cells. *J. Am. Chem. Soc.* **2018**, *140*, 7159-7167.

89. Yuan, J.; Zhang, Y.; Zhou, L.; Zhang, G., et al. Single-junction organic solar cell with over 15% efficiency using fused-ring acceptor with electron-deficient core. *Joule*, DOI.org/10.1016/j.joule.2019.01.004.

90. Zhang, J.; Tan, H. S.; Guo, X.; Facchetti, A.; Yan, H. Material insights and challenges for non-fullerene organic solar cells based on small molecular acceptors. *Nat. Energy* **2018**, *3*, 720-731.

91. Wadsworth, A.; Moser, M.; Marks, A.; Little, M. S.; Gasparini, N.; Brabec, C. J.; Baran, D.; McCulloch, I. Critical review of the molecular design progress in non-fullerene electron acceptors towards commercially viable organic solar cells. *Chem. Soc. Rev.* **2019**, *48*, 1596-1625.

92. Nielsen, C. B.; Holliday, S.; Chen, H.-Y.; Cryer, S. J.; McCulloch, I. Non-fullerene electron acceptors for use in organic solar cells. *Acc. Chem. Res.* **2015**, *48*, 2803-2812.

93. Mei, J.; Graham, K. R.; Stalder, R.; Reynolds, J. R. Synthesis of isoindigo-based oligothiophenes for molecular bulk heterojunction solar cells. *Org. Lett.* **2010**, *12*, 660-663.

94. Graham, K. R.; Mei, J.; Stalder, R.; Shim, J. W.; Cheun, H.; Steffy, F.; So, F.; Kippelen, B.; Reynolds, J. R. Polydimethylsiloxane as a macromolecular additive for enhanced performance of molecular bulk heterojunction organic solar cells. *ACS Appl. Mater. Interfaces* **2011**, *3*, 1210-1215.

95. Graham, K. R.; Stalder, R.; Wieruszewski, P. M.; Patel, D. G.; Salazar, D. H.; Reynolds, J. R. Tailor-made additives for morphology control in molecular bulk-heterojunction photovoltaics. *ACS Appl. Mater. Interfaces* **2013**, *5*, 63-71.

96. Elsawy, W.; Lee, C.-L.; Cho, S.; Oh, S.-H.; Moon, S.-H.; Elbarbary, A.; Lee, J.-S. Isoindigo-based small molecules for high-performance solution-processed organic

photovoltaic devices: The electron donating effect of the donor group on photo-physical properties and device performance. *Phys. Chem. Chem. Phys.* **2013**, *15*, 15193-15203.

97. Wang, T.; Chen, Y.; Bao, X.; Du, Z.; Guo, J.; Wang, N.; Sun, M.; Yang, R. A new isoindigo-based molecule with ideal energy levels for solution-processable organic solar cells. *Dyes Pigm.* **2013**, *98*, 11-16.
98. Tomassetti, M.; Ouhib, F.; Cardinaletti, I.; Verstappen, P.; Salleo, A.; Jérôme, C.; Manca, J.; Maes, W.; Detrembleur, C. Branched and linear A_2–D–A_1–D–A_2 isoindigo-based solution-processable small molecules for organic field-effect transistors and solar cells. *RSC Adv.* **2015**, *5*, 85460-85469.
99. Jung, J. W. A low band gap conjugated small molecule based on isoindigo flanked with diketopyrrolopyrrole for efficient organic solar cells. *Dyes Pigm.* **2017**, *137*, 512-517.
100. Liu, X.; Xie, Y.; Cai, X.; Li, Y.; Wu, H.; Su, S. J.; Cao, Y. Synthesis and photovoltaic properties of A–D–A type non-fullerene acceptors containing isoindigo terminal units. *RSC Adv.* **2015**, *5*, 107566-107574.
101. Quinn, J. T. E.; Zhu, J.; Li, X.; Wang, J.; Li, Y. Recent progress in the development of n-type organic semiconductors for organic field effect transistors. *J. Mater. Chem. C* **2017**, *5*, 8654-8681.
102. Wang, E.; Mammo, W.; Andersson, M. R. 25th anniversary article: Isoindigo-based polymers and small molecules for bulk heterojunction solar cells and field effect transistors. *Adv. Mater.* **2014**, *26*, 1801-1826.
103. Deng, P.; Zhang, Q. Recent developments on isoindigo-based conjugated polymers. *Polym. Chem.* **2014**, *5*, 3298-3305.
104. Stalder, R.; Mei, J.; Graham, K. R.; Estrada, L. A.; Reynolds, J. R. Isoindigo, a versatile electron-deficient unit for high-performance organic electronics. *Chem. Mater.* **2014**, *26*, 664-678.
105. Lei, T.; Wang, J. Y.; Pei, J. Design, synthesis, and structure–property relationships of isoindigo-based conjugated polymers. *Acc. Chem. Res.* **2014**, *47*, 1117-1126.
106. Wang, E.; Ma, Z.; Zhang, Z.; Henriksson, P.; Inganäs, O.; Zhang, F.; Andersson, M. R. An isoindigo-based low band gap polymer for efficient polymer solar cells with high photo-voltage. *Chem. Commun.* **2011**, *47*, 4908-4910.

107. Ma, Z.; Wang, E.; Vandewal, K.; Andersson, M. R.; Zhang, F. Enhance performance of organic solar cells based on an isoindigo-based copolymer by balancing absorption and miscibility of electron acceptor. *Appl. Phys. Lett.* **2011**, *99*, 143302-143305.

108. Wang, E.; Ma, Z.; Zhang, Z.; Vandewal, K.; Henriksson, P.; Inganäs, O.; Zhang, F.; Andersson, M. R. An easily accessible isoindigo-based polymer for high-performance polymer solar cells. *J. Am. Chem. Soc.* **2011**, *133*, 14244-14247.

109. Ho, C. C.; Chen, C. A.; Chang, C. Y.; Darling, S. B.; Su, W. F. Isoindigo-based copolymers for polymer solar cells with efficiency over 7%. *J. Mater. Chem. A* **2014**, *2*, 8026-8032.

110. Hu, H.; Jiang, K.; Kim, J.-H.; Yang, G.; Li, Z.; Ma, T.; Lu, G.; Qu, Y.; Ade, H.; Yan, H. Influence of fluorination on the properties and performance of isoindigo–quaterthiophene-based polymers. *J. Mater. Chem. A* **2016**, *4*, 5039-5043.

111. Lei, T.; Cao, Y.; Zhou, X.; Peng, Y.; Bian, J.; Pei, J. Systematic investigation of isoindigo-based polymeric field-effect transistors: Design strategy and impact of polymer symmetry and backbone curvature. *Chem. Mater.* **2012**, *24*, 1762-1770.

112. Mei, J.; Kim, D. H.; Ayzner, A. L.; Toney, M. F.; Bao, Z. Siloxane-terminated solubilizing side chains: Bringing conjugated polymer backbones closer and boosting hole mobilities in thin-film transistors. *J. Am. Chem. Soc.* **2011**, *133*, 20130-20133.

113. Ho, C. C.; Chang, S. Y.; Huang, T. C.; Chen, C. A.; Liao, H. C.; Chen, Y. F.; Su, W. F. Synthesis, characterization and photovoltaic properties of poly(cyclopentadithiophene-alt-isoindigo). *Polym. Chem.* **2013**, *4*, 5351-5360.

114. Stalder, R.; Grand, C.; Subbiah, J.; So, F.; Reynolds, J. R. An isoindigo and dithieno[3,2-b:2′,3′-d]silole copolymer for polymer solar cells. *Polym. Chem.* **2012**, *3*, 89-92.

115. Sonar, P.; Tan, H. S.; Sun, S.; Lam, Y. M.; Dodabalapur, A. Isoindigo dye incorporated copolymers with naphthalene and anthracene: Promising materials for stable organic field effect transistors. *Polym. Chem.* **2013**, *4*, 1983-1994.

116. Stalder, R.; Mei, J. G.; Subbiah, J.; Grand, C.; Estrada, L. A.; So, F.; Reynolds, J. R. n-type conjugated polyisoindigos. *Macromolecules* **2011**, *44*, 6303-6310.

117. Grenier, F.; Berrouard, P.; Pouliot, J. R.; Tseng, H. R.; Heeger, A. J.; Leclerc, M. Synthesis of new n-type isoindigo copolymers. *Polym. Chem.* **2013**, *4*, 1836-1841.

118. Lei, T.; Dou, J. H.; Ma, Z. J.; Yao, C. H.; Liu, C. J.; Wang, J. Y.; Pei, J. Ambipolar polymer field-effect transistors based on fluorinated isoindigo: High performance and improved ambient stability. *J. Am. Chem. Soc.* **2012**, *134*, 20025-20028.

119. Lei, T.; Dou, J. H.; Ma, Z. J.; Liu, C. J.; Wang, J. Y.; Pei, J. Chlorination as a useful method to modulate conjugated polymers: Balanced and ambient-stable ambipolar high-performance field-effect transistors and inverters based on chlorinated isoindigo polymers. *Chem. Sci.* **2013**, *4*, 2447-2452.

120. Zheng, Y. Q.; Wang, Z.; Dou, J. H.; Zhang, S. D.; Luo, X. Y.; Yao, Z. F.; Wang, J. Y.; Pei, J. Effect of halogenation in isoindigo-based polymers on the phase separation and molecular orientation of bulk heterojunction solar cells. *Macromolecules* **2015**, *48*, 5570-5577.

121. Ashraf, R. S.; Kronemeijer, A. J.; James, D. I.; Sirringhaus, H.; McCulloch, I. A new thiophene substituted isoindigo based copolymer for high performance ambipolar transistors. *Chem. Commun.* **2012**, *48*, 3939-3941.

122. Kim, G.; Kang, S. J.; Dutta, G. K.; Han, Y. K.; Shin, T. J.; Noh, Y. Y.; Yang, C. A thienoisoindigo-naphthalene polymer with ultrahigh mobility of 14.4 $cm^2/v\cdot s$ that substantially exceeds benchmark values for amorphous silicon semiconductors. *J. Am. Chem. Soc.* **2014**, *136*, 9477-9483.

123. Randell, N. M.; Douglas, A. F.; Kelly, T. L. 7-azaisoindigo as a new electron deficient component of small molecule chromophores for organic solar cells. *J. Mater. Chem. A* **2014**, *2*, 1085-1092.

124. Huang, J.; Mao, Z.; Chen, Z.; Gao, D.; Wei, C.; Zhang, W.; Yu, G. Diazaisoindigo-based polymers with high-performance charge-transport properties: From computational screening to experimental characterization. *Chem. Mater.* **2016**, *28*, 2209-2218.

125. Yue, W.; Nikolka, M.; Xiao, M.; Sadhanala, A.; Nielsen, C. B.; White, A. J. P.; Chen, H.-Y.; Onwubiko, A.; Sirringhaus, H.; McCulloch, I. Azaisoindigo conjugated polymers for high performance n-type and ambipolar thin film transistor applications. *J. Mater. Chem. C* **2016**, *4*, 9704-9710.

126. Müller-Buschbaum, P. The active layer morphology of organic solar cells probed with grazing incidence scattering techniques. *Adv. Mater.* **2014**, *26*, 7692-7709.

127. Randell, N. M.; Kelly, T. L. Recent advances in isoindigo-inspired organic semiconductors. *Chem. Rec.*, DOI:10.1002/tcr.201800135.

128. de Miguel, G.; Camacho, L.; García-Frutos, E. M. 7,7′-diazaisoindigo: A novel building block for organic electronics. *J. Mater. Chem. C* **2016**, *4*, 1208-1214.

129. Meager, I.; Nikolka, M.; Schroeder, B. C.; Nielsen, C. B., et al. Thieno[3,2-b]thiophene flanked isoindigo polymers for high performance ambipolar ofet applications. *Adv. Funct. Mater.* **2014**, *24*, 7109-7115.

130. Yue, W.; Ashraf, R. S.; Nielsen, C. B.; Collado-Fregoso, E., et al. A thieno[3,2-b][1]benzothiophene isoindigo building block for additive- and annealing-free high-performance polymer solar cells. *Adv. Mater.* **2015**, *27*, 4702-4707.

131. Neophytou, M.; Bryant, D.; Lopatin, S.; Chen, H.; Hallani, R. K.; Cater, L.; McCulloch, I.; Yue, W. Alternative thieno[3,2-b][1]benzothiophene isoindigo polymers for solar cell applications. *Macromol. Rapid Commun.* **2018**, *39*, 1700820-1700826.

132. Lei, T.; Dou, J. H.; Cao, X. Y.; Wang, J. Y.; Pei, J. Electron-deficient poly(p-phenylene vinylene) provides electron mobility over 1 cm^2/v·s under ambient conditions. *J. Am. Chem. Soc.* **2013**, *135*, 12168-12171.

133. Cao, Y.; Yuan, J. S.; Zhou, X.; Wang, X. Y.; Zhuang, F. D.; Wang, J. Y.; Pei, J. N-fused BDOPV: A tetralactam derivative as a building block for polymer field-effect transistors. *Chem. Commun.* **2015**, *51*, 10514-10516.

134. He, Y.; Guo, C.; Sun, B.; Quinn, J.; Li, Y. (3*E*,7*E*)-3,7-bis(2-oxoindolin-3-ylidene)-5,7-dihydropyrrolo[2,3-f]indole-2,6(1H,3H)-dione based polymers for ambipolar organic thin film transistors. *Chem. Commun.* **2015**, *51*, 8093-8096.

135. Randell, N. M.; Boutin, P. C.; Kelly, T. L. Bisisoindigo: Using a ring-fusion approach to extend the conjugation length of isoindigo. *J. Mater. Chem. A* **2016**, *4*, 6940-6945.

136. Jiang, Y.; Gao, Y.; Tian, H.; Ding, J.; Yan, D.; Geng, Y.; Wang, F. Synthesis and characterization of isoindigo[7,6-g]isoindigo-based donor–acceptor conjugated polymers. *Macromolecules* **2016**, *49*, 2135-2144.

137. Onwubiko, A.; Yue, W.; Jellett, C.; Xiao, M., et al. Fused electron deficient semiconducting polymers for air stable electron transport. *Nat. Commun.* **2018**, *9*, 416-424.

138. Jiang, Y.; Zheng, X.; Deng, Y.; Tian, H.; Ding, J.; Xie, Z.; Geng, Y.; Wang, F. Fused isoindigo ribbons with absorption bands reaching near-infrared. *Angew. Chem. Int. Ed.* **2018**, *57*, 10283-10287.

139. Randell, N. M.; Radford, C. L.; Yang, J.; Quinn, J.; Hou, D.; Li, Y.; Kelly, T. L. Effect of acceptor unit length and planarity on the optoelectronic properties of isoindigo–thiophene donor–acceptor polymers. *Chem. Mater.* **2018**, *30*, 4864-4873.

140. James, D. I.; Wang, S.; Ma, W.; Hedstroem, S., et al. High-performance hole transport and quasi-balanced ambipolar OFETs based on D-A-A thieno-benzo-isoindigo polymers. *Adv. Electron. Mater.* **2016**, *2*, 1500313-1500320.

141. Ganguly, A.; Zhu, J.; Kelly, T. L. Effect of cross-conjugation on derivatives of benzoisoindigo, an isoindigo analogue with an extended π-system. *J. Phys. Chem. C* **2017**, *121*, 9110-9119.

142. Liang, Y.; Xu, Z.; Xia, J.; Tsai, S.-T.; Wu, Y.; Li, G.; Ray, C.; Yu, L. For the bright future—bulk heterojunction polymer solar cells with power conversion efficiency of 7.4%. *Adv. Mater.* **2010**, *22*, 135-138.

143. Liao, S. H.; Jhuo, H. J.; Cheng, Y. S.; Chen, S.-A. Fullerene derivative-doped zinc oxide nanofilm as the cathode of inverted polymer solar cells with low-bandgap polymer (PTB7-TH) for high performance. *Adv. Mater.* **2013**, *25*, 4766-4771.

144. Chen, M. S.; Niskala, J. R.; Unruh, D. A.; Chu, C. K.; Lee, O. P.; Fréchet, J. M. J. Control of polymer-packing orientation in thin films through synthetic tailoring of backbone coplanarity. *Chem. Mater.* **2013**, *25*, 4088-4096.

145. Estrada, L. A.; Stalder, R.; Abboud, K. A.; Risko, C.; Bredas, J.-L.; Reynolds, J. R. Understanding the electronic structure of isoindigo in conjugated systems: A combined theoretical and experimental approach. *Macromolecules* **2013**, *46*, 8832-8844.

146. van Pruissen, G. W. P.; Brebels, J.; Hendriks, K. H.; Wienk, M. M.; Janssen, R. A. J. Effects of cross-conjugation on the optical absorption and frontier orbital levels of donor–acceptor polymers. *Macromolecules* **2015**, *48*, 2435-2443.

147. Rice, K. C.; Boone, B. J.; Rubin, A. B.; Rauls, T. J. Synthesis, antimalarial activity, and phototoxicity of some benzo[H]quinoline-4-methanols. *J. Med. Chem.* **1976**, *19*, 887-892.

148. Da Silva, J. F. M.; Garden, S. J.; Pinto, A. C. The chemistry of isatins: A review from 1975 to 1999. *J. Braz. Chem. Soc.* **2001**, *12*, 273-324.

149. Zhang, A.; Yu, M.; Lan, T.; Liu, Z.; Mao, Z. Novel synthesis of 4- or 6-substituted indirubin derivatives. *Synth. Commun.* **2010**, *40*, 3125-3134.

150. Mei, J.; Graham, K. R.; Stalder, R.; Reynolds, J. R. Synthesis of isoindigo-based oligothiophenes for molecular bulk heterojunction solar cells. *Org. Lett.* **2010**, *12*, 660-663.

151. Soriano, D. S. Example of the wolff-kishner reduction procedure suitable for an undergraduate organic lab experiment: Preparation of oxindole. *J. Chem. Educ.* **1993**, *70*, 332.

152. Bogdanov, A. V.; Mironov, V. F.; Musin, L. I.; Musin, R. Z. Facile synthesis of 1, 1′-dialkylisoindigos through deoxygenation reaction of isatins and tris (diethylamino) phosphine. *Synthesis* **2010**, *2010*, 3268-3270.

153. Zhao, N.; Qiu, L.; Wang, X.; An, Z.; Wan, X. Synthesis of a thiophene-fused isoindigo derivative: A potential building block for organic semiconductors. *Tetrahedron Lett.* **2014**, *55*, 1040-1044.

154. Cardona, C. M.; Li, W.; Kaifer, A. E.; Stockdale, D.; Bazan, G. C. Electrochemical considerations for determining absolute frontier orbital energy levels of conjugated polymers for solar cell applications. *Adv. Mater.* **2011**, *23*, 2367-2371.

155. Beaujuge, P. M.; Amb, C. M.; Reynolds, J. R. Spectral engineering in π-conjugated polymers with intramolecular donor–acceptor interactions. *Acc. Chem. Res.* **2010**, *43*, 1396-1407.

156. Voronina, Y. K.; Krivolapov, D. B.; Bogdanov, A. V.; Mironov, V. F.; Litvinov, I. A. An unusual conformation of 1,1′-dimethyl-isoindigo in crystals. *J. Struct. Chem.* **2012**, *53*, 413-416.

157. Yue, W.; He, T.; Stolte, M.; Gsanger, M.; Wurthner, F. Cyanated isoindigos for n-type and ambipolar organic thin film transistors. *Chem. Commun.* **2014**, *50*, 545-547.

158. Elgrishi, N.; Rountree, K. J.; McCarthy, B. D.; Rountree, E. S.; Eisenhart, T. T.; Dempsey, J. L. A practical beginner’s guide to cyclic voltammetry. *J. Chem. Educ.* **2018**, *95*, 197-206.

159. Bard, A. J.; Faulkner, L. R., *Electrochemical methods fundamentals and applications*, Second ed.; John Wiley & Sons, INC.: New York, United Sates of America, 2001.

160. Savoie, B. M.; Jackson, N. E.; Marks, T. J.; Ratner, M. A. Reassessing the use of one-electron energetics in the design and characterization of organic photovoltaics. *Phys. Chem. Chem. Phys.* **2013**, *15*, 4538-4547.

161. Larson, B. W.; Whitaker, J. B.; Wang, X. B.; Popov, A. A.; Rumbles, G.; Kopidakis, N.; Strauss, S. H.; Boltalina, O. V. Electron affinity of phenyl–C_{61}–butyric acid methyl ester (PCBM). *J. Phys. Chem. C* **2013**, *117*, 14958-14964.

162. Wienk, M. M.; Kroon, J. M.; Verhees, W. J. H.; Knol, J.; Hummelen, J. C.; van Hal, P. A.; Janssen, R. A. J. Efficient methano[70]fullerene/MDMO-PPV bulk heterojunction photovoltaic cells. *Angew. Chem., Int. Ed.* **2003**, *42*, 3371-3375.

163. Coropceanu, V.; Cornil, J.; da Silva Filho, D. A.; Olivier, Y.; Silbey, R.; Bredas, J. L. Charge transport in organic semiconductors. *Chem. Rev.* **2007**, *107*, 926-952.

164. Liao, H.-C.; Ho, C. C.; Chang, C. Y.; Jao, M. H.; Darling, S. B.; Su, W. F. Additives for morphology control in high-efficiency organic solar cells. *Mater. Today* **2013**, *16*, 326-336.

165. Noriega, R.; Rivnay, J.; Vandewal, K.; Koch, F. P. V.; Stingelin, N.; Smith, P.; Toney, M. F.; Salleo, A. A general relationship between disorder, aggregation and charge transport in conjugated polymers. *Nat. Mater.* **2013**, *12*, 1038-1044.

166. Nikiforov, M. P.; Lai, B.; Chen, W.; Chen, S.; Schaller, R. D.; Strzalka, J.; Maser, J.; Darling, S. B. Detection and role of trace impurities in high-performance organic solar cells. *Energy Environ. Sci.* **2013**, *6*, 1513-1520.

167. DeLongchamp, D. M.; Kline, R. J.; Fischer, D. A.; Richter, L. J.; Toney, M. F. Molecular characterization of organic electronic films. *Adv. Mater.* **2011**, *23*, 319-337.

168. Baker, J. L.; Jimison, L. H.; Mannsfeld, S.; Volkman, S.; Yin, S.; Subramanian, V.; Salleo, A.; Alivisatos, A. P.; Toney, M. F. Quantification of thin film crystallographic orientation using x-ray diffraction with an area detector. *Langmuir* **2010**, *26*, 9146-9151.

169. Rivnay, J.; Mannsfeld, S. C. B.; Miller, C. E.; Salleo, A.; Toney, M. F. Quantitative determination of organic semiconductor microstructure from the molecular to device scale. *Chem. Rev.* **2012**, *112*, 5488-5519.

170. Hexemer, A.; Muller-Buschbaum, P. Advanced grazing-incidence techniques for modern soft-matter materials analysis. *IUCrJ* **2015**, *2*, 106-125.

171. Wang, G.; Melkonyan, F. S.; Facchetti, A.; Marks, T. J. All-polymer solar cells: Recent progress, challenges, and prospects. *Angew. Chem. Int. Ed.* **2019**, *58*, 4129-4142.

172. Lin, Y.; Wang, J.; Zhang, Z.-G.; Bai, H.; Li, Y.; Zhu, D.; Zhan, X. An electron acceptor challenging fullerenes for efficient polymer solar cells. *Adv. Mater.* **2015**, *27*, 1170-1174.

173. Zhang, G.; Zhao, J.; Chow, P. C. Y.; Jiang, K.; Zhang, J.; Zhu, Z.; Zhang, J.; Huang, F.; Yan, H. Nonfullerene acceptor molecules for bulk heterojunction organic solar cells. *Chem. Rev.* **2018**, *118*, 3447-3507.

174. Zhang, Y.; Xu, Y.; Ford, M. J.; Li, F.; Sun, J.; Ling, X.; Wang, Y.; Gu, J.; Yuan, J.; Ma, W. Thermally stable all-polymer solar cells with high tolerance on blend ratios. *Adv. Energy Mater.* **2018**, *8*, 1800029.

175. Kim, W.; Choi, J.; Kim, J. H.; Kim, T.; Lee, C.; Lee, S.; Kim, M.; Kim, B. J.; Kim, T. S. Comparative study of the mechanical properties of all-polymer and fullerene–polymer solar cells: The importance of polymer acceptors for high fracture resistance. *Chem. Mater.* **2018**, *30*, 2102-2111.

176. Anthopoulos, T. D.; Leeuw, D. M. d.; Cantatore, E.; Hof, P. v. t.; Alma, J.; Hummelen, J. C. Solution processible organic transistors and circuits based on a C_{70} methanofullerene. *J. Appl. Phys.* **2005**, *98*, 054503-054508.

177. Zheng, Y. Q.; Lei, T.; Dou, J. H.; Xia, X.; Wang, J. Y.; Liu, C. J.; Pei, J. Strong electron-deficient polymers lead to high electron mobility in air and their morphology-dependent transport behaviors. *Adv. Mater.* **2016**, *28*, 7213-7219.

178. Frisch, M. J.; Trucks, G.; W Schlegel, H. B.; Scuseria, G. E.; Robb, M. A.; Cheeseman, J. R.; Scalmani, G.; Barone, V.; Mennucci, B.; Petersson, G. A., et al. *Gaussian 09, revision e.01*, Gaussian, Inc., Wallingford, CT, 2013.

179. Gorelsky, S. I.; Lever, A. B. P. Electronic structure and spectra of ruthenium diimine complexes by density functional theory and INDO/S. Comparison of the two methods. *J. Organomet. Chem.* **2001**, *635*, 187-196.

180. Gorelsky, S. I. *Swizard program*, Revision 5.0; Centre for catalysis research and innovation, University of Ottawa, Ottawa, Canada, 1999.

181. *Apex2*, 2014.3-0 ed; Bruker AXS Inc., Madison, WI, USA, 2014.

182. *Saint and sadabs*, v8.34a ed.; Bruker AXS Inc., Madison, WI, USA, 2013.

183. Sheldrick, G. Shelxs-97. *Acta Crystallogr., Sect. A.: Fundam. Crystallogr.* **2008**, *64*, 112.

184. Sheldrick, G. M. *Shelxl*, Version 2014/7; Program for the Solution of Crystal Structures, University of Göttingen, Göttingen, Germany, 2014.

185. Macrae, C. F.; Bruno, I. J.; Chisholm, J. A.; Edgington, P. R.; McCabe, P.; Pidcock, E.; Rodriguez-Monge, L.; Taylor, R.; Streek, J. v.; Wood, P. A. Mercury csd 2.0–new features for the visualization and investigation of crystal structures. *J. Appl. Crystallogr.* **2008**, *41*, 466-470.

186. Ilavsky, J. Nika: Software for two-dimensional data reduction. *J. Appl. Crystallogr.* **2012**, *45*, 324-328.

187. Oosterhout, S. D.; Savikhin, V.; Zhang, J.; Zhang, Y.; Burgers, M. A.; Marder, S. R.; Bazan, G. C.; Toney, M. F. Mixing behavior in small molecule:Fullerene organic photovoltaics. *Chem. Mater.* **2017**, *29*, 3062-3069.

188. Areephong, J.; San Juan, R. R.; Payne, A. J.; Welch, G. C. A narrow band gap isoindigo based molecular donor for solution processed organic solar cells. *New J. Chem.* **2015**, *39*, 5075-5079.

189. Parab, K.; Venkatasubbaiah, K.; Jäkle, F. Luminescent triarylborane-functionalized polystyrene: Synthesis, photophysical characterization, and anion-binding studies. *J. Am. Chem. Soc.* **2006**, *128*, 12879-12885.

190. Kung, H., K ; Kung, M. P. Phen-napthalene and phen-quinoline and their use for binding and imaging amyloid plaques. October 16, 2008.

191. Mei, J.; Bao, Z. Side chain engineering in solution-processable conjugated polymers. *Chem. Mater.* **2014**, *26*, 604-615.